

AD-A089 725

GENERAL ELECTRIC CO SANTA BARBARA CA TEMPO
PROCEEDINGS OF THE FIBER OPTICS IN THE NUCLEAR ENVIRONMENT SYMP--ETC(U)
APR 80 R C WEBB

F/G 20/6

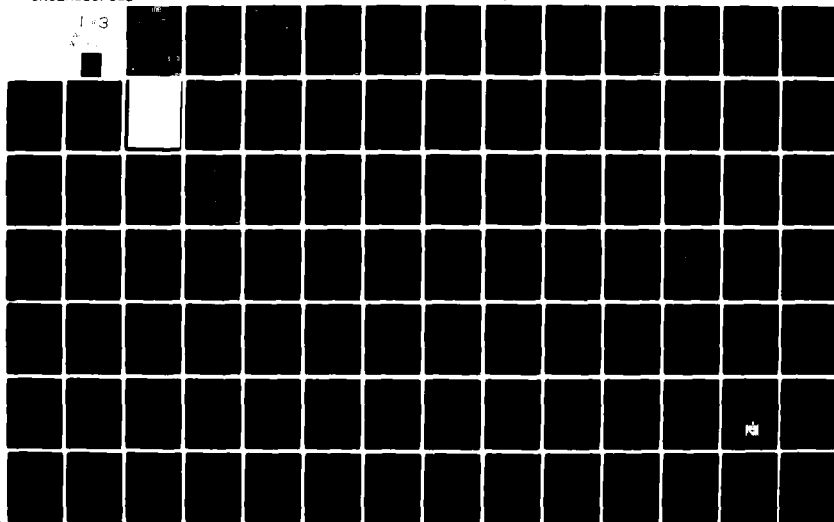
DNA001-79-C-0081

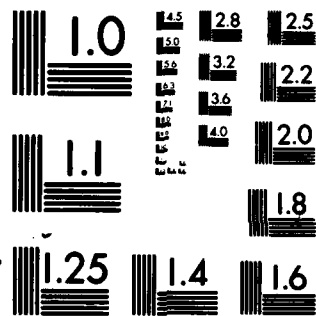
UNCLASSIFIED

DNA-5308P-2

NL

1-3





MICROCOPY RESOLUTION TEST CHART
NATIONAL BUREAU OF STANDARDS-1963-A

(12) LEVEL II
0.5

DNA 5308P-2

**PROCEEDINGS OF THE FIBER OPTICS
IN THE NUCLEAR ENVIRONMENT
SYMPOSIUM 25-27 MARCH 1980**

Volume II - Radiation Physics

R.C. Webb, Symposium Chairman

**General Electric Company—TEMPO
DASIAC
816 State Street
Santa Barbara, California 93102**

30 April 1980

Proceedings

CONTRACT No. DNA 001-79-C-0081

**THIS WORK SPONSORED BY THE DEFENSE NUCLEAR AGENCY
UNDER RDT&E RMSS CODE B337079464 P99QAXDC00809 H2590D.**

DISTRIBUTION STATEMENT A

**Approved for public release;
Distribution Unlimited**

**DTIC
ELECTE
SEP 30 1980
S B D**

Prepared for:

**Director
DEFENSE NUCLEAR AGENCY
Washington, D.C. 20305**

80 8 15 020

DNA 5308P-2

**PROCEEDINGS OF THE FIBER OPTICS IN THE NUCLEAR ENVIRONMENT
SYMPOSIUM 25-27 MARCH 1980
Volume II - Radiation Physics**

**52268025
AD A 089725**

DOC FILE COPY

Destroy this report when it is no longer needed. Do not return to sender.

PLEASE NOTIFY THE DEFENSE NUCLEAR AGENCY, ATTN: STTI,
WASHINGTON, D.C. 20305, IF YOUR ADDRESS IS INCORRECT,
IF YOU WISH TO BE DELETED FROM THE DISTRIBUTION LIST,
OR IF THE ADDRESSEE IS NO LONGER EMPLOYED BY YOUR
ORGANIZATION.

UNCLASSIFIED

SECURITY CLASSIFICATION OF THIS PAGE (When Data Entered)

17 REPORT DOCUMENTATION PAGE		READ INSTRUCTIONS BEFORE COMPLETING FORM	
1. REPORT NUMBER DNA 5388P-2 NH ✓	2. GOVT ACCESSION NO. AD A089725	3. RECIPIENT'S CATALOG NUMBER	
4. TITLE (and Subtitle) Proceedings of the Fiber Optics in the Nuclear Environment Symposium 25-27 March 1980, Volume II, Radiation Physics,		5. TYPE OF REPORT & PERIOD COVERED Proceedings	
7. AUTHOR(s) R.C./Webb Symposium Chairman		6. PERFORMING ORG. REPORT NUMBER	
8. PERFORMING ORGANIZATION NAME AND ADDRESS General Electric - TEMPO DASIAC 816 State Street, Santa Barbara, CA 93102		9. CONTRACT OR GRANT NUMBER(s) DNA001-79-C-0081 ✓	
11. CONTROLLING OFFICE NAME AND ADDRESS Director Defense Nuclear Agency Washington, D.C. 20305		10. PROGRAM ELEMENT, PROJECT, TASK AREA & WORK UNIT NUMBERS P99QAXDC00809	
14. MONITORING AGENCY NAME & ADDRESS (if different from Controlling Office)		12. REPORT DATE 30 Apr 1980	
		13. NUMBER OF PAGES 236	
		15. SECURITY CLASS. (of this report) Unclassified	
		15a. DECLASSIFICATION/DOWNGRADING SCHEDULE	
16. DISTRIBUTION STATEMENT (of this Report) Approved for public release; distribution unlimited.			
17. DISTRIBUTION STATEMENT (of the abstract entered in Block 20, if different from Report)			
18. SUPPLEMENTARY NOTES This work sponsored by the Defense Nuclear Agency under RDT&E RMSS Code B337079464 P99QAXDC00809 H2590D.			
19. KEY WORDS (Continue on reverse side if necessary and identify by block number) Applications Proceedings Communications Radiation physics Manufacturing technology Test results Optical fibers			
20. ABSTRACT (Continue on reverse side if necessary and identify by block number) This two-volume report is a compilation of papers presented at the Fiber Optics in the Nuclear Environment Symposium held at the Harry Diamond Laboratories in Adelphi, Maryland on 25-27 March 1980. The symposium was jointly sponsored by the Defense Nuclear Agency, U.S. Army Electronic Research and Development Command, and Harry Diamond Laboratories. Volume I contains the classified presentations and those unclassified presentations which were presented during the classified sessions of the symposium. Volume II contains the unclassified papers which were presented during the Radiation Physics session.			

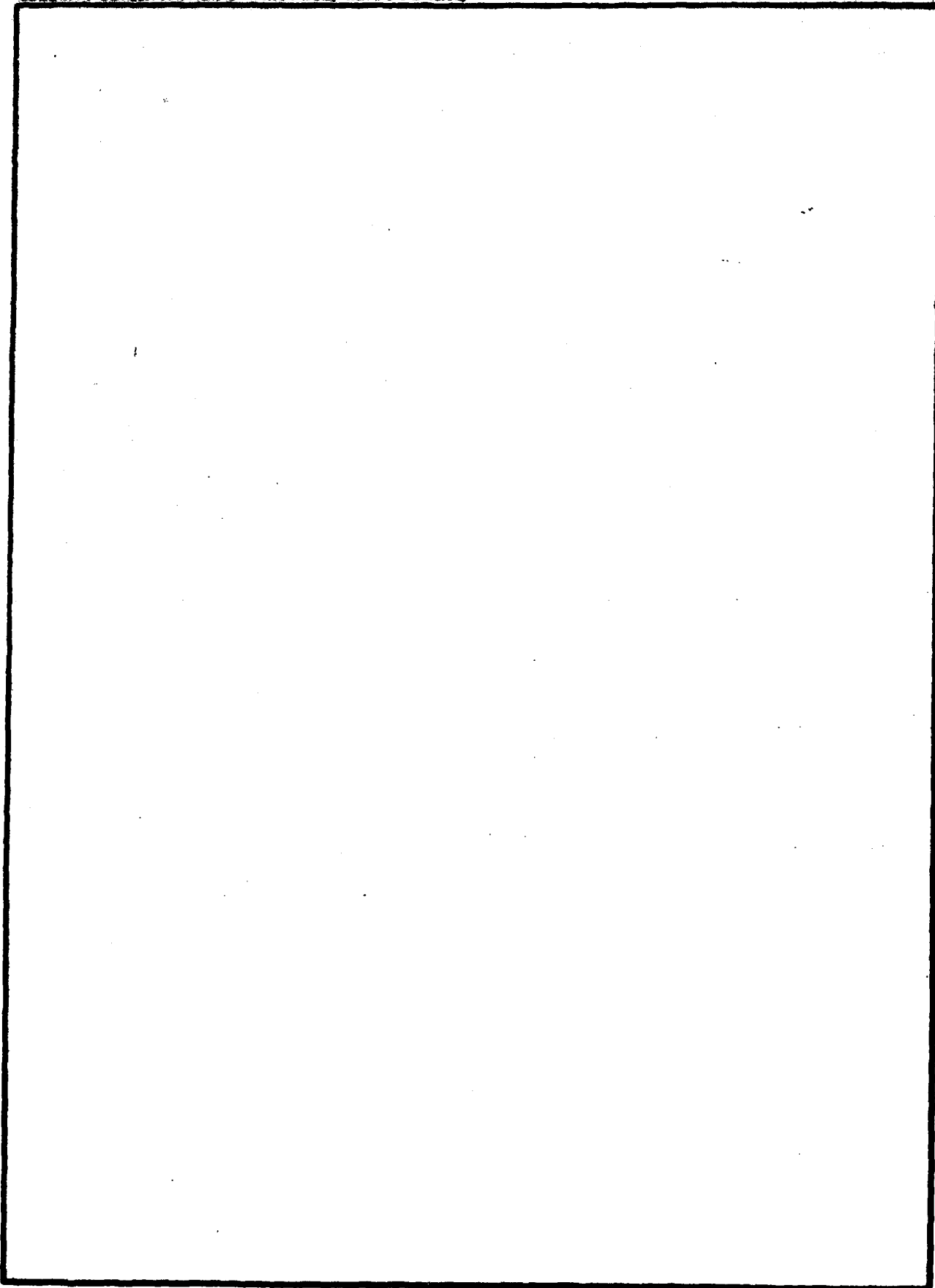
DD FORM 1 JAN 73 1473 EDITION OF 1 NOV 65 IS OBSOLETE

UNCLASSIFIED

SECURITY CLASSIFICATION OF THIS PAGE (When Data Entered)

UNCLASSIFIED

SECURITY CLASSIFICATION OF THIS PAGE(When Data Entered)



UNCLASSIFIED

SECURITY CLASSIFICATION OF THIS PAGE(When Data Entered)

TABLE OF CONTENTS :

	<u>Page</u>
AGENDA	3
ATTENDEES	7
RADIATION-INDUCED DEFECT CENTERS IN FIBER OPTIC GLASSES - D.L. Griscom, et al., NRL	11
THE ROLE OF THE MULTIDOPANTS Sb/P IN RADIATION HARDENING OF OPTICAL FIBERS - J.A. Wall and H. Posen, Hanscom AFB and R. Jaeger, Galileo Electro-Optics Co.	31
RADIATION DAMAGE OF OPTICAL FIBER WAVEGUIDES AT LONG WAVELENGTHS - E.J. Friebele and M.E. Gingerich, NRL	37
TEMPERATURE DEPENDENCE OF RADIATION DARKENING IN OPTICAL WAVEGUIDES - S. Share, HDL	49
RADIATION PERFORMANCE OF GERMANIUM PHOSPHOSILICATE OPTICAL FIBERS AS A FUNCTION OF TEMPERATURE - J.A. Wall and H. Posen, Hanscom AFB and R. Jaeger, Galileo Electro-Optics Co.	57
FAST RECOVERY IN OPTICAL FIBERS EXPOSED TO PULSED RADIATION - R.C. Webb, DNA and R.M. Gilbert and T. Oldham, HDL	71
SHORT-TERM RADIATION EFFECTS IN OPTICAL FIBERS - P.B. Lyons, R.E. Kelly, and L.D. Looney, LASL	83
RADIATION RESPONSE MEASUREMENT OF FIBERS IN THE PICOSECOND REGION - P. Zagarino, et al., EG&G, Inc.	117
PHOTOBLEACHING EFFECTS IN OPTICAL FIBER WAVEGUIDES - E.J. Friebele and M.E. Gingerich, NRL	129
ELECTRON-BEAM INDUCED ABSORPTION AND HARDENING IN FIBER-OPTIC WAVEGUIDES TO 1060-NM LASER PULSES - M.J. Landry and H.P. Davis, SLA	143

TABLE OF CONTENTS (continued)

	<u>Page</u>
CHARACTERIZATION OF LOW-LOSS MULTIMODE OPTICAL FIBERS FOR NUCLEAR DIAGNOSTICS - J.W. Ogle, et al., EG&G, Inc. and P.B. Lyons, LASL	159
RADIATION DEGRADATION AND RECOVERY IN LONG FIBER-OPTICS DATA LINKS - I. Arimura and R.S. Caldwell, Boeing Aero- space Co.	175
NEUTRON DAMAGE EFFECTS IN Ga _{1-x} Al _x As LEDs - C.E. Barnes, SLA	189
TEMPERATURE DEPENDENCE OF NEUTRON DAMAGE TO COMMERCIAL GaAsP LED DEVICES - J.M. Lambert, P.A. Treado, et al., Georgetown University and NRL	191
TRANSIENT EFFECTS OF IONIZING RADIATION IN Si, InGaAsP, GaAlSb, AND Ge PHOTODIODES - J.J. Wiczer, C.E. Barnes, and L.R. Dawson, SLA	209
A RADIATION-HARDENING SCHEME FOR AN ANALOG FIBER-OPTIC DATA LINK - Raine M. Gilbert, HDL	223

ACCESSION for	
WHS	White Section <input checked="" type="checkbox"/>
DDC	Buff Section <input type="checkbox"/>
UNANNOUNCED	<input type="checkbox"/>
JUSTIFICATION	
BY	
DISTRIBUTION/AVAILABILITY CODES	
Dist.	AVAIL. and/or SPECIAL
A	

AGENDA

FIBER OPTICS IN THE NUCLEAR ENVIRONMENT HDL, ADELPHI, MARYLAND

25-27 MARCH 1980

SYMPOSIUM CHAIRMAN—R.C. WEBB, DNA

Tuesday, 25 March

0800-0900 Registration/Badging

INTRODUCTION AND INVITED SPEAKERS

0900-0905	Welcoming Remarks	Col. Benoit, HDL
0905-9010	Introductory Remarks	Col. E.D. Frankhouser, DNA
0910-0930	Keynote Speaker	Dr. E. Conrad, DNA
0930-1000	Fiber Optics Technology	P. Lyons, LASL
1000-1030	Fiber Optics Manufacturing Technology	P. Schultz, Corning Glass
1030-1050	BREAK	
1050-1120	An Overview of Radiation Effects on Optical Fibers	G. Sigel, Jr., NRL

APPLICATIONS

Chairman—P. Lyons, LASL

1120-1150	Applications of Optical Fibers in Nuclear Test Diagnostics	P.B. Lyons, E.K. Hodson, L.D. Looney, LASL L. Franks, L.P. Hocker, S. Lutz, R. Malone, J. Manning, M.A. Nelson, R. Selk, D. Simmons, EG&G, Inc.
1150-1210	Movie—"Fiber Optics for Tactical Communications"	U.S. Air Force Systems Command
1215-1330	LUNCH	
1330-1350	Fiber Optic Receiver Hardening Techniques	A. Johnston, R. Caldwell, Boeing Aerospace Co.
1350-1410	An Improved Balun for the SXTF Fiber Optics Link	J. Vanderwall, HDL

APPLICATIONS (Cont'd)

1410-1430	A Multiplex Fiber Optics Link for 5 to 20 kHz Data in Nuclear Field Tests	W. Naumann, R. Hogg, ETI
1430-1450	Fiber Optics Data Link for Miners Iron*	E. Bick, W. Naumann, R. Hogg, ETI R. Webb, DNA
1450-1510	An Advanced 500 mHz Fiber Optic Signal Link	J. Blackburn, HDL
1510-1530	BREAK	
1530-1550	Common Timing of Fiber Cables in Imaging Experiment	J. Manning, C. Gow, J. Marshall, R. Malone, EG&G, Inc.
1550-1610	Fiber Optics Systems in a Nuclear Radiation Environment	B. Metcalf, J. Quarato, MITRE Corp.
1610-1630	Optical Fiber Impact Fuze Concept	J. Wiczer, SLA
1630-1640	Session Chairman Summary	
1700-1900	No Host Social Event	

Wednesday, 26 March

RADIATION PHYSICS Chairman—G. Sigel, Jr., NRL

0900-0905	Introduction	G. Sigel, Jr., NRL
0905-0920	Radiation Induced Defect Centers in Fiber Optic Glasses	D. Griscom, E. Friebele, M. Staplebrook, G. Sigel, Jr., NRL
0920-0940	The Role of the Multidopants Sb/P in Radiation Hardening of Optical Fibers	H. Posen, J. Wall, RADC R. Jaeger, Galileo Electro Optics Co.
0940-1000	Radiation Damage of Optical Fiber Waveguides at Long Wavelengths	E. Friebele, M. Gingerich, NRL
1000-1020	Temperature Dependence of Radiation Darkening	S. Share, HDL
1020-1040	Radiation Performance of Germanium Phosphosilicate Optical Fibers as a Function of Temperature	J. Wall, H. Posen, RADC R. Jaeger, Galileo Electro Optics Co.
1040-1100	BREAK	

* Presented on Wednesday, 26 March.

RADIATION PHYSICS (Cont'd)

1100-1120	Fast Recovery in Optical Fibers Exposed to Pulsed Radiation	R. Webb, DNA R. Gilbert, T. Oldham, HDL
1120-1140	Short Term Radiation Effects in Optical Fibers	P. Lyons, R. Kelley, L. Looney, LASL
1140-1200	Radiation Response Measurement of Fibers in the Picosecond Region	N. Norris, M. Nelson, J. Ogle, P. Zagarino, C. Lin, T. Davies, EG&G, Inc.
1200-1220	Photobleaching Effects in Optical Fiber Waveguides	E. Friebele, M. Gingerich, NRL
1220-1330	LUNCH	
1330-1350	Electron-Beam Induced Absorption and Hardening in Fiber Optic Waveguides to 1060nm Laser Pulses	M. Landry, H. Davis, SLA
1350-1410	Optical Fiber Characterization for Nuclear Diagnostics	J. Ogle, M. Nelson, EG&G, Inc. P. Lyons, LASL
1410-1430	Radiation Degradation and Recovery in Long Fiber Optics Data Links	I. Arimura, R. Caldwell, Boeing Aerospace Co.
1430-1450	Neutron Damage Effects in $Ga_{1-x}Al_xAs$	C. Barnes, SLA
1450-1510	BREAK	
1510-1530	Temperature Dependence of Neutron Damage to Commercial GaAsP LED Devices	R. Albas, P. Treado, NRL J. Lambert, L. Leopold Georgetown University
1530-1550	Transient Effects of Ionizing Radiation IN Si, InGaAsP, GaAlSb and Ge Photodiodes	J. Wiczer, C. Barnes, L. Dawson, SLA
1550-1600	Session Chairman Summary	

Thursday, 27 March

APPLICATIONS (Cont'd) Chairman—R. Gilbert, HDL

0900-0905	Introduction	R. Gilbert, HDL
0905-0930	Fiber Optics for Navy Systems Application	R. Greenwell, R. Kochanski, U.S. Navy, NOSC

APPLICATIONS (Cont'd)

0930-1000	Some Recent Fiber Optics Research, Development and Applications Conducted by the Air Force	E.W. Taylor, U.S. Air Force, AFWL
1000-1030	Review of the US Army CORADCOM Fiber Optics Nuclear Hardening Program	S. DiVita, A. Mondrick, L. Dworkin, U.S. Army CORADCOM
1030-1050	BREAK	
1050-1110	Hardened Fiber Optic Application in Ballistic Missile Defense	D. DeKalb, BMD Systems Command G. Landwehr, M. Price, Teledyne Brown
1110-1130	A Radiation Hardening Scheme for an Analog Fiber Optic Data Link	R. Gilbert, HDL
1130-1150	Miners-Iron Test of Optical Fibers	R. Heckman, J. Allen, S. Dolce, J. Hohlfelder, E. Machin, SLA
1150-1310	LUNCH	
1310-1330	Fracture Analysis of Optical Fibers	J. Mecholsky, SLA
1330-1350	Optical Sensors for Ground Shock Measurements	B. Armstrong, C. Welch, WES
1350-1410	Brightness Temperature Measurements for High Energy Jet Propagation	H. Glenn, LLL
1410-1430	A Summary of Seven Years Work in Radiation Effects on Electro-Optics	J. Mullis, 1st Lt. M. McQuade, AFWL
1430-1450	Session Chairman Summary	
1450-1515	Concluding Remarks	G. Sigel, Jr., NRL

ATTENDEES

Aggarwal, Ishwar (Valtec Corp.)	Davis, Hartwell (Merritt Cases)
Alcaraz, Ernest (JAYCOR)	Davis, William (Sperry Univac)
Alfonse, William (GE-TEMPO)	Dawson, Larry (SLA)
Allas, Richard (NRL)	DeKalb, Richard (BMD)
Andersen, Rodney (Galileo)	Deevy, Thomas (DNA/SPTD)
Arimura, Itsu (Boeing)	DeNobel, Richard (VITRO)
Armstrong, Byron (WES)	Derrington, Dolores (PAGE Comm.)
Ashley, Ernest (AVCO)	DeVita, Sam (CORADCOM)
Assendrup, James (Litton)	Dolce, Sanders (SLA)
Baba, Anthony (HDL)	Dudash, Michael (GE-TEMPO)
Balicki, Frederic (NWEPO)	Dunn, John (DNA)
Barnes, Charles (SLA)	Dworkin, Larry (CORADCOM)
Basdekas, Nicholas (ONR)	Eisen, Harvey (HDL)
Bauer, Martin (UCC-OFNL)	Femenias, Raymond (HDL)
Beasley, Marvin (DNA)	Flaming, Gilbert (ERADCOM)
Beaty, Randall (DNA)	Flory, Robert (DNA)
Belliveau, Louis (HDL)	Flory, Thomas (NWEPO)
Benoit, William (HDL)	Flyer, Irving (HDL)
Bernstein, Benjamin (ERADCOM)	Frankhouser, E.D. (DNA)
Bick, Frederick (ETI)	Friebele, Joseph (NRL)
Blackburn, James (HDL)	Funkhouser, Michael (HDL)
Blair, G. Richard (Hughes AC)	Gantick, Noel (DNA)
Boesch, Harold (HDL)	Gilbert, Raine (HDL)
Bonner, George (WES)	Gingerich, Michael (DNA)
Boss, William (DoE NV)	Glenn, H. (LLL)
Brandt, Howard (HDL)	Goucher, Allen (DoE)
Brown, Thomas (DNA)	Griscom, David (NRL)
Burres, Victor (GE)	Gullickson, Richard (DNA)
Bushell, Michael (HDL)	Gwaltney, James (NWEPO)
Byrn, N. Rick (Nichols Res.)	Halder, Ronald (USAF)
Cabayan, Hriar (LLL)	Halpin, Joseph (HDL)
Caldwell, Robert (Boeing)	Hardwick, Walter (JAYCOR)
Calovini, Joseph (Holmes & Narver)	Heckman, R. (SLA)
Campbell, Neil (DNA)	Hoehn, Hubert (NSA)
Cansler, Frank (Ft. Monmoth)	Hogg, Robert (ETI)
Carter, William (HDL)	Holland, John (FCDNA)
Chapman, Terry (DNA)	Huebner, Harley (Newport News Shipbuilding)
Chow, Kungta (LMSC)	Huybrechts, Luke (ITT)
Coleman, Philip (SSS)	Jaeger, Raymond (Galileo)
Concordia, John (HDL)	Janee, Helmar (GRC)
Conrad, Edward (DNA/DDST)	Johnston, Allan (Boeing)
Conway, Teresa (HDL)	Joonsar, Heikki (DNA)
Corrigan, John (NWEPO)	Kacur, John (Automation Industries)

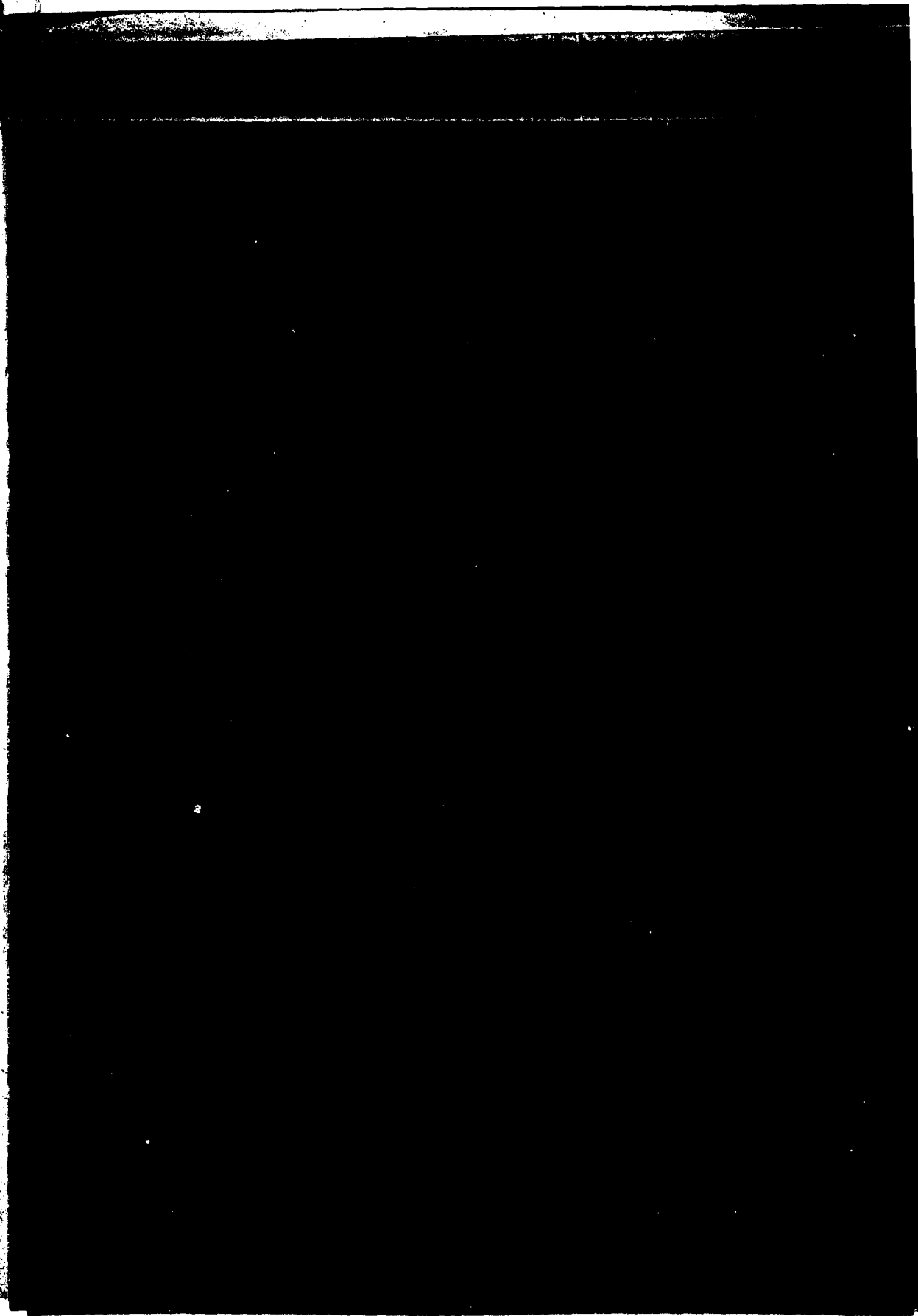
ATTENDEES (continued)

Kelley, Dennis (DLA/DESC)
 Kelley, Paul (Draper Labs)
 Kelly, Robert (LAAO)
 Kemp, Victor (DNA)
 Kennedy, Thomas (DNA/SPTD)
 Kinser, Donald (Vanderbilt Univ.)
 Klebers, John (HDL)
 Kleekamp, C. (MITRE)
 Knauer, James (LMSC)
 Knowles, C.P. (DNA)
 Kochanski, R. (NOSC)
 Kronenberg, Stanley (ET&DL)
 Kubo, Arthur (DNA)
 Lambert, James (NRL)
 Landry, Murphy (SLA)
 Landwehr, George (Teledyne-Brown)
 Leu, Vernon (DoE)
 Looney, Larry (LAAO)
 Lyons, Lawrence (DCA)
 Lyons, Peter (LASL)
 Manning, John (EG&G)
 Manriquez, Rolando (HDL)
 McGarrity, James (HDL)
 McGuire, Thomas (GeoCenters)
 McLean, Flynn (HDL)
 Mecholsky, John (SLA)
 Mehl, Clarence (SLA)
 Merkel, George (HDL)
 Metcalf, Bruce (MITRE)
 Meyer, Owen (HDL)
 Miller, Glenn (SLA)
 Miller, H. (SLA)
 Mohr, William (DNA)
 Moore, Raymond (NBS)
 Mostovoj, Vitali (SHAPE)
 Naumann, Walter (ETI)
 Nelson, Melvin (DoE)
 Nelson, R. (Ft. Huachuca)
 Nylund, Everett (GARD)
 Ogle, James (DoE)
 Oldham, Timothy (HDL)
 Orrell, Stanley (DoE)
 Osborn, Daniel (KSC)
 Patrick, Eugene (HDL)
 Pitt, Norman (USAF)
 Plimpton, James (SLA)
 Polimadei, Roland (NWEPO)
 Pollard, John
 Price, Melvin (Teledyne-Brown)
 Quarato, J. (MITRE)
 Raley, Robert (BRL)
 Randall, Eric (Galileo)
 Rathbun, Edwin (NSWC)
 Renzoni, Rosanna (BDM)
 Roark, Glenn (KSC)
 Roemer, William (NSA)
 Rogers, Samuel (RDA)
 Rosado, John (HDL)
 Sandoval, Liberato (EG&G)
 Shallhorn, Dale (HDL)
 Scharf, William (HDL)
 Schifano, Joe (HDL)
 Schiff, Alvin (CSC)
 Scott, Walter (HDL)
 Self, Charles (HDL)
 Share, Stewart (HDL)
 Shirkey, Robert (FCDNA)
 Shirn, Robert (FCDNA)
 Shunk, Reynold (Electromechanical Systems)
 Sigel, George (NRL)
 Sites, Kenneth (SAI)
 Solomon, Harvey (NSA)
 Sommers, Helmut (HDL)
 Spohn, Daniel (HDL)
 Stewart, Larry (Spectronics, Inc.)
 Stewart, Richard (IRT)
 Stover, Harris (DCA)
 Sturman, Patricia (GE-TEMPO)
 Swain, Ronald (Newport News Shipbuilding)
 Swanic, Anthony (DoE)
 Swant, David (GE)
 Tangonan, Gregory (Hughes AC)
 Tasca, Dante (GE)
 Taylor, Edward (AFWL)
 Taylor, Henry (NRL)
 Taylor, Robert (KSC)
 Teel, George (BRL)
 Thompson, Robert (ITT)
 Tobolski, Jan (McDonnell Douglas)
 Tracy, Philip (KSC)
 Treado, Paul (NRL)
 Ulrich, Reinhard (HDL)
 Vanderwall, Jonathan (HDL)
 Vassilakos, Demetrios (TRW)
 Vault, W. (HDL)
 Wall, James (Hanscom AFB)

ATTENDEES (continued)

Walter, Thomas (TRW)
Wasilik, John (HDL)
Webb, Robert (DNA/SPTD)
Weckback, James (Raytheon)
Whitten, James (GE)
Wiczer, James (SLA)
Wilkins, William (BDM)
Winokur, Peter (HDL)
Yang, Andrew (Hanscom AFB)
Yesensky, Richard (STRA)
Yorio, Francis (Corning Glass)
Zagarino, Paul (DoE)
Zann, David (Wright Patterson AFB)

THIS PAGE IS INTENTIONALLY LEFT BLANK



RADIATION-INDUCED DEFECT CENTERS IN FIBER OPTIC GLASSES

D. L. Griscom, E. J. Friebele, M. Stapelbroek, and G. H. Sigel, Jr.

**Optical Sciences Division
Naval Research Laboratory
Washington, DC 20375**

I. INTRODUCTION

While fiber optic waveguides possess many characteristics which are ideally suited for military voice channels and data links, it is now known that the fibers themselves are vulnerable to permanent or transient optical attenuation when placed in nuclear radiation environments.¹ The natures of the color centers responsible for this radiation-induced degradation are best probed by the technique of electron spin resonance (ESR). Types of information obtainable by ESR include atomic arrangements, bond angles, and the degrees of electron or hole localization on specific nuclei at the defect sites. Several recent review articles²⁻⁷ offer critical overviews of the vast literature dealing with ESR investigations of radiation-induced defects in glasses. The present paper serves the more limited purpose of summarizing a few of the important conclusions of these studies pertaining to glasses currently in use or envisioned for fiber optic applications.

In principle, the detailed understanding of radiation-damage mechanisms afforded by ESR should make it possible to tailor fiber compositions and/or processing parameters in such ways as to minimize the intensities and/or durations of the induced optical absorption in the wavelength windows of interest. In practice, however, it has proven difficult to make the needed correlations between optical bands and ESR centers. The present paper discusses some of the progress which has been made and mentions some opportunities for future advances in the radiation hardening of fiber optic waveguides.

II. DEFECTS IN OXIDE GLASSES

Figure 1 provides a broad-brush synopsis of some of the defect structures which are believed to exist in oxide glasses. A perfect glass, of course, is envisioned as a continuous random network⁸ of RO_4 tetrahedra and/or RO_3 triangles joined together at the corners. Here, R is a so-called network-forming ion such as Si, B, P, Ge, or Al. Negatively charged imperfections in the as-quenched glass include trivalent network-formers $R_B=B, Al$ in tetrahedral sites and also nonbridging oxygens (Fig. 1a). These species are generally charge compensated, however, by positively charged interstitial network-modifying cations C. Electrically neutral imperfections include the neutral oxygen vacancy, the peroxy linkage, and network modifiers R_A having the same valency as R but differing electron affinities (e.g., $R_A = Ge, R = Si$).

The primary effect of nuclear radiations on glasses is ionization⁷. In fact, many electron-hole pairs are formed, virtually all of which recombine within microseconds. Only a tiny fraction of these ionization-induced electrons and holes become separated from one another and trap at defect sites as schematically indicated in Fig. 1b. Note that the interstitial cations C then may diffuse to compensate and stabilize some of the trapped charges. Note also that the trapping sites illustrated here preexist in the glass prior to irradiation. Additional trapping sites in the form of broken bonds or atomic displacements may be created

by the radiation itself. Generally displacement damage does not become significant at doses lower than 10^8 rads, however.

Not shown in Fig. 1 are a number of defect types involving electron or hole trapping on multivalent elements. Examples include $\text{Fe}^{2+} \leftrightarrow \text{Fe}^{3+}$ and $\text{Cu}^+ \rightarrow \text{Cu}^{2+}$ conversions when iron or copper are present as impurities,⁹ but they also include $\text{Ti}^{4+} \rightarrow \text{Ti}^{3+}$ and $\text{Pb}^{2+} \rightarrow \text{Pb}^{3+}$ in fiber glasses where titanium¹⁰ or lead¹¹ is present as a major constituent. Due to limitations on length, the present paper will not further discuss trapping sites involving simple valence changes. Problems associated with such defects are not to be minimized, however.

III. SOME INTRINSIC DEFECT TYPES

The following sections will be concerned primarily with defect types in pure fused silica and doped fused silica, since these compositions are among the most promising for radiation hardened communications links spanning distances of the order of kilometers.

A. The aluminum-oxygen and boron-oxygen hole centers

The best known impurity-related color center in α -quartz (an optical quality crystalline polymorph of fused silica) is the so-called "Al center". Extensive and elegant ESR studies reviewed in Ref. 12 have shown this defect to have the structure illustrated in Fig. 2. Here the unpaired electron spin (in this case a hole) is trapped in a nonbonding 2p orbital of an oxygen bridging between a silicon and a silicon-substituted aluminum in the quartz structure. The hole is bound to the aluminum site because aluminum has a lower ionic charge (3+) than the silicon for which it is substituted (4+). Essentially the same defect has been shown to occur in glassy silica containing aluminum impurities (see Ref. 5 for a review).

Boron has the same valency as aluminum and, like aluminum, can exist in glasses in tetrahedral coordination. It is thus not surprising that the boron analogue of the "Al center" has been found to exist in¹³ irradiated boron-doped silica compositions relevant to fiber optics. The ESR data support a model analogous to that of Fig. 2 where the Al is replaced by B.

B. The E' center

The most familiar intrinsic defect center in both quartz and fused silica is the E' center, which is known to comprise an unpaired electron spin trapped at the site of an oxygen vacancy. The understanding of the nature of this center originally flowed from work in α -quartz, where a knowledge of the crystallography could be brought to bear (see, e.g. Ref. 5). However, in the case of silica glass, some controversy has persisted until only recently. The definitive demonstration of the nature of the E' center in silica involved first proving that an observed pair of hyperfine lines having a splitting of 420 Gauss (Fig. 3)

are due to ^{29}Si rather than to a proton. As seen in Fig. 3, this was done by isotopic substitution.¹⁴ The magnitude of the ^{29}Si hyperfine splitting showed that the unpaired spin must be localized in a dangling tetrahedral orbital of a single silicon atom in the glass network. The original assumption that this silicon is bonded to three equivalent oxygens (as illustrated) was recently confirmed¹⁵ by studies of samples enriched in ^{17}O (see spectra at the lower left of Fig. 3).

There remain the questions of whether the three-coordinated silicon trapping the unpaired spin resides at the site of an oxygen vacancy and whether it comprises a trapped hole¹⁶ or a trapped electron. It would appear that when boron¹³ or aluminum¹⁶ are present in an otherwise pure silica glass, the Si E' center may consist of an electron trapped at an isolated three-coordinated silicon in the network. But in high-purity, low-OH fused silicas evidence suggests¹⁷ that the E' center takes the form of a hole trapped at an oxygen vacancy; this model will be discussed further below.

The existence of E' centers localized on B and Al atoms in the glass network has also been demonstrated. The 4-line hyperfine structure of the B E' center¹³ and the 6-line structure of the Al E' center¹⁶ are easily distinguishable from the ^{29}Si doublet signature (Fig. 3) of the Si E' center. These centers are almost certainly the results of electron trapping at the sites of three-coordinated borons and aluminums in the glass structure.

C. Oxygen-associated hole centers

Another class of intrinsic defect centers in high-purity silicas are the oxygen-associated hole centers or OHCs.¹⁷ These defects are characterized by broad ESR spectra with positive g shifts (Fig. 4). Two varieties of OHCs have been distinguished so far; these were originally termed the "wet" and "dry" OHCs according to their relative prevalence in silicas of high and low OH contents, respectively. The "wet" OHC (Fig. 4b) was shown¹⁷ by ^{17}O -enrichment experiments to comprise a hole trapped in a pure p orbital of a single oxygen atom which was assumed to be nonbridging. The model suggested for the formation of the "wet" OHC is illustrated in Fig. 5.

On the other hand, the ^{17}O hyperfine structure of the "dry" OHC was the basis for identifying this particular defect as a peroxy radical.¹⁸ The proposed model for the formation of the peroxy radical defect is indicated in Fig. 6b. Namely, it has been suggested¹⁸ that this defect results from the trapping of a hole on a preexisting peroxy linkage in the glass network, followed by certain structural relaxations resulting in its stabilization. In this picture, the peroxy linkage precursor could be viewed as one half of a Frenkel defect pair--the other half being the neutral oxygen vacancy. As illustrated in Fig. 6a, the trapping of a hole at the vacancy site, followed by structural relaxation, would result in the formation of an E' center. The latter scheme has been proposed¹⁹ to explain the occurrence of E' centers in

α -quartz and has received wide general acceptance.⁵ It is also believed to be the mode of E' center production in high-purity low-OH fused silicas¹⁷.

D. Defects associated with germanium

Germanium is a common dopant employed to raise the index of the fiber core to produce waveguiding in all-glass fibers. As alluded to in Sec. II, a germanium atom substituted for a silicon is a potential electron trap. While the existence of substitutional-germanium trapped electron centers has been demonstrated in α -quartz (see, e.g., Ref. 5), they have never been detected in germanium-doped silica glass. Rather, the ESR spectra observed in irradiated $\text{SiO}_2\text{:GeO}_2$ glass have been ascribed²⁰ to a series of Ge E' centers with slightly differing spectral characteristics depending on the number of next-nearest-neighbor germanium atoms.

E. Defects associated with phosphorus

Phosphorus is another common dopant used in all-glass optical fibers and one which has a profound effect on the magnitude and fade rate of the radiation-induced optical attenuation.¹ While a thorough ESR study has not yet been carried out on phosphosilicate compositions, much is known about the natures of phosphorus-associated defects in pure phosphate glasses. The well-known "phosphorus-oxygen hole center" spectrum has been tentatively ascribed to a hole trapped on two nonbridging oxygens bonded to the same phosphorus atom.²¹ On the other hand, a pair of hyperfine doublets²¹ denoted P_1 and P_2 have been provisionally assigned to the trapped-electron structures schematically illustrated in Fig. 7b and c.

IV. PULSE ANNEALING EXPERIMENTS AND ESR-OPTICAL CORRELATIONS

Pulse annealing experiments are one means of establishing ESR-optical correlations, as well as a means of elucidating the kinetics of defect formation and decay. In such experiments the samples are irradiated at some fixed temperature and ESR (plus optical) spectra are obtained at the same temperature following a succession of isochronal (fixed time) anneals at higher temperatures. The examples of the present section will be specialized to high-purity fused silicas.

Figure 8 shows the relative populations of a variety of ESR defect centers in Suprasil W-1 (<5 ppm OH) and Suprasil 1 (\sim 1200 ppm OH) following γ -irradiation at room temperatures and a succession of 10-minute pulse anneals up to 650°C. It can be seen that there is an excellent correlation between the OHCs and an optical absorption band at 7.6 eV (163 nm) in the vacuum ultraviolet. A similar correlation (not shown) was also noted between the E' center and an optical band at 5.8 eV (215 nm). (The latter correlation was established earlier in an elaborate series of experiments.²²)

Another striking feature of Fig. 8 is the great qualitative difference in color center decay modes between high-OH and low-OH fused silicas. This difference is even more dramatically exemplified in Fig. 9, where the samples were x-irradiated at cryogenic temperature (77K) and observed as a function of pulse anneals up to 370°K.²³ The hydrogen atom (H^0) is the most plentiful defect observed in Suprasil 1 after irradiation at 77K, but it decays out totally at temperatures above 120K and is not even observed in samples irradiated at room temperature. It should be emphasized, however, that the ESR experiments are typically performed hours after irradiation. Thus, it is not ruled out (and in fact is quite likely) that hydrogen atoms are produced in high-OH silicas on a very short time scale following exposure to pulsed irradiation at ambient temperatures. As yet, no ESR-optical correlations have been attempted in the low-temperature range, but such experiments may one day provide the explanation of some features of the transient optical attenuation induced in pure-silica core fibers by pulsed irradiation¹.

The principal optical absorption bands of the E' center and the peroxy radical ("dry" OHC) fall in the UV and vacuum-UV, respectively, and hence are of little practical concern to fiber optic communications. The reason these particular correlations were emphasized in the preceding paragraphs is that the optical absorptions were particularly strong, thus greatly facilitating the experiments. By contrast, the induced absorptions in the visible-ir wavelength regime are much weaker, though still comprising contributions from several overlapping bands.^{1,24,25} Some pulse anneal data for Suprasil 1 are shown in Fig. 10,²⁶ where it can be seen that the induced absorption at 1.99 eV (620 nm) is ~ 10 times weaker than the absorption in the UV. While a good correlation is apparent between the E' center and the absorption at 5.78 eV, neither the E' center nor the OHCs correlate with the induced absorption near 620 nm. At the present, the color centers responsible for the optical bands in the latter region are unknown.

In this context, it is interesting to recall that an optical band at 630 nm can be produced in high-purity low-OH silicas by the mere act of drawing them into fibers.^{27,28} Despite intensive efforts,^{17,29} it has not been possible to correlate the drawing-induced optical band with any ESR signal. While it was shown that the peroxy radical could be induced in low-OH silicas by fiber drawing, its ESR spectrum did not correlate with the 630 nm band, as can be seen in Fig. 11. The origin of the drawing-induced absorption²⁹ (which may be identical with that of the radiation induced absorption)²⁹ at 630 nm remains an unsolved mystery. It would appear that the color center responsible is of the spin paired (diamagnetic) type.

V. SUMMARY AND FUTURE PROSPECTS

By means of electron spin resonance a wide range of defect centers in fiber optic glasses has been identified and characterized in considerable detail. Although some progress has been made in correlating these

defects with optical bands, to date most correlations have been with bands in the UV and vacuum-UV spectral regions. An important defect-associated band at 630 nm in high-purity fused silica seems to be due to a paired-spin (diamagnetic) center fundamental to SiO_2 . Time resolved spectral studies of the induced attenuation in silica-based optical waveguides are presently yielding important clues to the origin of this band.²⁵

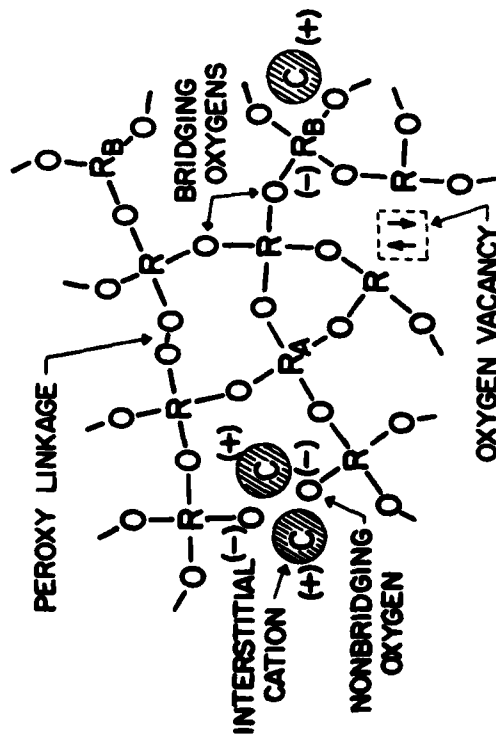
Many future fiber optic systems may operate in the near infrared (1.3-1.55 μm) spectral region to take advantage of the low intrinsic loss and low material dispersion afforded in that regime. However, it has been shown²⁴ that most candidate fiber glasses exhibit broad radiation-induced absorption bands centered near 1.5 μm . These bands are most likely due to oxygen-associated trapped-hole centers, since the ESR data for the boron-oxygen hole center and the peroxy radical predict^{19,24,30} the existence of absorption bands at 1.5 and 2.8 μm , respectively. Further combined ESR and optical studies may ultimately prove such correspondences and open the way to the development of optical fiber systems which are hardened against nuclear radiation.

REFERENCES

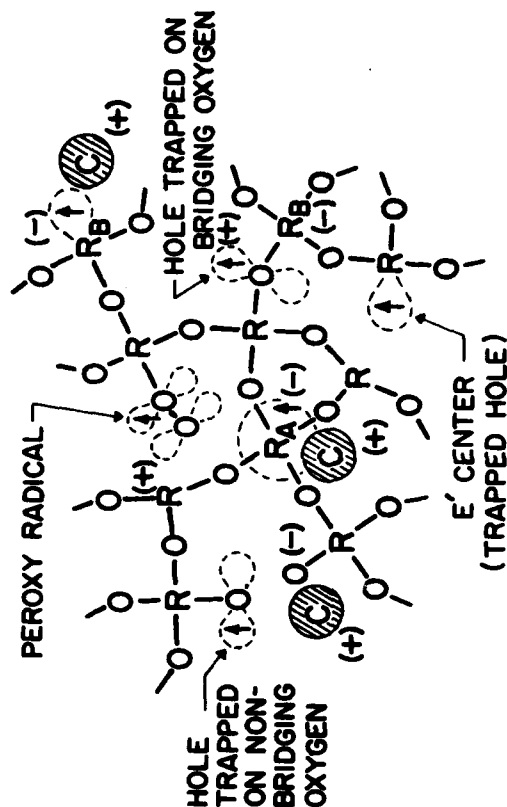
1. E. J. Friebele, Optical Engineering **18**, 552 (1979).
2. D. L. Griscom, J. Non-Cryst. Solids **13**, 251 (1973/74).
3. D. L. Griscom, in: Defects and Their Structure in Nonmetallic Solids, eds. B. Henderson and A. E. Hughes (Plenum, New York, 1976), p. 323.
4. D. L. Griscom, J. Non-Cryst. Solids **31**, 241 (1978).
5. D. L. Griscom, in: The Physics of SiO₂ and its Interfaces, ed., S. T. Pantelides, (Pergamon Press, New York, 1978), p. 232.
6. D. L. Griscom, Proc. of Conf. on Electrical, Magnetic, and Optical Properties of Glasses, J. Non-Cryst. Solids (in press, 1980).
7. E. J. Friebele and D. L. Griscom, in: Treatise on Materials Science and Technology, Vol. 17. Glass II, M. Tomozawa and R. Doremus (Academic Press, New York, 1979) p. 257.
8. H. Rawson, Inorganic Glass-Forming Systems, (Academic Press, New York, 1967).
9. G. R. News, P. Pantelis, J. L. Wilson, R. W. J. Uffen, and R. Worthington, Opto-Electronics **5**, 289 (1973); G. H. Sigel, Jr., in: Treatise on Materials Science and Technology, Vol. 12, Glass I, eds. M. Tomozawa and R. Doremus (Academic Press, New York, 1977), p.5.
10. E. J. Friebele, D. L. Griscom, R. J. Ginther, and G. H. Sigel, Jr., Proc. X Int. Cong. on Glass, Kyoto, Japan (1974), pp. 6-16.
11. E. J. Friebele, Proc. XI Int. Cong. on Glass, Vol. 3, Prague (1977), p. 87.
12. J. A. Weil, Radiation Effects **26**, 249 (1975).
13. D. L. Griscom, G. H. Sigel, Jr., and R. J. Ginther, J. Appl. Phys. **47**, 960 (1976).
14. D. L. Griscom, E. J. Friebele, and G. H. Sigel, Jr., Solid State Comm. **15**, 479 (1974); D. L. Griscom, Phys. Rev. B **20**, 1823 (1979).
15. D. L. Griscom, (to be published).
16. K. L. Brower, Phys. Rev. B **20**, (1979).

17. M. Stapelbroek, D. L. Griscom, E. J. Friebele, and G. H. Sigel, Jr., J. Non-Cryst. Solids 32, 313 (1979).
18. E. J. Friebele, D. L. Griscom, M. Stapelbroek, and R. A. Weeks, Phys. Rev. Lettr. 42, 1346 (1979).
19. F. J. Feigl, W. B. Fowler, and K. L. Yip, Solid State Comm. 14, 225 (1974); K. L. Yip and W. B. Fowler, Phys. Rev. B 11, 2327 (1975).
20. E. J. Friebele, D. L. Griscom, and G. H. Sigel, Jr., J. Appl. Phys. 45, 3424 (1974).
21. R. A. Weeks and P. J. Bray, J. Chem. Phys. 48, 5 (1968).
22. R. A. Weeks and E. Sonder, in : Symposium on Paramagnetic Resonance, Vol. 2, ed., W. Low (Academic Press, New York, 1963). p. 869.
23. M. Stapelbroek, (unpublished data): D. L. Griscom, M. Stapelbroek, and E. J. Friebele, (to be published).
24. E. J. Friebele, G. H. Sigel, Jr., and M. E. Gingerich, in Fiber Optics: Advances in Research and Development, eds., B. Bendow and S. S. Mitra (Plenum Press, New York, 1979), p. 355.
25. E. J. Friebele and M. E. Gingerich, Proc. XII Int. Cong. on Glass, Albuquerque, NM (1980), (to be published).
26. D. L. Griscom, G. H. Sigel, Jr., and E. J. Friebele, Proc. XI Int. Cong. on Glass, Vol. 1, Prague (1977) p. 6.
27. P. Kaiser, J. Opt. Soc. Am. 64, 457 (1974).
28. P. Kaiser, A. R. Tynes, H. W. Astle, A. D. Pearson, W. G. French, R. E. Jaeger, and A. H. Cherin, J. Opt. Soc. Am. 63, 1141 (1973).
29. E. J. Friebele, G. H. Sigel, Jr., and D. L. Griscom, Appl. Phys. Lett. 28, 516 (1976); E. J. Friebele, G. H. Sigel, Jr., and D. L. Griscom, Proc. 2nd Euro. Conf. on Optical Fiber Transmission, Paris (1976), paper III.1.
30. D. L. Griscom, (unpublished).

(a) Before Irradiation



(b) After Irradiation



R, R_A, R_B = Network Formers = Si, B, P, Ge, Al, ...

C = Monovalent Network Modifying Cation = H, Li, Na, K, ...

Figure 1 Schematic diagram of an oxide glass showing several types of radiation-induced paramagnetic centers (unpaired "spins" in (b)) in their relationships with pre-existing structures such as oxygen vacancies, nonbridging oxygens, peroxy linkages, and substitutional impurities as indicated in (a). Note the locally charge-compensated natures of most defect species. (After Refs. 6 and 7).

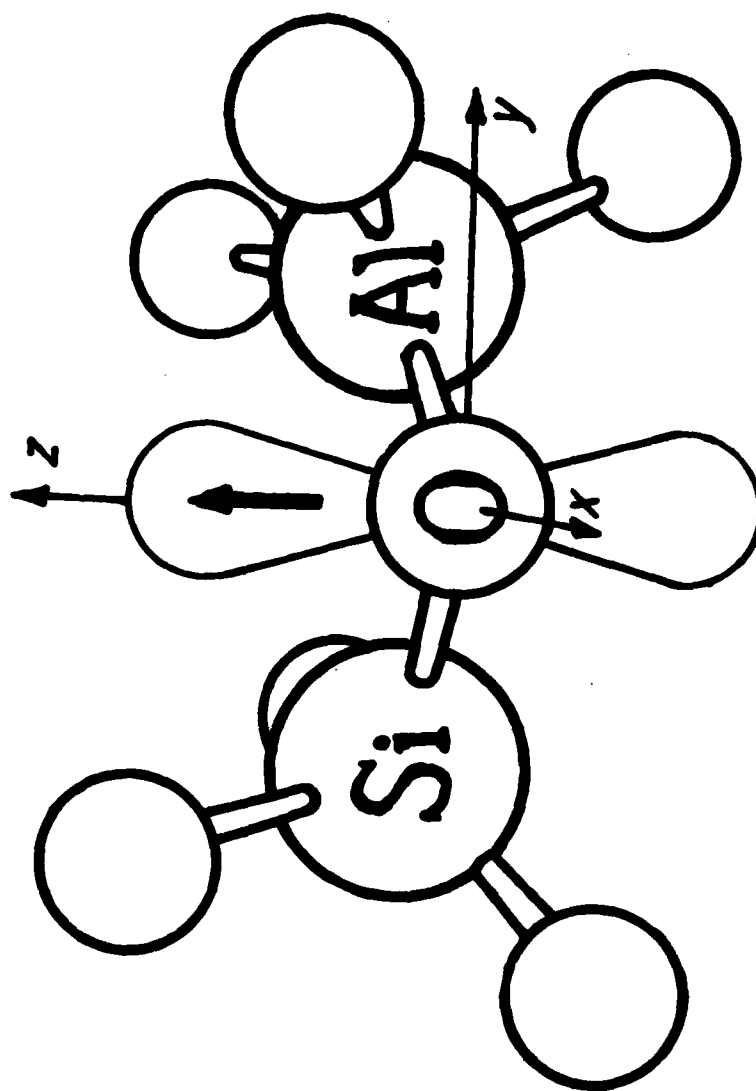


Figure 2 The "aluminum center" in α -quartz and fused silica. (After Ref. 5).

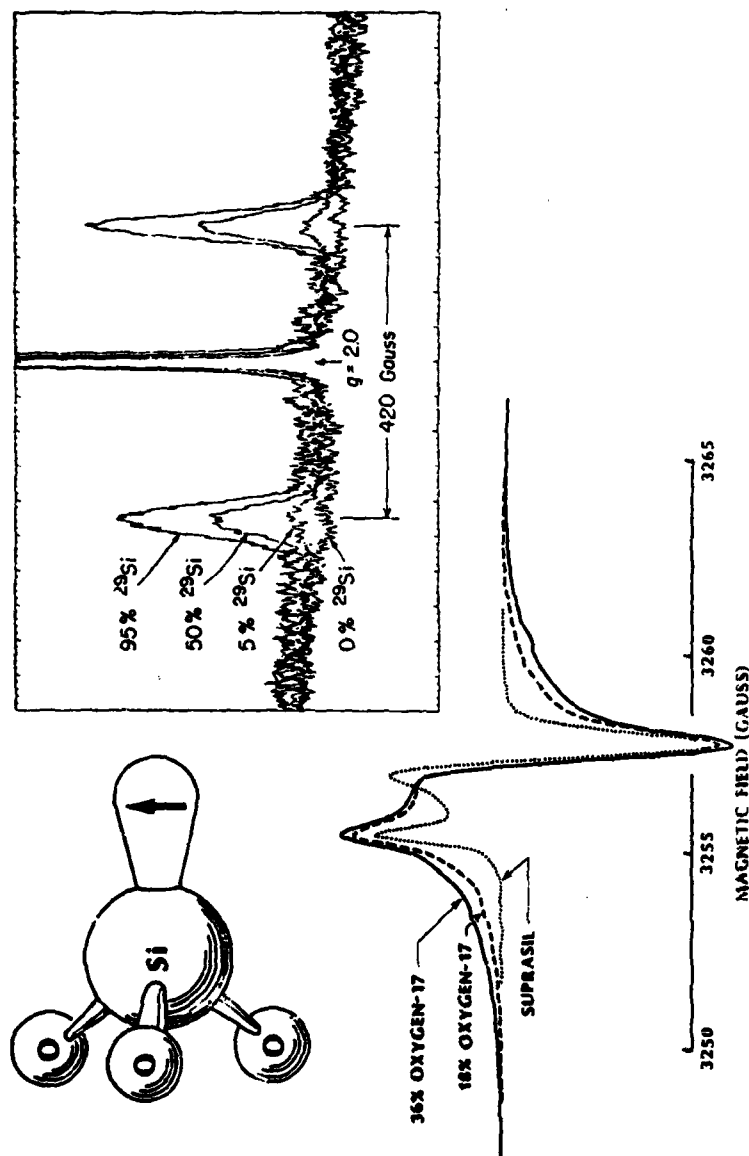


Figure 3 Determination of the structure of the E' center in silica glass by means of ^{29}Si and ^{17}O hyperfine structure. The 420-Gauss ^{29}Si splitting (right) shows that the unpaired spin is strongly localized in a dangling tetrahedral orbital of one silicon. The very weak ^{17}O splittings (bottom) shows not only that the spin stays away from these oxygens but also that there must be three of them bonded to the defect silicon. (After Refs. 14 and 15).

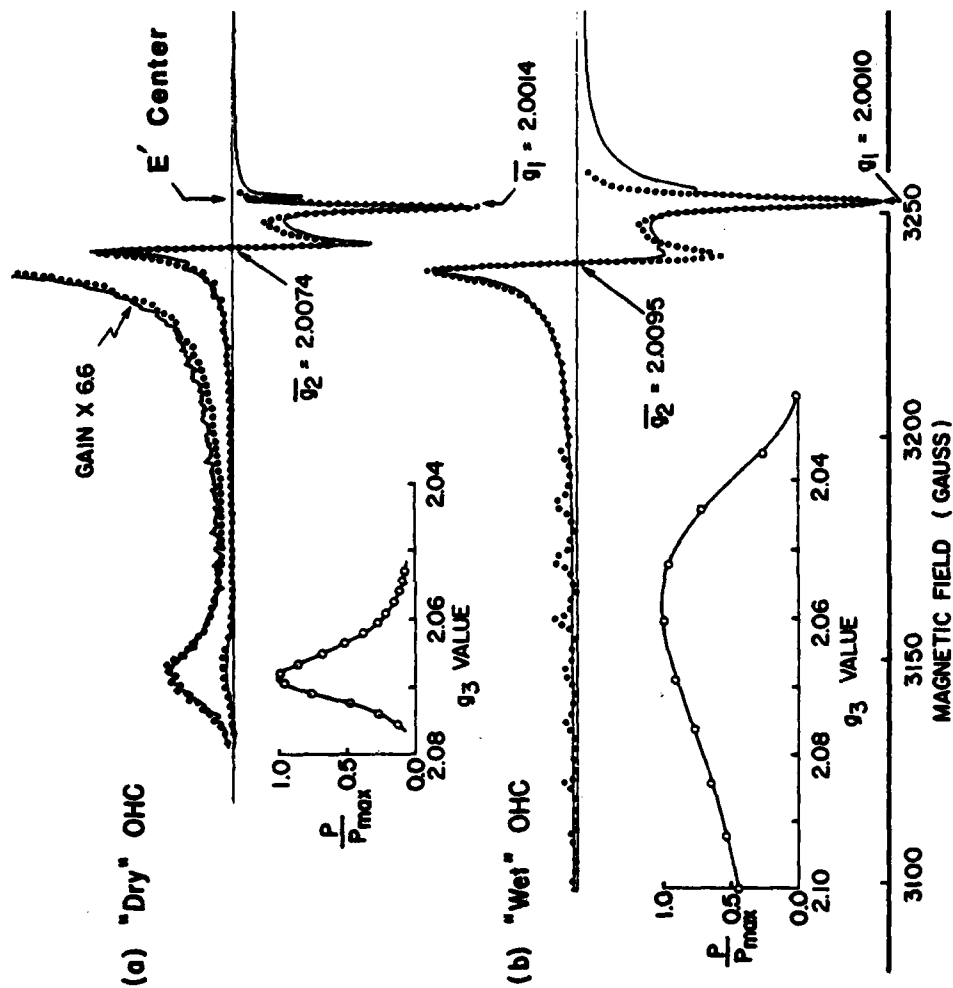


Figure 4 ESR spectra of oxygen-associated hole centers in irradiated, high-purity silicas. (a) The peroxy radical in Suprasil W1 following irradiation and annealing. (b) The nonbridging oxygen hole center in irradiated Suprasil 1. Dotted curves are computer simulations based on theory. (After Ref. 17).

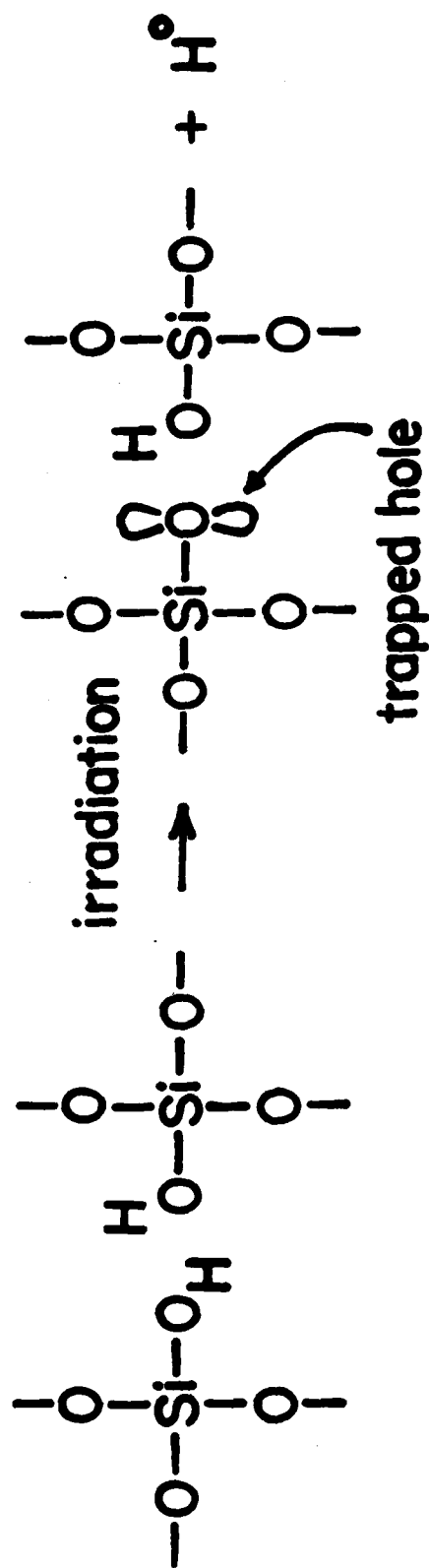
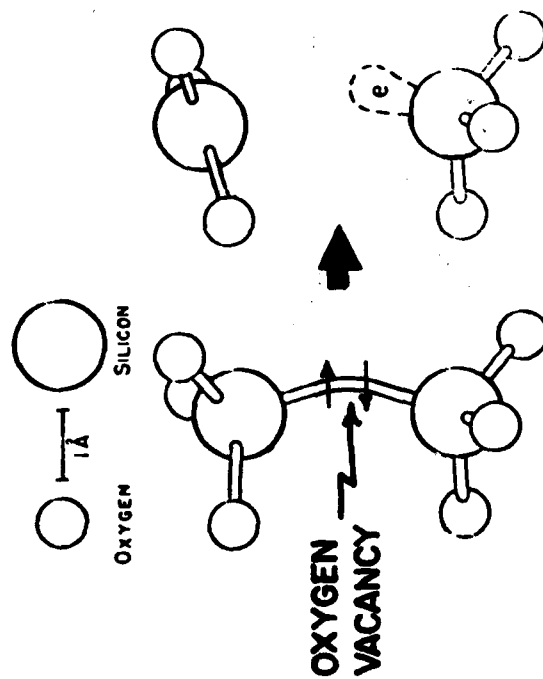


Figure 5 Model for the formation of the nonbridging oxygen hole center ("wet" OHC of Fig. 4b) in silicas of high OH contents. (After Ref. 17).

(a) The E' Center



(b) The Peroxy Radical

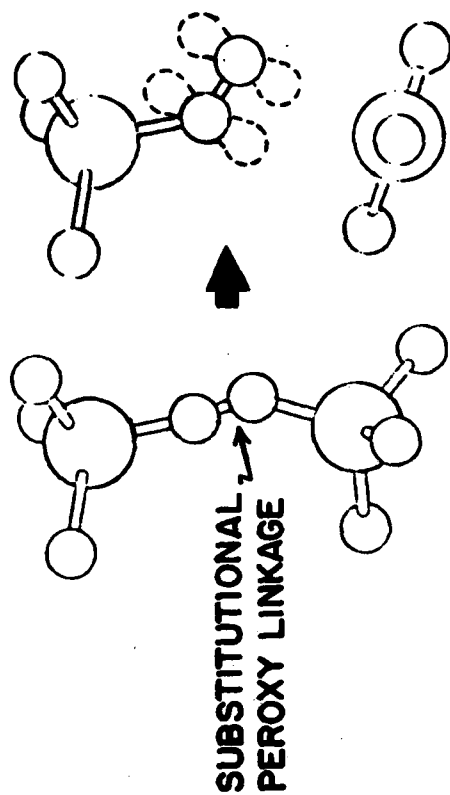


Figure 6

Models for the formation of an E' center (a) and a peroxy radical (b) in silica glass by hole trapping at the sites of an oxygen vacancy and a peroxy linkage, respectively. Note the structural relaxations which are believed responsible for the stability of these defects. The concept of E' center formation is due to Ref. 19; that for the peroxy radical was suggested in Ref. 17 and 18. (After Ref. 6).

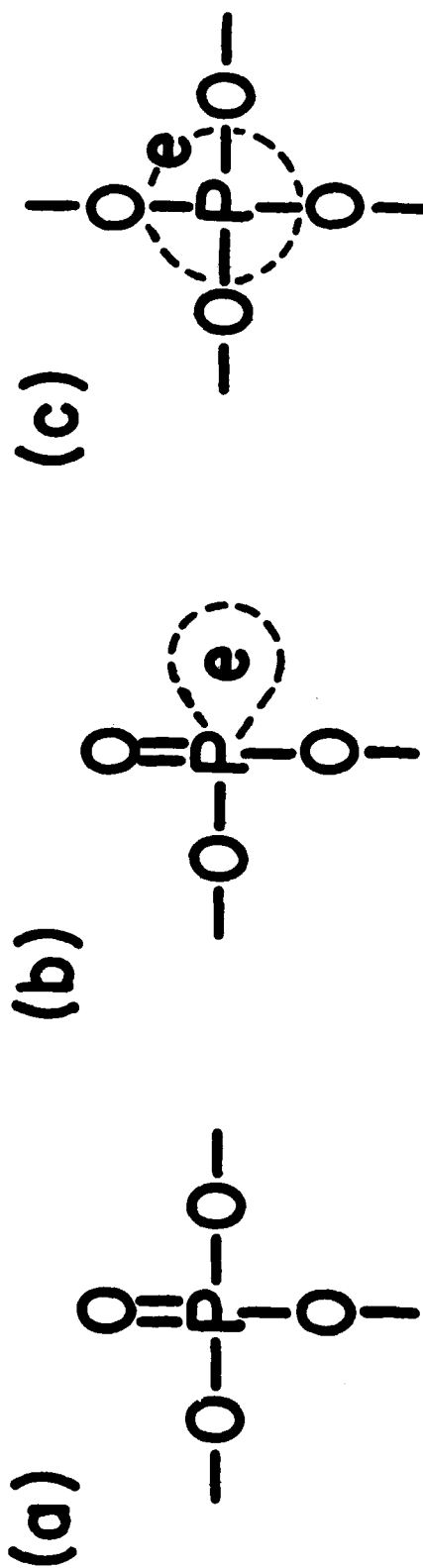


Figure 7 Schematic representation of the basic structural unit in P_2O_5 glass (a), together with two possible defect structures which could serve as electron traps. (After Ref. 7).

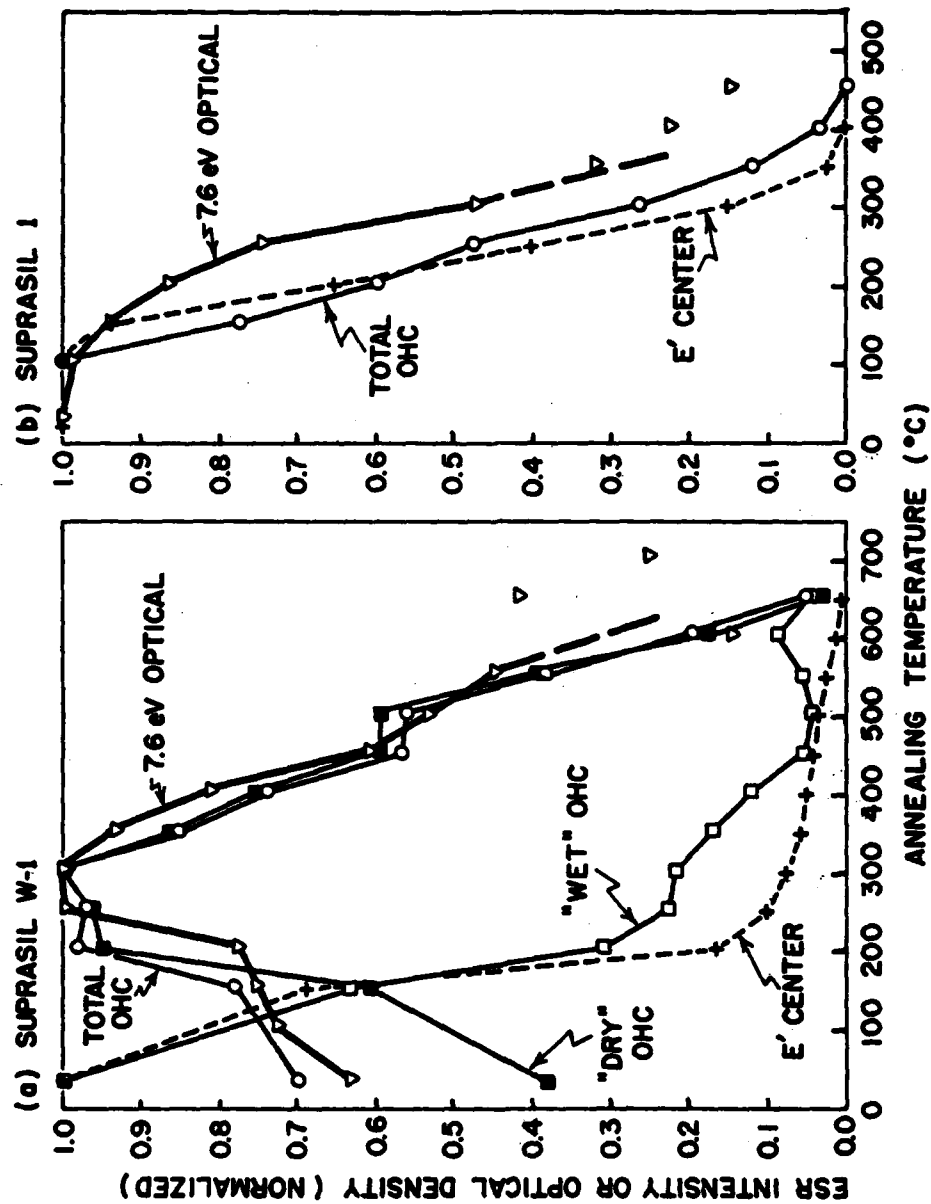


Figure 8 Annealing behavior of ESR centers in γ -irradiated Suprasil W-1 (a) and Suprasil 1 (b), with comparison to the optical density induced at 7.6 eV. Measurements were performed at room temperature following 10-minute pulse anneals at the indicated temperatures. (After Ref. 17).

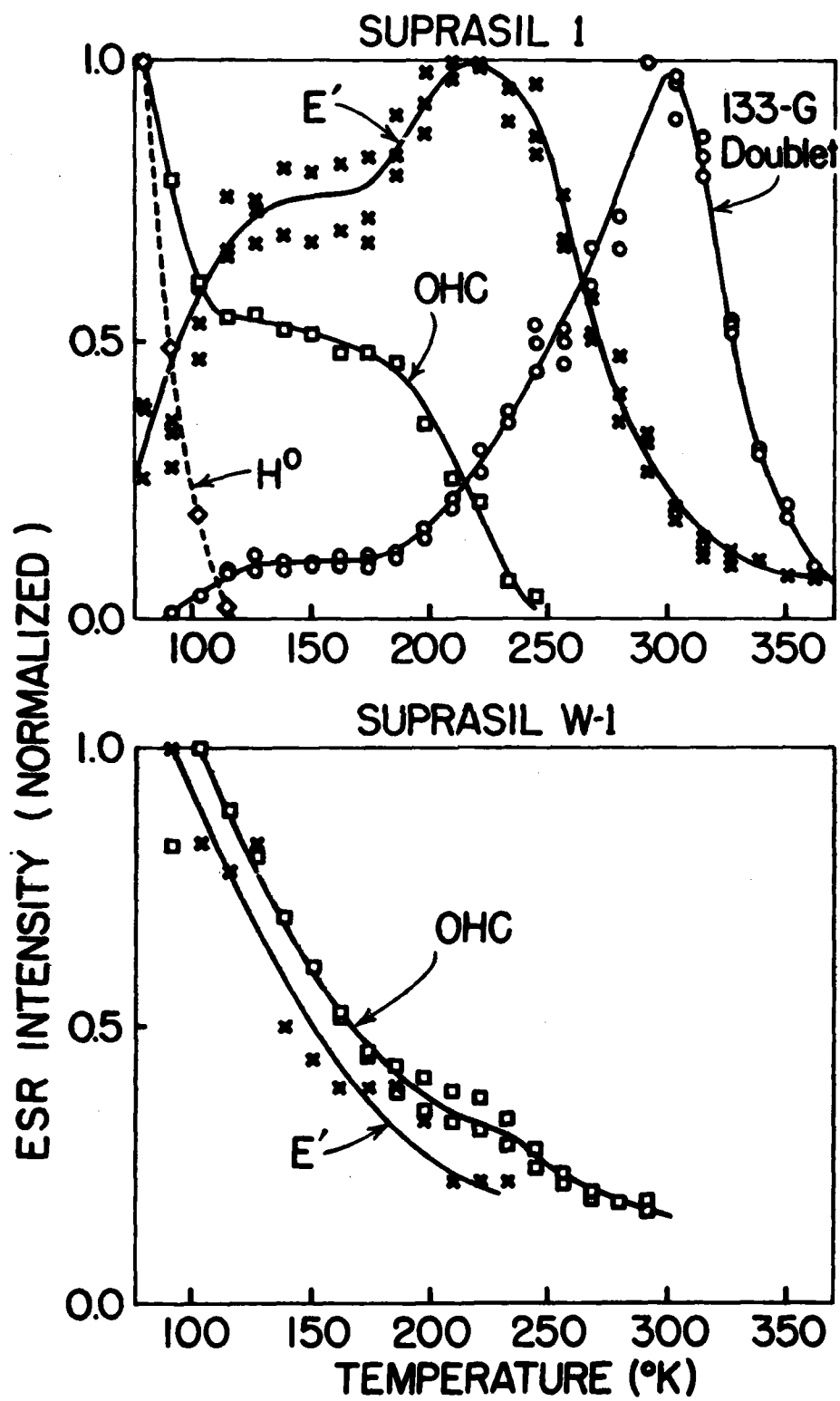


Figure 9 Annealing behavior of ESR centers in γ -irradiated Suprasil 1 and Suprasil W-1 following x-irradiation at 77K. Measurements were performed at ~ 95 K following 5-minute pulse anneals at the indicated temperatures. (After Ref. 23).

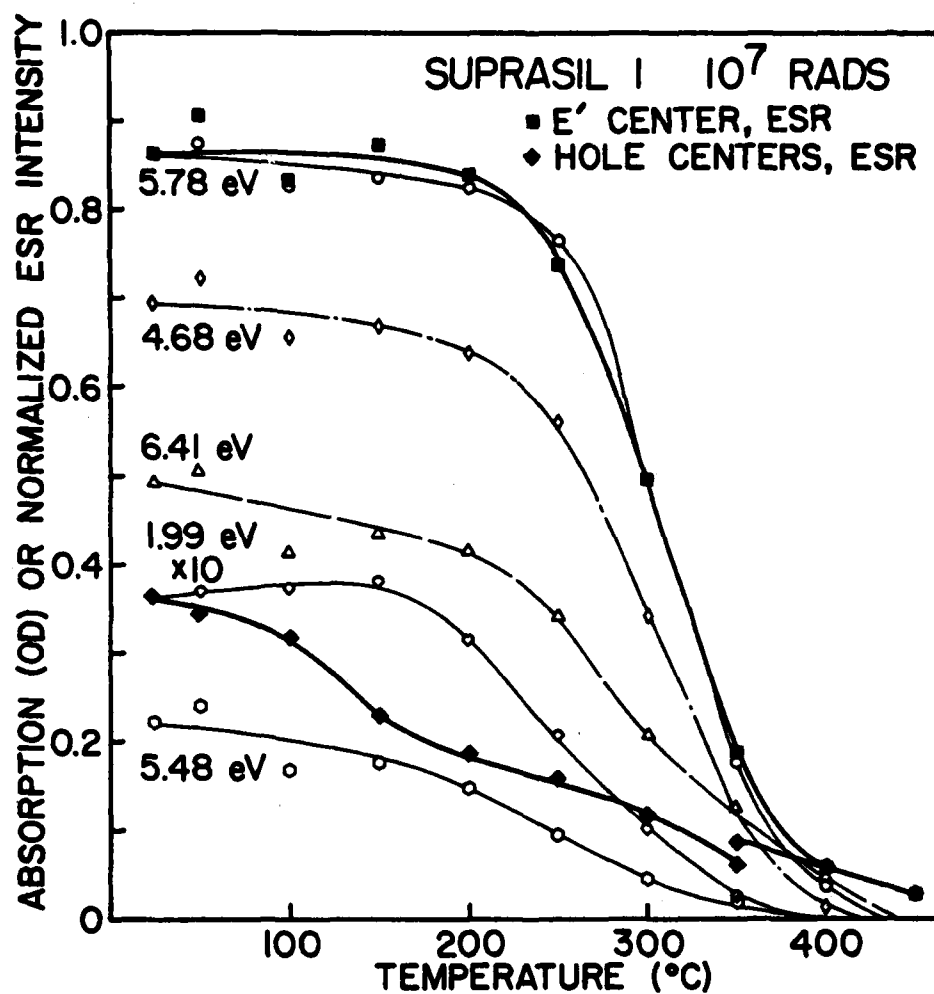


Figure 10 Annealing behavior of ESR and optical bands induced in Suprasil 1 by γ -irradiation. Measurements were performed at room temperature following 10-minute pulse anneals at the indicated temperatures. (After Ref. 26).

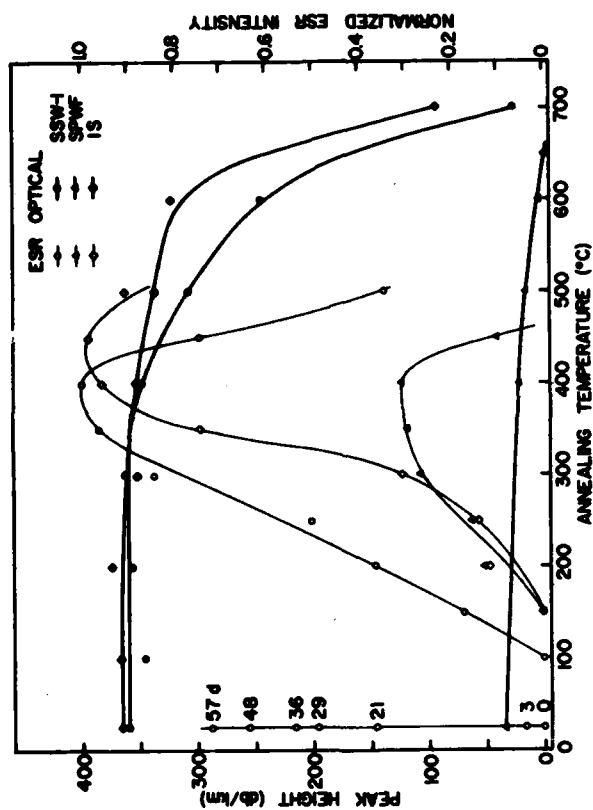


Figure 11 Annealing behavior of ESR and optical bands induced in high-purity, low-OH fused silicas by the act of fiber drawing. Measurements of the 630 nm optical band and the peroxy radical ESR spectrum were performed at room temperature following 10-minute pulse anneals at the indicated temperatures. Vertical line at 20°C indicates the growth of the ESR spectrum at room temperature as a function of time (days) after fiber drawing. (After Refs. 17 and 29).

The Role of the Multidopants Sb/P in Radiation Hardening of Optical Fibers

J. A. Wall, H. Posen*, Deputy for Electronic Technology,
Rome Air Development Center, Solid State Sciences Division, Hanscom AFB, MA
01731 (617)861-4031

R. Jaeger, Galileo Electro-Optics Co.,
Galileo Park, Sturbridge, MA 01518

Introduction

It is well known that small changes in the composition and impurity content of glasses can significantly affect their responses to energetic radiation, yet there have been very few studies of radiation effects on optical fibers in which these factors were known and controlled.¹ RADC has initiated a program to study the effects of radiation on optical fibers fabricated under well documented conditions from perform to drawing process. This paper presents preliminary results obtained as part of that program on the radiation response of germanium-silicate fibers doped with phosphorous and/or antimony.

Experimental

Several step index fiber preforms with $\text{GeO}_2\text{-B}_2\text{O}_3\text{-SiO}_2$ cores and T0-8 cladding were prepared using the CVD process. The nominal vapor composition of the cores before deposition was, in mole percent, 48% SiO_2 , 50% GeO_2 , and 2% B_2O_3 . Modifications were made in some of the core compositions, including the deliberate introduction of OH. Fibers drawn from these preforms were tested for their real-time response to steady state radiation and the results used to establish a baseline for the study of dopant effects. Additional preforms were then fabricated with compounds of phosphorous and/or antimony added to the vapor stream in place of, or in addition to, the boron. Table 1 lists the composition and optical properties of the four fibers on which radiation test results will be reported.

Table 1
Fiber Compositions and Optical Properties

Mole % in Gas Stream					OH ppm	N.A.	Attenuation at 900nm dB/km
Si	Ge	B	P	Sb			
61.4	37.2	1.4	-	--	8	0.17	8.3
65.9	33.9	-	0.2	--	3	0.19	7.9
61.3	36.5	1.4	-	0.8	13	0.18	6.8
61.7	37.4	-	0.2	0.8	2	0.21	5.3

*Deceased, December 1979

The radiation responses of the fibers were measured under both steady-state and transient conditions. The steady-state irradiations were performed using x-rays produced by 10 MeV electrons from the RADC linear accelerator (linac) incident on a tungsten target. The linac was set to produce 4.5 μ sec wide pulses of electrons and the pulse rate could be varied at will. This made it possible to change the average dose-rate to the fibers instantaneously during, and without interrupting, the irradiation to test dose-rate effects. 25 meters of fiber were wound on 13 cm diameter, 1 cm thick reels and positioned relative to the x-ray target to receive approximately one rad per linac pulse. The light source was a 905 nm LED pulsed with 10 μ sec wide pulses at a rate of 100 kilohertz. The detector was an APD-amplifier module. The source and detector were located out of the direct x-ray beam and were shielded from scattered radiation by lead bricks. The output of the detector was connected to an oscilloscope in the experiment control area which was used to observe and photograph the amplitude of the light pulses transmitted by the fiber during the irradiation. The fibers were irradiated until the transmitted pulse amplitude dropped to half its pre-irradiation value. At the beginning of the irradiations the linac pulse rate was set for 1 pps. The pulse rate was doubled at intervals during the irradiation. The maximum rate reached during any of the irradiations was 16 pps, giving an average dose-rate range of approximately 1-16 rads/sec.

Dosimetry for the steady-state irradiations was performed using thermoluminescent dosimeters (TLD's) placed in quadrature around the reels on both sides of the reels and in line with the fiber position. The TLD's measured the total dose accumulated by the fiber. During the irradiation, the number of linac pulses accumulated was registered on a counter and the fiber transmission was measured as a function of the number of linac pulses. Following the irradiation the total dose to the fiber as measured by the TLD's was divided by the total number of linac pulses accumulated to obtain an accurate measure of dose per linac pulse. The data was then converted to fiber transmission as a function of dose.

The transient radiation response measurements were performed using the RADC flash x-ray generator which produces single 20 nanosecond wide x-ray pulses of nominal 2 MeV peak energy. The APD module, which had a D.C. to 40 megahertz bandwidth, used for the steady-state irradiations was also used as the detector for these measurements. The LED light source was replaced by a quartz iodide lamp and monochromator set at 905 nm. The fiber lengths (25 meters) and reels were the same as for the steady-state tests. The light source was located in the irradiation area but out of the x-ray beam path. The output end of the fiber being irradiated was coupled to the detector in the experiment control area through a fiber-optic link. The output of the detector was connected to four oscilloscope inputs to obtain measurements over a time span from less than 50 nanoseconds to 100 milliseconds. The dose-rate received by the fiber was measured by means of a small PIN diode in contact with the fiber on the reel.

Results

Except for small deviations (which could have been instrumental in origin) below about 2 kilorads, all of the fibers tested showed a very linear induced loss as a function of dose over the range of doses used in the steady-state irradiations.

No changes in this linearity were observed as the dose-rates were changed. For the nine "baseline" germanium-borosilicate fibers, the average rate of induced loss was 2.9 dB/km per kilorad with a standard deviation of 1.0 dB/km per kilorad. Five of these nine had the same mole percentages of silicon, germanium and boron in the vapor stream and they showed an average rate of induced loss of 2.3 ± 0.4 dB/km per kilorad.

Figure 1 shows the results of the steady-state irradiations of the doped fibers and one of the baseline fibers. The addition of antimony to the vapor stream increased the rate of induced loss by approximately a factor of 4 over that of the baseline fiber, and substitution of phosphorous for boron increased the rate of induced loss by about a factor of 10. The addition of antimony to a phosphorous-doped fiber reduced the rate of induced loss to nearly the same as that for the antimony-boron combination.

In the transient tests the fibers were exposed to nominal dose rates of 10^8 and 10^9 rads/sec. At both dose rates an initial fluorescent pulse of sufficient amplitude to overload the detector module was observed for all fibers. The detector overload appeared as broadening of the pulse for up to 200 nanoseconds at the 10^8 rad/sec level and up to 600 nanoseconds at the 10^9 rad/sec level. This prevented loss measurements at times shorter than these. At 10^8 rads/sec only the boron and antimony + boron doped fibers showed induced losses and these losses were too small to make meaningful measurements from the oscilloscope photographs. Figure 2 shows the induced losses, at the nominal 10^9 rads/sec level (actual dose-rate 1.7×10^9 rads/sec) as a function of time over part of the time-span covered by the measurements. The actual measured losses have been divided by dose-rate in units of 10^8 rads/sec in figure 2 (normalized induced loss) for better comparison of results obtained for the different fibers. This is necessary because the output of the flash x-ray generator can vary by about 10% from pulse to pulse. No induced loss was observed for either fiber doped with phosphorous.

The antimony and boron doped fiber appears to show less induced loss than the boron doped fiber. However, there was an indication of a long (at least one microsecond) duration fluorescence generated in that fiber which could cause the measured loss to be less than the actual induced loss. The generation of this fluorescence was confirmed by tests of two other fibers doped with 2.5% and 4% antimony. For these fibers the fluorescence was evident for 200 and 600 microseconds, respectively, with no light input to the fibers.

For all the fibers tested under transient radiation the induced losses became undetectable within 100 milliseconds.

Conclusions

The substitution of phosphorous for boron in germanium-borosilicate fibers significantly reduced the induced loss under transient radiation conditions but increased the rate of induced loss by an order of magnitude under steady-state irradiation. The addition of antimony to the phosphorous-doped fiber improved the steady-state radiation response with no measureable effect on its transient response.

At present, the attainment of minimal induced loss under transient radiation appears incompatible with optimum fiber response under steady-state irradiation. The germanium-phosphosilicate fiber doped with antimony offers an improved possibility of meeting requirements under both radiation conditions. This result suggests that further improvements in the radiation hardness of optical fibers could result from continued, controlled investigations of the relationship between fiber composition and radiation response.

REFERENCES

1. S. Share, R. M. McCracken and I. Aggarwal, IEEE Trans. on Nuclear Science, NS-25, 1288 (1978).

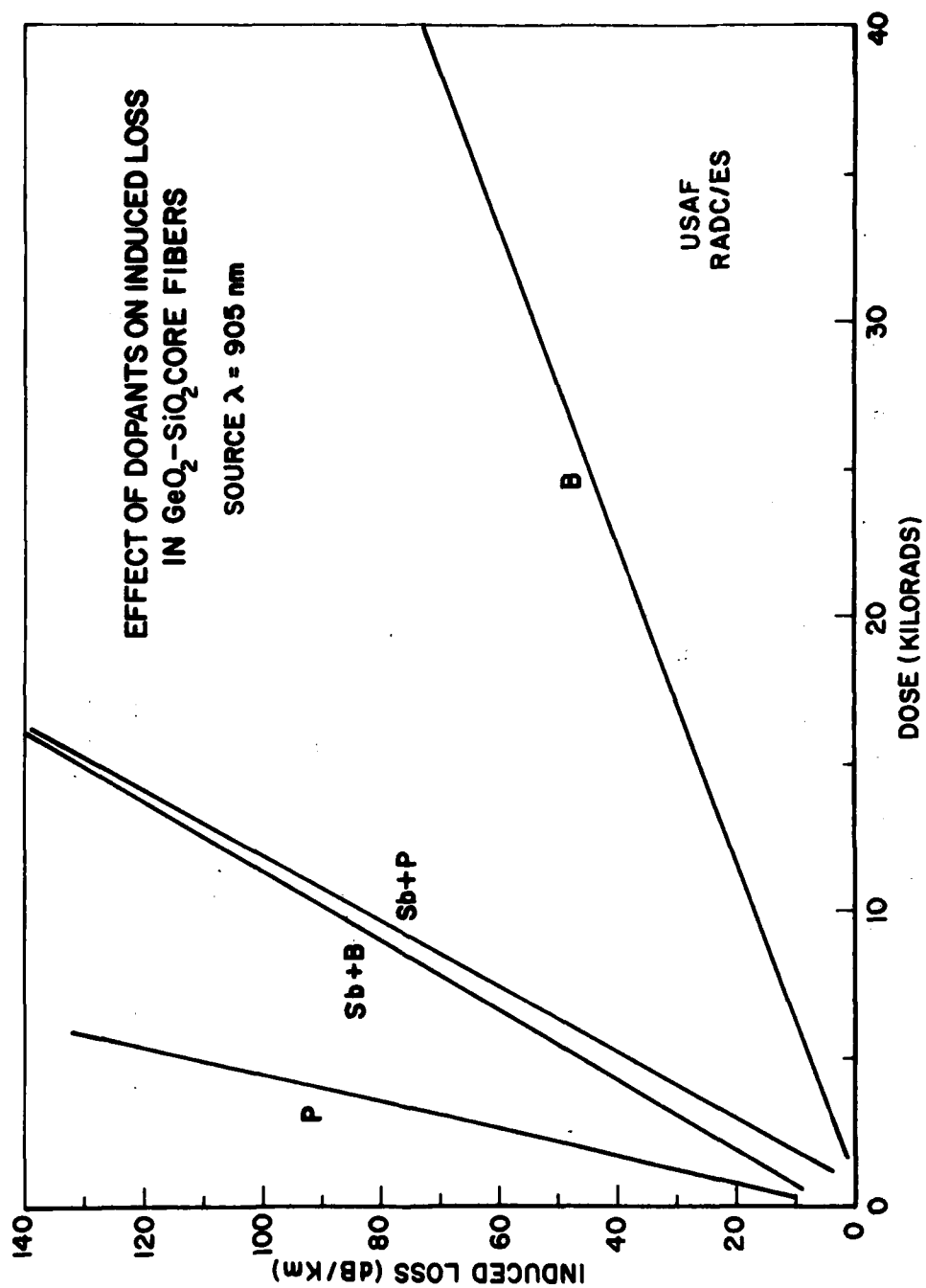


Figure 1

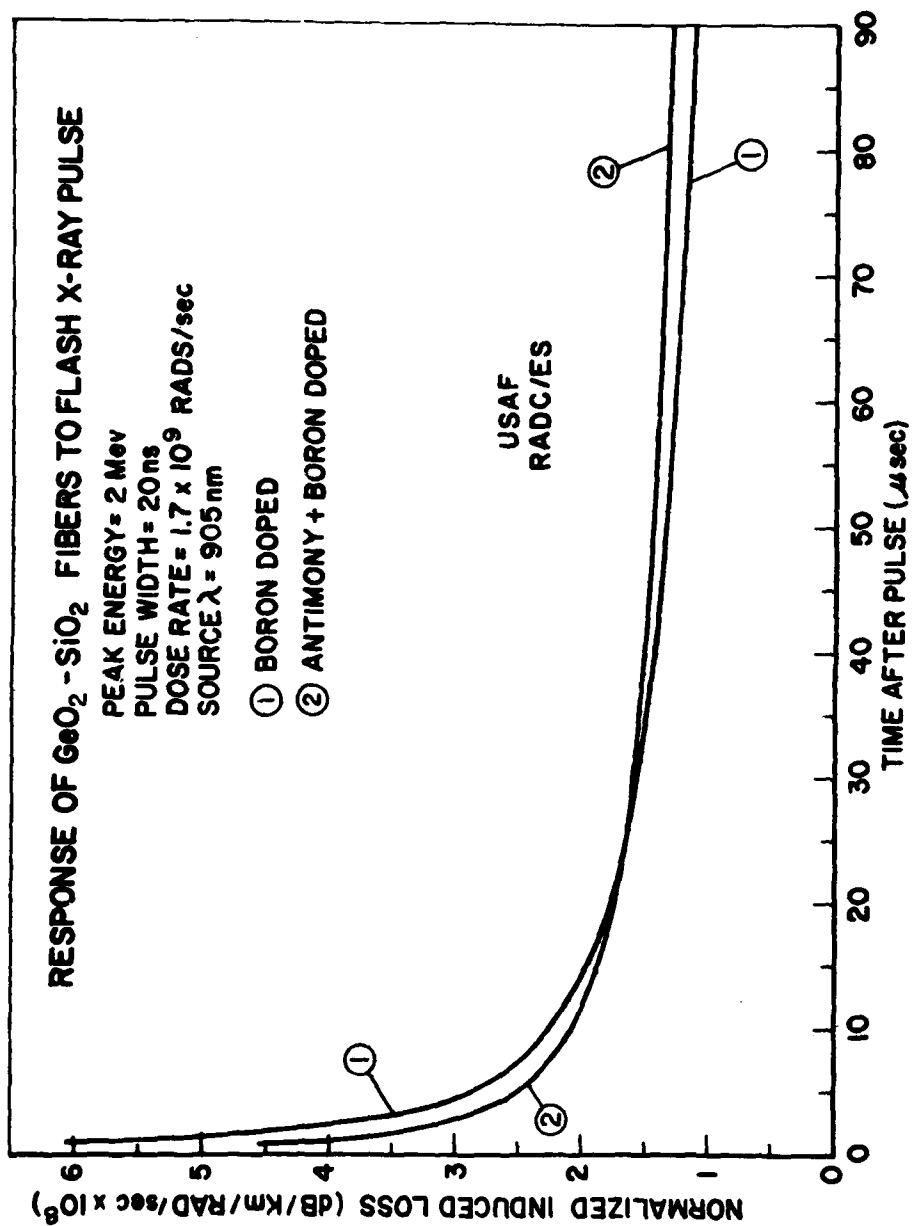


Figure 2

RADIATION DAMAGE OF OPTICAL FIBER WAVEGUIDES AT LONG WAVELENGTHS

E. J. Friebele and M. E. Gingerich

Naval Research Laboratory
Washington, DC 20375

ABSTRACT

Measurements of the radiation-induced optical loss at 1.3μ and the induced absorption spectra of state-of-the-art pure synthetic silica and doped silica core optical fiber waveguides have been undertaken in order to determine the optimum operating wavelength for the fibers in a radiation environment, to study the effect of variations in core composition and dopants on the radiation damage, and to understand the damage mechanisms responsible for the measured absorption. It has been determined that in general the induced loss is less at 1.3μ than it is at 0.82μ ; however, long wavelength bands in some fibers cause a minimum in absorption near 1.1μ and a subsequent increase at longer wavelengths. Fibers which contain P in the core have been found to be especially radiation sensitive in the $1.3 - 1.55 \mu$ range. The waveguides with the lowest sensitivity at 1.3μ have cores of pure fused silica; those with the lowest loss at 1.55μ have cores of either pure or binary Ge-doped silica, the latter fiber was clad with a boron-free material. Optimum operational wavelengths for fiber communication systems exposed to a nuclear radiation environment have been identified.

INTRODUCTION

Future long line, high bandwidth optical communications systems will operate at 1.3 or 1.55 μ to take advantage of the fiber's low intrinsic loss and minimum material dispersion in this spectral region. Although the feasibility of operating at these wavelengths has been demonstrated, little attention has been paid to the radiation response of the optical fibers at long wavelengths.

The radiation-induced optical absorption of some bulk glasses has been well characterized in the ultraviolet (and to a lesser extent in the visible) spectral regions,¹ and the response of state-of-the-art fiber waveguides has been extensively studied in the near infrared region where first generation fiber systems operate.² Previous studies of the radiation-induced absorption spectrum over the 0.4 - 1.1 μ range of Si photodetector sensitivity have indicated a general decrease in the damage with increasing wavelength, and it was anticipated that substantial advantage would be obtained by operating fiber optic communications systems at 1.3 or 1.55 μ in radiation environments. However, more recent spectral measurements extended to 1.7 μ have demonstrated a minimum in induced loss near 1.1 μ and a subsequent increase at longer wavelengths in some fibers.³

This paper will report explicit dose and time dependent data of the radiation-induced attenuation at 1.3 μ . In addition, we report systematic spectral measurements of the radiation-induced optical absorption in pure synthetic silica and doped silica core optical fibers in order to locate the optimum operating wavelength for systems exposed to nuclear radiation and to observe and characterize bands due to radiation-induced defects intrinsic to the glass structure.

EXPERIMENTAL

Fibers included in the study had cores of either pure fused silica with low (< 5 ppm) or high (\sim 1200 ppm) OH content, P-doped silica, Cs-doped silica, or Ge-doped silica with OH contents that varied from 3-200 ppm. Some of the cores of the latter fibers were also codoped with B and/or P. Both step and graded index fibers were studied. The experiments consisted of *in situ* measurements of the radiation-induced attenuation at 1.3 μ either during steady state ^{60}Co irradiation or following pulsed electron irradiation, spectral studies over the 0.4 - 1.1 μ range during steady state or after pulsed irradiations, and spectral measurements of the "permanent" loss over the 0.4 - 1.7 μ range one hour after a ^{60}Co irradiation of 10^5 rads. The time-resolved and dose-resolved spectral measurements were made with white probe light traveling down the fiber and spectrally dispersed onto a self-scanning photodiode array at the output end. By this technique instantaneous spectra of the light transmitted in the fiber could be obtained after the fiber had been exposed to specific doses during steady state irradiation or had faded for specific times after a pulsed irradiation. All measurements were made at room temperature.

RESULTS AND DISCUSSION

I. Ge-doped silica core fibers

Typical data of the radiation-induced loss at $1.3\ \mu$ measured as a function of dose during steady state irradiation are shown in Fig. 1. The level of damage in these Ge-doped silica core fibers is a factor of ~ 4 less at $1.3\ \mu$ than at $0.82\ \mu$, so some benefit is obtained in moving to the longer wavelength. It is apparent that similar to the results at $0.82\ \mu$,^{2,4} variations in the OH content of the fibers between 3 and 200 ppm do not have a significant effect on the radiation-induced loss at $1.3\ \mu$. This result is in contrast to the behavior of pure silica core fibers at $0.82\ \mu$, where decreased OH content has been found to increase the radiation response. It is apparent from Fig. 1 that the induced loss vs. dose data of the Ge-doped silica core fibers not codoped with P are virtually identical and much less than those of the fibers doped with P. Furthermore, the radiation-induced loss at $1.3\ \mu$ in these fibers is seen to increase with increasing P content.

The time evolution of the radiation-induced attenuation at $1.3\ \mu$ in these fibers following a 0.5 MeV, 3 nsec pulsed electron irradiation of 3.6×10^5 rads is shown in Fig. 2. Because of the high noise and poor stability of the Ge photodiode used in these measurements, it was necessary to expose the fibers to a high dose in order to maximize the signal-to-noise. However, one can linearly extrapolate the induced loss at short times to a lower dose because the apparent nonlinearity in the induced loss vs. dose behavior that is observed during steady state irradiation,^{2,4} in these Ge-doped silica core fibers is due to relatively slow recovery processes. The data of Fig. 2 show that the Ge-doped silica core fibers not codoped with P suffer transient upset at $1.3\ \mu$ at short times following a pulsed irradiation, similar to observation at $0.82\ \mu$. Extrapolating these data to the 3700 rad dose used for measurements of the damage at $0.82\ \mu$,^{2,4} reveals that the transient induced loss at $1.3\ \mu$ is ~ 100 times less than that measured at $0.82\ \mu$. This result extends the previous observation that the optical absorption spectrum of the transient induced loss of P-free Ge-doped silica core fibers between 0.4 and $1.1\ \mu$ consists of the tail of an intense UV absorption which decreases monotonically with increasing wavelength to $1.1\ \mu$. It is also apparent from Fig. 2 that the addition of P to the fiber core suppresses the Ge-related transient absorption at $1.3\ \mu$, as it does at $0.82\ \mu$, but that it leads to much larger permanent induced loss.

Optical absorption spectra of the radiation-induced loss over the $0.8 - 1.7\ \mu$ range in the Ge-doped silica core fibers are shown in Fig. 3. It is significant to note that the loss in the fibers decreases to a minimum near $1.1\ \mu$ and then increases at longer wavelengths. This result is of course contrary to the monotonic decrease with increasing wavelength expected on the basis of measurements with Si photodetectors over the $0.4 - 1.1\ \mu$ range. In the P-free fibers there is a broad minimum between 1.1 and $1.55\ \mu$ where the induced loss is less than 70 dB/km. Extrapolating this result from 10^5 rads to moderate tactical doses reveals that the radiation-induced loss in this wavelength range is quite encouraging. The damage measured in the P-doped fibers is greater than that in the P-free fibers at all wavelengths, as seen by comparing the upper set of curves in Fig. 3 with the lower. There is a minimum in the P-doped fibers near $1.1\ \mu$ with a sharp increase in induced loss at longer wavelengths; the level of damage increases with increasing P content in this region. Indeed,

it appears by comparing the radiation-induced absorption spectrum of these Ge-P-doped silica core fibers with that of a binary P-doped silica core fiber that the damage is almost entirely controlled by the presence of P in the fiber.

II. Pure fused silica core fibers

The radiation-induced spectra of high purity synthetic silica have been well characterized in the UV, and several conclusive correlations have been made between optical absorption bands and specific defect centers elucidated by electron spin resonance (ESR) spectroscopy.¹ However, the induced absorption in the vis-near IR is less well understood. Recent measurements of the growth and decay of the induced attenuation at one wavelength (0.82 μ) in silica core fibers have revealed unusual behaviors including: saturation at doses near 10^4 rads, a subsequent decrease of the induced loss with increasing irradiation dose, radiation hardening,^{2,5} and photobleaching.^{6,7} Spectral measurements are useful in understanding the origin of these phenomena as well as providing data for selection of an optimum operating wavelength for pure silica core fibers exposed to radiation. The radiation-induced optical absorption spectra of a polymer clad silica (PCS) fiber with a Suprasil core measured *in situ* during steady state ^{60}Co irradiation are shown in Fig. 4. At doses $<10^4$ rads, all components of the spectrum increase monotonically with increasing dose. However, at higher doses a band at 0.63 μ is seen to grow in while a broad absorption in the infrared decreases in intensity. The behavior of this broad IR absorption is responsible for the saturation in induced attenuation measured at 0.82 μ after a dose of $\sim 10^4$ rads and the subsequent decrease in attenuation with increasing dose.^{2,5} This band is also responsible for the radiation hardening observed in PCS fibers of high OH content cores -- fibers which had been pre-irradiated and then allowed to recover at room temperature were found to suffer lower induced attenuation at 0.82 μ during subsequent irradiations.^{2,5}

In addition to the 0.63 μ band and the broad IR absorption, there is an unresolved induced band in Fig. 1 that is susceptible to photobleaching.⁷ Subtraction of the induced spectrum measured with bleaching light traveling in the fiber from that measured without bleaching light reveals that the photobleached part of the induced spectrum consists of a broad band centered near 0.67 μ (see ref. 7, figs. 2 and 3). However, it should be emphasized that this band is present in addition to the broad IR absorption which decreases in intensity with increasing dose $> 10^4$ rads. Thus, the radiation-induced optical absorption of high OH content silica in the vis-near IR consists of a tail from the UV, a band at 0.63 μ , a broad, featureless IR absorption, and a band centered near 0.67 μ which is susceptible to photobleaching.

The radiation-induced optical absorption of low OH content silica core fibers is different from that of the high OH content fibers. As shown in Fig. 4 of ref. 7, the photobleached band is centered at a longer wavelength (0.76 μ), and it is broader and more intense, thus masking any evidence of a radiation-induced band at 0.63 μ . The intense 0.76 μ band in the dry silica core fiber dominates the radiation-induced absorption and causes the loss in the vis-near IR measured during or immediately after irradiation to be greater than that in the wet.^{2,5} Since this band apparently neither saturates with dose nor radiation hardens, these effects are not observed in dry silica core fibers.

The nature of the band at $0.63\ \mu$ has been the subject of considerable study. The intensity of the band in bulk high purity synthetic silica has been observed to increase with increasing dose up to 10^9 rads,⁸ so that it may be surmised that it is due to an intrinsic defect center in the glass which is likely created by the irradiation. In contrast, the attenuation at $0.82\ \mu$ does not continue to decrease with increasing dose,^{2,5} implying that although there may be a connection between the broad IR absorption and the $0.63\ \mu$ band, the latter does not grow exclusively at the expense of the former.

The band at $0.63\ \mu$ may also be induced by drawing low OH content silica into a fiber,⁹ and it has been suggested that the same defect center is responsible for the drawing-induced and radiation-induced absorptions.^{9,10} This premise is strengthened by the radiation-induced absorption spectra measured after the photobleached bands in the silica core fibers have been substantially eliminated (Fig. 5). It can be seen that there is significantly less radiation-induced intensity in the $0.63\ \mu$ band in the Suprasil W core fiber, which already had a $0.63\ \mu$ band present prior to irradiation due to fiber drawing, relative to the Suprasil core fiber which has no drawing-induced absorption. (A similar but much less pronounced effect has been noted for irradiated (10^8 rads) bulk rods of Suprasil and Suprasil W.¹¹ It is possible that these slight differences are due to defects introduced when the rods were extruded to small diameter.⁹) The same defect centers are thus created by fiber drawing of low OH content silica and by irradiation. It should be noted that these defect centers are not paramagnetic since no correlation has been made between the $0.63\ \mu$ band and any defect center elucidated by ESR.¹²

The similarity between the "permanent" induced losses of the Suprasil and Suprasil W core fibers measured 1 hour after irradiation, as shown in Fig. 5, is significant. The intense $0.76\ \mu$ band which is observed during irradiation of the dry fiber has decayed, leaving a residual induced loss which is almost identical to that of the wet fiber at wavelengths longer than $0.8\ \mu$. A connection between the growth of the radiation-induced band at $0.63\ \mu$ in wet silica and the decrease in the broad IR absorption has already been noted in Fig. 4. The similarity of the spectra of the wet and dry silica core fibers after room temperature annealing in Fig. 5 indicates that the presence of the drawing-induced band in the Suprasil W core fiber may similarly be related to the relatively low intensity of the radiation-induced broad IR absorption in this fiber. A possible explanation which is consistent with these data is that the broad IR absorption is due to charge trapping by the ~ 0.3 ppm metal ion impurities in the fibers. Irradiation of the high OH content fibers to doses $> 10^4$ rads or drawing of the low OH content silica into fibers creates defect centers in much larger concentrations which compete successfully with the metal ions for the charges. Thus, preirradiation of the high OH content fibers hardens them against further induced attenuation in the near IR. Attributing the broad IR absorption to impurities also explains the variation in induced attenuation observed in high OH content PCS fibers supplied by different manufacturers.⁵

III. Comparison of radiation-induced spectra in fibers

Fig. 5 also contains the radiation-induced optical absorption spectra of a number of representative doped silica core fibers, and it can be seen that

there are substantial differences in their responses to radiation. Intense induced absorptions in the UV in all fibers have tails extending well into the vis-IR. However, the absorption does not decrease monotonically with increasing wavelength; radiation-induced bands at long wavelengths cause minima between 1.0 and 1.6 μ and increased absorption at longer wavelengths.

Long wavelength induced bands are especially evident in the P-doped and Ge-P-B-doped silica core fibers, as discussed earlier. The spectral similarity of the induced optical absorption of these two fibers is evidence that the damage is dominated by absorptions associated with P-related defect centers. The lower intensity of the induced absorption in Ge-B-P-doped silica core fibers is a reflection of the lower concentration of P in this waveguide relative to that in the P-doped silica core fiber.

The induced absorption spectra of the Ge-B-doped silica core fiber and the Ge-doped silica core fiber supplied by Corning Glass Works are quite similar at the shorter wavelengths. The greater absorption noted in the Ge-B-doped fiber at wavelengths longer than 1.0 μ may be attributed to B-related defect centers in this fiber.³ The substantially lower response of the Bell Telephone Laboratories Ge-doped silica core fiber is consistent with this premise since this fiber had a pure silica cladding, whereas the CGW fiber had a boron-doped silica cladding, and the boron was also graded slightly into the core.⁴

It is significant to note from Fig. 5 that contrary to previous observation,³ no radiation-induced increase in the OH overtone and combination bands was evident in these fibers. In the present study, high index matching oil ($n = 1.67$) was used to strip the cladding modes, whereas glycerin ($n = 1.47$), was used in the previous study where such increases were observed.³ It has been concluded that the irradiation ionizes hydrogen in the protective polymer jacket which then bonds to oxygen at the glass-polymer interface, creating an increase in the OH absorption for light propagating in the cladding.⁴

CONCLUSIONS

The results described in this paper together with additional data to be presented at the meeting have established that in general the radiation-induced loss in optical fiber waveguides is less at long wavelengths than at 0.82 μ . However, the induced loss after low or moderate dose is still quite substantial and can be several orders of magnitude greater than the intrinsic loss of <1 dB/km, even at these long wavelengths. Optical fibers containing P in the core, such as the Ge-P-doped silica or binary P-doped silica core fibers under consideration for single mode waveguides, will be especially unsuitable for operation at 1.3 or 1.55 μ under moderate or high total dose conditions. However, we have identified several candidate fibers for use at long wavelength in radiation environments. The Ge-doped silica core fibers not codoped with P have a broad minimum in induced loss extending from 1.1 to 1.5 μ , so that these fibers can be used to advantage in this wavelength range. Pure fused silica core fibers of high OH content, such as PCS or borosilica-clad silica fibers, are best suited for operation at 1.06 μ in a radiation environment since this wavelength combines low intrinsic loss with the minimum in radiation-induced loss. Dry silica core fibers are also attractive candidates for long wavelength

operation; induced losses less than 20 dB/km have been measured between 1.5 and 1.65 μ one hour after an irradiation of 10^5 rads. Thus, it appears possible by careful selection of the fiber core material and inclusion of the radiation-induced loss in the total loss budget to deploy optical fiber links operating at long wavelengths that can withstand specific nuclear threats.

ACKNOWLEDGEMENTS

The authors would like to thank D. L. Griscom for his interest and helpful comments and discussions. This work would not have been possible without the generosity of the fiber waveguide industry in providing samples. In particular, P.C. Schultz, Corning Glass Works, K.Rau, Hereaus Quarzschmelze GmbH; W. G. French, J. W. Fleming and F. V. DiMarcello, Bell Laboratories, Inc.; R. E. Jaeger, Galileo Electro Optics; and D. W. Harper, Pilkington Brothers, Ltd. are thanked.

REFERENCES

1. E. J. Friebele and D. L. Griscom in Treatise on Materials Sciences and Technology Vol. 17: Glass II (M. Tomozawa and R. H. Doremus, Eds.), Academic Press, New York, 1979, pp. 257-351.
2. E. J. Friebele, Opt. Eng. 18, 552-561 (1979).
3. E. J. Friebele, G. H. Sigel, Jr., and M. E. Gingerich, in Fiber Optics: Advances in Research and Development (B. Bendow and S. S. Mitra, Eds.) Plenum Press, New York, 1979, pp. 355-367.
4. E. J. Friebele, P. C. Schultz, and M. E. Gingerich, Appl. Opt. (in press).
5. E. J. Friebele, R. E. Jaeger, G. H. Sigel, Jr., and M. E. Ginerich, Appl. Phys. Lett. 32, 95-97 (1978).
6. J. G. Titchmarsh, Electron Lett. 15, 111-112 (1979).
7. E. J. Friebele and M. E. Ginerich, "Photobleaching Effects in Optical Fiber Waveguides," Proc. DNA Symposium on Fiber Optics in the Nuclear Environment (1980).
8. G. H. Sigel, Jr., B. D. Evans, R. J. Ginther, E. J. Friebele, D. L. Griscom and J. Babiskin, NRL Memorandum Report 2934 (1974).
9. P. Kaiser, J. Opt. Soc. Am. 64, 475-481 (1974).
10. E. J. Friebele, G. H. Sigel, Jr., and D. L. Griscom, Appl. Phys. Lett. 28, 516-518 (1976).
11. B. D. Evans and G. H. Sigel, Jr., IEEE Trans. Nucl. Sci. NS-22, 2462-2467 (1975).
12. M. Stapelbroek, D. L. Griscom, E. J. Friebele, and G. H. Sigel, Jr., J. Non-Cryst. Solids 32, 313-326 (1979).

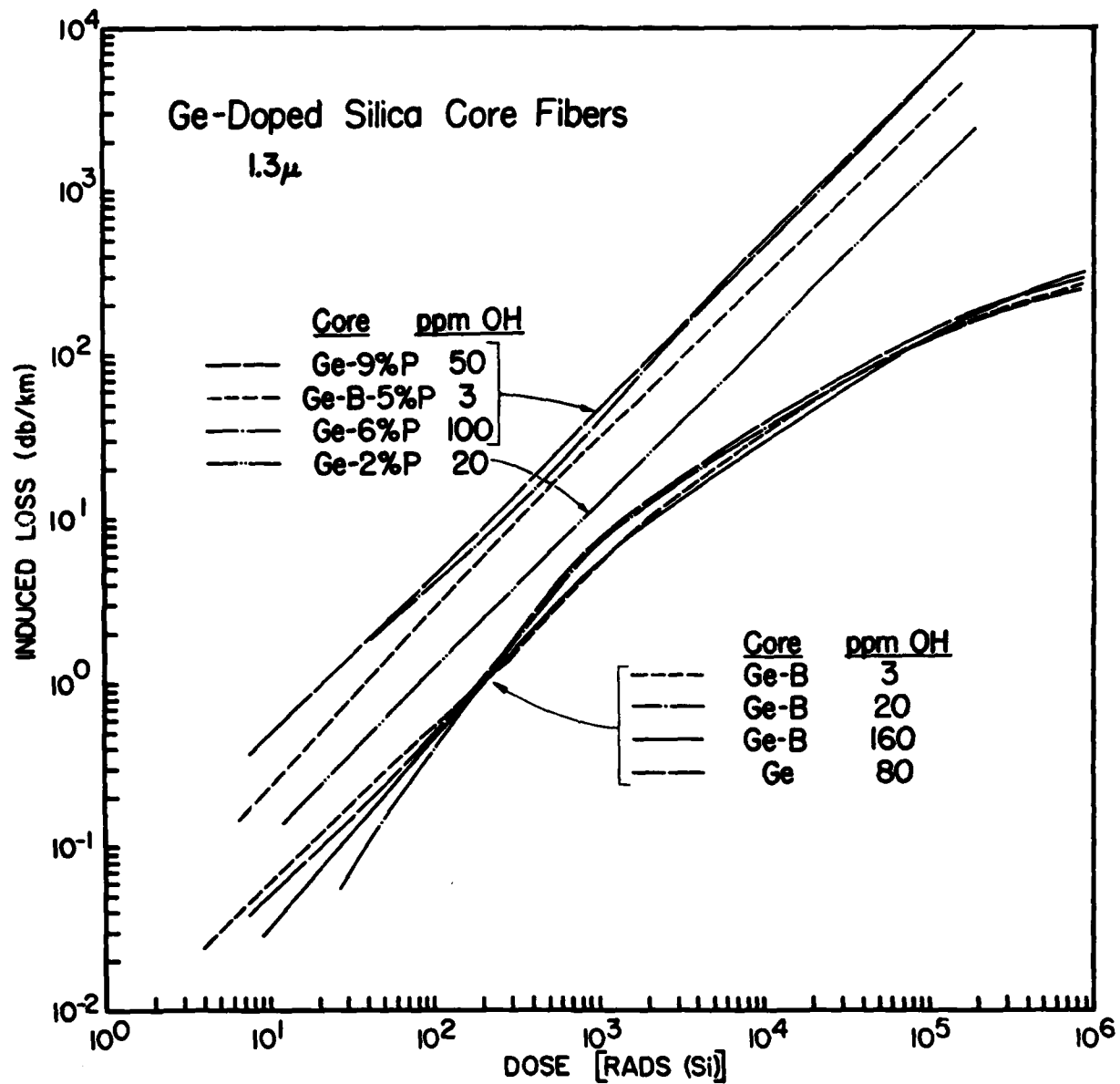


Figure 1

Growth of the radiation-induced attenuation of Ge-doped silica core optical fiber waveguides at 1.3 μ measured at room temperature during steady state irradiation. Dose rate = 1.8×10^4 rads/min.

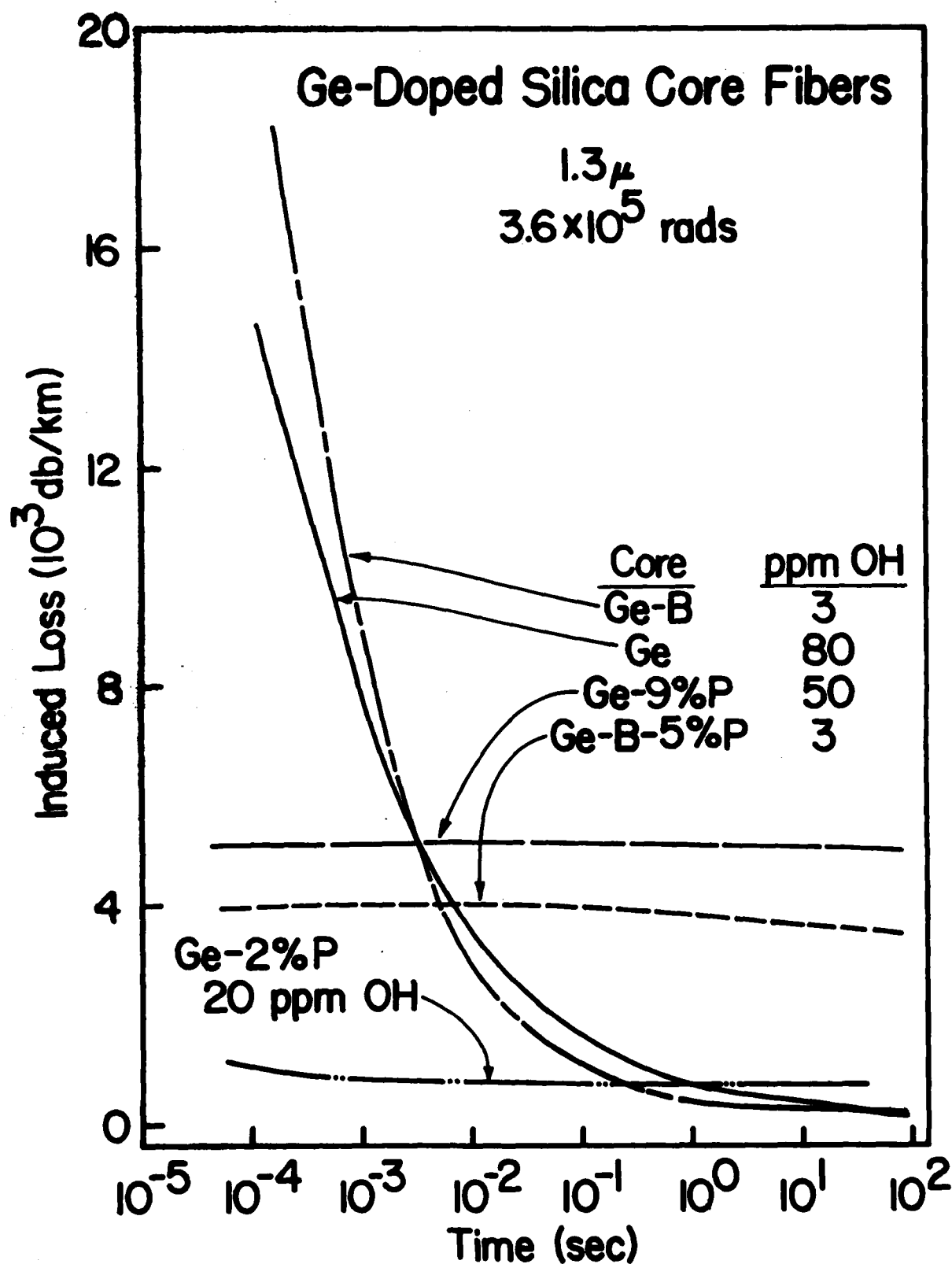


Figure 2

Decay of the radiation-induced attenuation of Ge-doped silica core waveguides at 1.3μ following a 5 nsec, 0.5 MeV pulsed electron irradiation of 3.6×10^5 rads.

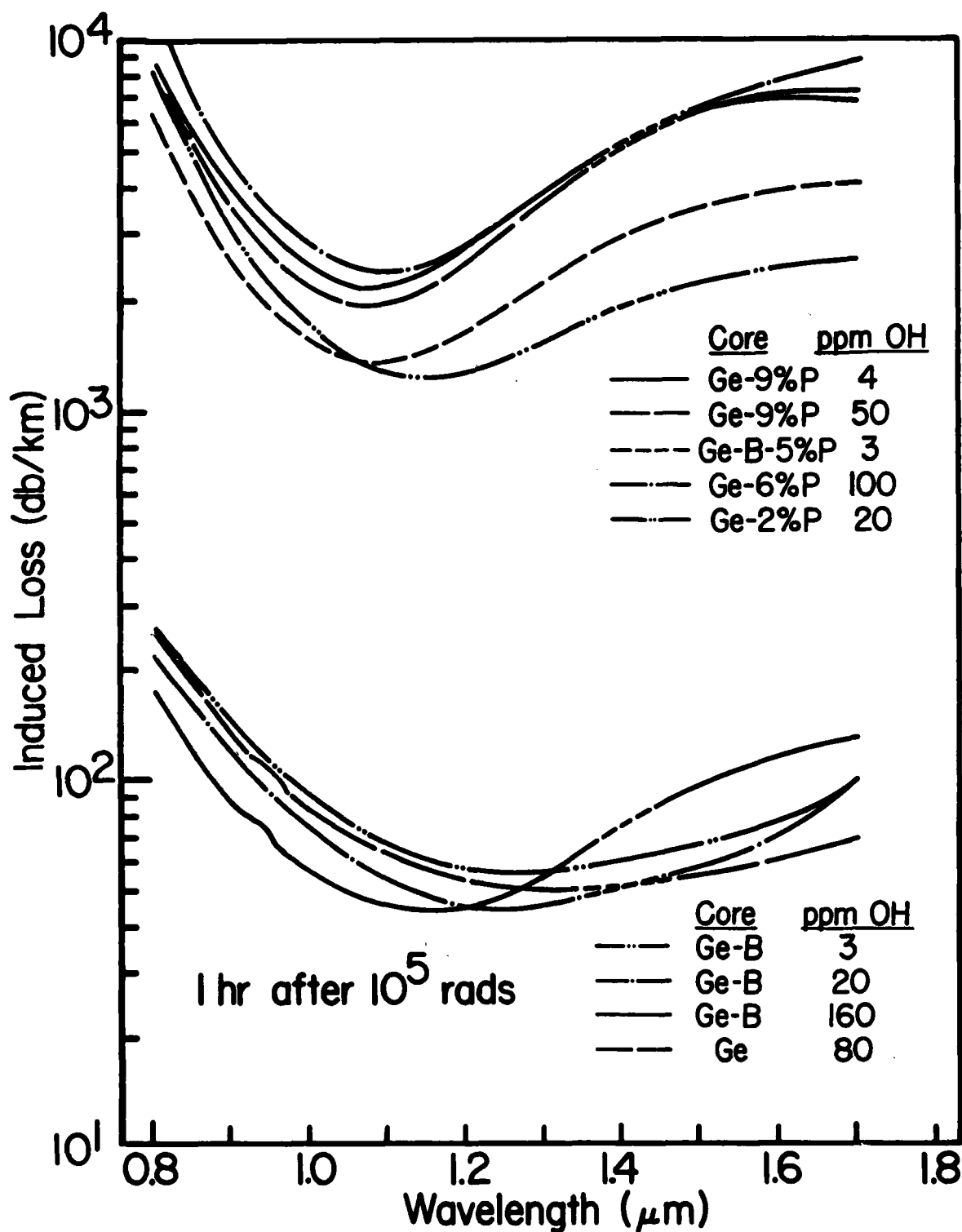


Figure 3 Radiation-induced optical absorption spectra of Ge-doped silica core fibers measured one hour after a ^{60}Co dose of 10^5 rads.

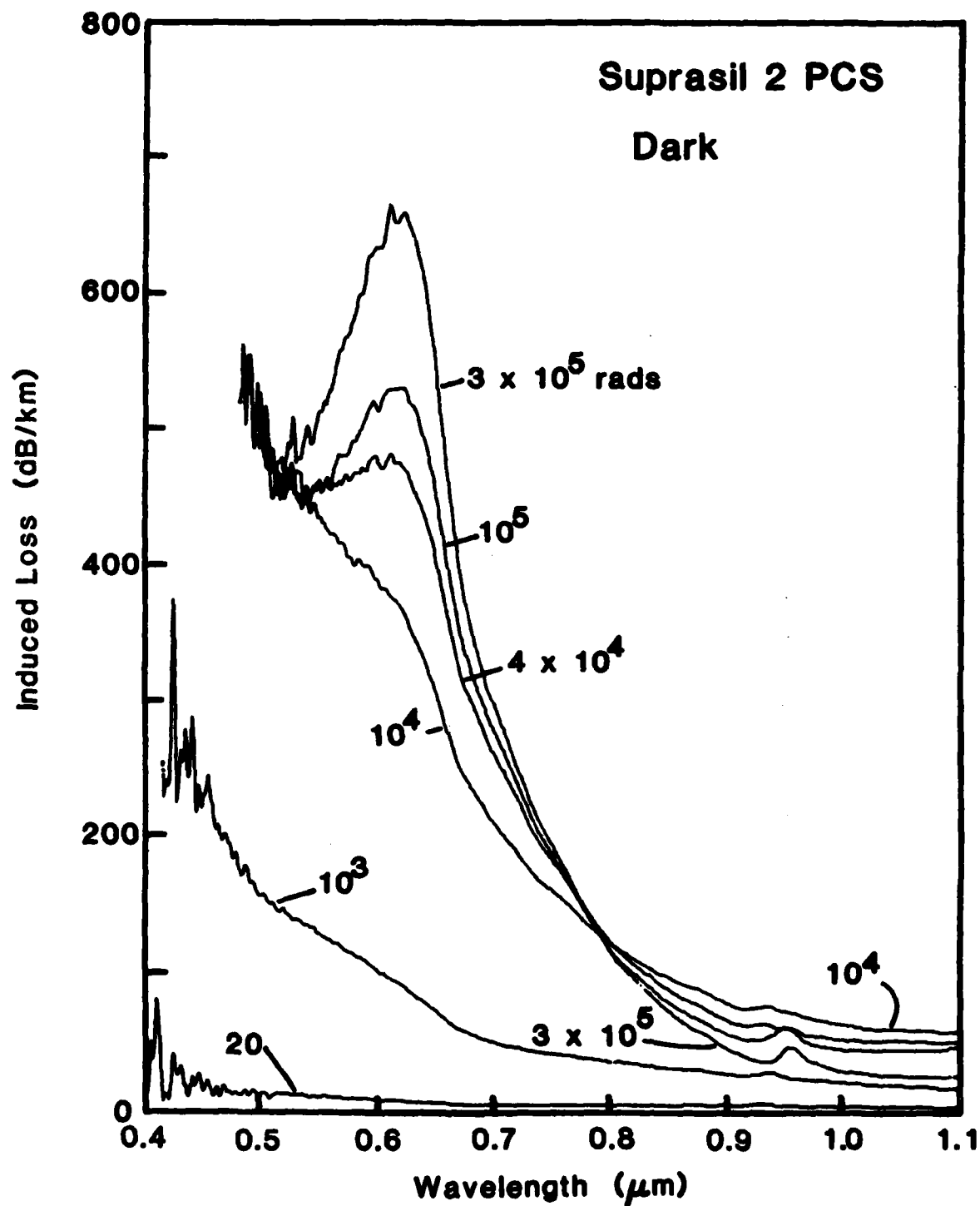


Figure 4 Radiation-induced optical absorption spectra of a high OH content polymer clad silica core fiber measured during room temperature steady state ^{60}Co irradiation.

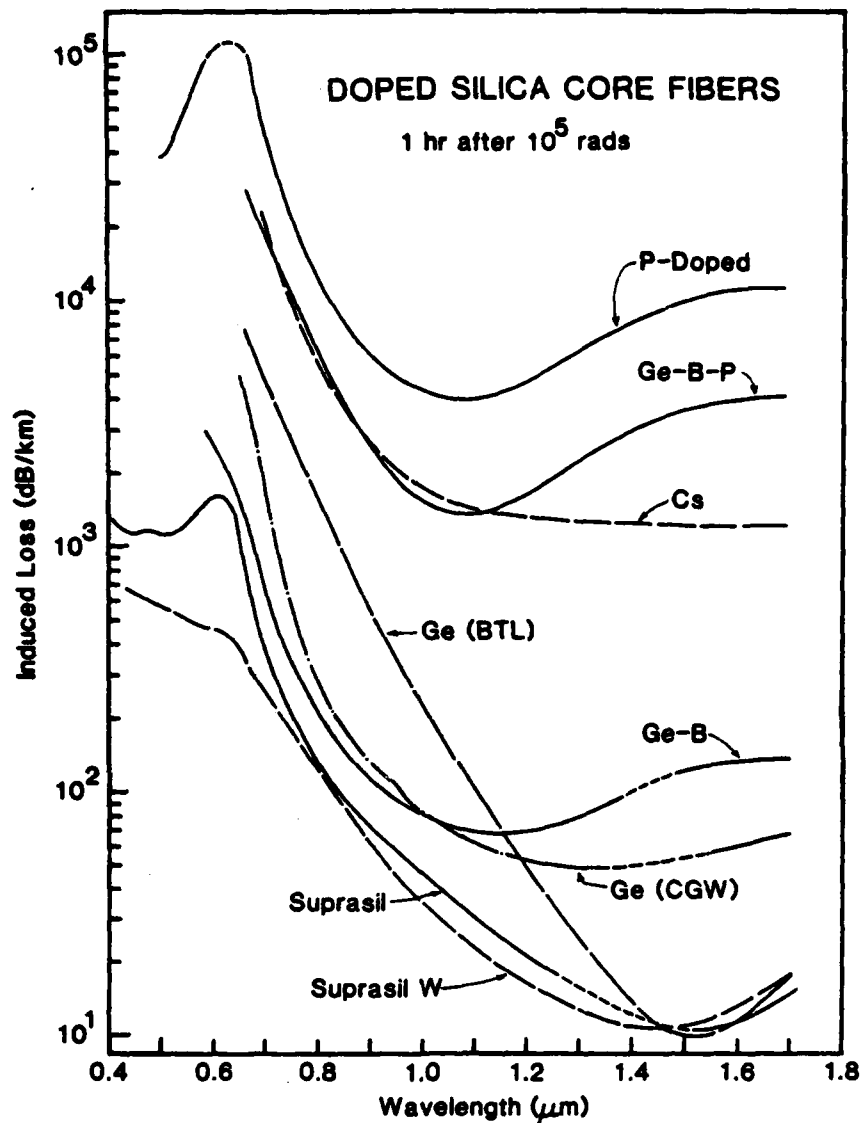


Figure 5 Radiation-induced optical absorption spectra of various pure synthetic silica and doped silica core optical fiber waveguides measured one hour after an irradiation of 10^5 rads. Dashed regions near 1.4μ in some fibers indicate that the intensity of the second OH overtone band at 1.37μ was too large to allow an accurate determination of the induced loss.

Temperature Dependence of Radiation Darkening in Optical Waveguides*

Stewart Share

U.S. Army Electronics Research and Development Command
Harry Diamond Laboratories
2800 Powder Mill Road
Adelphi, Maryland 20783

Introduction

A serious problem encountered by fiber-optic systems which operate in nuclear environments is radiation darkening of the optical waveguides. Room-temperature radiation measurements^{1,2,3} indicate that the magnitude of the radiation darkening depends on the composition of the fiber and the fiber fabrication technique. Many fiber-optic applications require operation over a wide range of temperatures. Temperature has been shown to affect the degree of radiation darkening in optical waveguides.^{4,5,6} In this paper we present the results to date of a study to identify a fiber composition and fabrication technique in which the radiation losses are minimal over the temperature range of operation. The temperature range we are considering is -50° to 70°C. We then specify survivable fiber-optic lengths for various digital and analog applications.

Survivability of fiber-optic systems in nuclear radiation environments depends on (1) the radiation conditions and (2) the system performance specifications. Radiation conditions depend on the total level of the radiation, on the rate at which the radiation is delivered, and on the distribution of the radiation over the fiber. In a tactical nuclear radiation environment, the initial radiation is delivered in a time on the order of tens of seconds, making a ⁶⁰Co gamma source a good simulation. The radiation may be either uniformly or nonuniformly distributed over the length of fiber, depending on the radiation pattern and on the system deployment. System performance specifications influencing survivability include fiber length, data rate, modulation format, off-the-air time, and operating temperature. It is the latter which we would like to discuss in this paper.

Fibers

The temperature dependence of the radiation darkening depends on the composition of the fiber and on the fiber fabrication technique. The fabrication techniques studied thus far are as follows: (1) the vapor-deposition techniques, which include the outside (O) process or outside vapor phase oxidation (OVPO) process and the inside process (I) or the modified chemical vapor deposition (MCVD) process, (2) the modified rod-in-tube technique (MRT), (3) the Phasil technique and finally (4) synthetic fused-

*Work supported by the U.S. Army Electronics Research and Development Command and the U.S. Army Communications Research and Development Command

silica techniques, which include the plasma oxidation (Pl-Ox) and the hydrolysis (H) processes. The fibers studied are listed in Table I. Included are the vendor, core composition, cladding composition, fabrication technique, and numerical aperture (NA). The room-temperature pre-irradiation intrinsic loss was equal to or less than 10 dB/km at 0.8 μ m in all these fibers except the Phasil fiber, which was 17 dB/km at 0.89 μ m. The manufacturers include Corning Glass Works (CGW), Bell Telephone Laboratories (BTL), Hughes Research Laboratory (HRL), Times Wire and Cable (TWC), Dainichi-Nippon Cables (DNC), Heraeus-Amersil (the fiber was pulled from an Heraeus-Amersil preform by Valtec) (HA/VAL), International Telephone and Telegraph (ITT), Galileo Electro-Optics (GEO), Canstar (CAN), Fiberguide (FG), and Maxlight Optical Waveguides (MAX).

Table I. Fibers Studied

Vender-Fiber	Core	Cladding	Fabrication technique	NA
CGW-OVPO	$\text{GeO}_2\text{-B}_2\text{O}_3\text{-SiO}_2$	$\text{B}_2\text{O}_3\text{-SiO}_2$	O	.21
CGW-SDF	$\text{GeO}_2\text{-SiO}_2$	$\text{B}_2\text{O}_3\text{-SiO}_2$	O	.30
CGW-IVPO	$\text{GeO}_2\text{-P}_2\text{O}_5\text{-B}_2\text{O}_3\text{-SiO}_2$	$\text{B}_2\text{O}_3\text{-SiO}_2$	I	.22
BTL-X1*	$\text{GeO}_2\text{-SiO}_2$	SiO_2	MCVD	.196
BTL-X2*	SiO_2	$\text{B}_2\text{O}_3\text{-SiO}_2$	MCVD	.15
BTL-X3*	$\text{GeO}_2\text{-P}_2\text{O}_5\text{-SiO}_2$	$\text{B}_2\text{O}_3\text{-SiO}_2$	MCVD	.34
HRL-P42479	$\text{GeO}_2\text{-P}_2\text{O}_5\text{-SiO}_2$	$\text{B}_2\text{O}_3\text{-SiO}_2$	MCVD	.23
HRL-P21279	$\text{GeO}_2\text{-P}_2\text{O}_5\text{-SiO}_2$	$\text{B}_2\text{O}_3\text{-SiO}_2$	MCVD	---
TWC-G5200	SiO_2	$\text{B}_2\text{O}_3\text{-SiO}_2$	O	.17
DNC-SM60ST	SiO_2	B-F-doped SiO_2	MRT	.17
HA/VAL	SiO_2	F-doped SiO_2	Pl-Ox	.17
ITT-7908143a	$\text{GeO}_2\text{-P}_2\text{O}_5\text{-SiO}_2$	$\text{B}_2\text{O}_3\text{-SiO}_2$	MCVD	.23
ITT-7904164	$\text{GeO}_2\text{-SiO}_2$	$\text{B}_2\text{O}_3\text{-SiO}_2$	MCVD	.19
GEO-81877	$\text{GeO}_2\text{-B}_2\text{O}_3\text{-SiO}_2$	$\text{B}_2\text{O}_3\text{-SiO}_2$	MCVD	.24
CAN	Cs-doped SiO_2	doped SiO_2	Phasil	---
FG-Superguide 1	SiO_2	Silicone	H	.23
FG-Anhydroguide Sp	SiO_2	Silicone	Pl-Ox	.23
ITT-8 mil 031577DE2	SiO_2	Silicone	H	.3
MAX-220792	SiO_2	Silicone	Pl-Ox	.32
MAX-2107782	SiO_2	Silicone	H	.32

* Author's Designation

Radiation Data

Figure 1 shows the losses induced at 0.8 μ m in the CGW $\text{GeO}_2\text{-B}_2\text{O}_3\text{-SiO}_2$ OVPO fiber from in-situ ^{60}Co irradiation as a function of temperature. The ^{60}Co dose rate was 95 rad(SiO_2)/s. The important point to note is the large increase in induced loss as the temperature is lowered. At -50°C the induced loss is greater than 1000 dB/km for a dose of 2000 rad(SiO_2); at 200 rad(SiO_2) the induced loss is 410 dB/km.

Figure 2 shows the losses induced from in-situ ^{60}Co irradiation in a TWC silica-core borosilica-clad fiber fabricated by an outside process. Here, as in the previous fiber, the losses increase with decreasing temperature, though at a rate not as fast as in the previous fiber. The losses at -50°C are again nearly 1000 dB/km for a 2000-rad(SiO_2) irradiation. Clearly, if fibers are to be used over a large range of temperatures, the induced losses must be

reduced.

Figure 3 shows the losses induced in an HRL doped-silica core fiber (P42479) fabricated by the MCVD process. The fiber was doped with Ge and P in the core. The induced losses increase as the temperature is reduced, but the magnitude of the losses is greatly reduced compared to the previous fibers. At -50°C the induced loss is 54 dB/km for a dose of 2000 rad(SiO_2) (95 rad(SiO_2)/s dose rate); at 200 rad(SiO_2) the induced loss is 6 dB/km.

Table II summarizes the losses induced at $0.8\text{ }\mu\text{m}$ in the fibers studied for in-situ ^{60}Co irradiations of 200 and 2000 rad(SiO_2). The dose rate was 95 rad(SiO_2)/s. The losses shown are the maximum losses measured over the temperature range from -50° to 70°C . The fibers showing the lowest losses are doped-silica-core fibers fabricated by the MCVD technique. This is followed by polymer-clad silica-core fibers, glass-clad silica-core fibers, and finally doped-silica-core fibers, fabricated by the outside process.

Table II. Summary of Radiation Losses
Wavelength: $0.8\text{ }\mu\text{m}$
Temperature: -50°C to 70°C

Vendor-Fiber	Induced loss (dB/km)	
	at 200 rad(SiO_2)	at 2000 rad(SiO_2)
CGW-OVPO	410	1730
CGW-SDF	130	840
CGW-IVPO	48	330
BTL-X1	12	66
BTL-X2	78	190
BTL-X3	8	75
HRL-P42479	6	54
HRL-P21279	8	83
TWC-G5200	120	850
DNC-SM60ST	80	200
HA/VAL	160	680
ITT-7908143a	10	133
ITT-79404164	32	170
GEO-81877	42	190
CAN	320	1360
FG-SUPERGUIDE 1	45	230
FG-ANHYDROGUIDE SP	52	205
ITT-8 MIL 031577DE2	31	123
MAX-220792	54*	360*
MAX-2107792	54*	280*

* -32° to 70°C

The MCVD fibers that showed minimal losses were doped with Ge and P or Ge in the core. The pure Ge-doped silica-core fiber contained no B in the cladding. The doped-silica-core fibers fabricated by the outside process contained either Ge or Ge and B in the core and no P. The claddings all contained B. We plan to study the effect of P on the low-temperature radiation response of doped-silica-core fibers fabricated by the outside process. We will also be measuring high-OH silica-core fibers with F-doped

silica claddings. It appears that silica-core fibers with high OH concentration may offer some advantage in radiation environments over low OH silica-core fibers.⁷

Survivable Fiber-Optic Length

The radiation-survivable fiber-optic length depends on the total radiation loss in the fiber and excess power that the system can allow as a margin for the fiber radiation losses. Various factors determine the fiber radiation loss and excess power. The fiber radiation loss depends on the level of the radiation and the rate at which the radiation is delivered. It also depends on the length of the fiber and the distribution of the radiation over the fiber; for example, whether the radiation is uniformly distributed over the fiber, or non-uniformly distributed such as from a point source. The fiber radiation loss also depends on the allowable off-the-air time. This is a factor because the induced losses can anneal following removal of the radiation. Finally, as we have seen, temperature affects the radiation-induced losses in the fiber.

The excess power in the system depends on the emitter output, data rate, modulation format, intrinsic fiber loss, connector loss, emitter coupling efficiency into the fiber, component radiation damage such as in detectors, and the system design margin. We consider all these factors in determining the survivable fiber-optic lengths.

Figure 4 shows the losses induced at 0.85 μm in the HRL Ge-P-doped silica core MCVD fiber from ^{60}Co irradiation. The data shown are given at -50°C for both in-situ irradiation ($95 \text{ rad}(\text{SiO}_2)/\text{s}$) and at 1000 s after irradiation. The lower values of induced loss observed at 1000 s result from annealing effects which occur after removal of the ^{60}Co source. The radiation losses shown in Figure 4 are the largest losses measured over the temperature range investigated (-50° to 70°C). For 2000-rad in-situ ^{60}Co irradiation the induced loss is 28 dB/km; at 5000 rad(SiO_2) the induced loss is 60 dB/km. At 1000 s after a 2000-rad(SiO_2) irradiation, the induced loss is less than 10 dB/km; at 1000 s after a 5000-rad(SiO_2) irradiation the loss is 16 dB/km.

Figure 5 plots the dependence of fiber radiation loss (dB) on length for the fiber shown in Figure 4. The radiation dose was 2000 rad(SiO_2) and the wavelength was 0.85 μm . The fiber radiation loss increases linearly with length for uniform irradiation. For nonuniform irradiation from a point source, the fiber radiation losses begin to level off for fiber lengths of 2 to 3 km. This is because the radiation field of a point source drops off rapidly with distance. For the case evaluated, increasing the length of fiber beyond 4 km does not significantly increase the fiber radiation loss.

Using the same fiber, wavelength, and total dose we evaluate the response of a digital communications link. Figure 6 plots the excess power (dotted lines) for a digital system with a nonreturn-to-zero modulation format. Data rates of 500 kb/s and 5 Mb/s are considered. A laser (-1 dBm power coupled into the fiber) and an avalanche photodiode (APD) are assumed. The bit-error-rate (BER) is 10^{-9} , and required optical power at the receiver was obtained from ref. 8. The intrinsic fiber loss was 10 dB/km. Assumed connector losses are 2 dB/connector (connectors were assumed at the fiber input and output and at every two km), and the design margin is assumed to be 7 dB; 12 dB is

allowed for damage to the APD from neutron irradiation measurements. From Figure 6, the survivable fiber length for a 2000-rad in-situ irradiation is 1.05 to 1.5 km, depending on data rate and radiation distribution. The survivable length is longer for the lower data rates because of the larger excess power associated with maintaining a BER of 10^{-9} . The survivable length increases, 2.2 to 3.8 km, at 1000 s after the irradiation because of annealing of the induced losses. The survivable lengths are longer for the nonuniform irradiation than for the uniform irradiation at a fixed data rate because of the lower fiber radiation-induced loss.

Figure 7 shows the predicted radiation response for an analog communication link with intensity modulation and a signal-to-noise ratio (S/N) of 40 dB. An LED (-9 dBm power coupled into the fiber) and an APD are assumed. Two data rates, 10 kHz and 5 MHz, are considered; the required optical power at the receiver was obtained from ref. 8. All other parameters are similar to the previous example. From Figure 7, the survivable lengths at 5 MHz are 0.2 to 0.45 km, depending on whether operation is desired in situ or at 1000 s following irradiation. It is noted that for the parameters chosen and a data rate of 5 MHz, the survivable length is not strongly dependent on the distribution of the radiation (i.e. uniform and nonuniform). For 10 kHz, the survivable lengths are 0.9 to 2.2 km and do depend on the distribution of the radiation.

Summary

In summary, doped-silica-core fibers fabricated by the MCVD technique showed the lowest radiation losses of the fibers measured over the temperature range from -50° to 70°C. The radiation losses were measured in situ during ^{60}Co irradiation of several thousand rad(SiO_2). Survivable lengths of fiber optic cables for analog and digital applications were shown to depend on data rate, off-the-air time, and radiation distribution.

References

1. E. J. Friebele, R. E. Jaeger, G. H. Sigel, Jr., and M. E. Gingerich; Appl. Phys. Lett. 32, 95 (1978).
2. E. J. Friebele, M. E. Gingerich and G. H. Sigel, Jr., Appl. Phys. Lett 32, 619 (1978).
3. E. J. Friebele, G. H. Sigel, Jr., and M. E. Gingerich, IEEE Trans. Nucl. Sci. NS-25, No. 6, 1261 (1978).
4. P. L. Mattern, L. M. Watkins, C. D. Skoog, and E. H. Barsis, IEEE Trans. Nucl. Sci. NS-22, No. 6, 2468 (1975).
5. S. Share, R. M. McCracken, and I. Aggarwal, IEEE Trans. Nucl. Sci. NS-25, No. 6, 1288 (1978).
6. S. Share and J. Wasilik, IEEE Trans. Nucl. Sci. NS-26, No. 6, 4802 (1979).
7. E. J. Friebele, Optical Engineering 18, No. 6, 552 (1979).
8. Glen R. Elion and Herbert A. Elion, Fiber Optics in Communication Systems, Marcel Dekker, Inc. (1978).

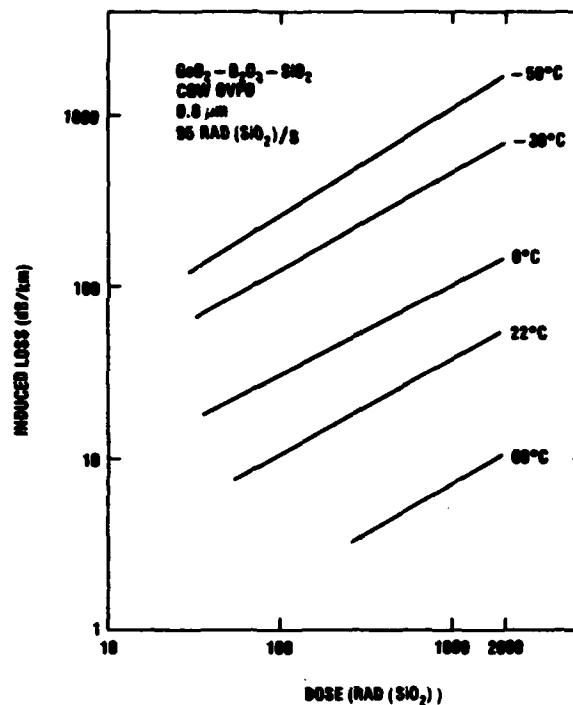


Figure 1. Induced loss at 0.8 μm in CGW $\text{GeO}_2\text{-B}_2\text{O}_3\text{-SiO}_2$ OVPO fiber from in-situ ^{60}Co irradiation at various temperatures. The ^{60}Co dose rate was 95 rad(SiO_2)/s.

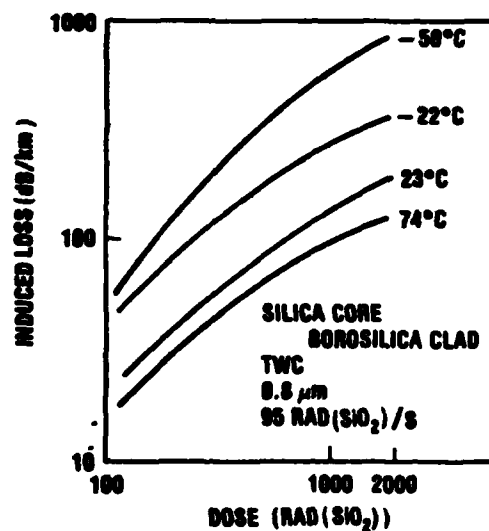


Figure 2. Induced loss at 0.8 μm in TWC silica-core borosilica-clad fiber from in-situ ^{60}Co irradiation at various temperatures. The ^{60}Co dose rate was 95 rad(SiO_2)/s.

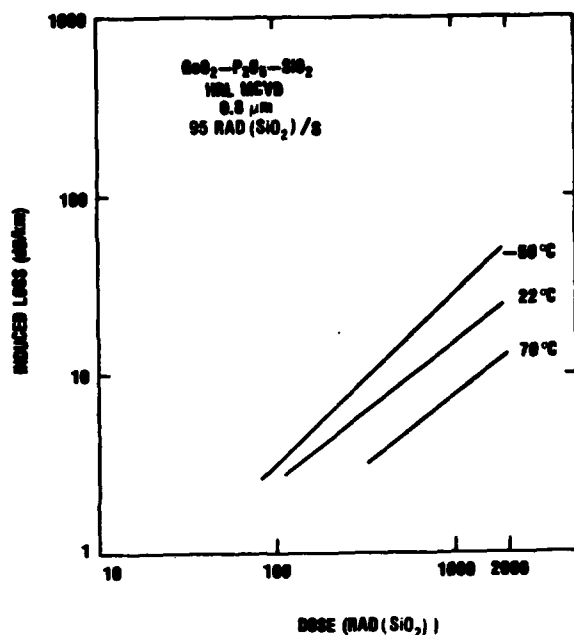


Figure 3. Induced loss at 0.8 μm in HRL GeO₂-P₂O₅-SiO₂ MCVD fiber from in-situ ⁶⁰Co irradiation at various temperatures. The ⁶⁰Co dose rate was 95 (rad(SiO₂)/s).

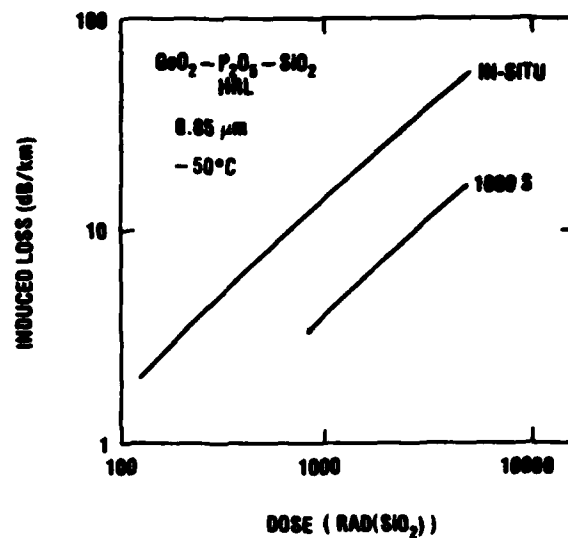


Figure 4. Induced loss at 0.85 μm in HRL GeO₂-P₂O₅-SiO₂ MCVD fiber from in-situ ⁶⁰Co irradiation (95 rad(SiO₂)/s dose rate) and at 1000 s after irradiation. The temperature was -50°C.

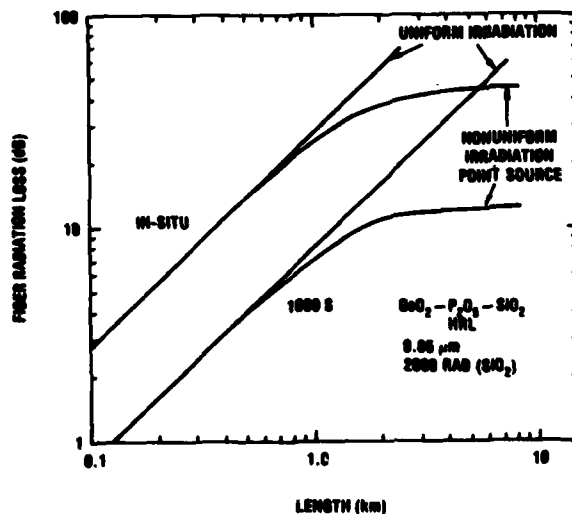


Figure 5. Dependence of fiber radiation loss (dB) at 0.85 μm and -50°C in HRL fiber on length of fiber for uniform irradiation and for nonuniform irradiation from a point source.

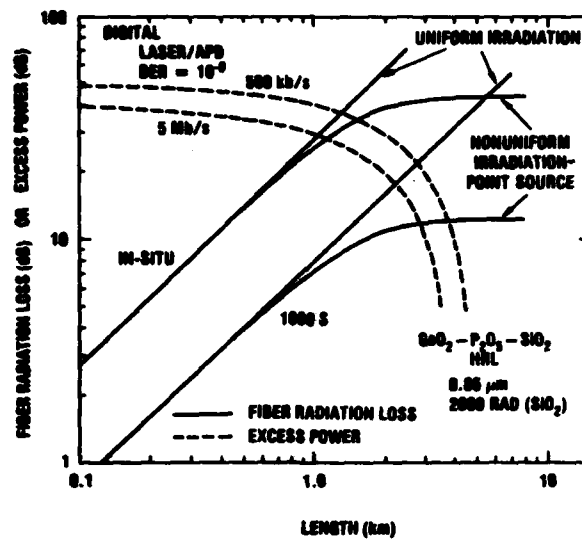


Figure 6. Fiber radiation loss (solid lines) and excess power (dotted lines) for a 500 kb/s and a 5 Mb/s nonreturn-to-zero modulated digital link versus fiber length.

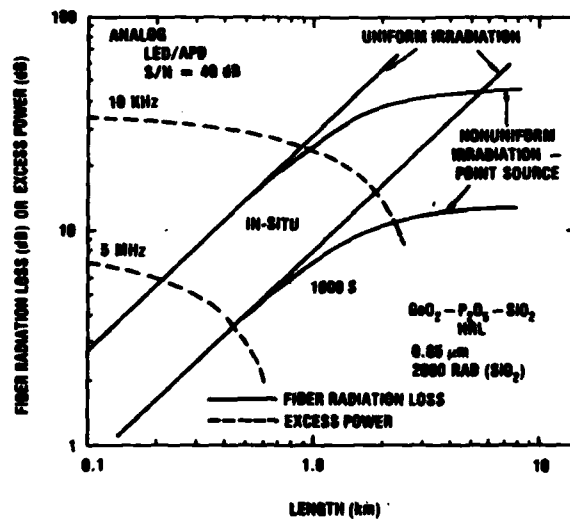


Figure 7. Fiber radiation loss (solid lines) and excess power (dotted lines) for a 10 kHz and a 5 MHz intensity modulated analog link versus fiber length.

Radiation Performance of Germanium Phosphosilicate Optical Fibers as a Function of Temperature

J. A. Wall, H. Posen*, Deputy for Electronic Technology
Rome Air Development Center, Solid State Sciences Division, Hanscom AFB, MA
01731, (617)861-4031

R. Jaeger, Galileo Electro Optics Co.,
Galileo Park, Sturbridge, MA 01518

Introduction

In the application of optical fibers to military systems, one of the principle types of fiber being considered by designers is the so-called "fat" fiber with high numerical aperture. The reasons for this choice are high source coupling efficiency and ease of handling in the field. Also, fibers with phosphorous-doped cores are considered desirable because of their known superior recovery characteristics in transient radiation environments. However, no real-time radiation response tests of this type of fiber over the mil-spec temperature range of -55°C to $+125^{\circ}\text{C}$ have previously been performed. This paper presents data on such tests.

The tests were performed in response to a request from the Air Force Avionics Laboratory for information on a commercially available Germanium Phosphosilicate fiber. The fiber has a core/clad ratio of 125/200 μm and a numerical aperture of 0.25. Unjacketed versions of this fiber were specially fabricated for these tests. Real-time steady-state and transient radiation response tests were performed at temperatures of -55°C , $+25^{\circ}\text{C}$ and $+125^{\circ}\text{C}$ on two of these fibers. For reference purposes, the fibers are designated WP-2 and WP-6, with WP-6 having a higher germanium content in the core and a numerical aperture of 0.26. All tests were performed on lengths of fiber taken from a single draw in order to avoid any variations in test results that might be caused by differences between preforms or drawing processes.

Experimental Procedures

A temperature control chamber, specially designed for use with the RADC/ES radiation facilities, was constructed for the tests. Except for heating elements and wiring which are located some distance from the fiber position, it is made of all low atomic number materials to prevent perturbation of the radiation fields at the sample position. The walls are double plywood with fiberglass insulation and the sample chamber is aluminum. The chamber is divided by aluminum baffles to one of which is mounted a 900 watt heating element used to attain temperatures up to $+150^{\circ}\text{C}$. The lower part of the chamber serves as a liquid nitrogen reservoir. The fibers are wound on 13 cm diameter, 1.5 cm thick aluminum reels which mount on the upper end of a moveable aluminum strut. The base of the strut rests on the bottom of the chamber so that it serves as a cold finger when the reservoir is filled with liquid nitrogen. A low-power heating element attached to the strut controls the temperature, measured by a thermocouple, at the sample position.

*Deceased, December 1979

Temperatures are maintained to within $\pm 1^\circ\text{C}$ by proportional controllers and thyristor packs mounted in a console which can be located up to 25 meters from the chamber and radiation sources. The console also includes a digital thermometer for continuous temperature monitoring and an automatic liquid nitrogen fill controller which, in conjunction with a 60 liter pressurized dewar, can maintain the lower temperatures for at least six hours.

Steady-state irradiations were performed using x-rays generated by 10 MeV electrons incident on a tungsten target. The electron source was the RADC linear accelerator (linac) which was set to produce electron pulses 4.5 μsec wide at an approximate rate of 5 pps. The fiber, mounted in the temperature control chamber, was positioned relative to the x-ray target so that it received a uniform irradiation of about 0.5 rads per (linac) pulse. The ends of the fiber were brought out of the chamber and coupled to an 850 nm LED source operated in continuous mode and a PIN photodiode-amplifier detector. The source and detector were located out of the direct x-ray beam and shielded from scattered radiation by two inches of lead. The output of the detector was fed to the experimental control area by coaxial cable and connected to a digital voltmeter and chart recorder for continuous observation of the fiber transmission. A pulse counter was used to measure the accumulated number of linac pulses. The voltmeter reading was recorded as a function of total linac pulses at frequent intervals while the chart recorder provided a continuous reading of the detector output as a function of time. Following the irradiation, the chart recorder was used to monitor recovery of the induced loss.

Dosimetry was performed using thermo-luminescent dosimeters (TLD's) mounted in quadrature on each side of the fiber reel at the fiber position. The TLD's measured the total dose to which the fiber was exposed during the irradiation. Dividing this total dose by the total number of linac pulses generated during the irradiation gave an accurate measure of the dose produced by each linac pulse. The data taken in terms of induced loss as a function of accumulated linac pulses was then converted to loss as a function of dose.

Because the linac is a pulsed radiation source, a set of irradiations was also performed on one of the fibers using the RADC Co-60 source to check the validity of using the linac for steady-state tests. The arrangement was similar to that using the linac except that the source and detector were located outside the cobalt cell and an ionization chamber was used to monitor accumulated dose. The ionization chamber could not be operated at the temperature extremes in these tests, so it was located outside and adjacent to the temperature control chamber in a position where it received approximately the same exposure as the fiber. The chamber readout was set to indicate accumulated dose and its output connected to a second pen on the chart recorder so that induced loss and accumulated dose could be measured simultaneously. As with the linac irradiations, TLD's were used as a final calibration of the dose indicated by the ionization chamber since it was not located at the fiber position. These irradiations also provided a calibration of the TLD's at $+125^\circ\text{C}$, a temperature at which they had never before been irradiated.

The transient tests were performed using the RADC flash x-ray generator which produces a 20 nanosecond pulse of nominal 2 MeV peak energy. Tests were performed at two dose-rates on the order of 10^8 rads per second and 10^9 rads per second. An 820 nm laser diode operated in continuous mode was used as the light source

and a PIN photodiode and 50 megahertz bandwidth amplifier was used as the detector. The source was located in the irradiation area but out of the x-ray beam. The output end of the fiber was coupled through a fiber-optic link to the detector located in the experiment control area. The detector output was connected to four oscilloscope inputs and an X-Y recorder (with time base) to obtain a time span from less than 50 nanoseconds to over 60 seconds. Dosimetry was performed using a small pin diode in direct contact with the fiber on the reel, except at +125°C where the PIN could not be operated. In the latter case, dose-rate was estimated from the average of dose-rates measured in preceding "shots" at lower temperatures in the same position relative to the flash x-ray target.

For both the steady state and transient tests, 75 meter lengths of fiber were irradiated. New lengths of fiber were used for each irradiation with the exception of the transient tests at 10^8 rads per second where it was found in preliminary trials that the results of several "shots" on the same fiber were indistinguishable from one another. It was also found that the results of two or three irradiations on the same fiber at 10^9 rads per second appeared identical, but it was decided to maintain the use of fresh fiber for each irradiation at this level.

Before presenting the radiation test results, it is important to mention significant changes in fiber transmission observed during variations of temperature. The greatest change was observed during warmup. As the fiber was heated from room temperature (about 20°C) the detected light output from the fiber dropped steadily until at +125°C it was more than an order of magnitude lower than its starting level. The major cause of this loss in transmission is probably stress produced by expansion of the aluminum reel, even though the fiber was wound on the reel as loosely as possible while maintaining thermal contact. However, other factors such as the expansion of the fiber's protective coating, cannot be ruled out.

As the fibers were cooled below room temperature a drop in signal level was also observed, but not nearly as severe as with increasing temperature, being down on the order of 10 percent at -55°C. In either case, however, once temperature had been reached signal fluctuations were observed as the temperature cycled around its control point. These fluctuations have an important bearing on the accuracy of the steady-state test results. Without the fluctuations the estimated accuracy is ± 1 dB/km and at -55°C and +25°C the fluctuations change this to ± 2 dB/km. At +125°C, as a result of the severe loss in signal, the accuracy is probably reduced to ± 10 dB/km. For the transient tests estimated accuracy is ± 3 dB/km based on the readability of oscilloscope photographs. Because of the short time spans over which the transient measurements were made, the signal variations should not change this. However the loss of signal at +125°C probably reduces the accuracy to ± 6 dB/km due to the decrease in signal to noise ratio.

Results of Steady-State Tests

Figure 1 shows the steady-state induced loss as a function of dose measured for fiber WP-2 at -55°C, +25°C and +125°C. Although it was intended to irradiate all the test fibers to 10 Krads, the data at -55°C and +125°C ends at just over 6 Krads. This was due to temporary failure of the linac, and because the fibers had received sufficient dose for purposes of the tests, the irradiation was stopped in order to obtain data on the recovery of induced loss following continuous irradiation.

iation. (There was not enough of this fiber available from a single draw to repeat the test.) The interesting features of this data, are the increasing rate of induced loss with temperature and the significant change in slope with increasing dose at +125°C. Figure 2 shows the recovery of induced loss, expressed as a fraction of the loss at the end of irradiation, for this fiber. There is significant recovery only at +125°C. At -55°C, recovery could be followed only for 5 hours due to depletion of the liquid nitrogen. As the temperature increased from -55°C, the loss increased until at +25°C it was 1.2 times the loss at the end of irradiation.

Figure 3 shows the results of the steady-state irradiations of fiber WP-6. The rates of induced loss are significantly less than those for fiber WP-2. The data taken at +125°C does not follow the trend of increasing rate of induced loss with increasing temperature, nor does it show the significant change in slope observed with WP-2. This is probably due to a small temperature excursion near the beginning of the irradiation which may be indicated by the slightly concave portion of the plot near 1 Kilorad. Also, the data shown for +125°C is the second of two irradiations (a new length of fiber was used for the second irradiation). The data from the first irradiation was not used because the dosimetry showed an unexpected decrease in dose per pulse from the linac. The first set of data did show a significantly higher rate of induced loss at the beginning of the irradiation. Figure 4 shows the recovery of induced loss following irradiation for WP-6. Significant recovery occurs only at +125°C and the rate of recovery is less than for WP-2. Again, when the fiber irradiated at -55°C returned to +25°C the loss increased by a factor of 1.2 times that at the end of irradiation.

Figure 5 shows the results of the steady-state Cobalt 60 irradiations of fiber WP-6. The consistent increase in rate of induced loss with increasing temperature, not seen in the linac data, is clear in this case. Comparison with the linac data shows that the data taken at -55°C are essentially identical and the data at +25°C are very nearly the same. The difference in the data at +125°C is probably due to the high sensitivity of the fiber transmission to small changes in temperature at this temperature. (The control of temperature in the linac irradiation area is somewhat more difficult at +125°C than in the cobalt cell because of a fast-moving air stream required to remove ozone during linac operation).

Results of Transient Tests

Figure 6 shows the induced loss as a function of time for fiber WP-2 following a 20 nanosecond, 2×10^9 rad/sec pulse from the flash x-ray generator. The induced loss has been normalized to actual dose rate and is presented in units of dB/km per 10^8 rads/sec. The reason for this normalization is that the flash x-ray does not necessarily produce the same dose from pulse to pulse. Although the variation in output for a given series of irradiations is only about 10 percent, greater variations can occur over time as the flash x-ray cathode ages. The normalization helps in comparing sets of data by essentially cancelling these variations.

As Figure 6 shows, the amount of transient loss induced in the fiber decreases with increasing temperature, opposite to what was observed in the steady state irradiations. The rate of decay of the induced loss increases with temperature. The actual induced loss at zero time is undoubtedly much greater than the maximum shown by the data. An initial fluorescent pulse (probably Cerenkov radiation)

obscures the loss at early times and, since the fluorescence generated in the fiber has a transit time of about 5 nanoseconds per meter of fiber the true loss is not observable until 400 nanoseconds after the radiation pulse (5 nanoseconds per meter times 80 meters of fiber including leads). At all three temperatures the chart recorder showed a residual loss out to 70 seconds of the order of 0.1 dB/km per 10^8 rads per second, which is below the estimated accuracy of the measurement.

For the nominal 10^8 rads/sec irradiations (actual dose-rate 1.6×10^8 rads/sec) the observed induced losses were close to the limit of measurement. No induced loss was observable at $+125^\circ\text{C}$. At $+25^\circ\text{C}$ the maximum induced loss was approximately 2 dB/km per 10^8 rads/sec and at -55°C it was about 4 dB/km per 10^8 rads/sec. Loss was detectable beyond the maximum only at -55°C , and this appeared to go to zero at 30 μsec after the x-ray burst.

Figure 7 shows the response of fiber WP-6 to a nominal 10^9 rads/sec (actual dose rate 1.1×10^9 rads/sec) x-ray burst. The results are similar in form to those obtained for WP-2, but the normalized induced losses are about twice those for WP-2 and the rate of recovery is slower.

The 10^8 rad/sec (actual dose rate 1.3×10^8 rads/sec) exposure showed induced losses near the measurable limit but greater than those for WP-2. At -55°C the maximum observed loss was 8 dB/km per 10^8 rads/sec and loss was evident to 7 milliseconds. At $+25^\circ\text{C}$ the maximum loss was about 3.5 dB/km per 10^8 rads/sec with no loss detectable beyond 5 microseconds. At $+125^\circ\text{C}$ a maximum loss of 1 dB/km per 10^8 rads/sec only was seen.

Summary

The results of the tests may be summarized as follows:

1. Under steady-state irradiation the rate of induced loss as a function of dose increases with increasing temperature.
2. Under transient radiation conditions the maximum induced loss decreases with increasing temperature while the rate of recovery increases with temperature.
3. Significant recovery of induced loss following steady-state irradiation occurs only at higher temperatures.
4. The use of a linear accelerator, a pulsed radiation source, to simulate steady-state irradiation is valid, assuming the differences between the linac and Cobalt-60 results observed at $+125^\circ\text{C}$ are due to the sensitivity of the fiber transmission (in the test configuration used) to small changes in temperature.
5. Following steady-state irradiation at -55°C , the radiation induced loss increases as the temperature is increased. When the fiber temperature returns to $+25^\circ\text{C}$, the loss is about the same as if the fiber had been irradiated at that temperature.
6. An increased percentage of germanium in the fiber core results in a decrease in the rate of induced loss as a function of dose under steady-state

irradiation and an increase in induced loss under transient irradiation.

The tests results reported here are for specific fiber compositions. The differences observed between the radiation responses of fibers WP-2 and WP-6 show that the results should not be generalized as representative of all germanium-phosphosilicate fibers.

RESPONSE TO 10 MeV LINAC X-RAYS
FIBER: WP-2

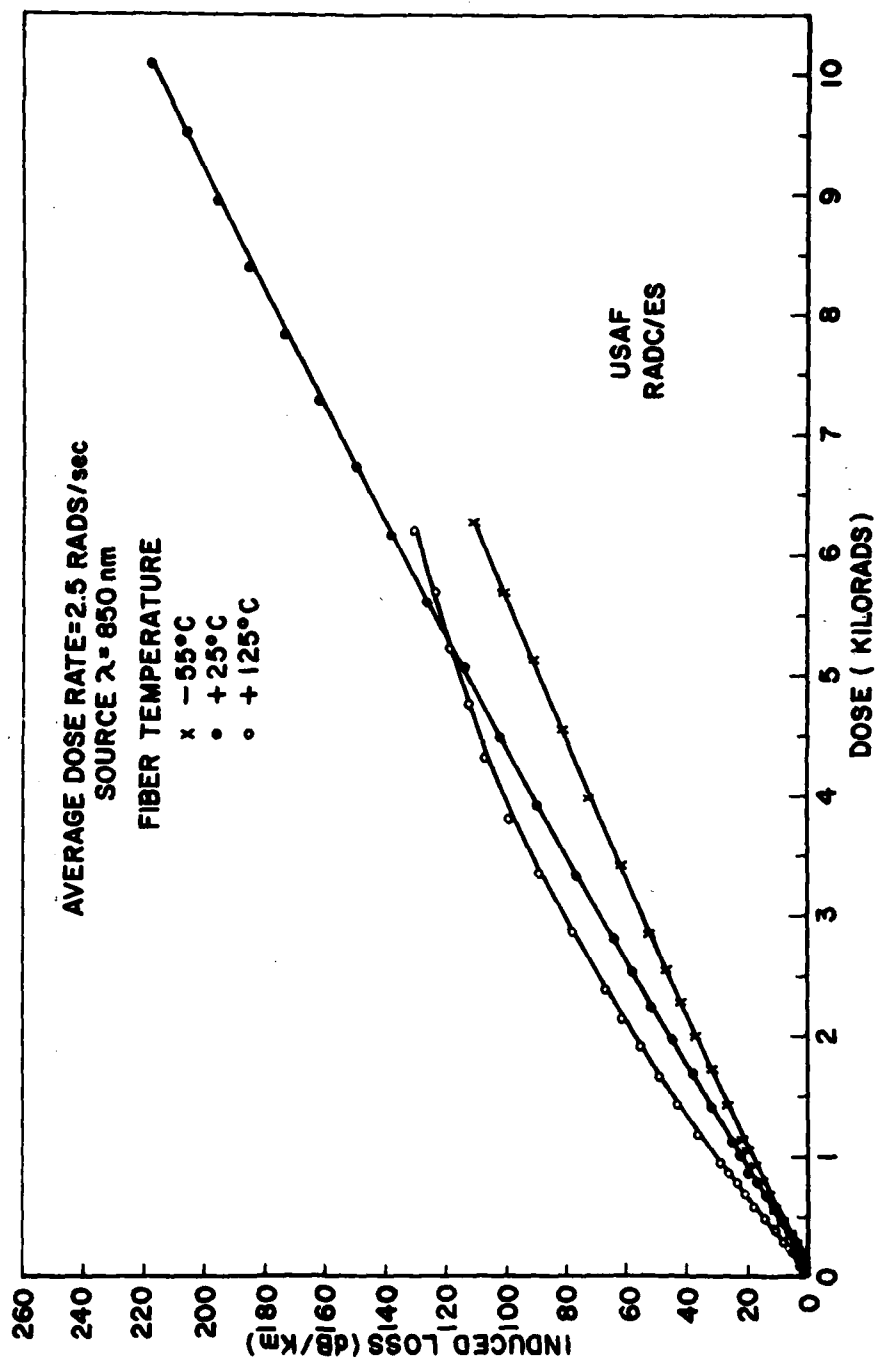


Figure 1

RECOVERY OF RADIATION INDUCED LOSS FIBER WP-2

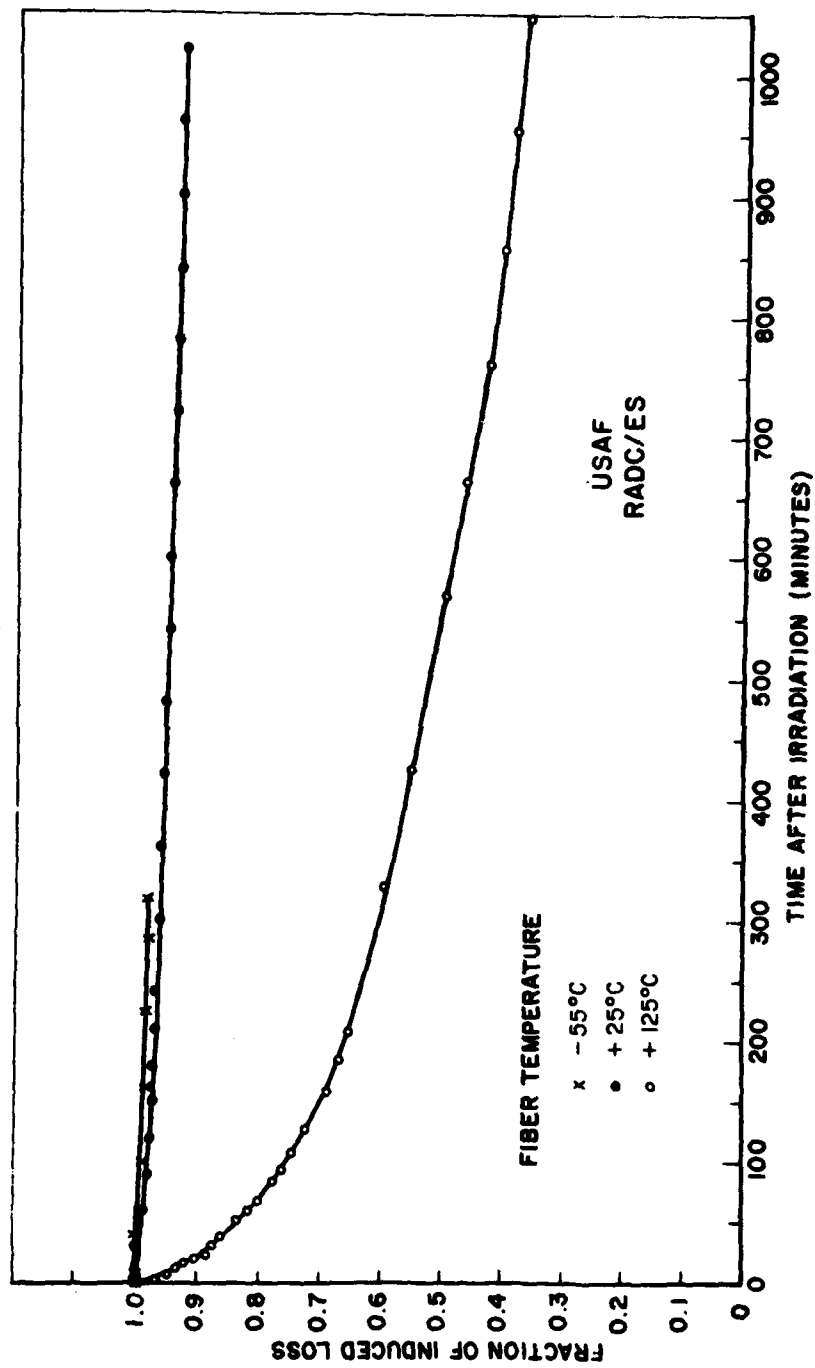


Figure 2

RESPONSE TO 10 Mev LINAC X-RAYS
FIBER: WP-6

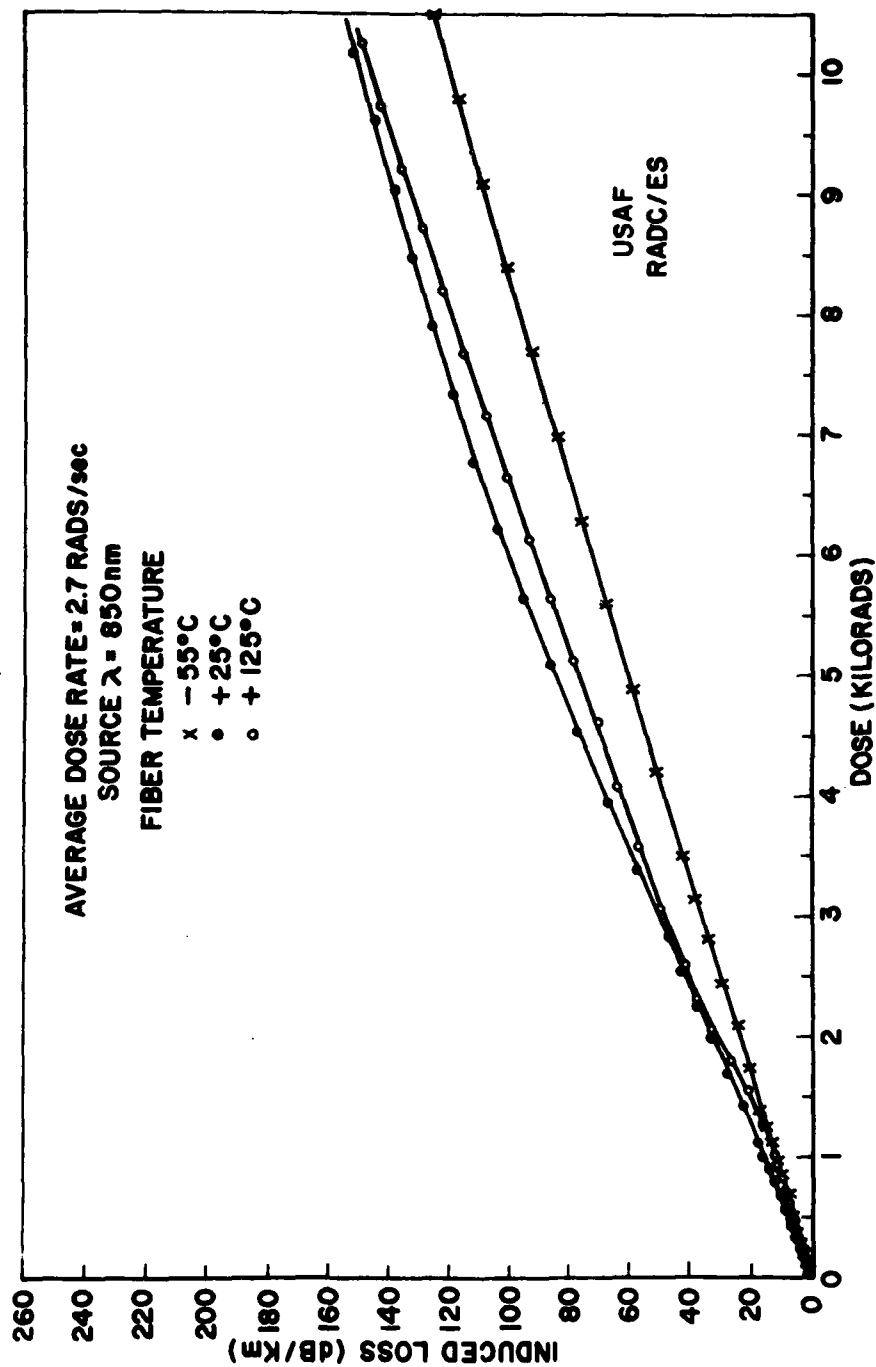


Figure 3

RECOVERY OF RADIATION INDUCED LOSS FIBER: WP-6

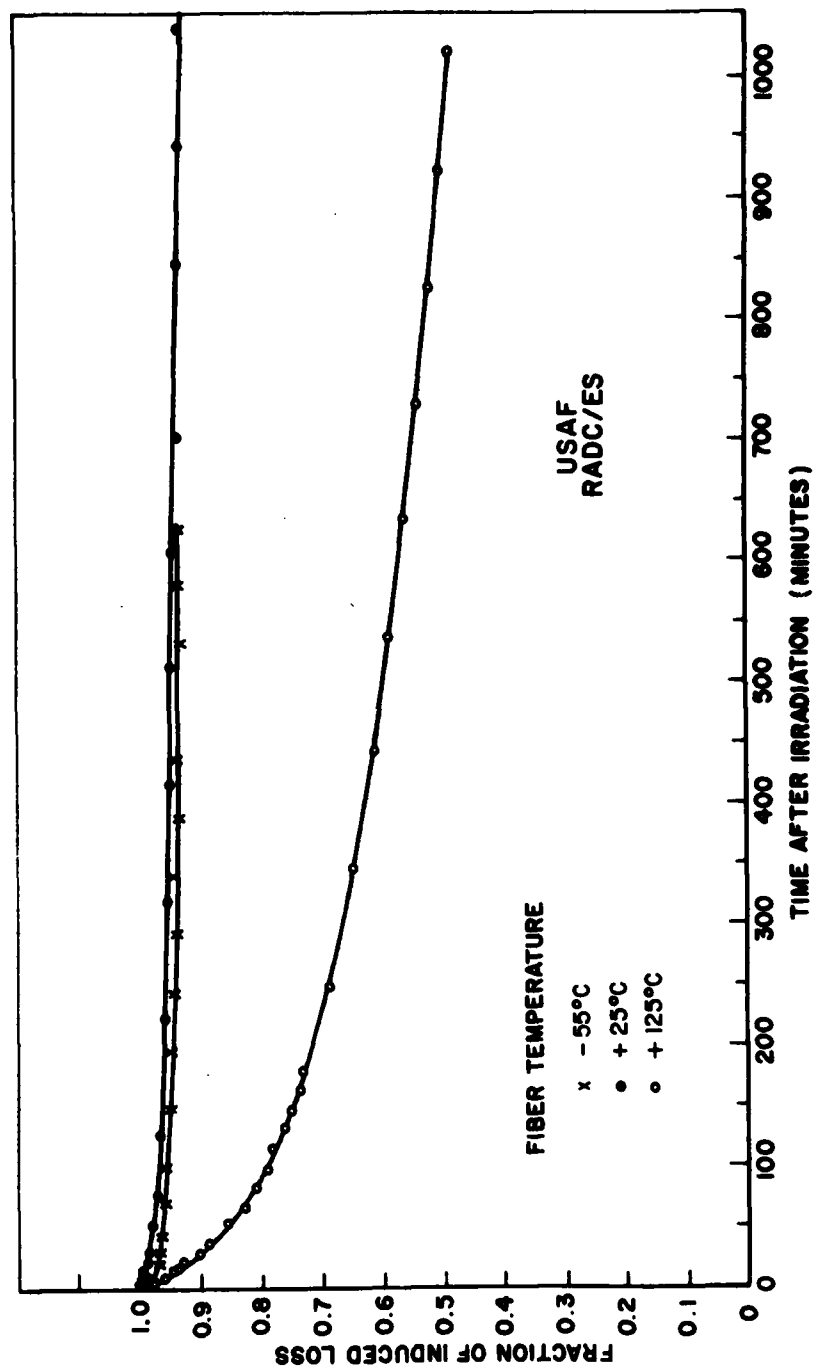


Figure 4

RESPONSE TO Co-60 RADIATION FIBER: WP-6

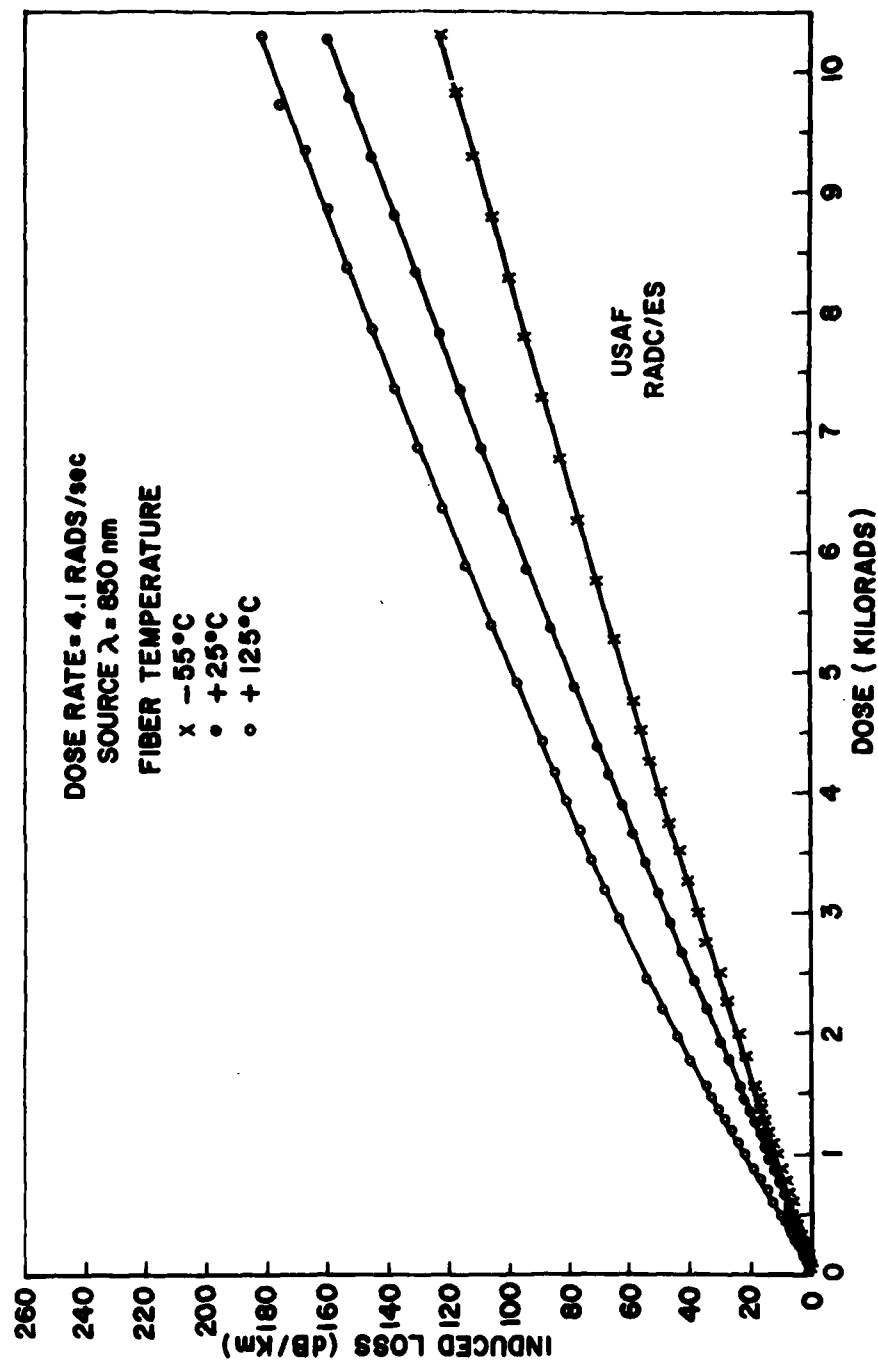


Figure 5

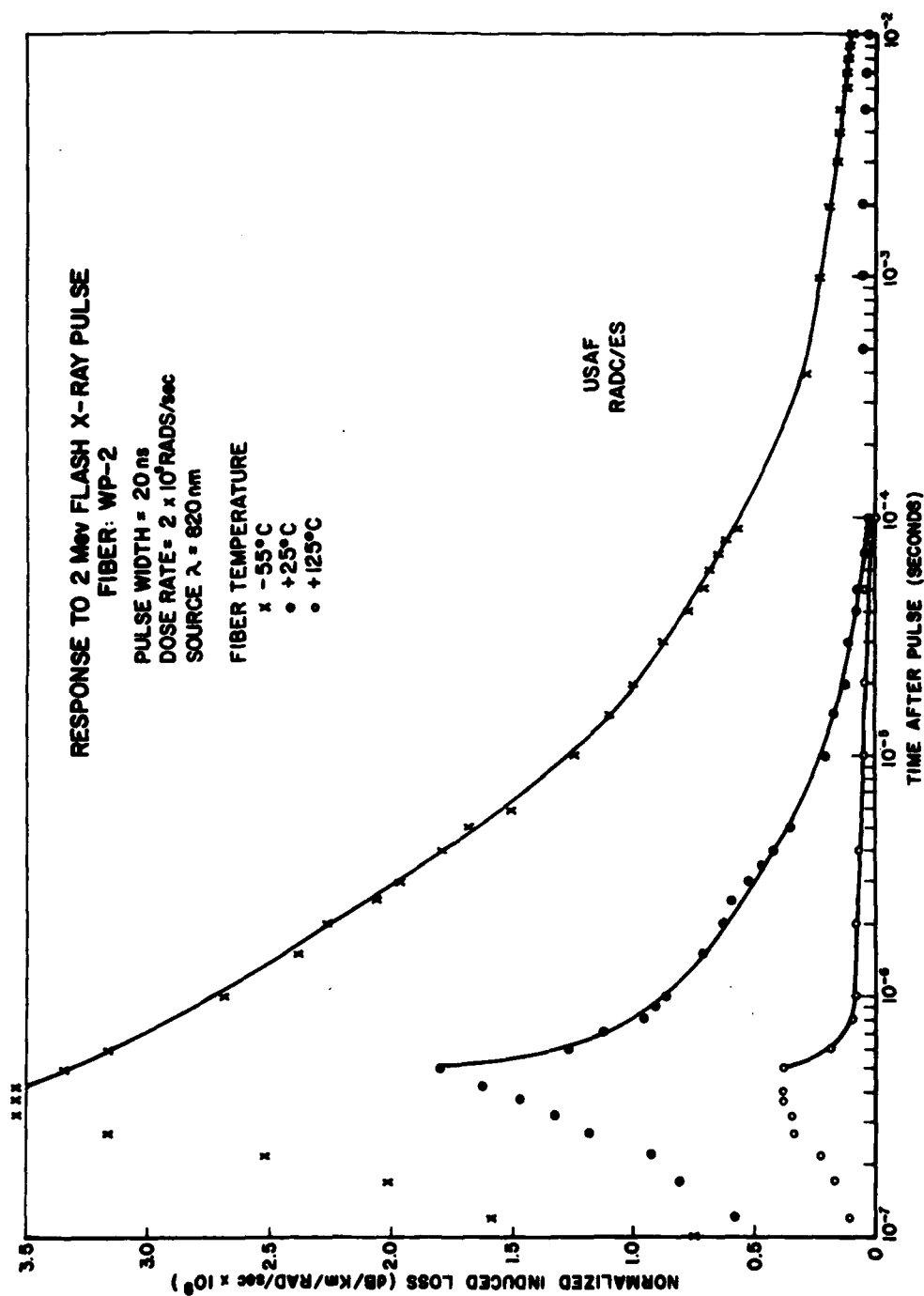


Figure 6

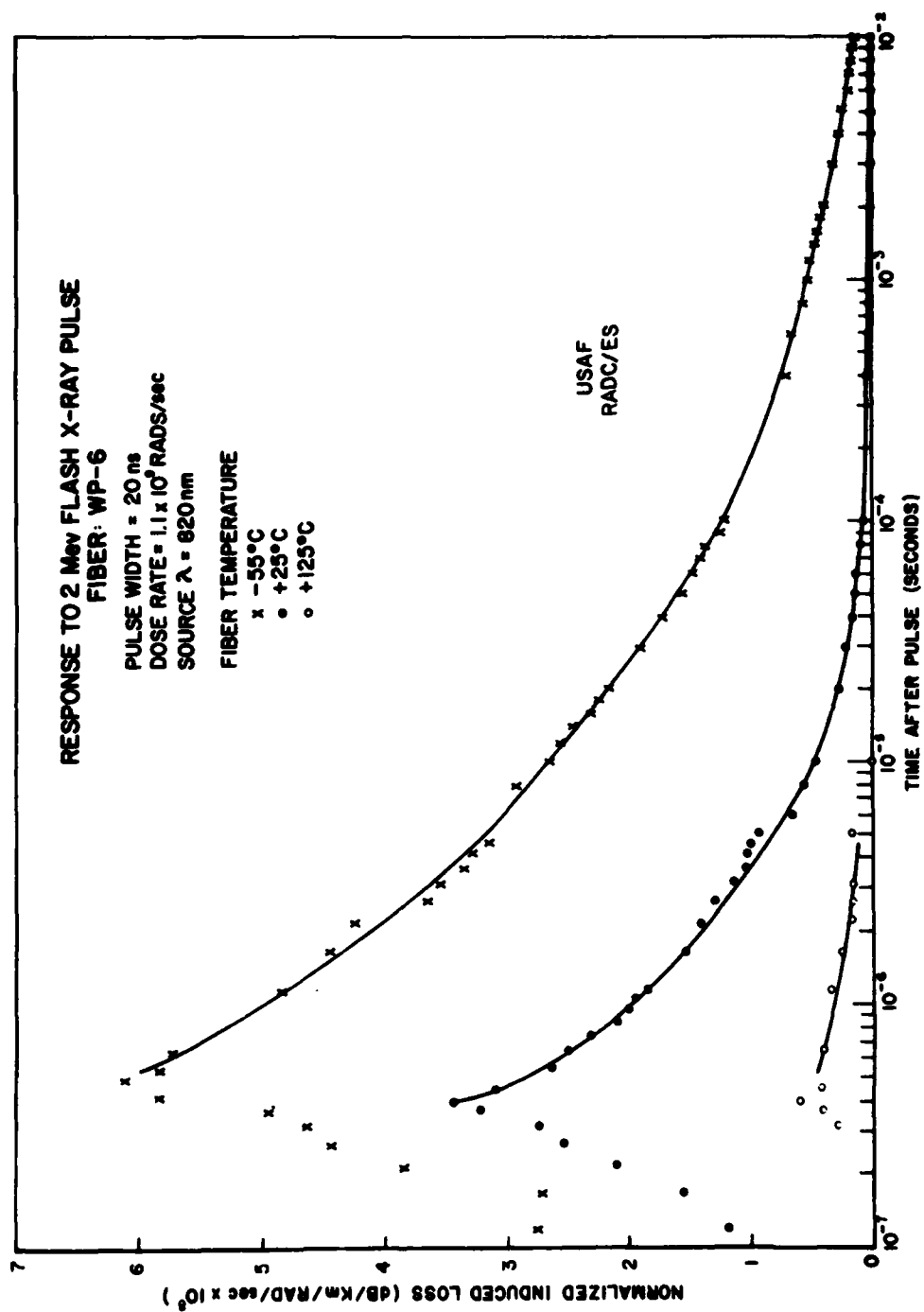


Figure 7

THIS PAGE IS INTENTIONALLY LEFT BLANK

Fast Recovery in Optical Fibers
Exposed to Pulsed Radiation^{*}
R. M. Gilbert,⁺ R. C. Webb,⁺⁺ T. R. Oldham⁺

Introduction

It has been shown that optical fibers exposed to fast pulses of ionizing radiation experience a commensurately fast optical darkening followed by a partial recovery whose rate and extent depend on the temperature and composition of the fiber.^{1,2,3} For many fiber optics applications, this transient darkening is not a serious problem because dose rates are low, the fiber's transient darkening and recovery occur too fast to interfere with data transmission, or the upset is easily circumventable. In one class of applications, however, the transient response of fibers to fast pulses of radiation poses a serious threat to the proper functioning of the fiber-optic system. In this category are the fiber optic analog data links used in nuclear radiation-effects testing. For these links, the most important test data to be transmitted are usually produced during and tens of ns after the radiation pulse, when fibers are most affected by the radiation. Most of the fiber-response data available in the literature describe transient recovery in fibers for times in the interval 10^{-7} seconds to 10's of seconds, or give composite fiber responses that reflect not only the effects of darkening but also the contributions from Cerenkov luminescence. This paper describes first an experiment to measure the effects of early-time darkening in several commercially available fibers exposed at room temperature to radiation pulses, and second, the data analysis required to extract from these measurements the intrinsic darkening response of the fibers.

The Experimental Configuration

Figure 1 shows the configuration of the experiment. A 200-MHz cw sine wave was used to modulate an injection laser diode in the transmitter. The resulting light signal was launched simultaneously into both a control fiber and two test fibers. Segments of the test fibers were coiled and mounted for exposure in front of the Harry Diamond Laboratories FX45 flash x-ray machine. To exclude interference from Cerenkov luminescence, the receiver ends of the test fibers were coupled to narrow bandpass filters placed in front of optical detectors in a multichannel receiver. The electrical signal output from each test channel in the receiver was divided into four equal parts using matched impedance TEE's and connected to the vertical amplifiers of paired TEK 7844 dual-beam oscilloscopes. Using a common trigger signal from the flash x-ray machine and 7B92A time bases, the lower of the two signal traces on each CRT display was delayed a desired time interval relative to the top trace, which itself was synchronized to display the pre-radiation amplitude of the cw signal, as well as the onset of fiber darkening. All sweep speeds were set at 20 ns/div. Figure 2 shows a representative result taken for an ITT step-index T103 fiber, 20 meters in length. The lower trace has been delayed by 100 ns relative to the top trace. The advantage of this instrumentation configuration is that no matter what the shot-to-shot

^{*} This work was sponsored under Defense Nuclear Agency subtask J24AAXYX959

⁺ Harry Diamond Laboratories, Department of Army, Adelphi, MD 20783.

⁺⁺ Test Division, Defense Nuclear Agency, Washington, D.C. 20305

variations in laser modulation signal or laser operating point, each photograph contains the necessary and sufficient information for unfolding real-time fiber darkening and recovery ratios. Thermoluminescent dosimeters were used to measure the ionization dose produced by the machine's 0.2 - 2.0 bremsstrahlung, approximately 450 rads(Si) per pulse. The shot-to-shot reproducibility of the FX45 radiation pulse permitted the compiling of a single recovery history spanning many orders of magnitude of time delay, using a series of flash x-ray shots on a given fiber. The monitor channel was used to measure cumulative permanent darkening effects over the shot sequence. The four fibers tested were the Corning graded-index IVPO and OVPO fibers, the ITT step-index T103 fiber, and the ITT graded-index T223 fiber.

Data Analysis

Figure 2 shows the amplitude modulation of an optical signal during its passage through a fiber exposed to a pulse of radiation; the amplitude envelope is

$$x(t) = \int_{-\infty}^{\infty} T(t-t')F(t')dt', \quad (1)$$

where $x(t)$ is normalized to the pre-attenuation amplitude, $F(t')$ is the time history of dose accumulation in the fiber, and $T(t-t')$ is the darkening response of the fiber sample for an instantaneous deposition of the pulse dose. Since $x(t)$ is the measured data and $F(t')$ is known, $T(t-t')$ may be found using standard Fourier transform and convolution techniques.^{4,5} The response function T depends on dose D and sample length L . The intrinsic response of the fiber may be calculated by fitting an analytical expression to T and allowing for the progressive attenuation of the light signal as it moves through the darkened fiber. Inspection of the raw data taken on the fibers suggested the presence of two recovery processes, one fast and the other slow. Assuming the anneal of radiation-induced color centers follows Poisson statistics and obeys an exponential time dependence, the model for the observed recovery is then

$$T(t_j) = \sum_{k=1}^j \frac{1-a_0}{\pi} e^{-k\lambda_0 \Delta t} \quad \frac{1-a_1}{\pi} e^{-k\lambda_1 \Delta t} \quad \dots \text{ for } j \leq \tau_L/\Delta t, \quad (2)$$

$$T(t_j) = \sum_{k=j-\tau_L/\Delta t}^j \frac{1-a_0}{\pi} e^{-k\lambda_0 \Delta t} \quad \frac{1-a_1}{\pi} e^{-k\lambda_1 \Delta t} \quad \dots \text{ for } j > \tau_L/\Delta t,$$

where Δt is the time step selected for the computation; τ_L is the time required for light to traverse the fiber length L ; the sample constants a_0 , λ_0 and a_1 , λ_1 represent the fast and slow processes, respectively; and

the product operation π accounts for the progressive attenuation of the light signal as it moves through the fiber. This model is then fitted to the Fourier-unfolded function by adjustment of a_0 and λ_0 ; a_1 and λ_1 are taken directly from the late-time recovery data. The intrinsic response parameters of the fiber, independent of pulse dose and sample length, are then given by

$$a_0' = - \frac{10 \log (1-a_0)^P}{DL}, \quad \lambda_0' = \lambda_0$$

and

(3)

$$a_1' = - \frac{10 \log (1-a_1)^P}{DL}, \quad \lambda_1' = \lambda_1,$$

where P is the number of time steps required for light to traverse the unit length, a_0' and a_1' are now attenuation factors in units of dB/(m-rad(Si)), λ_0' and λ_1' are time constants in units of s^{-1} .

Figures 3-6 give the results for the T-103 step index fiber. Figure 3 shows transmission factors determined experimentally for two sample lengths, 4 m and 20 m. Figure 4 shows the response function $T(t-t')$ unfolded from the measured result for the 4-m length and the analytical fit of (2) to this unfolded $T(t-t')$. The value of the parameters used to obtain this analytical fit are given in Table I. Figures 5 and 6 show the experimentally determined transmission factors and calculated transmission factors arrived at by time and distance convolutions of the intrinsic fiber parameters. One can see that the agreement is quite satisfactory for both sample lengths. The slight displacements in time seen in the calculated curves relative to their experimental counterparts are within the uncertainties in time measurements.

Figures 7 and 8 give similar results for the T-223 graded index fiber. Figure 7 shows measured transmission factors for 4-m and 20-m sample lengths. The parameters listed in Table I for T-223 fiber were derived from the 4-m data. Figure 8 offers a comparison of the measured transmission factors with transmission factors calculated using these intrinsic response parameters. For the 4-m sample, the agreement is very good, as one would expect. For the 20-m sample, the agreement is good at first, but less so beyond 200 nsec. At 500 nsec, the difference between the two curves is about 30%.

Figure 9, gives the experimental result for a 10-m length of IVPO fiber. In Figure 10, the IVPO experimental result (plotted on a different time scale) is compared with the calculated result convolved from the IVPO parameters shown in Table I. Again, the agreement is good.

In Figure 11, the experimental transmission history is given for a 2-m length of Corning OVPO fiber. In Figures 12 and 13, the early and late time experimental results, respectively, are compared to the calculated results arrived at using the OVPO parameters in Table I.

To determine the sensitivity of the analytic solution to parameter variations, as well as to optimize the curve fits, the value of the intrinsic response parameters in Table I were varied over a wide range. Not unexpectedly, it was found that the solution was most sensitive to variations in a_0 : a change of 15% in a_0 caused a change of slightly less than 15% in the peak calculated attenuation. Since the difference between measured and calculated results is generally less than 15%, it is concluded that the values given in Table I are probably accurate to within $\pm 15\%$.

Total dose accumulations in the fiber samples were 1-2 krad (Si), too small to produce measurable permanent darkening in this configuration. This was not surprising, especially since significant anneal of darkening could be expected during the tens of minutes of laser signal injection carried on between flash x-ray shots.

CONCLUSION

This paper has described a successful experimental approach for measuring the early darkening history of optical fibers exposed to a fast pulse of ionizing radiation. In addition, an analytical procedure has been demonstrated that takes the transmission factors measured for a given fiber sample and a given radiation pulse and converts them into intrinsic response parameters. The latter then may be convolved over other radiation-dose time histories and other sample lengths to predict the darkening of optical signals appropriate to those conditions.

The restrictions on the applicability of this procedure are the following: 1) the peak transient darkening (in dB/m) is assumed to vary linearly with dose, an assumption that should hold for most fibers at least into the 10^3 to 10^4 rad(Si) range; 2) the unfold uncertainties inherent in the procedure limits the minimum length of fiber one can treat accurately to about 1/5th the fiber length used to generate the intrinsic response parameters (in this experiment, the parameters obtained using the 20-m samples were within 40% of the parameters obtained using the 4-m samples); and 3) the effect of fiber length is assumed to follow the multiplicative form given in (2).

REFERENCES

1. "Short-Term Transient Radiation Effects in Optical Fibers," P. B. Lyons et al, presented at Optical Fiber Communication Conference, Washington, D.C., 6 March 1979.
2. "Radiation Response of Large Core Polymer Clad Silica Optical Fibers," G. E. Sigel et al, IEEE Transactions on Nuclear Science, Vol NS-26, No. 6, p. 4796-801, December 1979.
3. "Radiation Effects in Doped-Silica Optical Waveguides," S. Share and J. Wasilik, IEEE Transactions on Nuclear Science, Vol. NS-26 No. 6 p. 4802-4807, December 1979.
4. G. Arfken, Mathematical Methods for Physicists, Academic Press (1968).
5. P. M. Morse, and H. Feshbach, Methods of Theoretical Physics, McGraw-Hill (1953).
6. J. E. Midwinter, "Optical Fibers for Transmission", Wiley, p. 197, (1979).

TABLE I: TRANSIENT RESPONSE PARAMETERS

FIBER	a'_0 (dB/m-rad(Si))	λ'_0 (s ⁻¹)	a'_i (dB/m-rad(Si))	λ'_i (s ⁻¹)
T-103 (ITT)	9.1×10^{-4}	1.6×10^7	1.3×10^{-4}	5.0×10^4
T-223 (ITT)	2.7×10^{-3}	5.4×10^7	7.6×10^{-4}	7.5×10^5
IVPO (CGW)	9.1×10^{-4}	1.1×10^7	2.0×10^{-4}	4.0×10^4
OVPO (CGW)	2.2×10^{-3}	2.9×10^6	1.3×10^{-2}	2.2×10^4

T-103: Step-index, glass on glass (GeO₂; P₂O₅; OH<2 PPM)

T-223: Graded-index (GeO₂; P₂O₅; OH<2 PPM)

IVPO: Graded-index (B₂O₃; GeO₂; P₂O₅; OH<5 PPM)

OVPO: Graded-index (B₂O₃; GeO₂; OH-50 PPM)

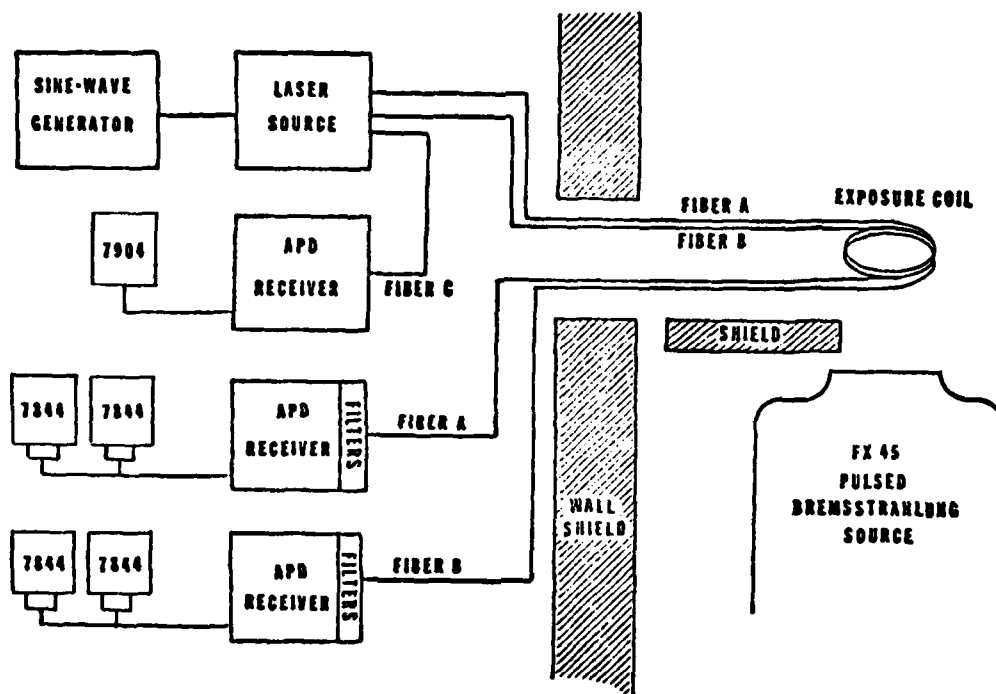


Fig. 1 Test configuration for simultaneous pulsed irradiation of two fibers.

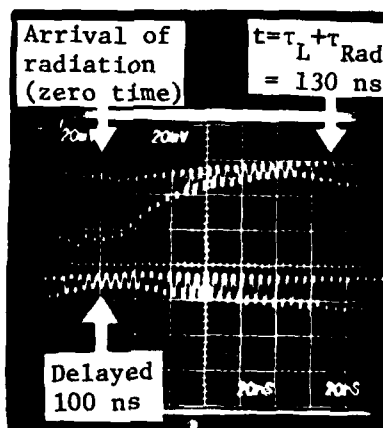


Fig. 2 Typical data traces.

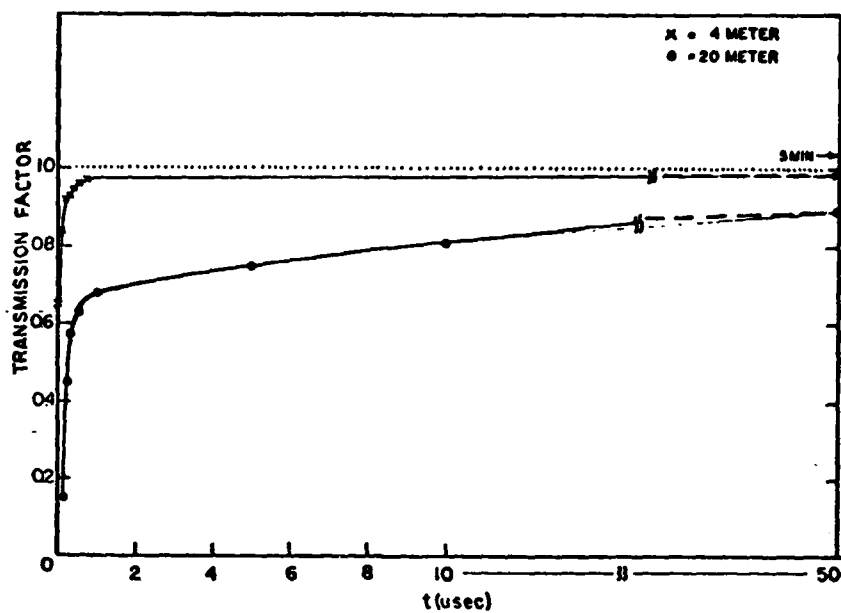


Fig. 3 Experimental transmission factors for two lengths of T-103 fiber

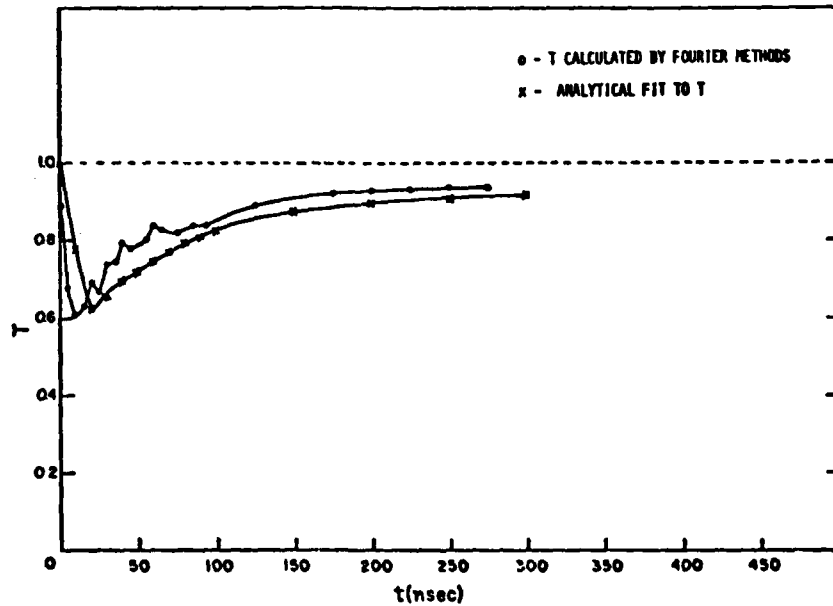


Fig. 4 Fourier unfold of transmission data for 4 m of T-103 fiber

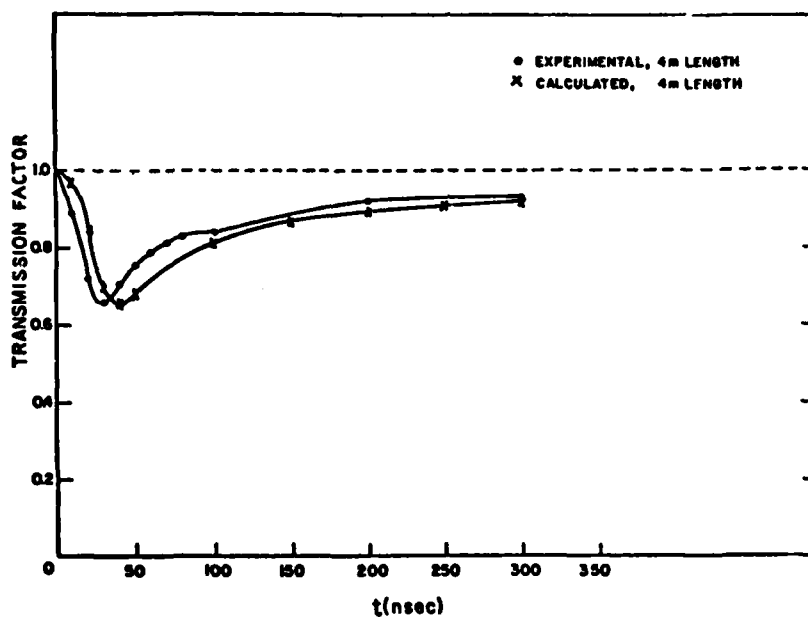


Fig. 5 Experimental and calculated transmission factors (4 m, T1³)

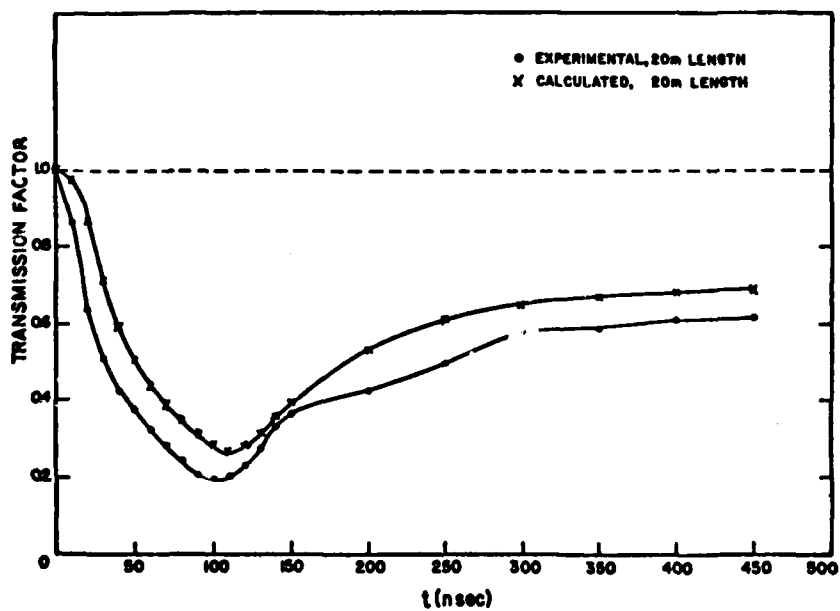


Fig. 6 Experimental and calculated transmission factors (20 m, T103)

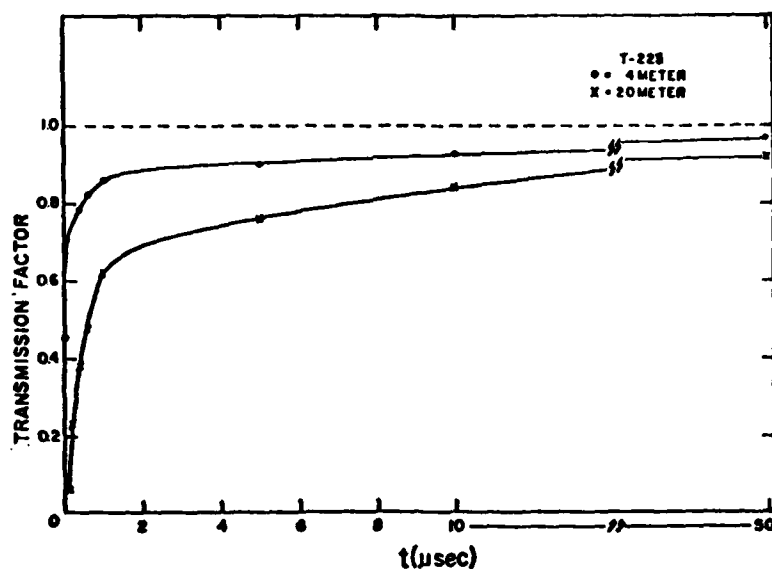


Fig. 7 Experimental transmission factors for two lengths of T223 fiber

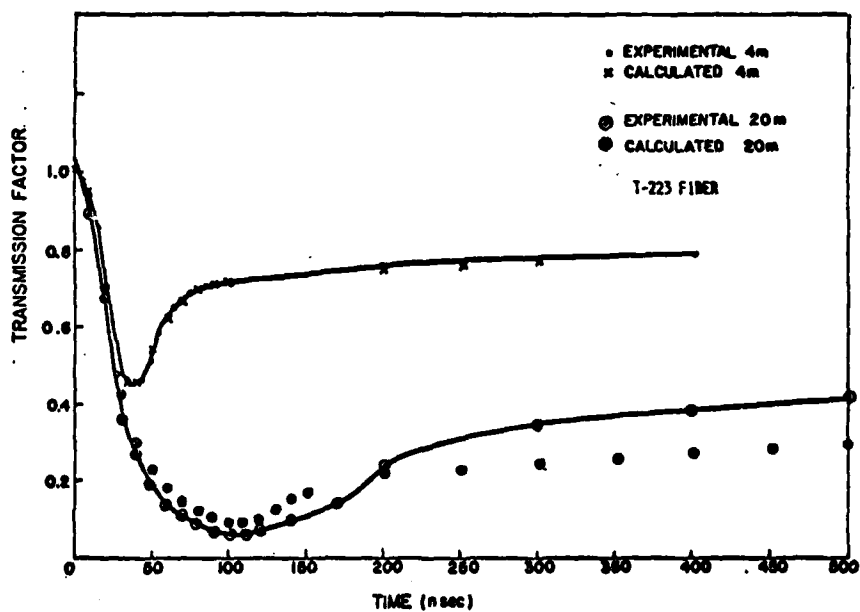


Fig. 8 Experimental and calculated transmission factors for two lengths of T223 fiber

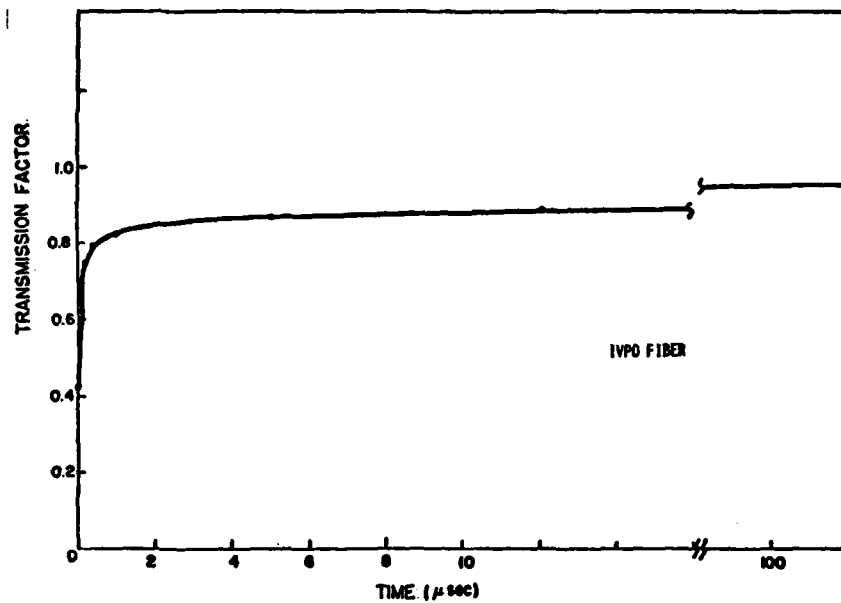


Fig. 9 Experimental transmission factors for 10 m of IVPO fiber

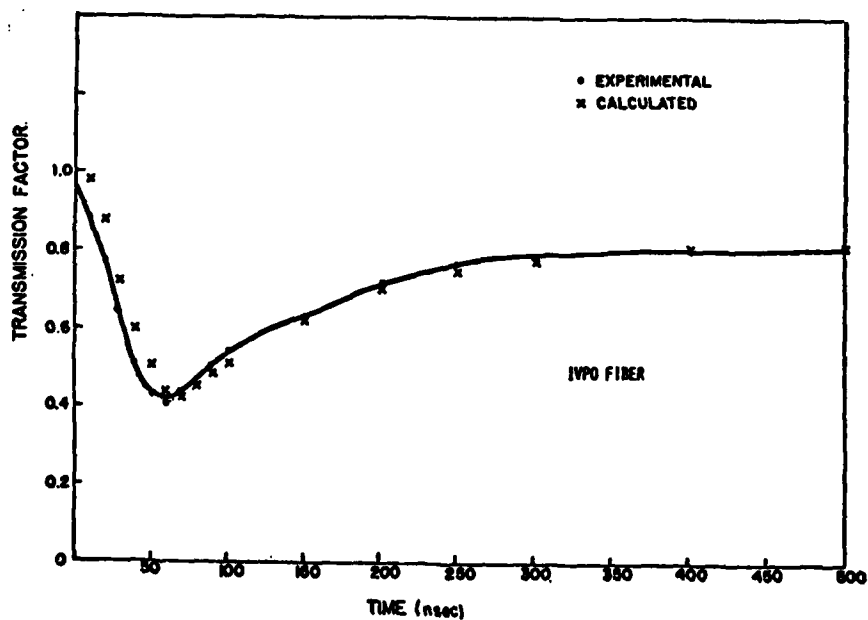


Fig. 10 Experimental and calculated transmission factors (10 m, IVPO Fiber)

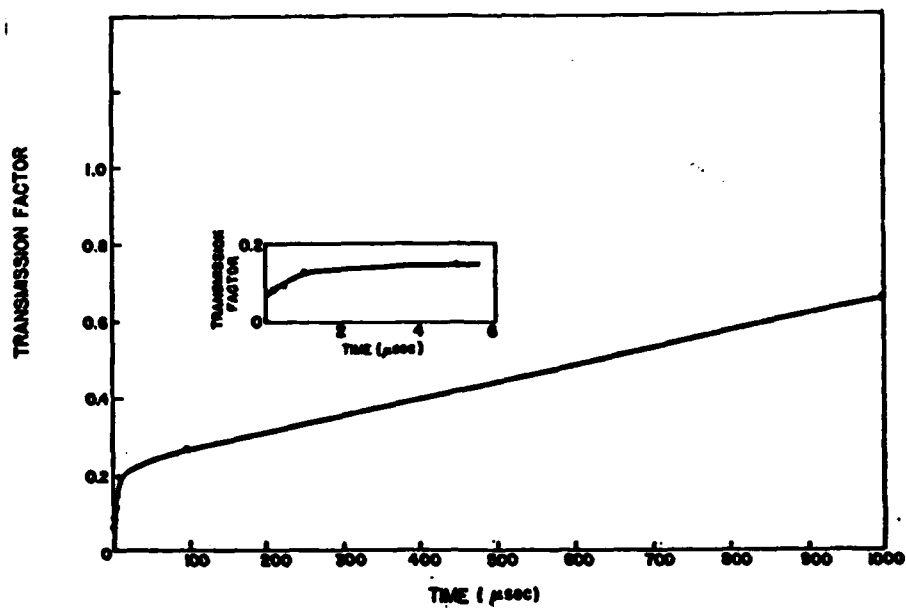


Fig. 11 Experimental transmission factors
for 2 m of OVPO Fiber

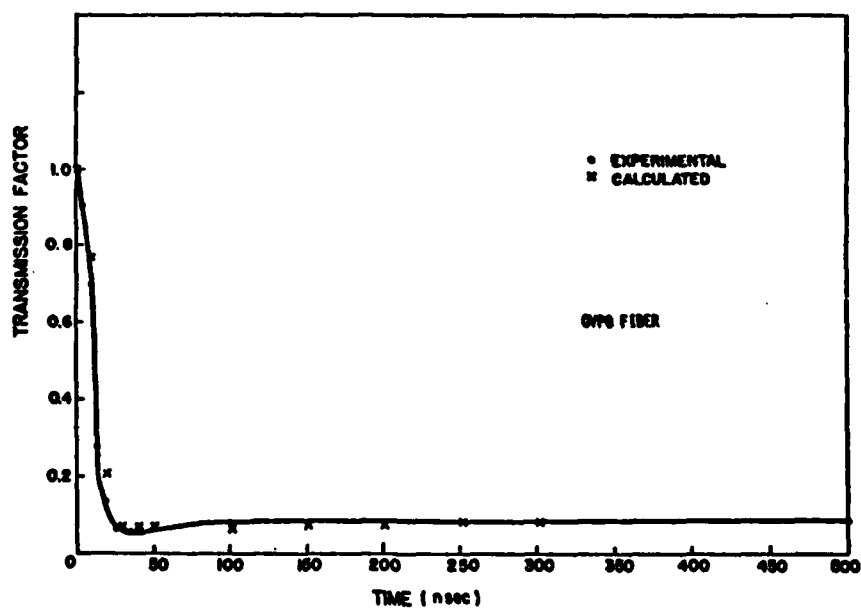


Fig. 12 Experimental and calculated transmission
factors (2 m, OVPO Fiber), early-time

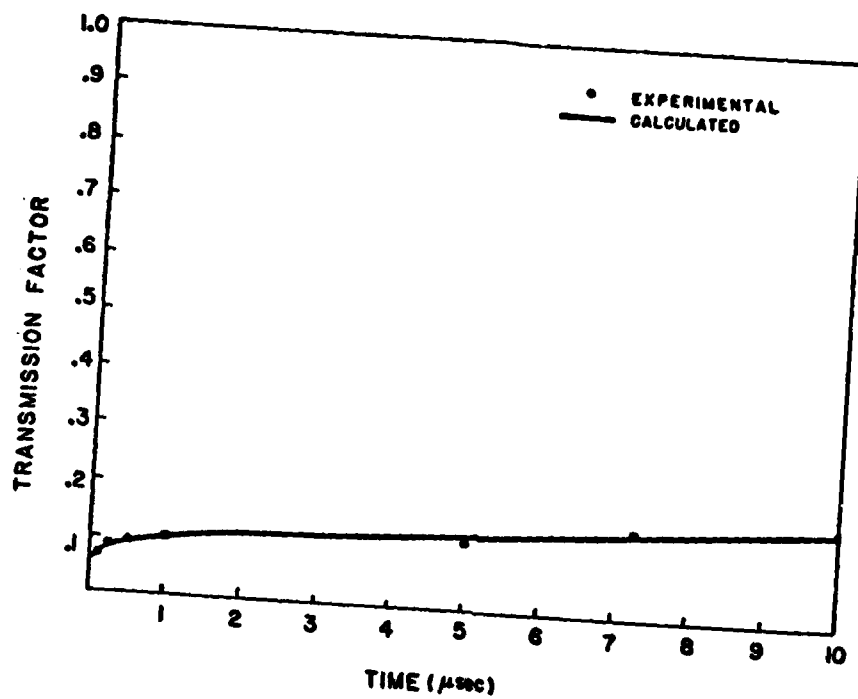


Fig. 13 Experimental and calculated transmission factors (2 m, OVPO Fiber), late-time

SHORT-TERM RADIATION EFFECTS IN OPTICAL FIBERS

by

P. B. Lyons, R. E. Kelly, L. D. Looney

Los Alamos Scientific Laboratory
Los Alamos, NM 87544

Radiation-induced transient absorption and luminescence in optical fibers can limit potential applications of fiber systems. A detailed knowledge of such effects is essential to the system designer whenever irradiation of fibers can occur in a particular application.

Optical fibers have been studied by the Los Alamos Scientific Laboratory (LASL) with emphasis on systems for transmitting nuclear device diagnostic data during, or shortly after, a nuclear explosion. This interest has required knowledge of transient effects in the time regime from 0-1000 ns. This report will summarize the past LASL fiber effects studies^{1,2,3} as well as cover some new results.

The LASL studies have been in progress for about five years. During that time both the experimental systems and our understanding of the damage mechanisms have evolved. We have not reached a level of expertise which would allow prediction of damage from a knowledge of an irradiation history. This remains our goal for this study.

Experimental Techniques--Laboratory

Laboratory transient absorption experiments have been conducted using two different radiation sources and two types of light sources. Laboratory experiments utilize either a Febetron 705 or 706 electron accelerator, as shown in Fig. 1. The Febetron sources provide electron energies up to 600 KeV (706) or 2.2 MeV (705) in a pulse duration of 3 ns (706) or 30 ns (705). Dosimetry is provided by radiachromic films from Far West Technology, Inc. for pulse doses above about 5 KRad (using multiple pulses where necessary) and by TLD chips for the limited studies below a few KRad. Collimators and shielding confine the irradiated region.

Early experiments used a pulsed flash lamp as a light source, but all recent data were acquired with a laser light source. The laser was a Chromatix CMX-4 dye laser, which produced a 1- μ s pulse tunable throughout the visible region. An optical parametric oscillator crystal was used to extend the output into the infrared to obtain 800 nm data. The CMX-4 coupled up to 20 W of power into the fiber at 600 nm to far exceed any radiation-induced luminescence.

The light sources and Febetrans were synchronized in time. Jitter of the laser is about 200 ns while either Febetron demonstrates jitter in the few ns range.

The diode outputs were routed to the two input channels of a Tektronix 7844 dual-beam oscilloscope. The lengths of the fibers and the lengths of

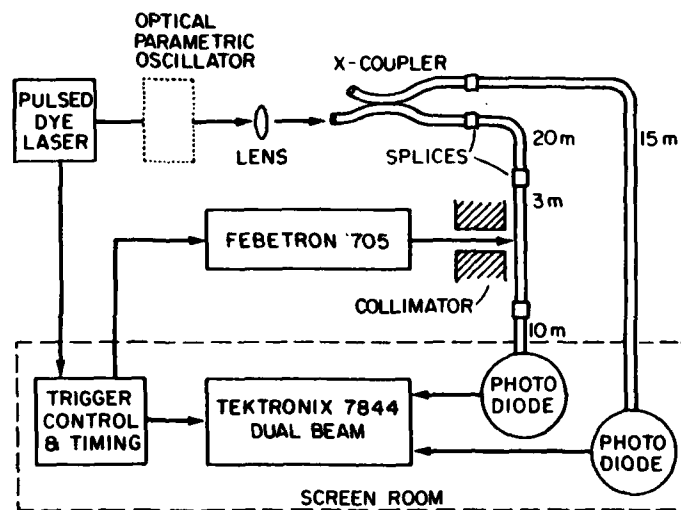


Fig. 1. Schematic of the experimental apparatus.

the signal coax lines were adjusted to provide equal time delays and both channel input sensitivities were adjusted to overlay the two resulting traces. When the electron pulse occurred, the two traces separated. A measure of the amplitude difference allowed a determination of induced absorption as a function of time after the electron pulse (up to 2.5 μ s). Typical data are shown in Fig. 2.

Some recent data have required writing speeds near the limit of the 7844 scope. Some high-speed data used a 7904 Tektronix scope for data below 10 ns. In those cases, the monitor beam was not available, but the input pulse is smooth enough to ignore its changes over 10 ns.

Luminescence experiments have also been conducted in the laboratory using the setup of Fig. 3. The end of the fiber in the radiation cell was immersed in coupling grease to prevent reflections.

Experimental Techniques--Field

Another experiment has been conducted at the Nevada Test Site (NTS) using a nuclear device² to study both absorption and luminescence.

A schematic overview of the experiment is shown in Fig. 4. Gamma and neutron doses were adjusted with various attenuators in the line-of-sight. Two fiber dose locations were available at 5.7 m and 8.7 m from the device center. The fiber types were: 1) a germanium-doped core, graded-index (GI) fiber with 75 μ core diameter and 0.18 N.A. (manufactured by Corning) and 2) a borosilicate-doped cladding, pure fused silica core, step index (SI) fiber with 78 μ core diameter and 0.15 N.A. [manufactured by Fiber Communications, Inc. (FCI)*]. Only the GI fiber was exposed at the 9-m position since the low dose at that position was not expected to affect the radiation resistant FCI fiber.

At each exposure position two fibers of a given type were routed through the beam at a 45° angle to the beam axis (close to the expected Cerenkov angle). One of the fibers transmitted an intense broadband light signal from a pulsed flashlamp (EG&G # FX-12). The other fiber was routed along the path of the first fiber but did not view the flashlamp. The two fibers provided both absorption and luminescence data. Two additional fibers of each type were routed in an identical fashion except that they did not traverse the beam pipe. These fibers served as background data channels. At the uphole end, a lense/mirror/filter system allowed recording at 600 and 800 nm.

A complicated trigger system, shown in Fig. 5 was needed to pretrigger the downhole flashlamp ahead of the nuclear output.

*Now Times Fiber Communications, Inc.

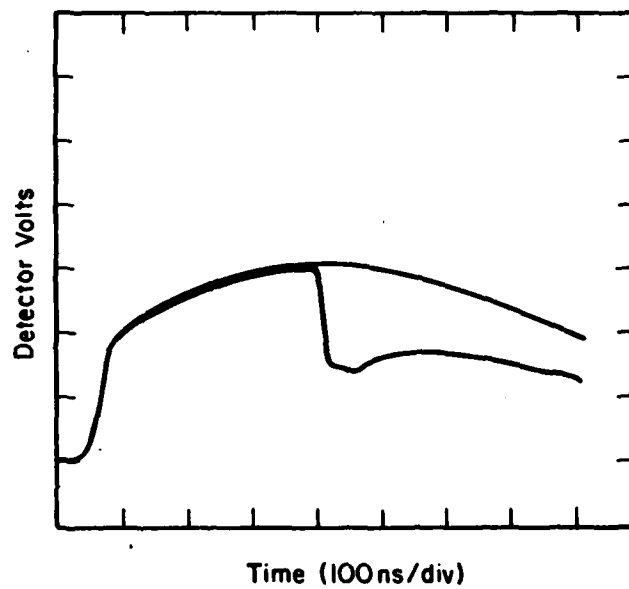


Fig. 2. A typical data trace from the dual-beam oscilloscope.

RADIATION EFFECTS SCHEMATIC

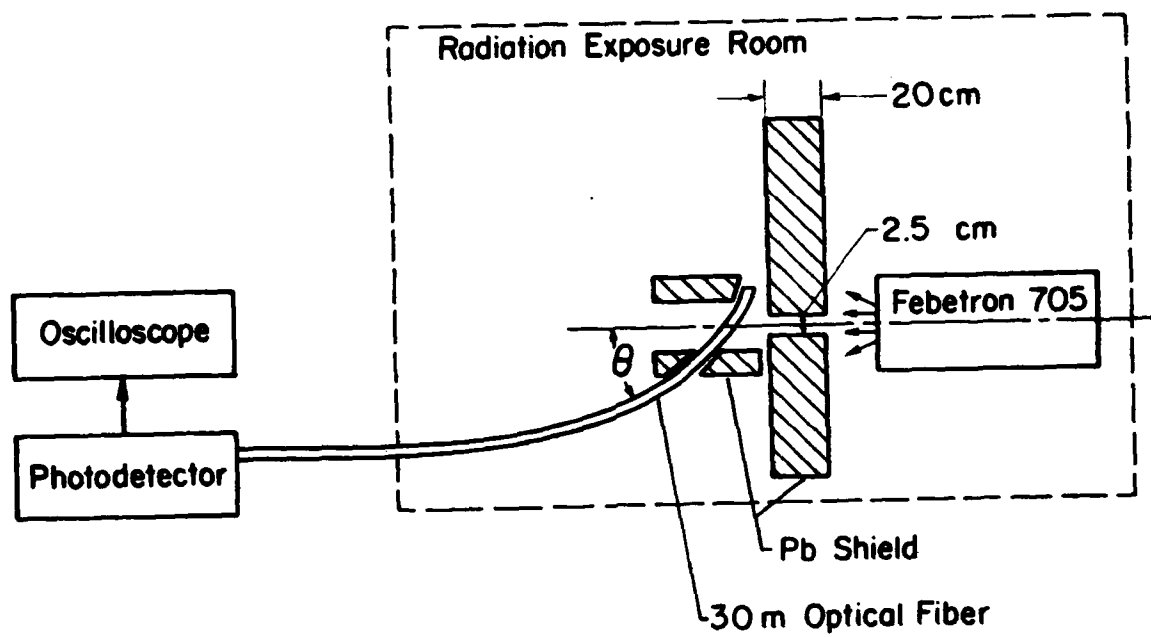


Fig. 3. Diagram of luminescence experiment.

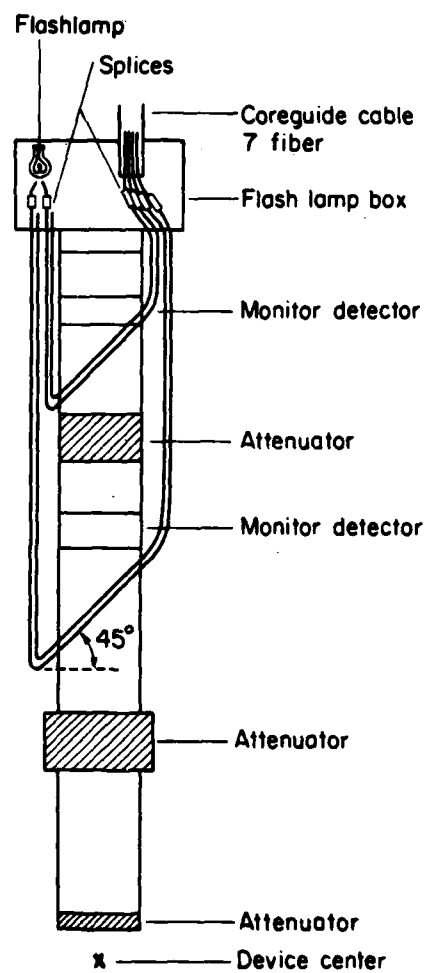


Fig. 4. Schematic view of the experimental geometry.

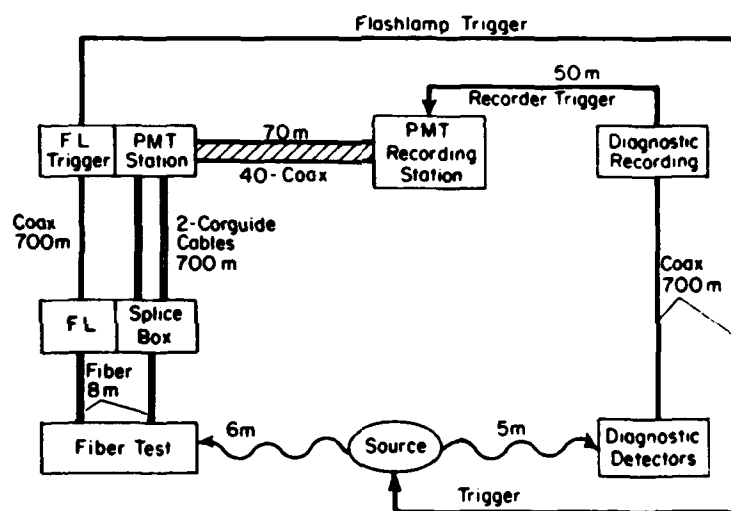


Fig. 5. Coaxial and fiber optic cable diagram.

Compilation of Results

Luminescence

Using the system in Fig. 3, the data of Fig. 6 were obtained with the 705 Febetron. The strong angle dependence and the observation of the peak signal at $\sim 45^\circ$ are strongly indicative of the Cerenkov process. Further confirmation of the Cerenkov origin of the light is given in Fig. 7. Other researchers have observed light at very late times. Fluorescence mechanisms can yield such light. From the data of Figs. 6 and 7, however, we conclude that the prompt light emission at wavelengths of 500 nm and longer is of Cerenkov origin.

The NTS test yielded the data shown in Table I. Note that the luminescence power levels were well above Fig. 7. This demonstrates the extreme sensitivity to the energy spectrum of the radiation source. In the field test, a hardened fission gamma spectrum was used in contrast to the softer Febetron spectrum. Uncertainty in the field test was large ($\pm 50\%$). Note the very low neutron-induced luminescence. Both field and laboratory data were corrected for any induced absorption.

Absorption-- $t > 50$ ns--Fibers

In most of the early LASL studies, only a "peak transient absorption" was reported. This was defined as the greatest absorption observed at the conclusion of the radiation pulse (~ 40 - 60 ns after pulse initiation). Figure 8 collects Febetron 705 data for both step and graded fibers from two vendors at two wavelengths.¹ We conclude that step and graded fibers exhibit very similar absorption when the same dopants are used in each.

Data from the field test appear in Fig. 9. The agreement between the field γ data and the laboratory e-beam data should be anticipated. Of great importance, however, was the agreement between the field neutron data and the other data. This showed that neutron induced displacement mechanisms do not seriously change the absorption of the fiber and that absorption effects are a function only of absorbed dose.

More recently, data from Febetron 705 irradiation were used to determine absorption as a function of time. This was done both to allow comparison with data obtained at NRL for $t > 10$ μ s and to compare to theoretical expectations of absorption recovery. Data in Fig. 10 show two P/Ge-doped graded fibers and ITT PCS, Suprasil core, fiber at 600 nm. The P-doped fibers show very little recovery with long times, the dashed values show attenuation at 30 s. Fig. 11 shows similar data at 800 nm for four fibers. The PCS, the ITT P/Ge step, and one of the CGW IVPO fibers are repeated from Fig. 10. The dashed values for the ITT step and one of the CGW fibers again refer to 10 s data, and again very little recovery is evident at very long times. Fiber 10108101 was obtained from NRL⁴ after they had measured its recovery from 10 μ s and longer times. The NRL data was scaled linearly with dose to compare to Fig. 11. Note that both the 10 μ s and 10 s NRL data are within a factor of ~ 2 of the LASL value (the LASL 10 μ s data can be roughly extrapolated from the LASL data to 2 μ s). Given the difficulty of dosimetry on e-beams, this agreement is acceptable. The

Cerenkov Sensivity per Unit Length

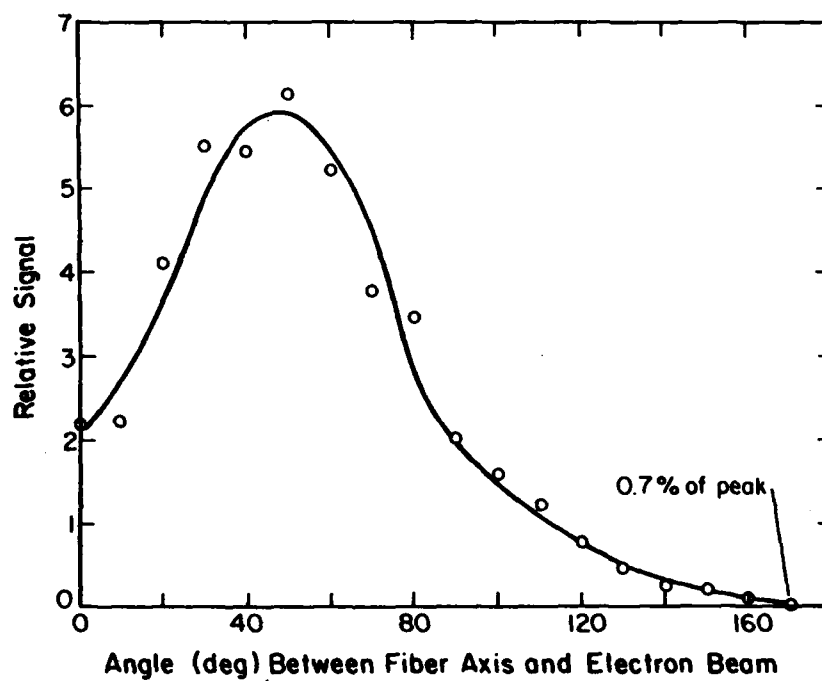


Fig. 6. Luminescence sensitivity per unit length vs angle between fiber and radiation beam.

AD-A089 725

GENERAL ELECTRIC CO SANTA BARBARA CA TEMPO
PROCEEDINGS OF THE FIBER OPTICS IN THE NUCLEAR ENVIRONMENT SYMP--ETC(U)
APR 80 R C WEBB

DNA001-79-C-0081

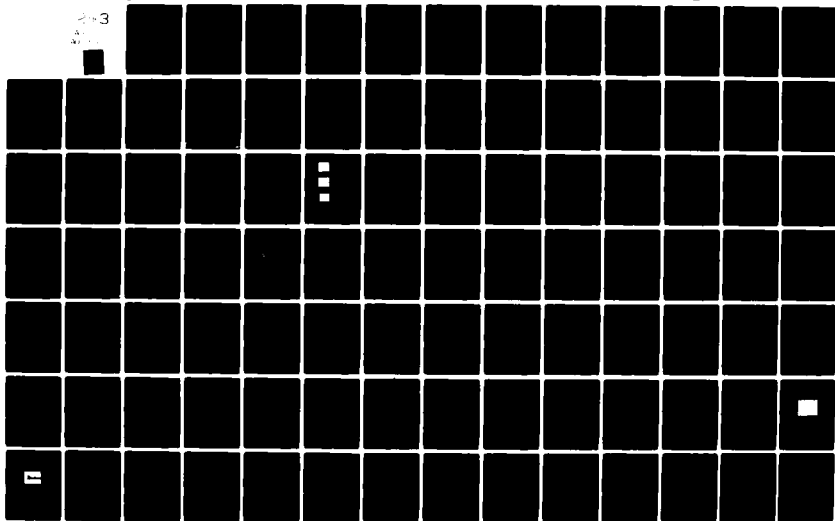
F/G 20/6

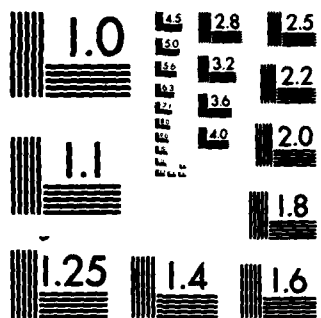
UNCLASSIFIED

DNA-5308P-2

NL

3





MICROCOPY RESOLUTION TEST CHART
NATIONAL BUREAU OF STANDARDS-1963-A

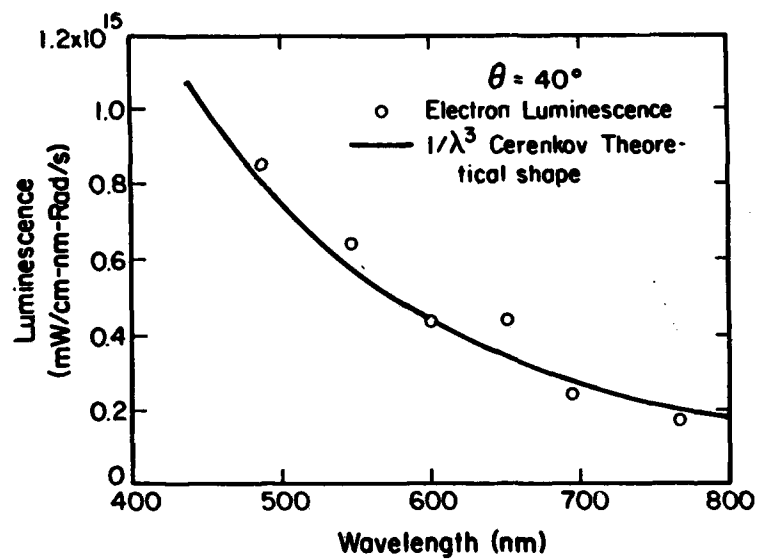


Fig. 7. Luminescence induced in an FCI step-index fiber vs wavelength. The solid curve is the theoretical Cerenkov shape and the data points for electron excitation follow this curve within experimental accuracy.

TABLE I
TRANSIENT LUMINESCENCE DATA

<u>FIBER</u>	<u>DOSE (RAD)</u>	<u>RADIATION</u>	<u>LUMINESCENCE (mJ/nm-cm-Rad)</u>	
			<u>600 nm</u>	<u>800 nm</u>
GE-DOPED	280	γ	2.4×10^{-15}	1.3×10^{-15}
GRADED INDEX	2200	γ	1.8×10^{-15}	1.1×10^{-15}
	325	n	4.5×10^{-16a}	$<1.1 \times 10^{-16b}$
<hr/>				
BOROSILICATE CLAD	2200	γ	5.6×10^{-15}	4.9×10^{-16}
PURE SILICA CORE	1.8×10^4	n	1.6×10^{-16}	1.4×10^{-17}
STEP INDEX	--	e^c	4.3×10^{-16}	1.3×10^{-16}

^aPoor Statistics

^bNo Observed Signal

^cLaboratory Measurement, Febetron 705

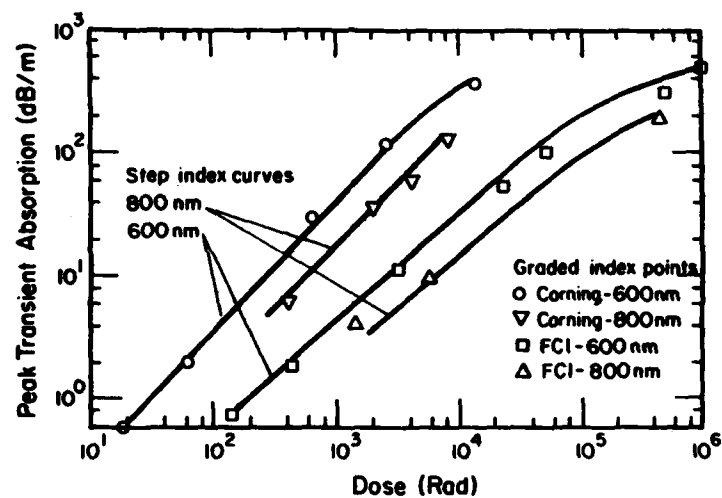


Fig. 8. Peak transient absorption data for step- and graded-index fibers. Lines show data for step-index fibers; data points are for graded-index fibers.

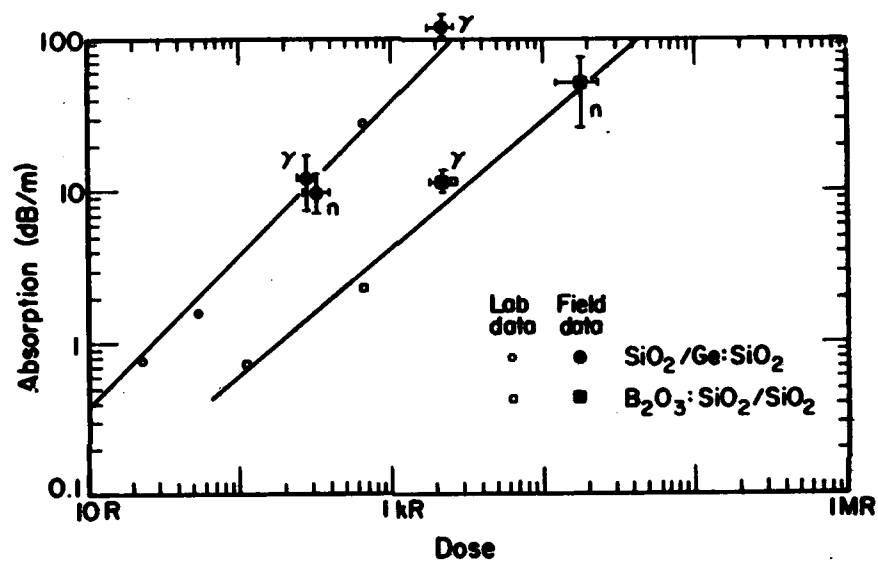


Fig. 9. Comparison of field and laboratory data for Ge- and B-doped fibers.

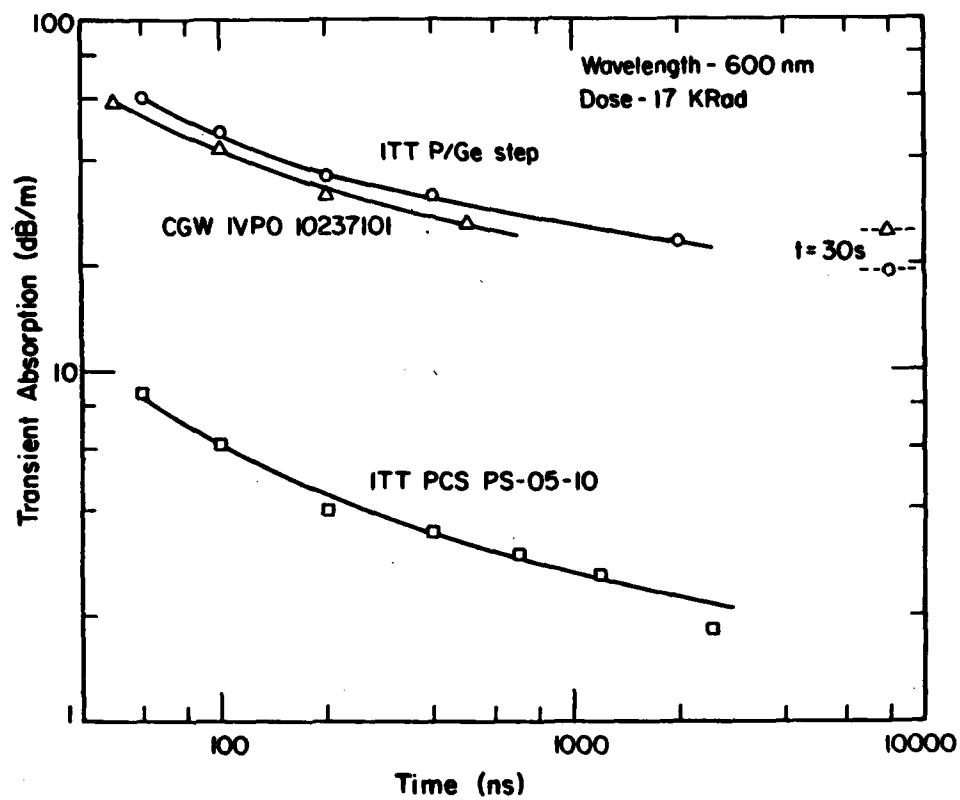


Fig. 10. Transient absorption recovery data.

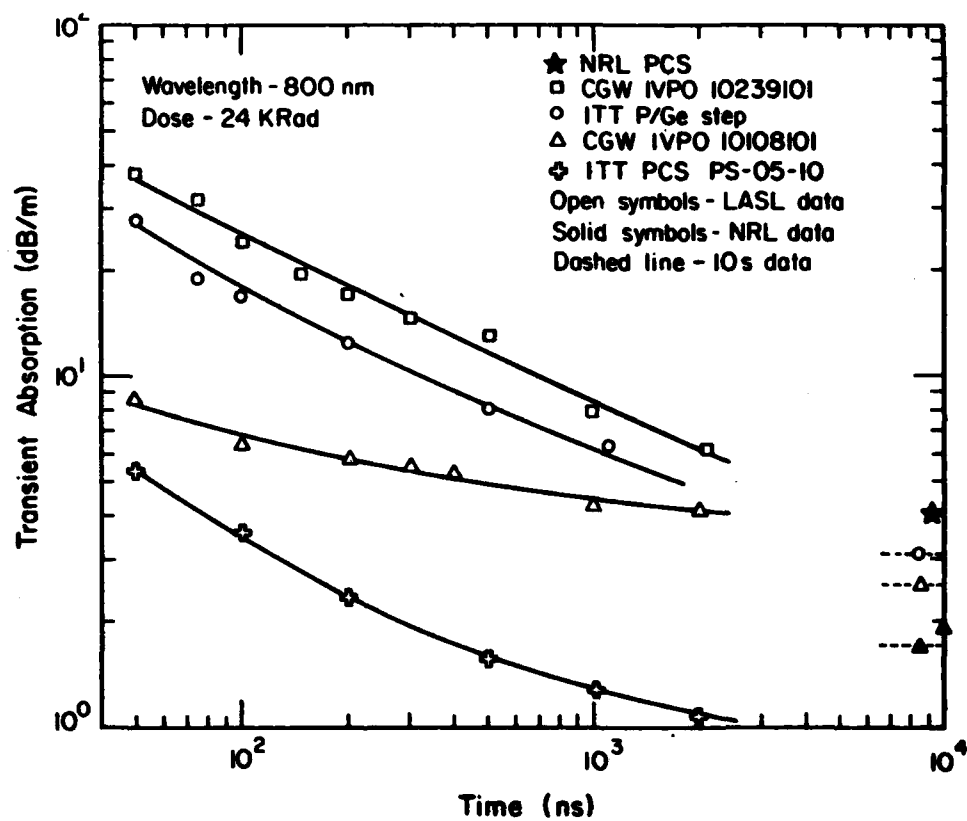


Fig. 11. Transient absorption recovery data.

NRL data used a Febetron 706 with low-beam energy which further complicates comparison to Febetron 705 data.

Of special interest in Fig. 11 is the 10 μ s data point for PCS fiber measured at NRL. Clearly the ITT PCS LASL data is in serious disagreement with the NRL data.⁵ The NRL data used Galileo PCS fiber and subsequently the NRL group has measured a variety of PCS types. The latest NRL data concurs in identifying ITT PCS fiber as a superior PCS fiber for short-time application. In Ref. 6, the NRL group obtained a value which when scaled linearly with dose to match Fig. 11 is about 0.8 dB/m for ITT PCS at 10 μ s.

The study in Fig. 12 was prompted by observations in the literature of radiation-induced hardening of PCS fiber for long-term irradiations.⁶ The opposite is observed in Fig. 12 for predosed PCS ITT fiber at early times. The data of Fig. 12 are consistent with observations of Skoog in Ref. 7. Such softening is also observed with repetitive Febetron 705 pulses.

The most recent Febetron 705 data used several commercial PCS fibers, all with very high purity core materials. The transient absorption is collected in Table II for 600 nm wavelength at a time 100 ns after pulse initiation. New fiber was used for most shots. Several bulk materials (quartz and sapphire) were also included to study possible improvements in short time damage relative to fused silica.

Absorption--t > 50 ns--Bulk Samples

All fiber data for short time absorption are consistent with one general observation: the higher the purity, the lower the absorption. The draw process is itself quite capable of inducing defect centers in fibers. This motivated a study of absorption in bulk fused silica materials. Several 1-mm diameter rods were exposed on the Febetron 705. Fig. 13 presents data for the Corning OVPO (GE-doped), IVPO (P/Ge), and ITT PCS (Suprasil core) fibers. Three bulk samples are shown. The Suprasil rod was also annealed for an additional data point. The agreement between ITT PCS, bulk Suprasil, and annealed bulk Suprasil is very evident. Draw-induced defects seem to play no role for the ITT fiber at short times. Suprasil W was distinctly inferior and T08, as expected, was quite poor.

Absorption--t < 50 ns--Fibers

The Febetron 706 has recently been used to irradiate several commercial PCS fibers, all with very high purity core materials. The fiber diameters vary from 125 μ m to 200 μ m and cladding thicknesses differ somewhat. For this reason, the actual dose to the fiber core is open to some question. The data in Fig. 14 were obtained for ITT PCS at 600 nm wavelength at a dose near 200 KRad. Dosimetry is far more reliable with the Febetron 705 and a better view of fiber absorption follows from Table II. For these measurements, care was given to the bandwidth of the recording system. The PCS fiber length from Febetron to detector was 3.5 m. (For short PCS lengths, we observe 130 ps/m modal dispersion.) The detector was an ITT F114A biplanar photodiode with a FWHM near 500 ps. The coax and 7844 scope were measured to have a 700 ps risetime. Overall system response is thus about 950 ps.

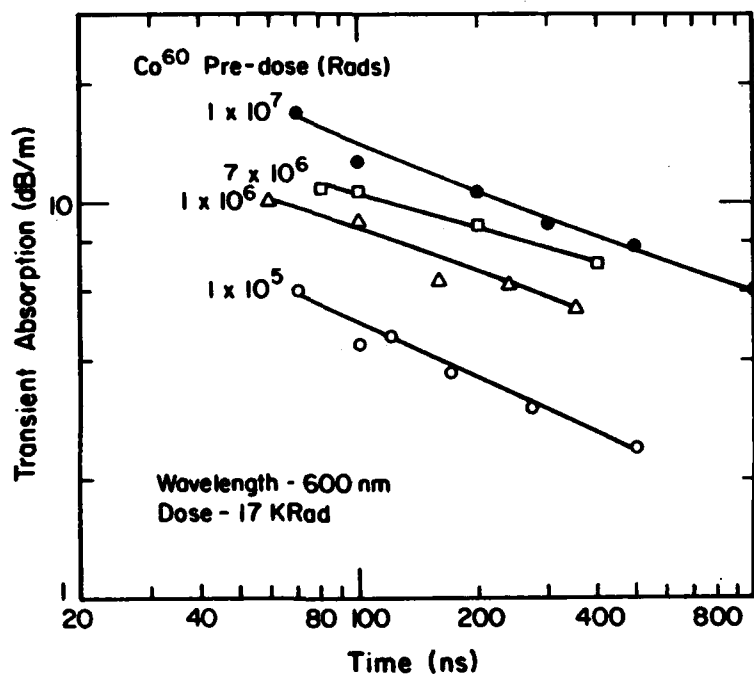


Fig. 12. Transient absorption recovery data for pre-irradiated PCS fiber.

TABLE II

Transient Absorption Data $t = 100$ ns

600 nm

Febetron 705 - 24 KRad

<u>Vendor</u>	<u>Description</u>	<u>Core Size, μm</u>	<u>Attenuation</u>
ITT	Suprasil T303	125	7.7 dB/m
Fiberguide	Superguide I	200	8.8
Fiberguide	Superguide II	150	12.8
Fiberguide	Super Anhydroguide	200	19.3
Fiberguide	Anhydroguide	200	> 250
QPC	QSF A	125	25.7
Sawyer	Cultured Quartz	1000	37
Linde	Sapphire*	1000	85

*Standard or UV grade.

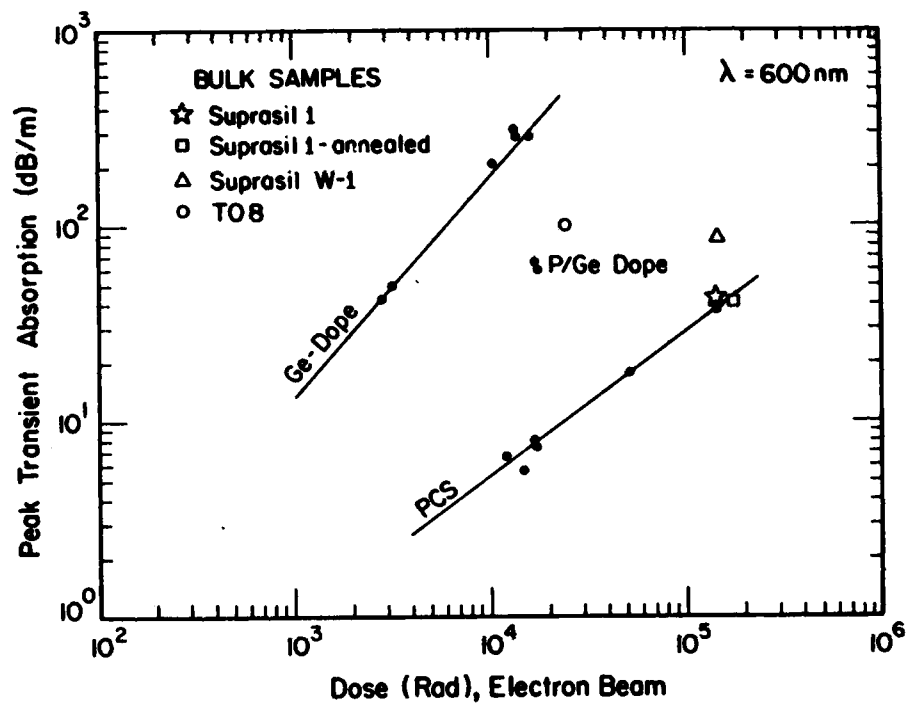


Fig. 13. Peak transient absorption for bulk silica samples.

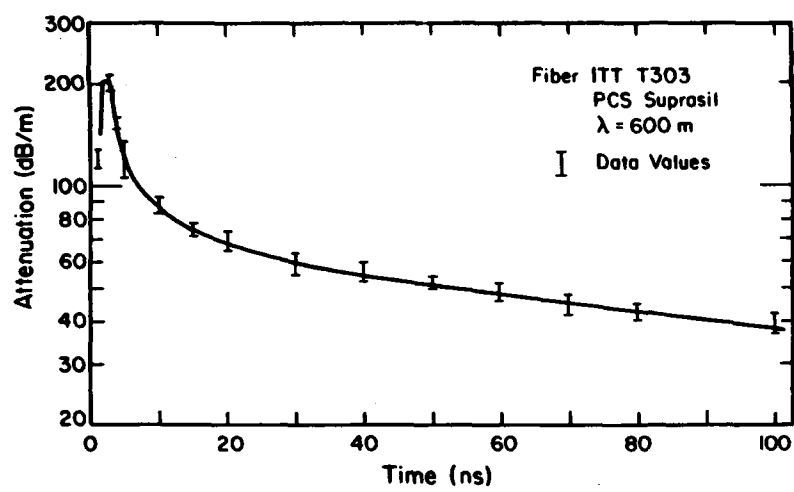


Fig. 14. Attenuation measurement of ITT PCS.

The time history of the e-beam pulse is given in Fig. 15 with a fast (4 GHz) Faraday Cup, a Tektronix 7904 scope, and only 8 m of high-quality foam heliax coaxial cable. The observed 1.6 ns FWHM corresponds to a FWHM near 1.4 ns after correction for the scope and cable. This pulse FWHM is better than the 3 ns quoted for a Febetron 706. It was obtained by running the beam energy at 600 keV and passing the beam through a thin (69 mg/cm²) aluminum sheet. This served to strip off low-energy electrons which provide much of the pulse broadening. As a point of interest, multiple-pulse radiation "softening" is not observed on the Febetron 706, despite doses more than ten times above the 705 system.

Theoretical Progress

Fiber Recovery

The damage and subsequent recovery of an optical fiber exposed to a radiation pulse depends upon a number of factors, not all of which are quantitatively understood. The more important parameters are pulse duration, dose, nature and energy of the radiation (neutrons, gammas, fission fragments, etc.), temperature, fiber composition, and purity. Other factors such as dose rate during the pulse and the pre-existing solid state defects (dislocations, color centers, etc.) probably also affect the response to radiation. In addition, optical attenuation is wavelength dependent.

The effect of neutrons is mainly that of atomic displacement in the solid matrix via collisions and nuclear reactions, with the consequent production of vacancies and interstitials. This produces localized energy levels that serve as electron and hole traps, causing an increase in optical attenuation. The neutron recoil products subsequently lose energy to ionization. Damage due to gammas and electrons may be treated as a unit, since the former mainly interact through the photoelectric effect, Compton effect, or pair production to produce electrons. In contrast to neutrons, electrons and gammas transfer nearly all of their energy to atomic electrons in the fiber; that portion resulting in displacements is small. For some materials, detailed calculations⁹ exist to identify the neutron energy deposited in displacement and ionization mechanisms. Such calculations for SiO₂ have not been located, but Ref. 9 calculates no greater than 4% energy deposition in displacement processes for a variety of other materials for 14 MeV neutrons. The above mechanisms all contribute to a time-dependent optical attenuation coefficient that is superimposed upon the intrinsic, unradiated coefficient.

Since the radiation-induced attenuation coefficient of a solid is proportional to the defect concentration,¹⁰ the transient absorption coefficient should follow the same response as the ion pair concentration. In particular, the theory of geminate recombination¹¹ predicts that, on a short time scale, the probability that the ion pair will recombine together by diffusion is quite high. On a longer time scale, those electrons that escape nearly immediate recombination may encounter a trap in the fiber lattice and have a lifetime dependent upon the trap depth, width, ground state energy, and distance to the nearest scavenger molecule.¹²

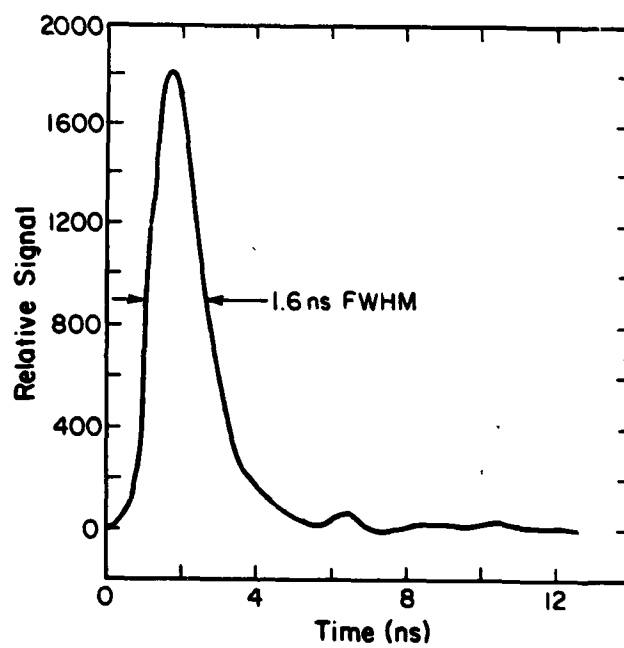


Fig. 15. Current vs time for Febetron 706 pulse.

Based upon geminate recombination theory,¹¹ the (radiation induced) attenuation, for a radiation pulse at $t = 0$, should follow

$$\beta = \beta_0 e^{\lambda t} \operatorname{erfc} \sqrt{\lambda t} \quad , \quad (1)$$

where β and β_0 are the attenuation coefficients at time t and $t = 0$, respectively, and λ is a parameter that is a measure of recombination rate. The complementary error function is defined as

$$\operatorname{erfc} x = 1 - \operatorname{erf} x = 1 - \frac{2}{\sqrt{\pi}} \int_0^x e^{-u^2} du = \frac{2}{\sqrt{\pi}} \int_x^\infty e^{-u^2} du \quad . \quad (2)$$

Note that λ determines the decay rate, and from diffusion theory, it should vary as

$$\lambda_0 \exp(-\epsilon/kT) \quad , \quad (3)$$

where ϵ is the barrier height for diffusion. There is some evidence to suggest that λ may be dose dependent.

While the emphasis here is on recovery after termination of the pulse, there will be some recovery during the pulse, which will tend to decrease the peak transient absorption to a value below what it would attain if no recovery mechanism occurred. Thus, the peak transient absorption should be a function of dose, pulse length and shape, and temperature for a given fiber.

To test this model, the Febetron 706 data were used to determine a value of λ . For the Febetron, the dose rate was assumed to follow the electron pulse $I(t)$. $I(t)$ was taken from Fig. 15 and normalized to unity. Then the observed attenuation $\beta'(t)$ becomes

$$\beta'(t) = k \int_0^\infty I(t') e^{\lambda(t-t')} \operatorname{erfc} \sqrt{\lambda(t-t')} dt' \quad . \quad (4)$$

Two adjustable parameters, λ and k , are then available.

The value of λ in Eq. (4) obviously plays the major role in determining the observed attenuation coefficient at any given time. To investigate this effect, Fig. 16 was constructed for a large range of λ values. In Fig. 16 the geminate recombination function β from Eq. (1) was calculated. These functions were then convolved with the Febetron current pulse, as in Eq. (4), and the resulting $\beta'(t)$ values are shown in Fig. 17. It should be noted that the $\beta'(t)$ values for $t < 10$ ns are strongly dependent on λ . The FWHM of $\beta'(t)$ varies from 3.7 ns for $\lambda = 10 \text{ ns}^{-1}$. In these calculations, it is implicitly assumed that defect generation rate is proportional to fiber dose rate. It is certainly possible, and even probable, that some classes of defects saturate early in the pulse history.

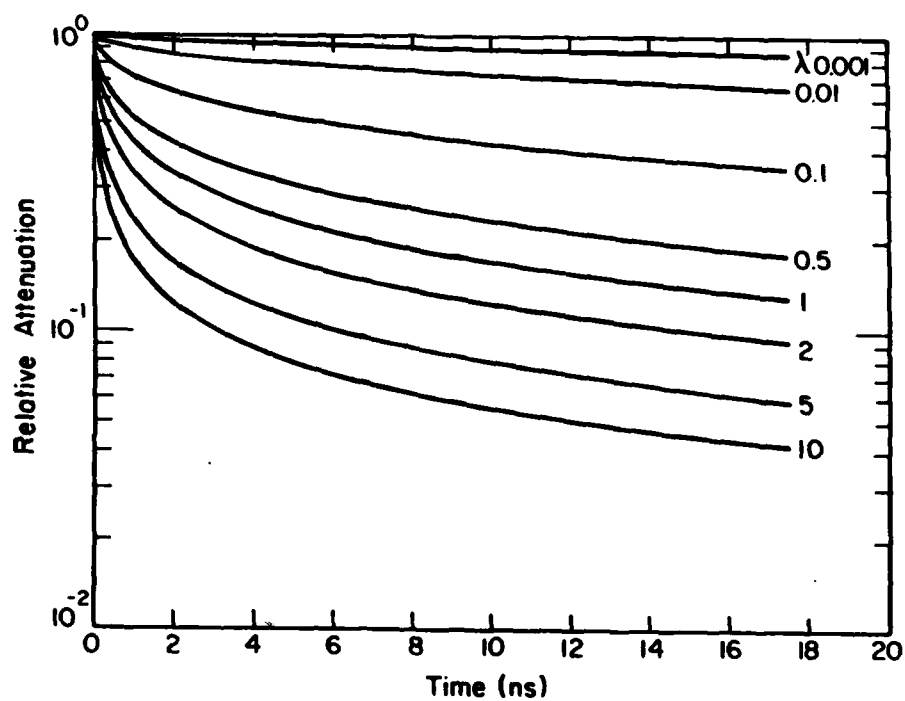


Fig. 16. Geminate recombination function, $\beta = e^{\lambda t} \text{erfc } \sqrt{\lambda t}$, λ in ns^{-1} .

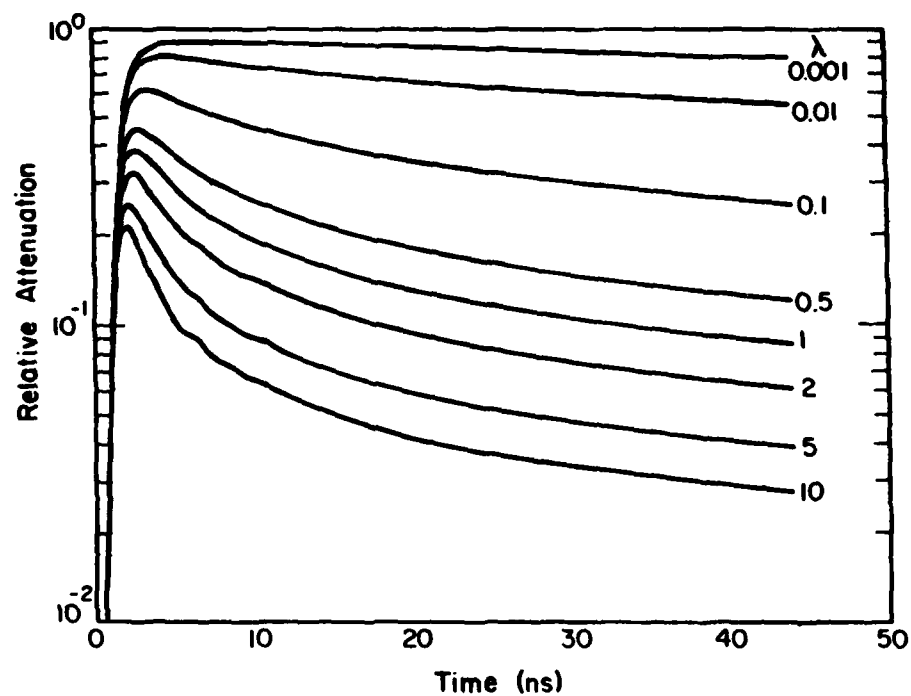


Fig. 17. Convolution of Geminate Recombination Function, $\beta = e^{\lambda t} \operatorname{erfc} \sqrt{\lambda t}$, and normalized Febe-tron current pulse, λ in ns^{-1} .

The calculations of Fig. 17 were compared to the measured attenuation data of Fig. 14. With an observed FWHM of the β' curve of ~ 5.3 ns, the system response of 950 ps should be modifying the measured value negligibly. Emphasis was placed on matching the observations at early times since other mechanisms (trapping, etc.) may predominate at later times. The best fit was obtained with $\lambda = 5 \text{ ns}^{-1}$. An expanded view of both the geminate recombination function and its convolution with the driving pulse is given in Fig. 18. Nonlinearity in the defect generation process is of serious concern, and represents an uncertainty in this fitting procedure. As one test for such effects, the dose was reduced by a factor of almost two. The attenuation curve shape was not altered.

A comparison of the measured data and the convolved curve is given in Fig. 19. The fit for $t < 6$ ns is good, but the measured attenuation far exceeds the predictions at later times. This implies that trapping mechanisms play a predominant role after about 30 ns. The sensitivity of the fit to λ suggests that $5 \pm 2 \text{ ns}^{-1}$ is a reasonable estimate of uncertainty, but this estimate is complicated by the possible problem connected with nonlinear defect production.

Further tests with shorter radiation pulses, different dose, and different temperatures will be needed to confirm the identification of the early time history as geminate recombination. Data at 800 nm must also be acquired.

Cerenkov Light Coupling

A complete treatment of Cerenkov coupling has not been accomplished yet. However, several interesting relations have been derived which are useful in specific cases. Consider the two coordinate sets (x,y,z) and (x',y',z') shown in Fig. 20. The fiber axis is oriented along the z -axis and an electron beam is oriented along the z' axis. The angle ψ then represents the angle between the fiber axis and the electron beam axis. Cerenkov light is radiated in a cone of polar angle θ measured relative to the z' axis and that light is uniformly distributed azimuthally about the z' axis. If $\theta' = \theta_c$ is the azimuthal angle about z' in the (x',y',z') system, the polar angle θ relative to the fiber axis can be shown to be

$$\cos \theta = \cos \theta_c \cos \psi - \sin \theta_c \sin \phi' \sin \psi . \quad (5)$$

The Cerenkov angle θ_c is related to electron velocity by

$$\cos \theta_c = 1/\beta n \text{ where } \beta = v/c \quad (6)$$

for a material (in this case the fiber core itself) of index n . Note that for $\psi = \theta_c$ and $\phi' = 270^\circ$, $\theta = 0$.

Equation (5) is exact, but a more useful relation follows if a small angle approximation is made for θ , since only small θ values will couple into guided fiber modes. In addition small values of ϕ' and ψ can be

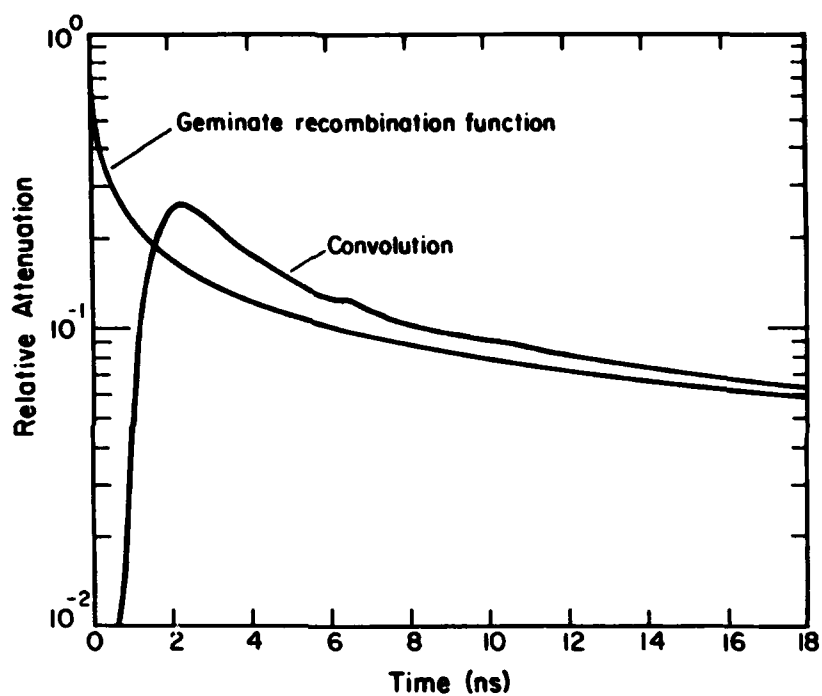


Fig. 18. Overlay of Geminate Recombination Function ($\lambda = 5 \text{ ns}^{-1}$) and Convolution of Function with Normalized Febetron Current Pulse.

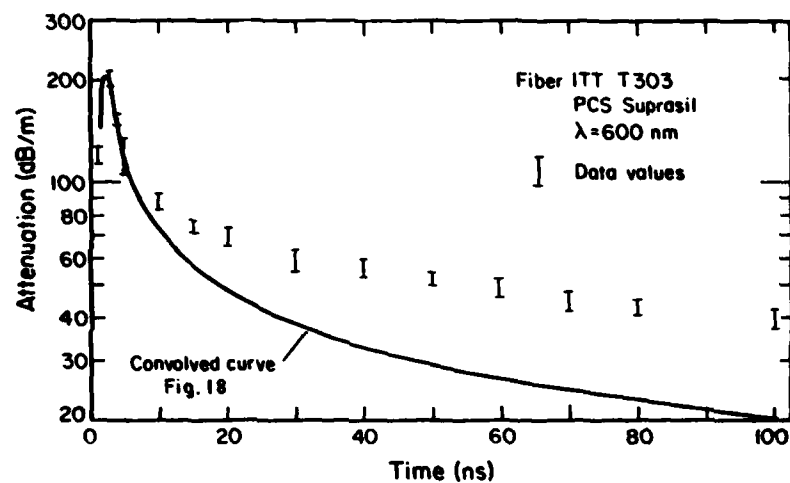


Fig. 19. Comparison of Geminate Recombination Theory and Attenuation Measurements.

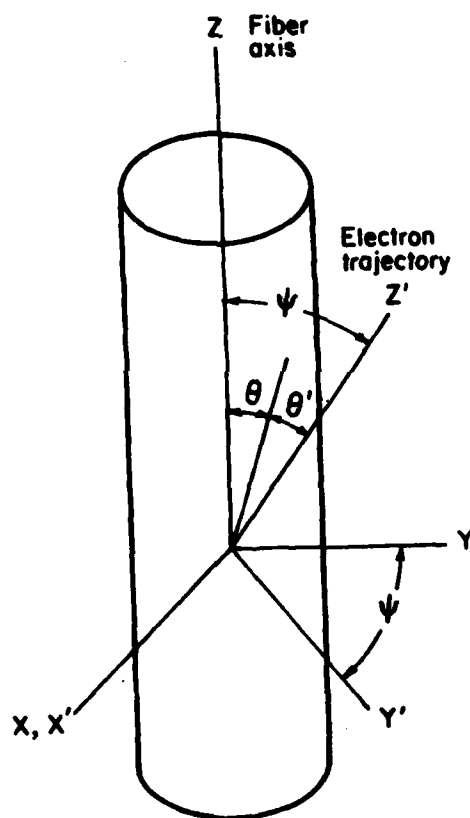


Fig. 20. Geometry for fiber/electron beam coupling calculation.

considered if we redefine the origin of ϕ' to be at 270° and the origin of ψ to be θ_c , since only for values near the new origins can light couple into the fiber. Thus

$$\cos \theta = \cos \theta_c \cos (\theta_c + \psi) - \sin \theta_c \sin (270^\circ + \phi') \sin (\theta_c + \psi) \quad (7)$$

and if all terms above third order in ϕ' and ψ are dropped

$$\theta = \sqrt{\psi^2 + \phi'^2 \sin^2 \theta_c + \phi'^2 \psi \sin \theta_c \cos \theta_c} \quad (8)$$

where ψ = departure of electron trajectory from θ_c .

Note in Eq. (8) that a Cerenkov light trajectory of $\theta = 0$ (along the fiber axis) is possible only if $\psi = 0$, i.e., the electron trajectory is at the Cerenkov angle relative to the fiber. Thus low-order fiber modes can be excited only with an electron beam at the Cerenkov angle relative to the fiber. As the electron/fiber angle departs from θ_c , only higher-order modes become excited. Fig. 21 shows some typical cases and demonstrates that for a fiber with N.A. = 0.20, only ϕ' within $\pm 10^\circ$ actually couples into propagating fiber modes. The Cerenkov light is uniformly distributed in ϕ' , thus only $\sim 6\%$ (20/360) of the Cerenkov light is coupled into the fiber.

Equation (8) assumed a monoenergetic, collimated electron beam incident on the fiber. In a real field situation, the electrons probably originate from photon conversion processes, resulting in a broad range of electron angles and energies. Transport of the electrons will further broaden the angular distribution and the energy range. A complete calculation of coupled power becomes very difficult as all these variables are included and has not been attempted yet. One simple case can be calculated in which a uniform distribution of electron trajectories in ψ is assumed. For this case, the fiber light coupling distribution becomes Lambertian.

Equation (8) and its consequences have serious implications if a fiber is used as a high-bandwidth radiation detector using the Cerenkov process. The details of light distribution among fiber modes are clearly influenced by orientation of the fiber and the electron angular distribution. If such a detection system were calibrated by a well-collimated electron beam, the modal excitation would not match a field application. To avoid this concern, the electron beam collimation is destroyed by a scatter plate in the calibration process to more closely approach the field situation.

Conclusion

This paper has presented a current status report on a continuing project. Prompt luminescence has been shown to be of Cerenkov origin and a calculation of Cerenkov light injection angle as a function of electron trajectory has been given. The more complicated calculation of Cerenkov

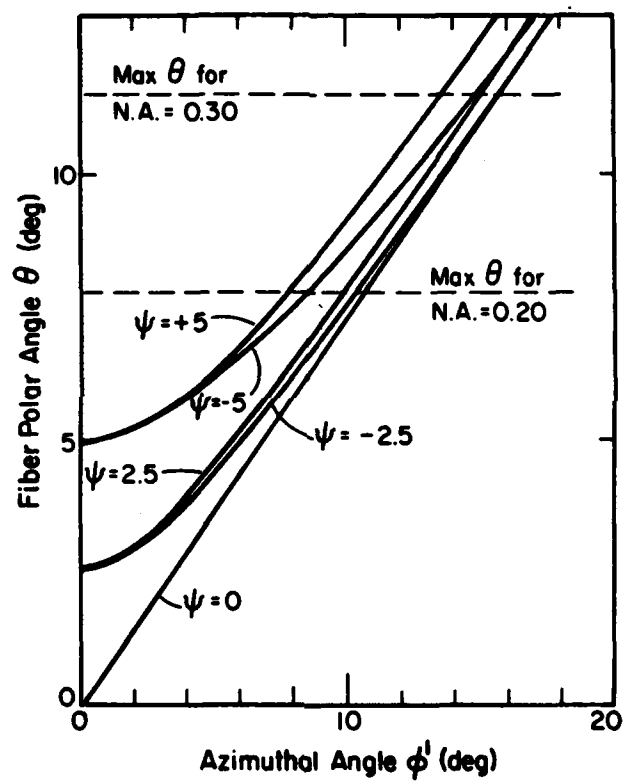


Fig. 21. Light ray angle within fiber core for various azimuthal angles.

coupling for an incident gamma beam onto a converter has not been attempted yet.

Short-term transient damage has been studied for a variety of fibers and doses. Neutron-induced transient absorption (for 14 MeV neutrons) was determined to produce absorption equivalent to an equal absorbed dose of gammas or electrons. Thus, neutron-induced displacement mechanisms appear to be negligible in their short time effects.

Suprasil core PCS fiber has been shown to be the most radiation resistant for short time applications. Fiber from two vendors yielded comparable damage resistance at $t = 100$ ns. Predosed PCS fiber is less radiation resistant at short times. Bulk silica samples demonstrated attenuation similar to silica fiber samples of the same grade of silica, suggesting that draw-induced defects are negligible. Two bulk materials, quartz and sapphire, did not offer improved resistance at 600 nm.

Repetitive Febetron 705 pulses (24 KRad) were observed to lead to increased transient absorption in the 50-100 ns time range. But Febetron 706 pulses near 200 KRad did not lead to such an increase. The 705 pulses, with peak electron energy of 1150 keV onto the fiber may cause lattice damage while the 706 pulses, with peak electron energy of 500 keV onto the fiber, may not be able to displace lattice atoms.

Early time data for $t > 3$ ns were used to identify diffusion parameters for PCS fiber. While a geminate recombination model provided a fit to very early times ($t < 10$ ns), the model did not fit the observations at later times. Some other mechanism, perhaps a trapping phenomena, must account for the attenuation at longer times.

Future project emphasis will be placed on short time measurements with shorter radiation pulses, different temperatures, and different wavelengths.

REFERENCES

1. J. E. Golob, P. B. Lyons, and L. D. Looney, IEEE Trans. Nuc. Sci. NS-24 (1977) p. 2164.
2. P. B. Lyons, L. D. Looney, J. E. Golob, R. Robichaud, R. Seno, J. Madrid, L. Hocker, and M. Nelson, Plenum Publishing Corp., Proceedings of 1978 Conf. on Physics of Fiber Optics, p. 379.
3. P. B. Lyons, J. E. Golob, and R. E. Kelly, "Short-Term Transient Radiation Effects in Optical Fibers," OSA Meeting on Optical Fiber Communication (March 1979) Washington, DC.
4. G. H. Sigel, E. J. Friebele, 1979, Naval Research Laboratory.
5. E. J. Friebele, G. H. Sigel, and M. E. Gingerich, Laser Focus 14, No. 9 (1978) p. 50.
6. G. H. Sigel, E. J. Friebele, M. E. Gingerich, and L. M. Hayden, IEEE Trans. Nuc. Sci. NS-26 (1979) p. 4796.
7. C.D. Skoog, "A Summary of Radiation-Induced Transient Absorption and Recovery in Fiber Optic Waveguides," Sandia Lab Report 76-8056 (November, 1976).
8. M. S. Maklad, G. W. Bickel, and G. H. Sigel, Opt. Fiber Transmission II (Optical Society of America, Washington, 1977) paper TuD8.
9. W. L. Bendel, IEEE Trans. Nuc. Sci. NS-24 (1977) p. 2516.
10. A.E. Hughes and D. Pooley, Real Solids and Radiation (Wykeham, London, 1975), p. 80.
11. S.J. Rzed, P.P. Infelta, J.M. Warman, and R.H. Schuler, J. Chem. Phy., 52, No. 8, 15 April 1970.
12. J.R. Miller, J. Chem. Phy., 56, No. 10, 15 May 1972.

THIS PAGE IS INTENTIONALLY LEFT BLANK

RADIATION RESPONSE MEASUREMENT OF FIBERS
IN THE PICOSECOND REGION*

P. Zagarino, C-H. Lin, M.A. Nelson, T.J. Davies,
N.J. Norris, and J.W. Ogle
EG&G, Santa Barbara Operations

ABSTRACT

The prompt radiation response of optical fibers has previously been measured within a few nanoseconds of a radiation pulse. A new capability has been developed that allows response measurements during exposure to a 50-psec burst of radiation. Transmission through a fiber or other optically transparent sample is interrogated using a 3-psec dye laser pulse that is scanned through the synchronous 50-psec ionizing radiation pulse. This system will be described and data recording techniques discussed. Results of fiber measurements will be presented.

*This work was performed under the auspices of the U.S. Department of Energy under Contract No. DE-AC08-76NV01183. NOTE: By acceptance of this article, the publisher and/or recipient acknowledges the U.S. Government's right to retain a nonexclusive royalty-free license in and to any copyright covering this paper.

Reference to a company or product name does not imply approval or recommendation of the product by the U.S. Department of Energy to the exclusion of others that may be suitable.

RADIATION RESPONSE MEASUREMENT OF FIBERS IN THE PICOSECOND REGION*

P. Zagarino, C-H. Lin, M.A. Nelson, T.J. Davies,
N.J. Norris, and J.W. Ogle
EG&G, Santa Barbara Operations

INTRODUCTION

Optical fibers are finding increasing use for high-frequency nuclear diagnostic measurements, which demand knowledge of the short-term transient effect of radiation on the fibers. Considerable work in this area has been carried out at Los Alamos Scientific Laboratory¹ using Febetron radiation sources, and at EG&G's Santa Barbara Operations using Febetrons and a linear accelerator (linac). The accelerator has the advantage of producing a very short burst of radiation. This paper will describe two experimental methods for measuring radiation-induced transient absorption in optical fibers that are being used at the DOE/EG&G linac at Santa Barbara. One technique uses a relatively wide laser pulse (~ 2.5 μ sec) as a carrier for the absorption signal caused by the fast radiation pulse (~ 50 psec) produced by the linac. In this method, the signal is recorded as a single sweep on a wide band oscilloscope; therefore, the measurement is bandwidth-limited by the photodetectors and vertical amplifiers of the real time oscilloscope. The maximum repetition rate of the pulse laser is too slow for a sampling oscilloscope to be used. The second approach involves an optical sampling technique wherein a fast laser probe pulse (< 3 psec) samples the transmission of the fiber at various times with respect to the radiation pulse. Although this method can measure the absorption signal at very large bandwidths, as presently instrumented it is limited to a relatively short total time window (< 12 nsec) and it subjects the fiber to repeated radiation pulses. Consequently, both methods are used to completely characterize the time response of radiation-induced transient absorption in optical materials.

EXPERIMENTAL METHOD FOR REAL TIME MEASUREMENT

Figure 1 represents schematically the basic features of the experimental technique for single-sweep recording of the transient absorption in an optical fiber exposed to a radiation pulse. A pulse dye laser is triggered first,

*This work was performed under the auspices of the U.S. Department of Energy under Contract No. DE-AC08-76NV01183. NOTE: By acceptance of this article, the publisher and/or recipient acknowledges the U.S. Government's right to retain a nonexclusive royalty-free license in and to any copyright covering this paper.

Reference to a company or product name does not imply approval or recommendation of the product by the U.S. Department of Energy to the exclusion of others that may be suitable.

producing a 600-nm light pulse of relatively long duration and high power ($\sim 2.5 \mu\text{sec}$ and $>500 \text{ W}$ peak) which is coupled into a low-bandwidth fiber to smooth out high-frequency laser noise. The light is then split and coupled into two high-frequency link fibers which carry the light from the laser to the accelerator cell, where a short length of test fiber is connected to one link fiber and positioned across the linac electron beam window. The other link fiber is kept out of the electron beam, since it is used to provide the laser pulse shape reference. Both link fibers then continue to the linac control room where the optical signals are detected by 2-inch vacuum photodiodes and recorded on a dual beam oscilloscope.

When the linac is triggered, it produces a 3-5 nC, 50-psec pulse of 6-MeV electrons across the test fiber. Dosimetry is done by integrating the charge in the electron pulse on a stopping block set right behind the test fiber. The data acquisition system for the linac has been described elsewhere.²

Since the linac is a traveling wave accelerator, its output is in phase with the linac master oscillator. The linac trigger generator also runs off the same oscillator and provides the laser pretrigger, the injector trigger, and a trigger for the recording oscilloscope. Although the laser pulse timing has about 50 to 100 nsec of jitter, the oscilloscope trigger is always precisely timed with the radiation pulse. Therefore, the absorption signals can be recorded at the maximum sweep speed the scope can achieve.

EXPERIMENTAL RESULTS FOR REAL-TIME MEASUREMENT

Figure 2a shows the reference trace (upper) and signal trace resulting from exposing 20 cm of plastic-clad silica (PCS) test fiber to a single 560-rad pulse of 6-MeV electrons. Only the top 600 mV is shown, since ground potential has been offset offscreen. At 200 nsec/division sweep speed the fast leading edge of the absorption signal can barely be seen. Figure 2b shows the same signals recorded at 20 nsec/division horizontal sweep speed. The signal level (lower trace) is 520 mV and the absorption level is 495 mV. This calculates to a peak attenuation of 0.02 dB/cm-krad in the test fiber.

EXPERIMENTAL METHOD FOR OPTICAL SAMPLING MEASUREMENT

Figure 3 illustrates the basic idea of the optical sampling technique. The fundamental feature of this approach is the operation of the picosecond pulse modelocked laser in such a manner that its output pulse train is synchronous with the linac output electron pulse. This is done by deriving the modelock frequency from the linac master oscillator. When the laser is operated in this mode the observed time jitter between the laser pulse train and the linac electron pulses is less than 30 psec. By shifting the phase of the modelock frequency relative to the linac frequency, the laser pulses can be moved precisely in time with respect to the linac electron pulse. Therefore, by passing the laser probe pulse through a fiber exposed to the electron beam, its transmission can be sampled at any time relative to the electron pulse. The laser pulse is again split and coupled into two fibers so that one fiber can carry a reference pulse. The laser probe pulse and reference pulses are detected by photomultiplier tubes. Their output is digitized and recorded by an online minicomputer which normalizes the probe pulse amplitude by the reference pulse amplitude on a pulse-by-pulse basis to remove laser amplitude jitter.

In Figure 4, a more detailed diagram of the experimental arrangement, it can be seen that the linac and laser do not run at the same repetition rate. However, a Pockels cell is used to synchronously gate out the laser pulses at the repetition rate of the linac (360 pulses per second). The phase shifter is a slide trombone coaxial air line. The shifted frequency is sent to the laser to move the laser pulse in time with respect to the electron pulse; it is also sent to the synchronous delay unit so that the trigger to the Pockels cell high voltage amplifier, and hence the optical gate, will move in time with the laser pulse train. Deutsch fiber connectors are used to splice the high frequency link fibers to the test fiber located across the electron window.

One advantage of this technique is that the transmission at a particular time can be measured repeatedly, thus allowing the average transmission versus time to be recorded. The signal averaging improves the detectability of small attenuations on the order of a few percent.

RESULTS OF OPTICAL SAMPLING MEASUREMENT

Figure 5 shows the results of the first test of the optical sampling system to make a fiber absorption measurement. A 13.5-cm length of Corning graded-index fiber was exposed to a repetitive 500-rad pulse of 6-MeV electrons. A total peak absorption of 17% was recorded. Normalizing for the length of fiber and the amount of radiation gives a peak attenuation of 0.12 dB/cm-krad. The leading edge of the absorption signal has a rise time of approximately 600 psec. This is approximately the time of flight of the light through the 13.5 cm length of fiber radiated. Therefore, the recording system bandwidth is not limiting the response time. The 2.5 nsec of signal recorded after the absorption peak shows little recovery.

Figure 6 shows results of radiating 3.2-cm of a different type fiber. The 136-psec rise time recorded is again approximately the time of flight of light through the radiated length of fiber. These results are the second test of the optical sampling system. They show a substantial improvement in the signal to noise ratio from increasing the intensity of the laser pulses so the photomultiplier tubes could be run at lower gain. This improves the photomultiplier statistics. It can be seen in Figure 6 that 50% fiber recovery occurs in the first 3.4 nsec after the peak, compared to approximately 15% further recovery in the remaining 2 nsec.

DISCUSSION

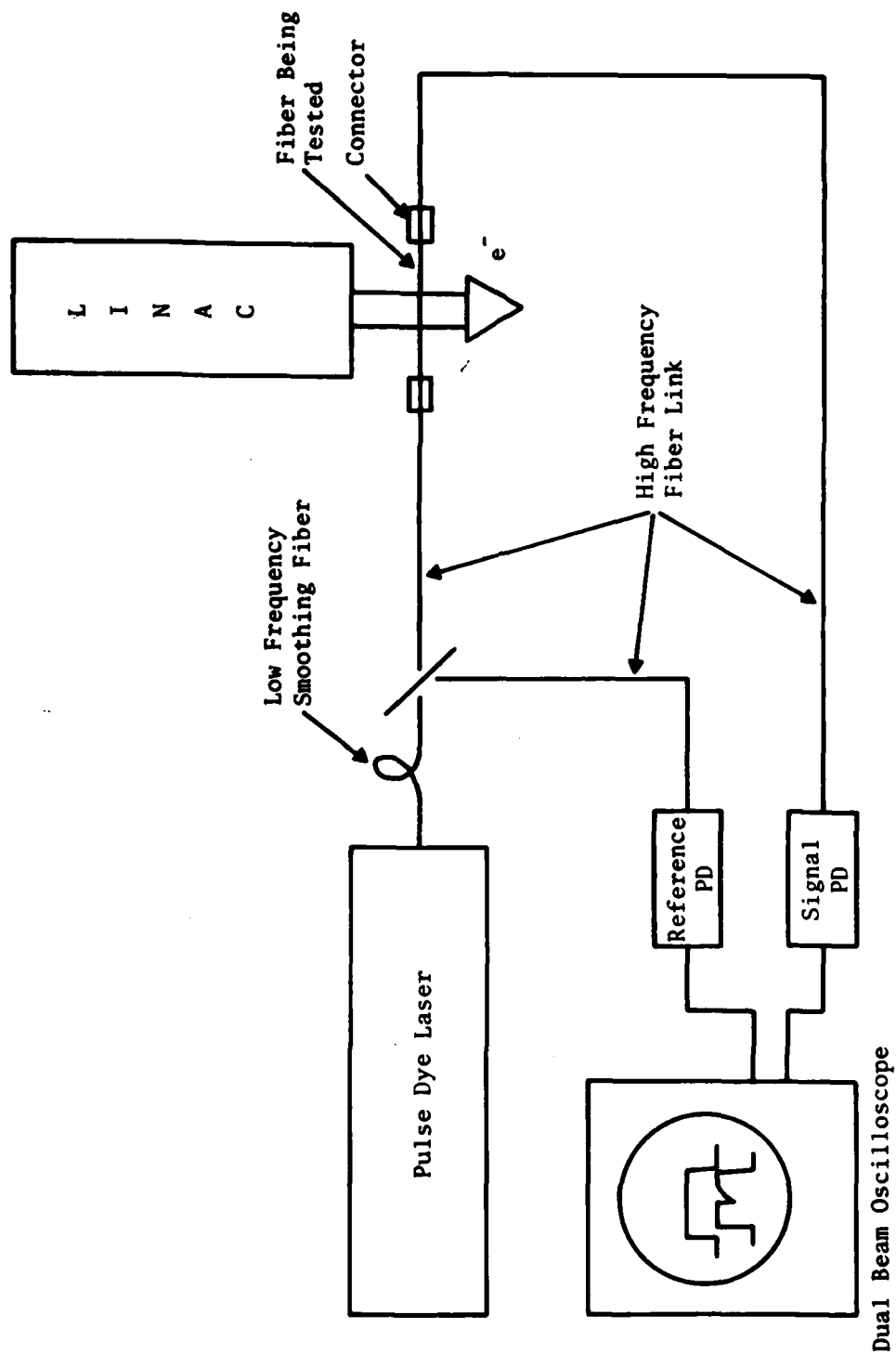
The results of these measurements are preliminary. Our major objective has been to develop an optical sampling system to measure radiation-induced transient absorption in optical materials including, but not limited to, optical fibers. The results so far, though limited, have demonstrated the ability of the optical sampling system to record small attenuations at very high bandwidths.

ACKNOWLEDGMENT

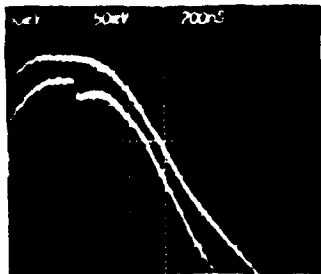
Certain phases of this work were developed under EG&G's internally directed R&D program sponsored by the U.S. Department of Energy through the Nevada Operations Office under Contract No. DE-AC08-76NV01183.

REFERENCES

1. Lyons, P.B., L.D. Cooney, J.E. Golob, and R.E. Kelly, "Short-Term Transient Radiation Effects in Optical Fibers," Topical Meeting on Optical Fiber Communication, Washington, D.C. (6-8 March 1979).
2. Zagarino, P.A., L.P. Hocker, and J.B. Sweeney, "Linac Data Acquisition System," Intra-Program Technical Colloquium, "Minicomputers in Data Acquisition Systems," Las Vegas, Nevada (October 1979).

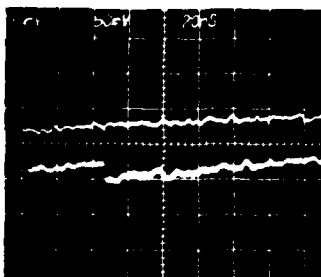


1. Real time measurement of transient absorption in a fiber.



Vertical: 50 mV/division
Horizontal: 200 nsec/division

a. Reference (upper) and signal (lower) trace. 20 cm of PCS test fiber.



Vertical: 50 mV/division
Horizontal: 20 nsec/division

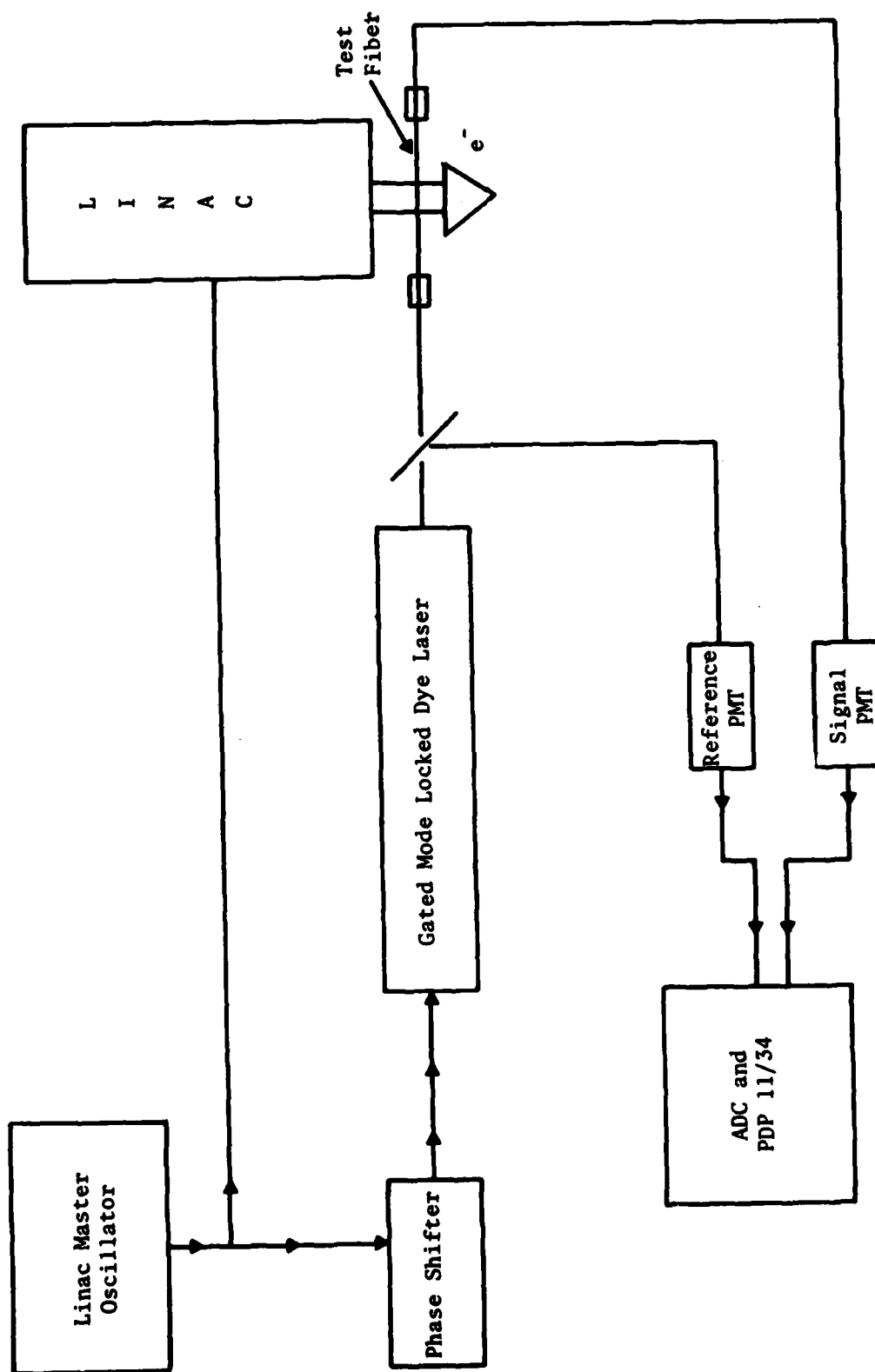
b. Same. Sweep expanded to show radiation-induced absorption (lower trace). Electron charge 2.8 nC/cm^2 . Approximately 560 rads dose.



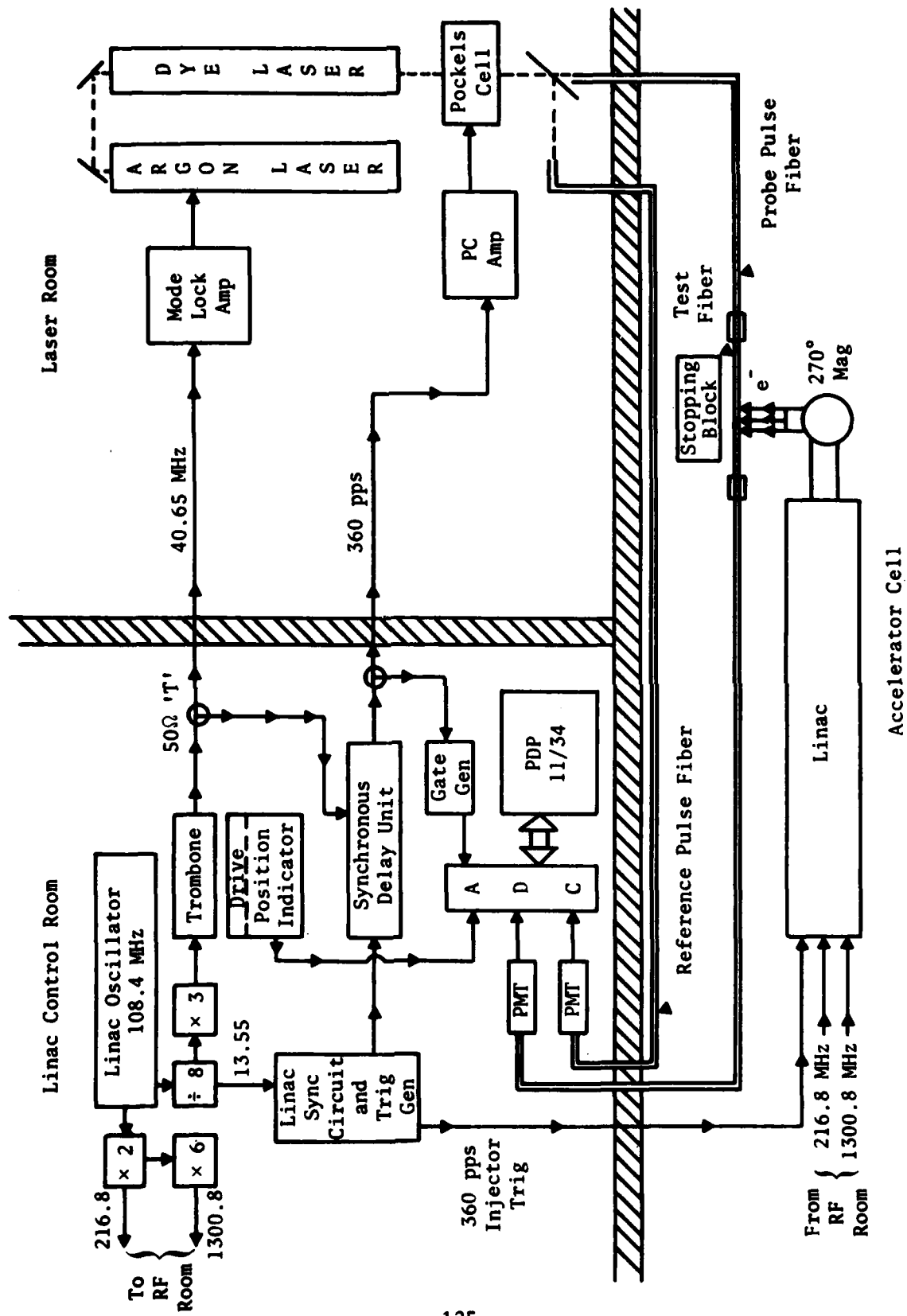
Vertical: 50 mV/division
Horizontal: 2 nsec/division

c. Same. Signal only.

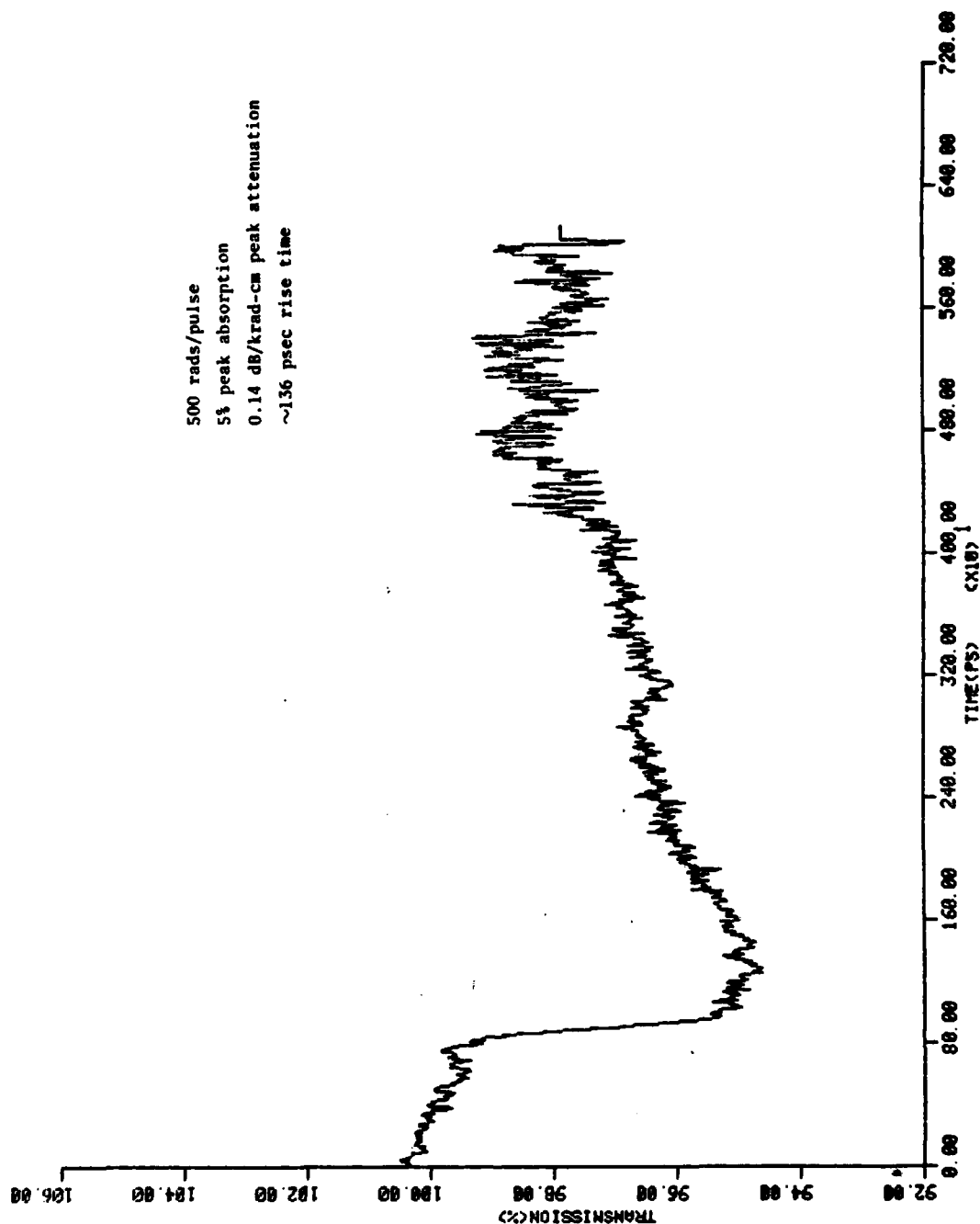
2. Real time fiber absorption data.



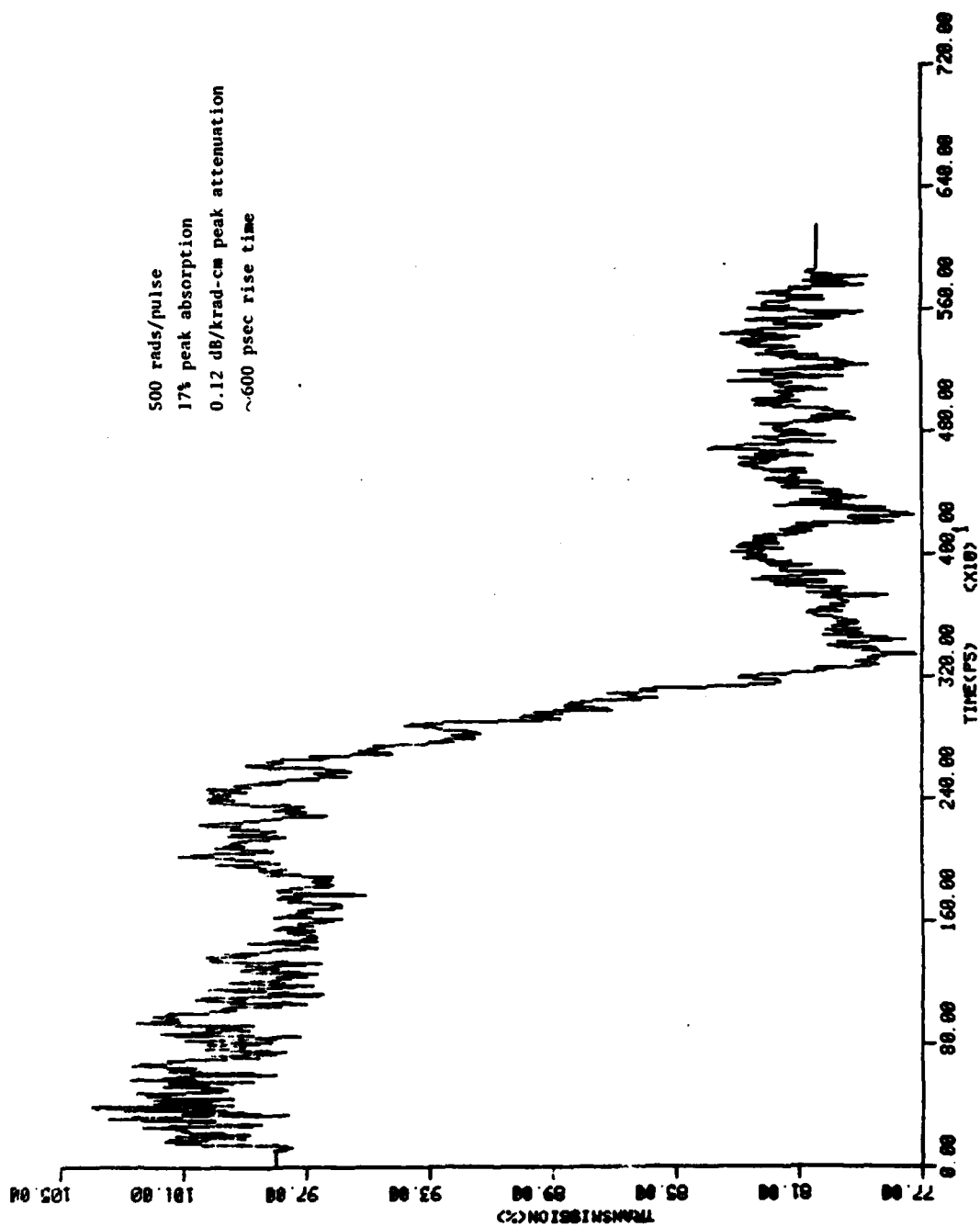
3. Optical sampling measurement technique of transient absorption in a fiber.



4. Detailed block diagram of fiber transient absorption experiment.



5. Measured radiation absorption of 13.5-cm-long graded-index fiber.



6. Measured radiation absorption of 3.2-cm-long graded-index fiber.

THIS PAGE IS INTENTIONALLY LEFT BLANK

PHOTBLEACHING EFFECTS IN OPTICAL FIBER WAVEGUIDES

E. J. Friebele and M. E. Gingerich

Naval Research Laboratory
Washington, D.C. 20375

ABSTRACT

The effect of bleaching light on the radiation-induced optical absorption spectra in state-of-the-art low loss polymer clad silica (PCS) and Ge-doped silica core optical fiber waveguides has been studied. Significant photobleaching was observed in radiation-induced bands centered near 0.7μ in both high and low OH content silica core fibers; however, a broad induced absorption in the infrared which could not be photobleached was found to limit the amount that the radiation-induced loss could be decreased. Photobleaching of the radiation-induced spectra of Ge-doped silica core fibers was also observed; the shape of the bleached spectrum consisted of the tail of a band centered at $\lambda < 0.4 \mu$.

INTRODUCTION

The sensitivity of optical fiber waveguides to ionizing radiation has been well established; radiation-induced attenuations far exceeding the intrinsic loss of low loss fibers are experienced following exposure to relatively moderate doses.¹ Recovery of the radiation-induced absorption has been shown to occur by a thermally activated process in some state-of-the-art fibers.²⁻³ In addition, optical bleaching has been reported in a moderate OH content (40-60 ppm) silica core fiber by Titchmarsh,⁴ who observed that the decay of the radiation-induced attenuation in a Fiberopsil core PCS fiber at 0.85 μ was enhanced by exposure of the fiber to 0.85 μ or continuous white light from a tungsten lamp. The present study was undertaken to characterize more thoroughly this photobleaching effect in fibers and to investigate the spectral nature of the photobleaching. We wished to extend the results of Titchmarsh to other fibers, such as the more common high OH content (1200 ppm) Suprasil core PCS fibers, a low OH content silica core fiber, and Ge-doped silica core fibers used for high bandwidth-long line systems. Photobleaching has been observed in all fibers although the effect was found to be most significant in the pure silica core waveguides of low OH content.

EXPERIMENTAL

Measurements of the radiation-induced optical spectra of the fiber waveguides were made primarily during and after steady state ⁶⁰Co irradiation. White tungsten probe light was injected into the fiber, which was tethered to a coil placed in a sample can in the source in a manner similar to that used for measurements of the radiation-induced loss at 0.82 and 1.3 μ as a function of dose during steady state irradiation.¹ The output of the fiber was collimated with a microscope objective and spectrally dispersed onto a self-scanning linear photodiode array. Thus, the spectrum of the light transmitted through the fiber after a given dose of irradiation or after a given length of fading time could be recorded virtually instantaneously. The output of the array was interfaced to a Nicolet 1080 minicomputer, permitting digital calculation of the radiation-induced loss relative to the transmitted light prior to irradiation.

In order to study the effect of photobleaching during and after irradiation, a length of fiber was irradiated while the tungsten light was blocked by a shutter, except for 0.5 sec intervals at various doses during which the transmitted light was recorded. A second identical irradiation was performed on a fresh length of fiber with the tungsten source unblocked at all times during the irradiation. Photobleaching by other sources such as a He-Ne laser or xenon lamp was studied in a similar manner by shuttering the tungsten source as in the first irradiation and injecting the bleaching light into the fiber via a beam splitting cube. Data were recorded both as a function of dose during irradiation and of time following irradiation. All measurements were made at room temperature; the integrated intensity of the bleaching light traveling in the fiber was approximately 80-100 μ W, as measured by a power meter at the output end.

RESULTS AND DISCUSSION

I. Pure Fused Silica Core Fibers

The radiation-induced optical absorption spectra of a Suprasil core PCS fiber irradiated without bleaching light are shown in Fig. 1. It can be seen that the damage in this high OH content fiber appears to comprise a tail from bands in the ultraviolet (UV), a band centered near 0.63μ which grows in strongly at doses greater than 10^4 rads, and a broad infrared (IR) absorption which increases with increasing dose up to 10^4 rads and then decreases as the dose is increased above this level. A thorough discussion of the spectral nature of the radiation damage in silica core fibers is included in another paper in this conference,⁵ as well as in reference 6.

In addition to the radiation-induced optical absorption bands enumerated above, there is a band in the high wavelength tail of the 0.63μ band that is susceptible to photobleaching. This effect can be clearly seen in Fig. 2, where the propagation of white tungsten light or 0.6328μ light from a He-Ne laser in the fiber during irradiation is seen not only to reduce the intensity in the region of the UV tail and the 0.63μ band, but also to change the shape of the spectrum between 0.6 and 0.9μ . It is significant to note that the bleaching light had no effect on the induced spectrum at wavelengths longer than 0.9μ ; therefore, it is not expected that photobleaching will decrease the radiation-induced absorption of all-glass silica core fibers with high OH content cores at long wavelengths such as 1.3 or 1.55μ , although explicit studies at these wavelengths must be carried out for positive verification.

The spectrum of the photobleached band was obtained by subtracting the radiation-induced absorption spectrum of the fiber at a given dose measured with bleaching light propagating during irradiation from that measured without bleaching light. Typical results are shown in Fig. 3. It can be seen that both the tungsten and He-Ne light have bleached out a band centered near 0.67μ with a tail extending out to near 0.9μ . Thus, it is the tail of this band which affects the radiation damage behavior of high OH content silica core fibers operating in the near IR spectral region. However, since the radiation damage in this region after photobleaching is dominated by the broad IR absorption seen in Fig. 1, the ultimate reduction in radiation-induced attenuation obtainable by photobleaching is limited by this broad band. Note from Fig. 3 that the tail of the photobleached band does not extend past 0.9μ , so that little effect can be anticipated at longer wavelengths.

Fig. 4 contains the radiation-induced spectra of a low OH content (5 ppm) silica core fiber. It is observed by comparing Figs. 1 and 4 that the photobleachable band is much more intense in the Suprasil W core fiber than in the Suprasil core fiber; it is centered at longer wavelength (0.76μ) and is broader. In addition, the induced absorption that is not photobleached in the dry core fiber is more intense than its counterpart in the wet. These data are in agreement with previous studies,^{1,7,8} where it has been observed that the radiation-induced attenuation in low OH content silica core fibers is much larger than in analogous high OH content fibers. Because of the large width of the photobleached band in the dry silica core fiber and its central position at 0.76μ , it can be inferred that photobleaching will be effective in decreasing

the induced attenuation at $\lambda > 1.1 \mu$ in these fibers, whereas this is not the case for the high OH content silica core fibers, as deduced from Figs. 2 and 3.

Another interesting property of the photobleached bands in the wet and dry silica core fibers is that they also fade substantially at room temperature in the dark. Fig. 5 shows representative recovery data for the Suprasil core PCS fiber after ^{60}Co irradiation. The 0.67μ band fades out almost entirely within 90 sec after the termination of the irradiation. Similar behavior is observed for dry silica core fibers, with the result that the radiation-induced spectra of high and low OH content silica core fibers measured 1 hour after an irradiation of 10^5 rads are virtually identical at wavelengths longer than 0.7μ .^{5,6}

II. Ge-Doped Silica Core Fibers

The spectral nature of the radiation damage in Ge-doped silica core fibers is quite different from that of the pure fused silica core fibers. As shown in Fig. 6, in the doped silica waveguides the radiation-induced absorption in the vis-near IR region of the spectrum shows little evidence of resolved bands; rather, it appears that tails from intense induced bands in the UV cause the attenuation measured in these fibers near $0.8\text{--}0.9 \mu$. (There is a minimum in induced absorption near 1.1μ and a subsequent increase at wavelengths longer than 1.1μ due to bands centered $\geq 1.7 \mu$ in fibers codoped with P and/or B.^{1,5,6})

The attenuation induced in Ge-doped silica core fibers codoped with P in the core has been found to be greater than that of P-free fibers,^{1,3,5,9} and this behavior is evident in Fig. 6 as well. It is also apparent from Fig. 6 that injection of tungsten light during the steady state irradiation decreases the level of induced absorption at all wavelengths. Photobleaching of these fibers does not reveal the presence of any band in the vis-near IR; subtraction of the spectra measured with tungsten light propagating in the fiber during irradiation from those measured without yields only the tail of a band (or bands) located at $< 0.4 \mu$ identical in shape to the radiation-induced loss itself. The percent reduction in induced attenuation achieved by photobleaching is independent of wavelength over the $0.4\text{--}1.1 \mu$ range. However, photobleaching may be less effective at longer wavelengths, depending upon whether or not the long wavelength ($> 1.7 \mu$) induced bands, which account for the loss at $\lambda \geq 1.1 \mu$, can be photobleached. These studies are in progress.

CONCLUSIONS

The present study has established that photobleaching decreases the radiation-induced optical absorption in fiber waveguides with cores of both pure fused silica and Ge-doped silica. A tabulation of the amount of this reduction in the fibers studied is shown in Table I. It is immediately obvious that photobleaching is much more effective in reducing the induced attenuation in the dry fused silica core fiber than in any of the others. The decrease in the effectiveness of photobleaching that is evident with increasing dose in the Suprasil W and the binary Ge-doped silica core fibers can be attributed to increased absorption at the higher dose due to radiation-induced bands that are not photobleachable. Likewise, the constant amount of photobleaching that is observed with increasing

dose in the Ge-2% P-doped silica core fiber is interpreted as being due to a constant fraction of photobleachable induced absorption at the two doses. In contrast, the greater photobleaching measured at 10^5 rads in the Suprasil core fiber arises because the broad IR absorption decreases in intensity at doses above 10^4 rads (Fig. 1). Thus, the photobleached band in this fiber comprises a greater fraction of the induced loss at the higher dose.

The measurements of the present study were carried out using principally tungsten light to photobleach the fibers so that the spectral nature of the photobleaching could be studied. In an actual battlefield deployment, the optical communications system will operate with a laser diode or LED as the source. Although it is conceivable that an additional, high intensity source may be used to photobleach radiation damage, the relatively low intensity monochromatic data transmission source may be the only light available for photobleaching. Titchmarsh⁴ has already established a decrease in the radiation-induced attenuation at 0.85μ when an 0.85μ signal is propagated in a moderate OH content PCS fiber. We have observed analogous behavior at 0.82μ in a high OH content PCS fiber. Indeed, a 22% reduction in induced loss was measured during steady state irradiation at 10^4 rads and 37% at 10^5 rads, agreeing well with the data shown in Table I. Similar measurements are in progress on the other fibers and will be reported at the meeting.

Thus, the present work has shown that the radiation damage in both silica and doped silica core optical fiber waveguides may be reduced by photobleaching. Systems which are operating during and after a radiation exposure will consequently experience less degradation in optical transmission than those which are quiescent. Although photobleaching is effective in decreasing the induced loss, it does not eliminate it; radiation-induced attenuation still remains a serious problem for optical communications systems deployed in radiation environments.

ACKNOWLEDGEMENTS

The authors would like to thank P. C. Schultz, Corning Glass Works, K. Rau, Heraeus Quarzschmelze, and F. V. DiMarcello, Bell Laboratories for samples used in this study, and D. L. Griscom for helpful discussions.

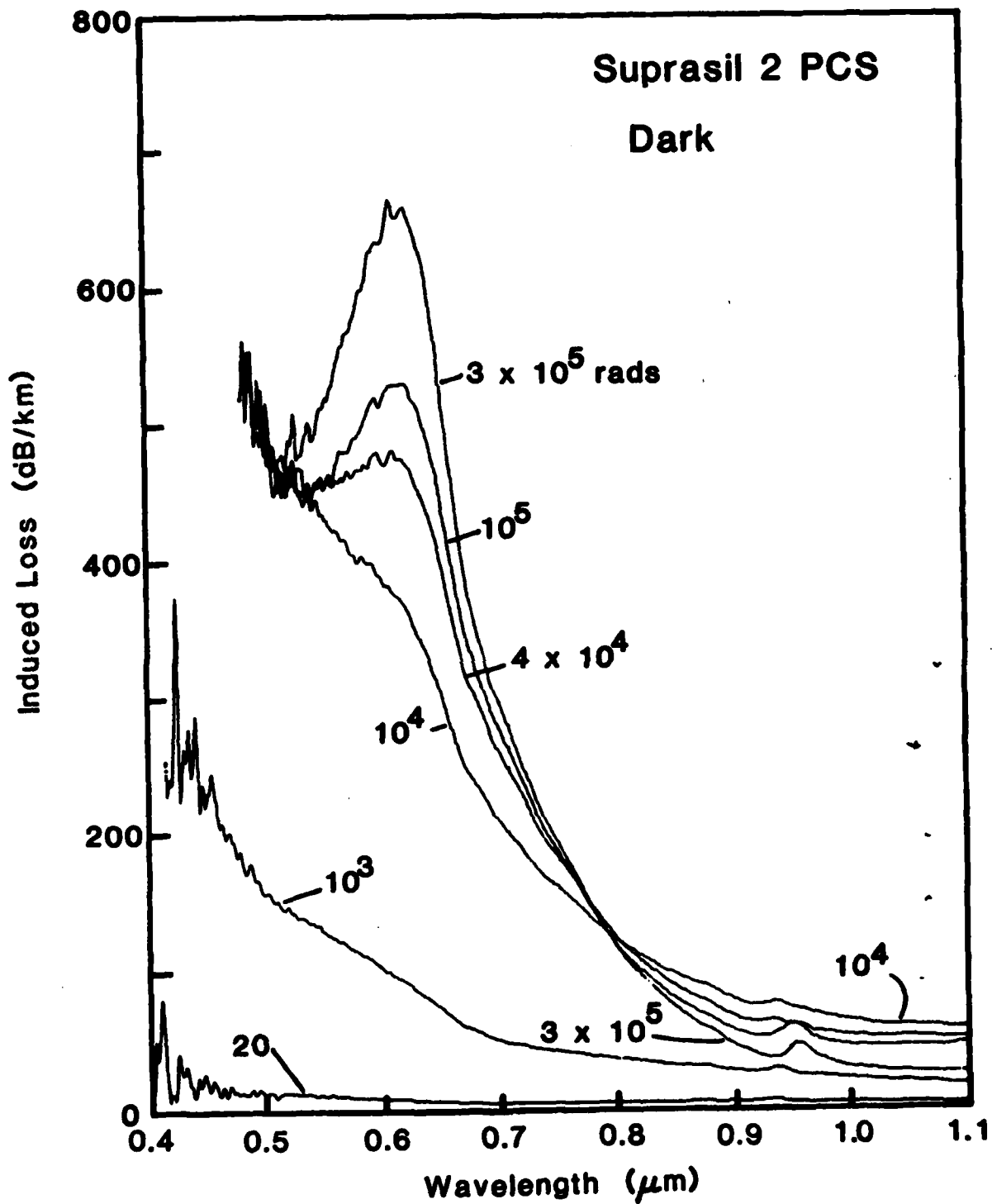
REFERENCES

1. For a recent review of radiation damage in optical fiber waveguides, see E. J. Friebele, Opt. Eng. 18, 552 (1979).
2. S. Share, R. M. McCracken and I. Aggarwal, IEEE Trans. Nucl. Sci. NS-25, 1288 (1978).
3. S. Share and J. Wasilik, IEEE Trans. Nucl. Sci. NS-26, 4802 (1979).
4. J. G. Titchmarsh, Electron. Lett. 15, 111 (1979).
5. E. J. Friebele and M. E. Gingerich, "Spectral Studies of Radiation Damage at Long Wavelengths in Optical Fiber Waveguides," Proc. DNA Symposium on Fiber Optics in the Nuclear Environment (1980).
6. E. J. Friebele and M. E. Gingerich, Proc. XII International Congress on Glass, Albuquerque, N.M. (1980), in press.
7. E. J. Friebele, R. E. Jaeger, G. H. Sigel, Jr., and M. E. Gingerich, Appl. Phys. Lett. 32, 95 (1978).
8. G. H. Sigel, Jr., E. J. Friebele, M. E. Gingerich and L. M. Hayden, Trans. Nucl. Sci. NS-26, 4796 (1979).
9. E. J. Friebele, P. C. Schultz and M. E. Gingerich, and L. M. Hayden, Optical Fiber Communication (Optical Society of America, Washington, D.C., 1979), p. 36; and E. J. Friebele, P. C. Schultz, and M. E. Gingerich, Appl. Opt., in press.

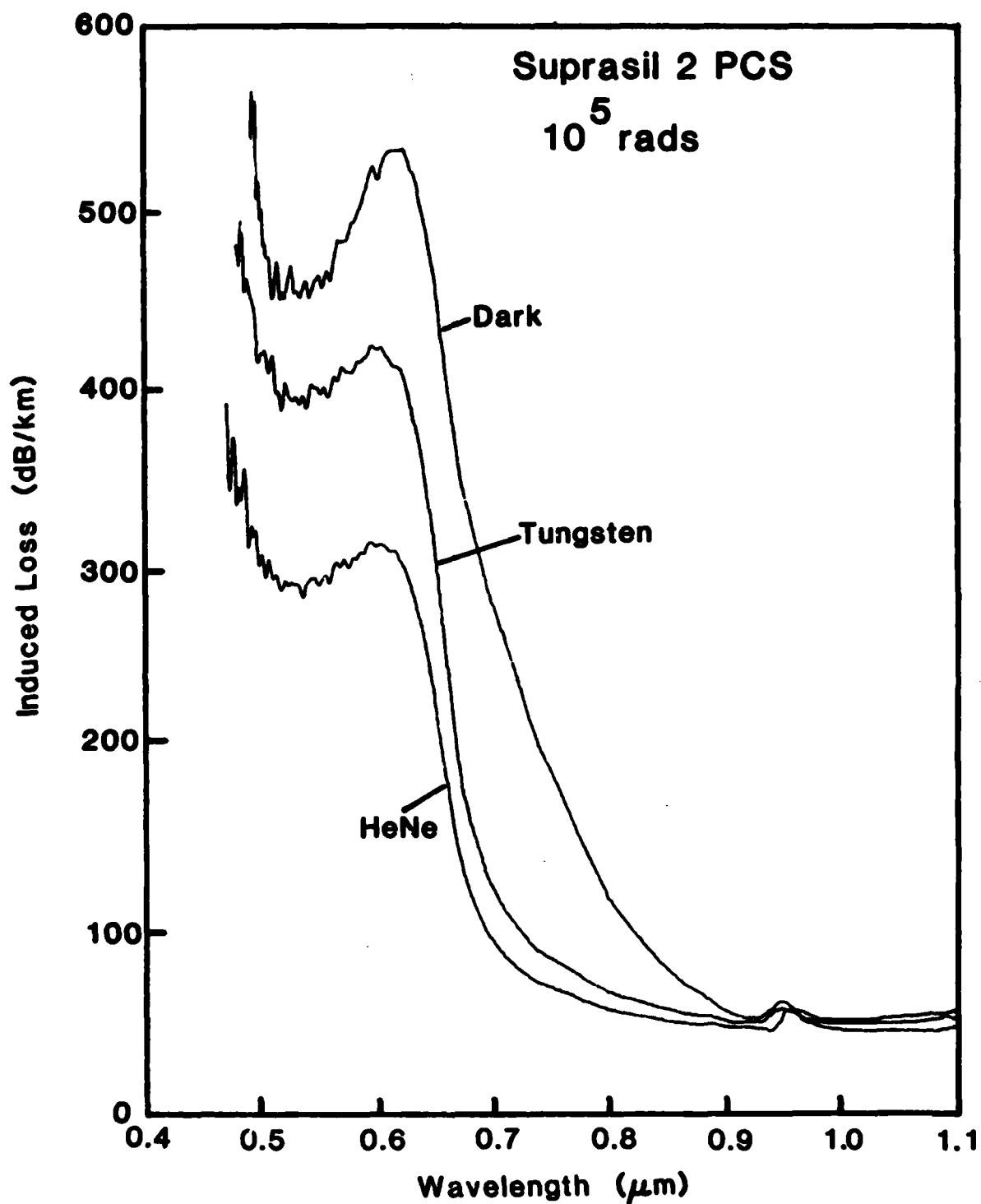
Table I

Percentage Reduction of the Radiation-Induced Attenuation at 0.8μ By Photobleaching With Tungsten Light, as Measured In Situ During Steady State ^{60}Co Irradiation.

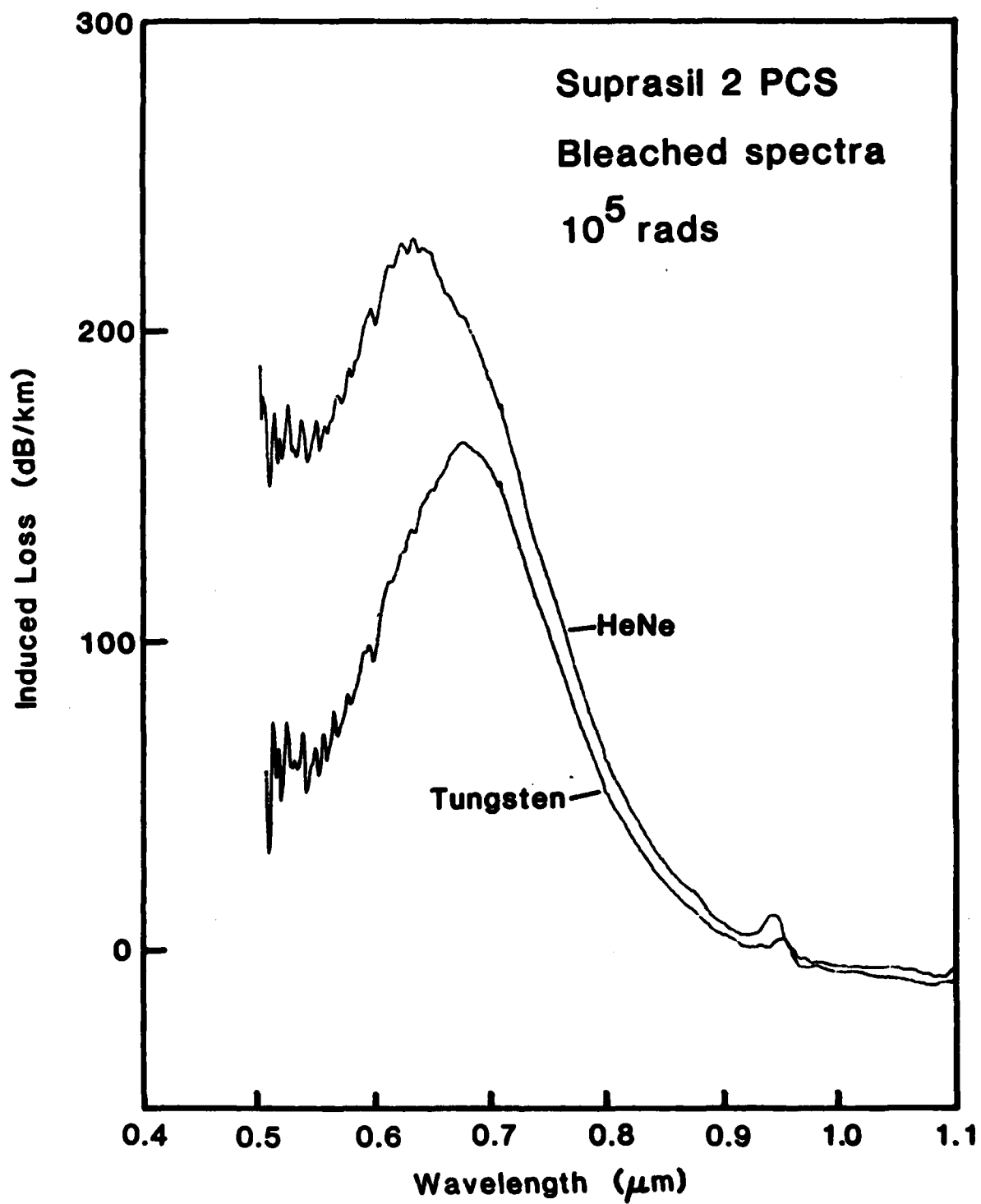
<u>Fiber Core</u>	<u>10^4 rads</u>	<u>10^5 rads</u>
Suprasil	27	39
Suprasil W	70	58
Ge-Doped Silica	44	39
Ge-2% P-Doped Silica	24	25



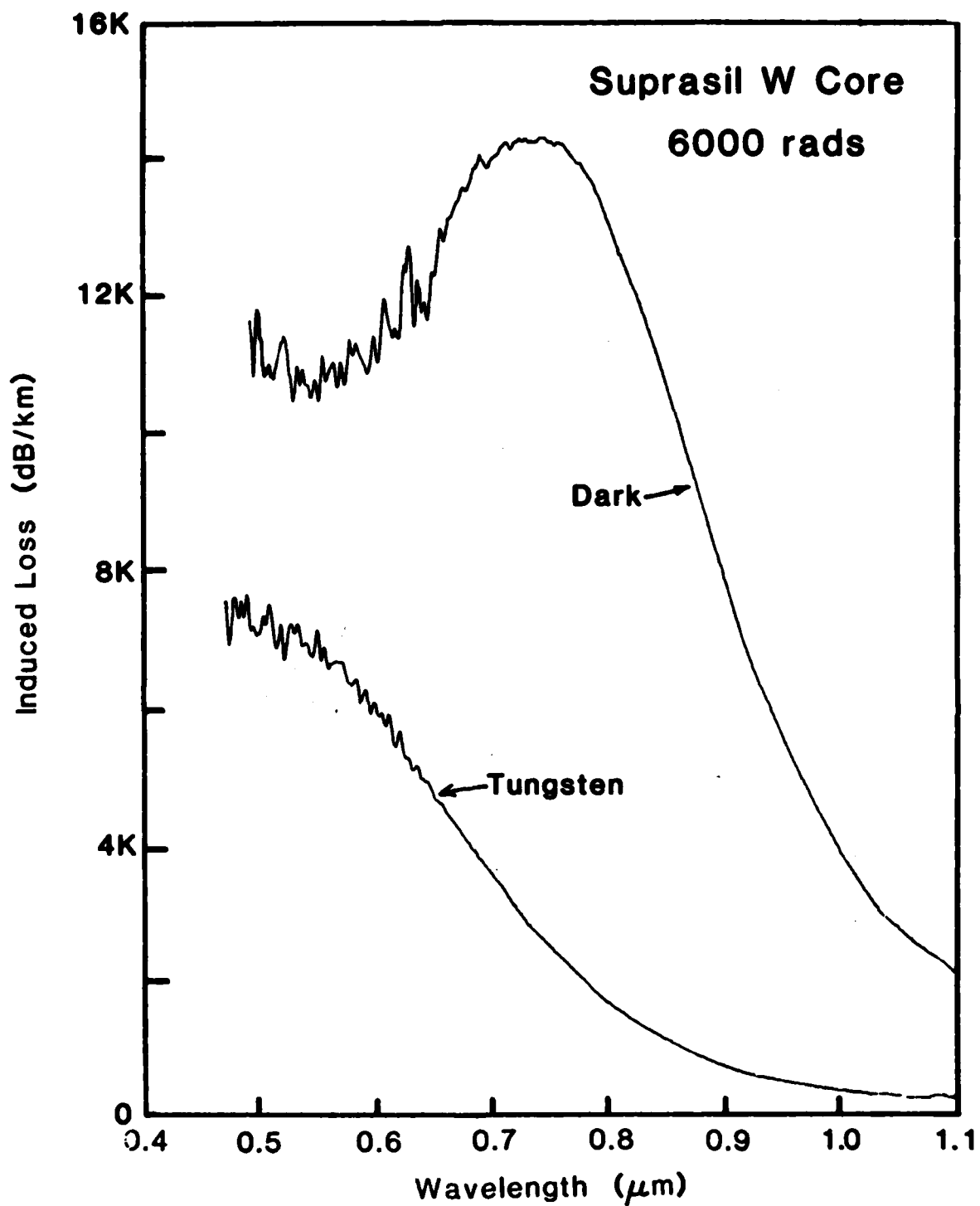
1. Radiation-induced optical absorption spectra of a high OH content silica core fiber measured during steady state irradiation with no bleaching light propagating in the fiber.



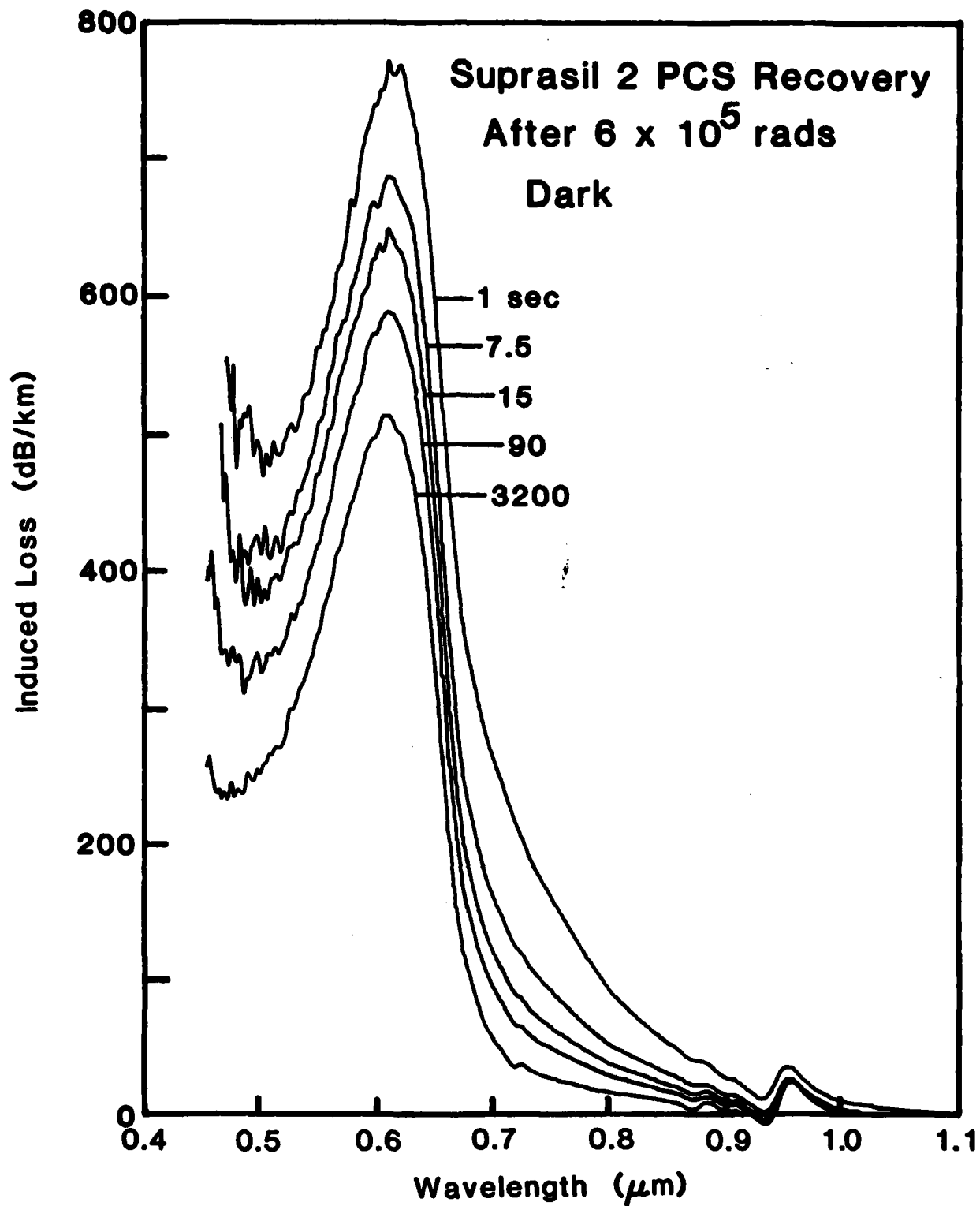
2. Comparison of the radiation-induced optical spectra of a high OH content silica core fiber measured during steady state irradiation without bleaching light and that measured with tungsten white light or 0.6328 μ light from a He-Ne laser propagating in the fiber.



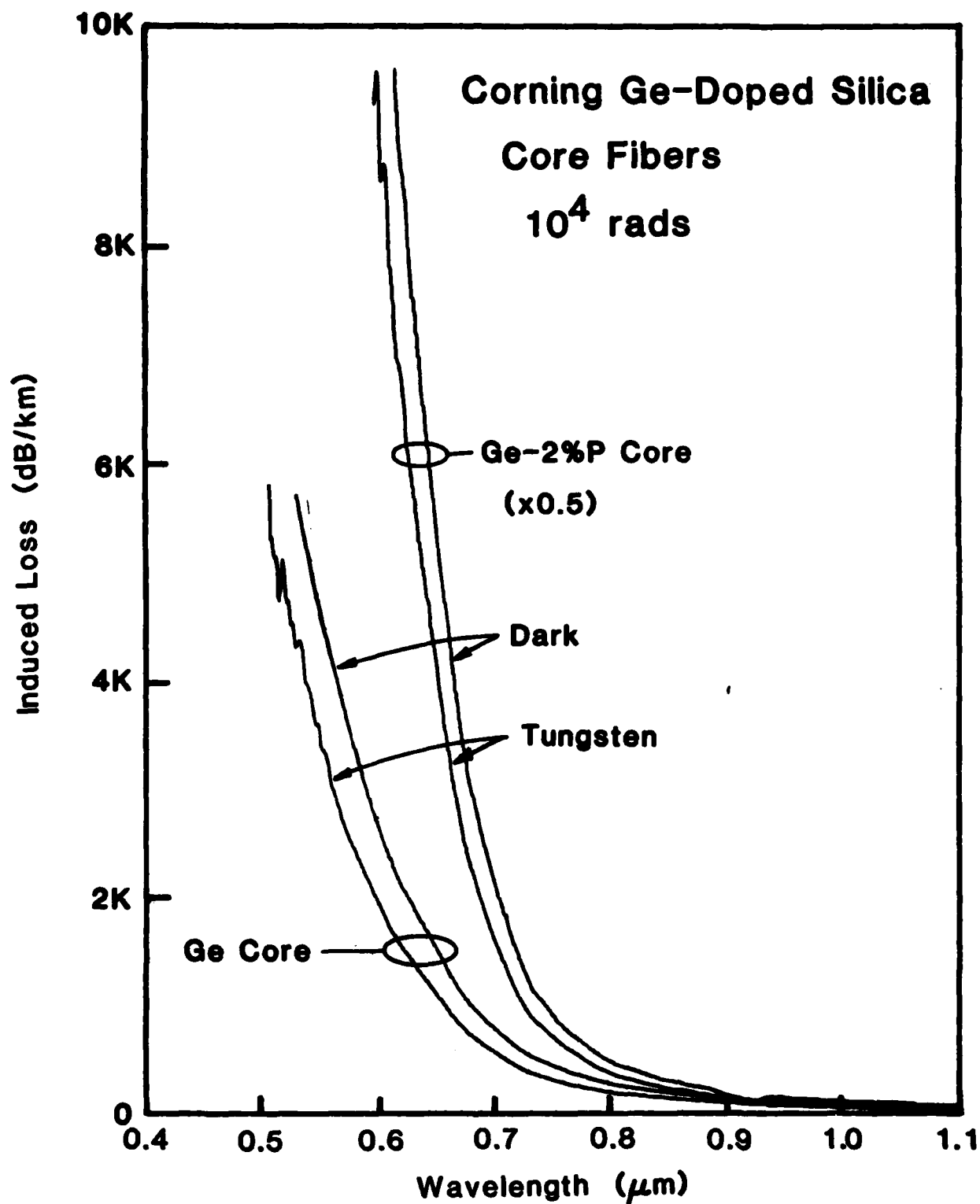
3. Spectra of the photobleached optical absorption bands of a high OH content silica core fiber.



4. Radiation-induced optical absorption spectra of a low OH content silica core fiber measured without bleaching light and with tungsten light propagating in the fiber.



5. Recovery of the radiation-induced optical absorption of a high OH content silica core fiber at room temperature without light propagating in the fiber.



6. Comparison of the radiation-induced optical absorption spectra of Ge-doped silica and Ge-2% P-doped silica core fibers measured during steady state ^{60}Co irradiation without bleaching light and with tungsten white light propagating in the fiber.

THIS PAGE IS INTENTIONALLY LEFT BLANK

Electron-Beam Induced Absorption and
Hardening in Fiber-Optic Waveguides
to 1060 nm Laser Pulses*

M. J. Landry and H. P. Davis
Sandia Laboratories
Electro-Optics Division Division 2152
Albuquerque, New Mexico 87185
(505) 264-8548

Abstract

For Corning Glass Work (CGW) and Valtec Corporation (VC) fiber-optic waveguides (FOWs), we have determined the coupling efficiencies (output/input energy) before (R_1) and after (R_2) electron-beam irradiation, the output energy density, the induced attenuation or loss (L_1) and its decrease as a function of time, and hardening as a function of number of Febetron shots (N_T). The FOWs were electron-beam irradiated with 8.3 to 12.3 J/cm² for a 2.36 to 2.84 x 10⁶ R (⁶⁰Co equivalent) dose. The output laser energy density varied from 0.19 to 2.12 kJ/cm² which was about 50 percent of the input surface threshold damage level previously measured in similar FOWs. The values of R_1 , 40.1 to 67.0 percent, were less than those previously measured. The induced attenuation (L_1) as a function of recovery time (after electron-beam irradiation) was linear on log-log plot for a short time ($<2.2 \times 10^{-4}$ s), changing from 1.8 to 0.2 dB/cm in slightly larger than a one order of magnitude change in time. The rate of recovery decreased with increasing time so that the total change in L_1 was about 3 orders of magnitude in 6 orders of magnitude change in time. A slight hardening (decrease in R_1/R_2) occurred in CGW fibers with an increasing number of Febetron electron pulses.

*Work supported by the Department of Energy and AFWL/ELP, P077-134.

I. INTRODUCTION

Fiber-optic waveguide (FOW) systems are being considered and used in many military and commercial applications because of inherent advantages over hardwire transmission links. These advantages include reduced susceptibility to EMP, better electrical isolation between circuits, lighter weight, larger bandwidth for multiplexing, and expected lower cost. One application under consideration includes transmitting through such fibers multimode free-running laser pulses¹⁻³ (400- μ s duration) containing high energy and power. It is a concern whether sufficient energy density ($>100 \text{ J/cm}^2$) can be transmitted through FOWs to perform a required function after the fibers are subjected to high electron-radiation doses ($>10^6 \text{ rad(Si)}$) at dose rates of greater than 10^{14} rad/s . Recent measurements have been made in FOWs of radiation-induced transient and permanent attenuation⁴⁻²⁰ caused by different levels of gamma,^{3-14,17-20} X-ray,^{8,15,16} electron,^{8-13,15-20} and neutron^{12,20} ionization radiations. With low-to-moderate optical energy, these attenuations were measured in fibers with fused silica,^{6,8,12,13,15-20} doped fused silica,^{6-10,12,14-20} glass,^{4-9,11,13,14,17,19} and plastic^{8,10,12,13,18,19} cores. One study³ used high laser energy densities after fibers were gamma-ray irradiated, but no similar measurements have been made after fibers were electron irradiated. Of concern is possible bleaching,¹⁶ radiation hardening,^{17,18} or increased residual damage in certain fibers when high laser energy interacts with the irradiated fibers.

II. EXPERIMENTAL SETUP

A. Mechanical and Optical

The mechanical and optical setup used in studying the radiation induced loss at high laser transmitted energy in FOWs is shown in Figure 1. The laser oscillator²¹ (OSC) and amplifier (AMP), the He-Ne laser, and associated mirrors used in aligning and directing the laser beams, and the beam sampling stations (STA) #1 and STA #2 were as illustrated and described in previous reports.^{3,22}

STA #1 and STA #2 sampled the OSC and AMP beams, respectively. The responses of the KDI photodiodes, D_1 and D_2 (manufactured by Hadron), were calibrated by energy meters EM_1 and EM_2 (manufactured by Quantronic), respectively. EM_3 measured the energy transmitted through the fiber. KDI photodiode D_3 responded to the temporal profile of the laser pulses after they passed through the fiber. The Reticon Arrays (RA) were used to determine the intensity profile of the laser beam in the directions orthogonal to its propagation direction. All mirrors, which reflected both the He-Ne and the Nd^{3+} laser beams, were coated for high reflectivity at both 632.8 and 1060 nm.

The lens (L), inside the screen room, was a Hadron trinocular viewing and focusing (HTVF) system. Its flip-flop mirror allowed easy alignment of the FOW to the laser beam.

Both the OSC and AMP were operated at only one high output level. Filter F₁ was used to attenuate the laser beam to the proper amplitude before it entered the fiber. Filter F₂ was added in the laser beam only during the alignment of the HTVF system.

Febetron

The Febetron, Model No. 706, its controlling electronics, gas bottles of purified air (A) and freon (F), the HTVF system, electron beam calorimeter, paper recorder, and the FOW being tested were all located inside a double-screened Faraday Screen Room. The specially modified Febetron was hung so that the output of Model No. 5515 Electron Tube pointed vertically downward. The HTVF system was secured onto the Electron Tube housing flange. The fibers were secured onto a kinematic-type mount, (for ease of removal and precise repositioning without realignment) which was also attached to the Electron Tube housing flange. This mount also held the electron beam calorimeter. Small holes in the walls of the screen room allowed the pulse laser beam in (hole diameter about 1 cm) and the FOWs out (hole diameter about 0.5 cm).

The Febetron delivered a 3 ns-duration electron pulse of up to 0.6 MeV. The integrated electron-beam energy (E_e) was measured with an aluminum calorimeter as defined in the Febetron operating manual dated 1969. Our Febetron system delivered an average of 2.7×10^6 R (^{60}Co equivalent) at 30 kV, an exposure rate of 9.0×10^{14} R/s, at a distance of 2.54 cm from the window of the Electron Tube. Thermoluminescent $\text{Li}_4\text{B}_4\text{O}_7$ crystals (TLD-800) were used to verify the dose. The FOWs absorbed $\approx 0.47 \times 10^6$ rad, which corresponds to an absorption rate of 1.57×10^{14} rad/s.

Details of the electrical connections and timing have been previously described.²² The signal to trigger the Febetron circuits was provided through the screen wall by an optical switch. This eliminated wires to the electronic units inside the screen room.

III. EXPERIMENTAL RESULTS

Free-running laser pulses were transmitted through FOWs manufactured by Corning Glass Works (CGW) and Valtec Corporation (VC).²³ Most of the results were obtained from CGW fibers whose 90 μm silica cores were doped with Ge and whose silica claddings were doped with boron. The VC fibers had pure $\sim 120\text{-}\mu\text{m}$ silica cores and plastic claddings. Measurements were made before, during, or after the fibers were irradiated with electrons.

Initially, only about 1 cm of the 30-cm-long FOW bundle, left in their jackets, was electron irradiated. The energy transmitted through the fibers was coupled to EM₃ or D₃ by a previously tested^{1,2,24,25} American Optical Co. (AOC) fiber bundle. Failure to detect induced attenuation led to irradiating longer, unshielded fibers. These fibers were held in a single flat-layer coil. Only approximately 1 cm of fiber length per turn was irradiated. The coil contained up to 50 turns for VC fibers and up to 70 turns for CGW

fibers. Repeated laser shots caused deterioration at the input end of the AOC coupling fiber. This led to its replacement and finally its removal from the system. The single unshielded output end of the FOWs was pulled through the screen room and their outputs were directed into EM₃ or D₃ (Figure 1).

Table I lists the specifics, results, and calculations pertaining to the FOWs tested. These include the number of turns of FOW exposed to electron irradiation (N_T), the electron-beam energy density (E_e) to FWHM of the beam, the laser energy density through the FOWs (E_1) obtained by dividing the energy transmitted through the FOW core by its area, the ratio of laser energy transmitted through the FOWs before (E_2) and during or after (E_2') the electron-beam irradiation compared to that of the laser energy incident onto the input face of the FOW before (E_1) and during or after (E_1') the electron-beam irradiation ($R_1 = E_2/E_1$ and $R_2 = E_2'/E_1'$), the ratio of R_2 to R_1 ($R_3 = R_2/R_1$), the induced loss caused by electron-beam irradiation (L_I), and the time between the center of the 400 μ s-duration laser pulse and the electron emission pulse (t). For a specific fiber, when the number of Febetron shots was greater than 1, the listing in Table I pertains to the first Febetron shot into the fiber. FN12 had 2, FN19 had 2, FN23 had 8, FN27 had 2, FN37 and FN38 had 5, and FN39 had 3 Febetron shots in them. The remaining FOWs received only 1 shot.

In determining L_I in the FOW, it was important that the laser pulse not change its beam characteristics, i.e., divergence, beam direction, and energy. The L_I values were determined from

$$L_I (\text{dB/cm}) = (10 \text{ Log } R_3) / n l \quad , \quad (1)$$

where n is the number of turns of fiber being electron irradiated over an effective length of $l = 0.92$ cm which is the FWHM of the electron-beam energy. Equation (1) becomes

$$L_I (\text{dB/cm}) = (10 \text{ Log } E_2' / E_2) / \ln \quad , \quad (2)$$

since $E_1 \approx E_1'$, $P_2' = E_2' / \tau$, $P_1 = E_1 / \tau$, and τ is the laser pulse duration of 400 μ s.

The spread in the electron-beam energy density E_e of 8.3 to 12.3 J/cm² resulted in a spread in the electron-beam power density ($E_e / 3 \times 10^{-9}$ s) of 2.7 to 4.1 GW/cm². The spread in laser energy density E_1 of 0.19 to 2.12 kJ/cm² resulted in a spread in the average laser power density ($E_1 / 4 \times 10^{-4}$ s) of 0.48 to 5.3 MW/cm².

TABLE I

SPECIFICS, RESULTS, AND CALCULATIONS FOR FIBER-OPTIC WAVEGUIDES

Fiber No.*	N _T	E _e (J/cm ²)	E ₁ (kJ/cm ²)	R ₁ (%)	R ₂ (%)	R ₃ (%)	L _I (dB/cm)	t (s)
FN11	51	10.0	.52	16.2	1.7	10.9	.21	2.2x10 ⁻⁴
FN12	12	10.6	.28	17.1	8.7	51.0	.26	2.2x10 ⁻⁴
FN13	12	8.9	.19	15.1	5.6	36.7	.39	2.2x10 ⁻⁴
FN18	13	9.9	1.22	51.2	26.6	46.1	.28	2.2x10 ⁻⁴
FN19	13	10.5	1.27	48.2	40.9	84.9	.059	2.2x10 ⁻⁴
FN20	13	11.2	1.31	48.0	39.0	81.2	.076	2.2x10 ⁻²
FN22	13	9.7	1.24	54.9	43.4	79.1	.085	2.2x10 ⁻⁴
FN23	13	10.3	.77	59.5	49.1	82.5	.070	.4x10 ⁻³
FN24	20	10.8	1.02	53.4	31.4	58.8	.130	2.2x10 ⁻⁴
FN25	20	11.2	1.56	57.8	48.2	83.3	.043	1.2x10 ⁻³
FN26	20	10.0	1.59	52.4	51.6	98.4	.0038	1
FN27	20	10.2	2.12	59.4	52.6	88.5	.029	7x10 ⁻⁴
FN28	20	9.9	1.95	48.0	46.8	97.5	.006	10 ⁻²
FN29	20	10.5	2.09	67.0	50.6	75.5	.066	2.2x10 ⁻⁴
FN30	20	9.9	2.09	59.0	50.0	84.7	.039	1.2x10 ⁻³
FN31	20	11.2	1.88	57.2	46.6	81.4	.049	1.2x10 ⁻³
FN32	20	10.5	1.67	55.4	45.7	82.4	.046	7x10 ⁻⁴
FN33	20	9.9	1.77	59.6	56.6	94.9	.012	10 ⁻²
FN37	70	9.2	1.04	40.1	37.6	93.8	.0043	300
FN38	20	10.9	.68	45.8	26.5	56.0	.14	2.2x10 ⁻⁴
FN39	20	10.6	1.21	--	--	--	--	--
FN40	20	12.2	.27	21.8	21.6	99.1	.0021	2.2x10 ⁻⁴
FN41	50	8.3	.69	55.4	53.7	96.7	.0074	2.2x10 ⁻⁴

*FN11 through FN39 are CGW FOWs, FN40 and 41 are VC FOWs

The largest laser energy density levels were about 50 percent less than the values which caused damage to similar CGW FOWs.¹⁻³ The values of R₁, the coupling efficiency, varied from 40.1 to 67.0 percent when the AOC transfer filter was not used. These values of

coupling efficiency are smaller* than those previously measured into similar CGW FOWs.¹⁻³ The smaller values of R_1 for FN11, FN12, and FN40 were due to the loss in coupling the test fiber to the AOC transfer fiber. R_2 and R_3 also depended upon N_T and t . For comparable values of t , R_2 and R_3 decreased with increase in N_T . For the same N_T , R_2 and R_3 increased with an increase in t .

The specific changes in induced losses (L_I) as a function of recovery time (t) for two sets of CGW FOWs are illustrated in Figure 2. Each data point represents the first Febetron shot followed by a laser shot in one FOW sample. One set covers only about 2 orders of magnitude of t , while the other covers 4 orders. The maximum change in L_I was ≈ 35 times.

For FN39, the induced losses (L_I) for values of recovery time (t) less than 2×10^{-4} s were estimated using detector D_3 instead of energy meter EM_3 (see Figure 1). The amplitudes of the individual laser spikes after the Febetron pulse were compared to the one laser spike amplitude before the Febetron pulse. Figure 3 shows that the induced loss (L_I) of CGW FN39 as a function of recovery time (t) is linear (within experimental error) on a log-log plot. The data were taken after the third electron pulse. (In this case, t is the time for emission of the specific laser spike in the laser emission pulse train being measured. The spread in the data is due to the statistical variation in the amplitude of the free-laser pulses.

Figure 4 illustrates the induced loss (L_I) as a function of recovery time (t) for the data in Table I, Figure 2, and Figure 3. For CGW fibers about 3 orders of magnitude changes in L_I were observed for 8 orders of magnitude changes in recovery time between 10^{-5} to 10^3 s for FN18-FN38. The largest L_I value measured was 1.83 dB/cm, and the smallest was 0.0021 dB/cm. The spread in L_I at $t = 2.2 \times 10^{-4}$ s was from 0.059 to 0.28 dB/cm. This spread is attributed to material variations in FOWs as previously suggested¹⁵ since for all test parameters equal the R_1 values in CGW FOWs varied only from 40 to 67 percent.)

The two VC-fused quartz core FOWs exhibited a change in L_I at $t = 2.2 \times 10^{-4}$ s of from 0.0021 to 0.0074 dB/cm or about 3.5 times. The average of L_I for the VC FOWs was at 0.0048 dB/cm, or an absorption coefficient about 35 times less than for the average of the CGW FOWs.

*The smaller values of R_1 for these CGW FOWs, than for similar FOWs tested previously, could have been caused by the different technique used to hold the input end of the FOWs and the position of the attenuation filters, F_2 .

The two VC FOWs exhibited a change in L_I of less than 1 order of magnitude for 7 orders of magnitude of t , starting at $t = 2.2 \times 10^{-4}$ s. Over the same time span, the CGW FOWs exhibited a greater than 2 orders of magnitude change in L_I . The reduced changes in L_I for fused quartz FOWs were expected and agree with previous measurements.^{8,13,15-20}

Figure 5 illustrates an apparent hardening effect which we observed in three doped CGW FOWs (FN23, 37, and 38), not observed in previous measurements.¹⁸ Hardening has been observed in pure silica (Suprasil 1) FOWs.¹⁷ The specifics for FOWs FN23, 37, and 38 are given in Table I with $N_T = 13, 70$, and 20 , and $E_1 =$ from 0.77 to 0.92 , 0.99 to 1.1 , and 0.58 to 0.68 kJ/cm², respectively. The different absolute value of R_3 for each FOW is time (t) dependent, the FOW with the largest value of t (the time between the Febetron and laser pulses) producing the largest value of R_3 or the smallest induced absorption loss. Each FOW experienced an increase in R_3 or a decrease in induced absorption loss for increased number of Febetron shots (N_F). The values of R_3 for FN23 and 38 were due to transient- and residual-induced absorption losses, while the values of R_3 for FN37 were due to residual-induced absorption losses.

For FN37 at $t = 5$ min, the value of R_3 is greater than 1.00 after the third Febetron shot, i.e., $R_2 > R_1$ or $E_2'/E_1' > E_2/E_1$. With $E_1' \approx E_1$ this implies that $E_2' > E_2$. This can occur if (1) the input or output surface losses of the FOW decreased, (2) the laser beam moved or increased in energy in such a way to increase R_2 and not R_1 , or (3) the intrinsic or inherent absorption loss in the FOW decreased. Both (1) and (2) could occur since the output laser energies E_2' and E_2 were measured for different laser shots. From previous data^{1,3,24} it is unlikely that the input or output surface losses of the FOWs decreased because the input laser energy density level, about 1.0 kJ/cm², caused surface cleaning. The laser did not increase in output energy in such a way as to increase R_2 and not R_1 , rather the output of the laser varied statistically. The value of R_1 changed a maximum of 3.6 percent for FN23, 2.9 percent for FN37, and 4.6 percent for FN38 when three laser shots were used in determining the average value of R_1 . R_1 was used in determining each value of R_3 in Figure 5 and Table I. The small variation in R_1 also indicates that the laser beam did not move in such a manner as to increase R_2 and R_1 .²⁴ A reduction in the intrinsic or inherent absorption could occur if the number of electron-ion pairs¹⁵ or free radicals producing the intrinsic absorption are disassociated by the electron-beam irradiation or its irradiation rate and caused a decrease in the number of pairs with an increased number of Febetron shots. More data are required before this last conjecture can be verified.

IV. CONCLUSION

The CGW and VC FOWs were irradiated with an electron beam containing from 8.3 to 12.2 J/cm² of energy density, corresponding from 2.36 to 2.84 x 10⁶ R (⁶⁰Co equivalent). The output laser energy density of 0.19 to 2.12 kJ/cm² incident onto the input end of the FOWs was about 50 percent below the damage level of similar FOWs previously tested.³ The values of R_I measured, from 40.1 to 67.0 percent, were less than those previously coupled in similar CGW FOWs.¹⁻³ For CGW FOWs, the induced absorption L_I values changed about 3 orders of magnitude in about 8 orders of magnitude of time (between 10⁻⁵ to 10³ s after the Febetron shot). For short delay times after electron irradiation, the L_I vs. t values resulted in a straight line on a log-log plot. Smaller changes in L_I were observed for VC fused-quartz core FOWs than for CGW FOWs at a lower average value of L_I. An apparent slight hardening effect was observed in CGW FOWs for both transient- and residual-induced absorption losses.

V. ACKNOWLEDGMENTS

The authors thank R. C. Hughes, P. M. Beeson, and G. E. Raybon for technical discussions pertaining to system operation of the Febetron system. We greatly appreciate the assistance of W. H. Buckalew, F. A. Hasenkamp, and especially that of D. J. Thompson in calibrating the electron emission from the Febetron. We also gratefully acknowledge technical discussions with Capt. Robert Dunn.

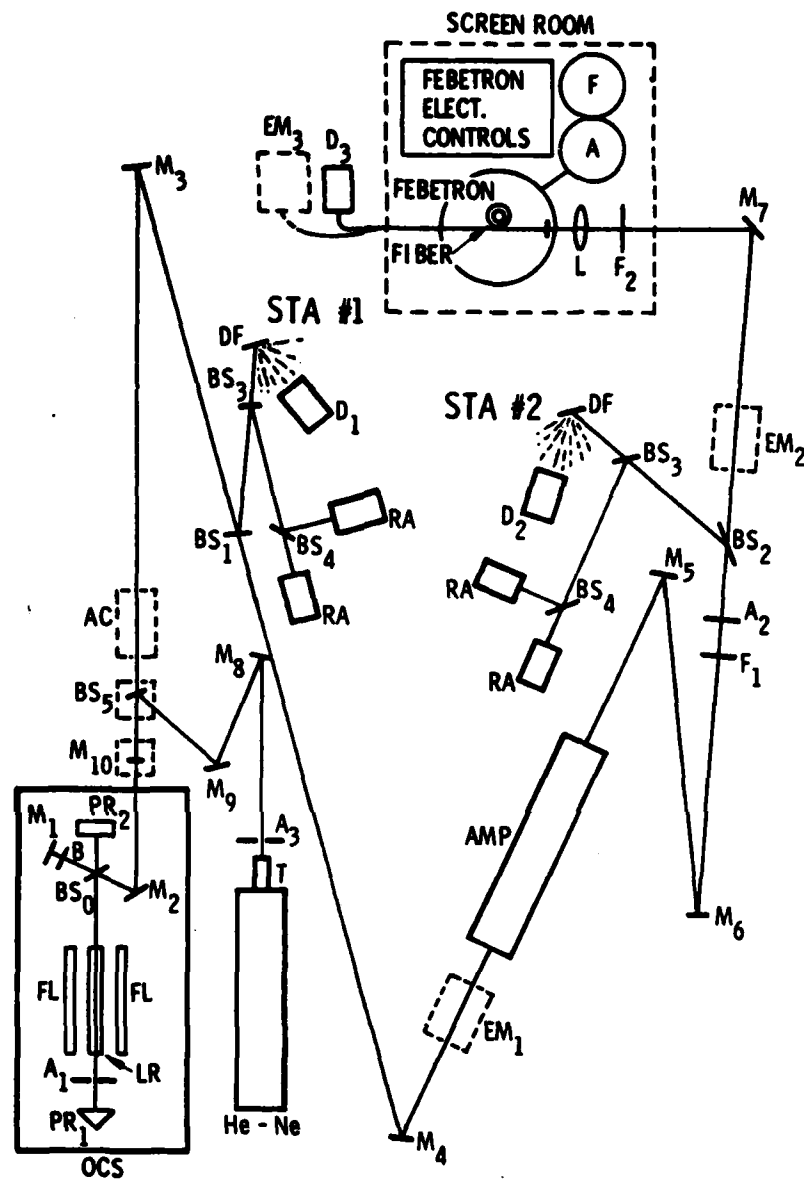
REFERENCES

1. M. J. Landry, "Large Giant and Free-Running Laser Pulse Energy and Power Densities through Optical Fibers," 4th ASTM Symp., Laser Induced Damage in Optical Materials, Ed. by A. J. Glass and A. H. Guenther, NBS Spec. Pub. No. 541, pp. 168-189, 1978.
2. M. J. Landry, "Large Laser Energy and Power Densities through Optical Fibers, 1978 Annual Mtg. of OSA., San Francisco, California.
3. M. J. Landry, "Transmission of Free-Running Laser Pulses of High Energy and Power Densities through Previously Gamma-Radiated Fiber Optic Waveguides," Sandia Laboratories, Albuquerque, New Mexico, SAND79-0411, 1979.
4. R. D. Maurer, E. J. Schiel, S. Kronenberg, and R. A. Lux, "Effects of Neutron- and Gamma-Radiation on Glass Optical Waveguides," Applied Optics, Vol. 12, pp. 2024-2026, 1973.

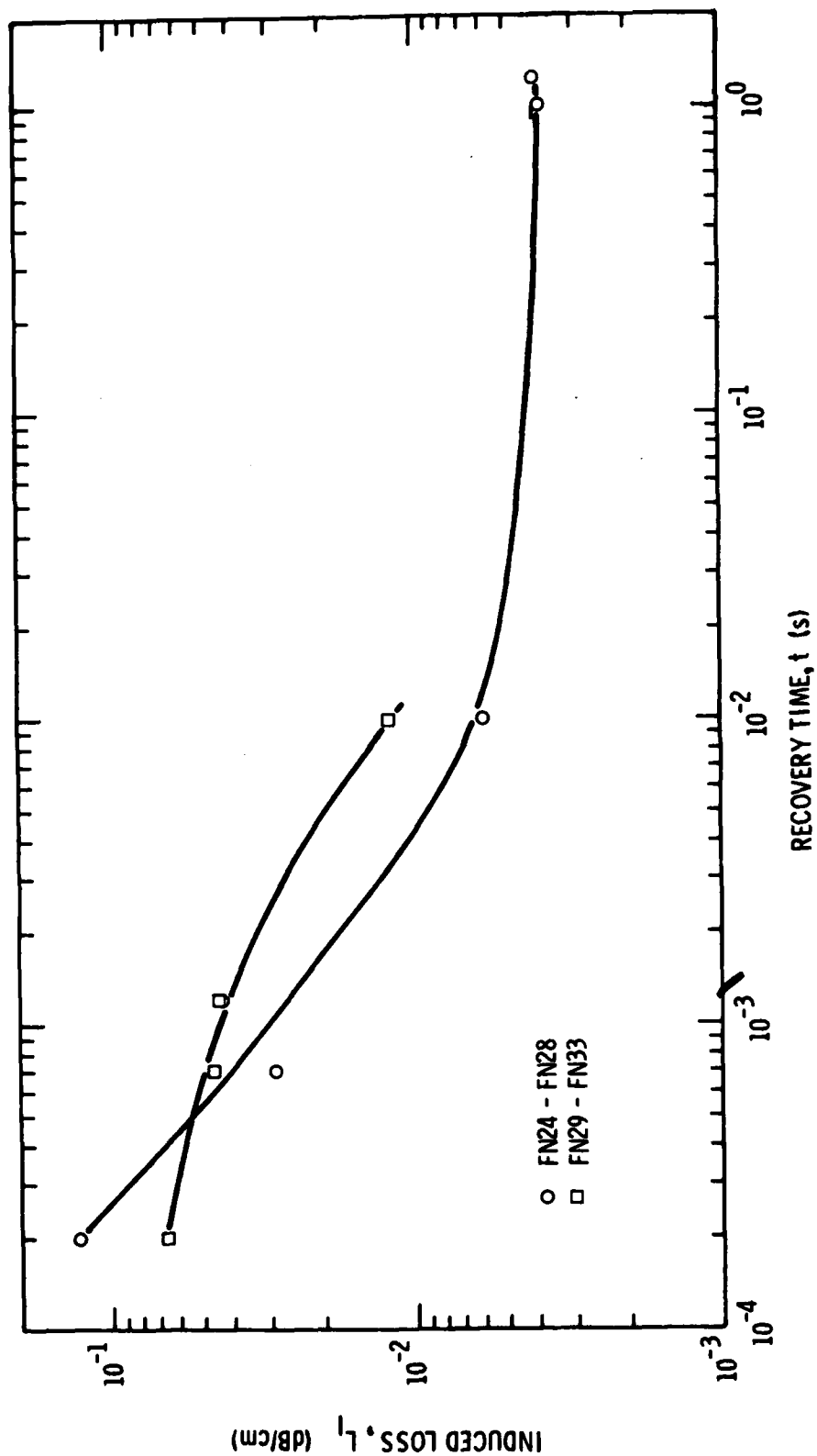
5. K. I. White, K. J. Beales, J. E. Midwinter, and G. R. News, "Radiation Effects on Absorption Losses in Some Optical Glasses," Opto-Electronic, Vol. 6, pp. 313-315, 1974.
6. E. J. Friebele, R. J. Genther, and G. H. Sigel, Jr., "Radiation Protection of Fiber Optics Materials: Effects of Oxidation and Reduction," Applied Physics Letters, Vol. 24, pp. 412-414, 1974.
7. G. H. Sigel, Jr. and B. D. Evans, "Effects of Ionizing Radiation on Transmission of Optical Fibers," Applied Physics Letters, Vol. 24, pp. 410-412, 1974.
8. P. L. Mattern, L. M. Watkins, C. D. Skoog, J. R. Brandon, and E. H. Barsis, "The Effects of Radiation on the Absorption and Luminescence of Fiber Optic Waveguides and Materials," IEEE Transactions on Nuclear Science, Vol. NS-21, pp. 81-95, 1974.
9. B. D. Evans and G. H. Sigels, Jr., "Permanent and Transient Radiation Induced Losses in Optical Fiber," IEEE Transaction on Nuclear Science, Vol. NS-21, pp. 113-118, 1974.
10. L. M. Watkins, "Absorption Induced in Fiber Waveguides by Low Dose-Rate Electron and Gamma Ray Radiation," Sandia Laboratories, Livermore, California, SAND75-8222, 1975.
11. E. J. Friebele, "Radiation Protection of Fiber Optic Material: Effect of Cerium Doping on the Radiation-Induced Absorption," Applied Physics Letters, Vol. 27, pp. 210-212, 1975.
12. P. L. Mattern, L. M. Watkins, C. D. Skoog, and E. H. Barsis, "Absorption Induced in Optical Waveguides by Pulsed Electrons as a Function of Temperature, Low Dose-Rate Gamma and Beta Rays, and 14 MeV Neutrons," IEEE Transactions on Nuclear Science, Vol. NS-22, pp. 2468-2474, 1975.
13. B. D. Evans and G. H. Sigel, Jr., "Radiation Resistant Fiber Optic Materials and Waveguides," IEEE Transactions on Nuclear Science, Vol. NS-22, pp. 2462-2467, 1975.
14. S. P. Faile, J. J. Schmidt, and D. M. Roy, "Irradiation Effects in Glasses: Suppression by Synthesis Under High-Pressure Hydrogen," Science, Vol. 156, pp. 1593-1594, 1967.
15. C. D. Skoog, "A Summary of Radiation-Induced Transient Absorption and Recovery in Fiber Optic Waveguides," Sandia Laboratories, Livermore, California, SAND76-8056, 1976.
16. J. E. Golob, P. B. Lyons and L. D. Looney, "Transient Radiation Effects in Low-Loss Optical Waveguides," IEEE Transactions on Nuclear Science, Vol. NS-24, pp. 2164-2168, 1977.

17. E. J. Friebele, R. E. Jaeger, G. H. Sigel, Jr., and M. E. Gingerich, "Effects of Ionizing Radiation on the Optical Attenuation in Polymer-Clad Silica Fiber Optic Waveguides," Applied Physics Letters, Vol. 32, pp. 95-97, 1978.
18. E. J. Friebele, M. E. Ginerich, and G. H. Sigel, Jr., "Effect of Ionizing Radiation on the Optical Attenuation in Doped Silica and Plastic Fiber-Optic Waveguides," Applied Physics Letters, Vol. 32, pp. 619-621, 1978.
19. E. J. Friebele, G. H. Sigel, Jr., and M. E. Gingerich, "Radiation Response of Fiber-Optic Waveguides in the 0.4 to 1.8 Region," IEEE Transactions on Nuclear Science, Vol. NS-25, pp. 1261-1266, 1978.
20. P. B. Lyons, L. D. Looney, J. Golob, R. Robichaud, R. Seno, J. Madrid, L. Hocker, and M. Nelson, "Neutron and Gamma-Induced Transient Effects in Optical Fibers," Conf. on Physics of Fiber Optics, University of Rhode Island, 1978.
21. M. J. Landry and H. P. Davis, "Characteristics of a Stable Pulse Laser Operating at 1060 nm in its Free-Running and Q-Switch Modes," Sandia Laboratories, Albuquerque, New Mexico, SAND79-1639, 1979.
22. M. J. Landry and H. P. Davis, "Electron-Beam Induced Absorption and Hardening in Film-Optic Waveguides to 1060 nm Laser Pulses," Sandia Laboratories, Albuquerque, New Mexico, SAND79-1208, 1979.
23. a. CGW fibers were Code No. 1452-1300 and Code No. 49-1003 OVPO with intrinsic attenuation of 3.7 dB/km at $\lambda = 820$ nm.
b. VC fibers were PC05 with intrinsic attenuation of < 40 dB/km at $\lambda = 820$ nm.
24. M. J. Landry, "Large Laser Energy and Power Transmitted through Optical Fibers," Sandia Laboratories, Albuquerque, New Mexico, SAND78-0602, 1978.
25. M. J. Landry, "Large Giant Laser Pulse Energy and Power Densities through Optical Fibers," International Conference on Laser '78, Orlando, Florida, 1978.

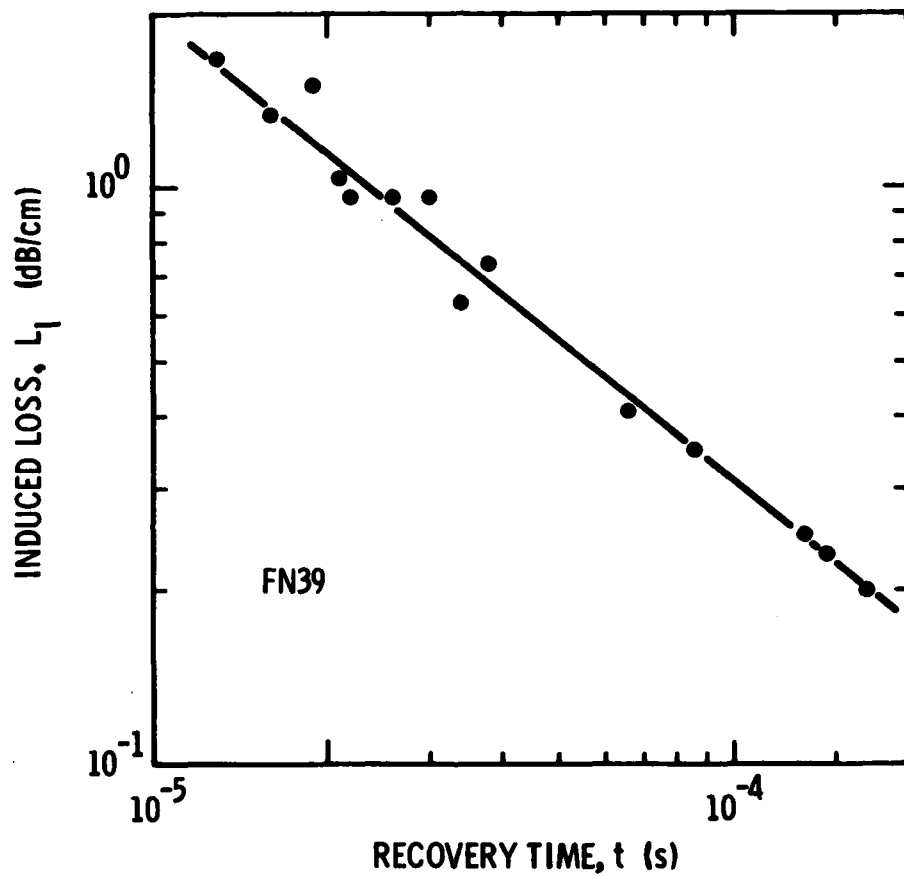
MJL:rcc:3665A:02/07/80



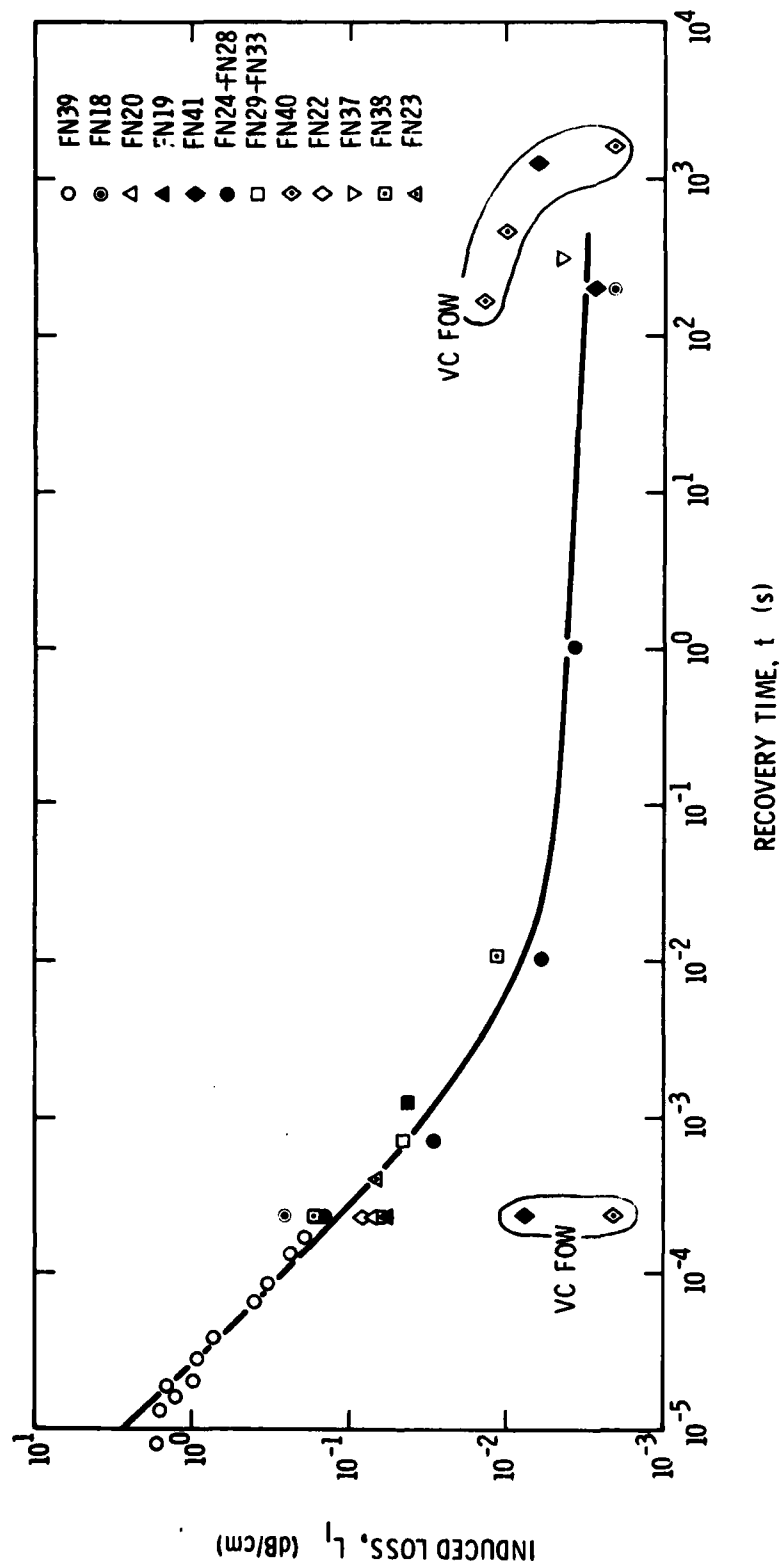
1. The mechanical and optical setup, used in studying the radiation-induced loss to high laser energy in fiber-optic waveguides, included these components: Nd^{3+} laser oscillator (OSC) and amplifier (AMP), energy meters (EM_1 , EM_2 , and EM_3), lens systems (L), auto-collimator (AC), fiber-optic waveguide (fiber), directing mirrors (M_3 , M_4 , M_5 , M_6 , M_7 , M_8 , M_9 , and M_{10}), beamsplitters (BS_1 , BS_2 , and BS_5), optical filters (F_1 and F_2), helium neon laser (He-Ne), restricting apertures (A_2 and A_3), Febetron, Febetron electronic controls, freon (F), and air (A). Each beam sampling section had two beamsplitters (BS_3 and BS_4), a diffuser (DF), a photodiode (D_1 or D_2), and two linear diode arrays (RA).



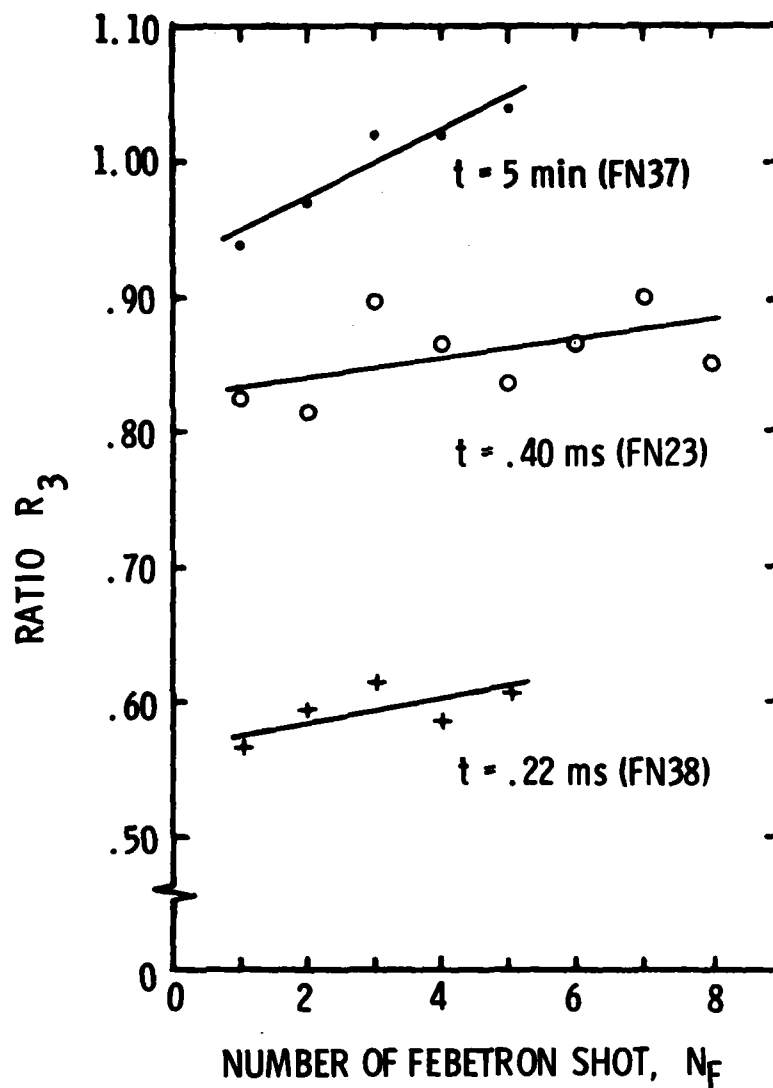
2. The changes in induced losses (L_I) in CGW FOWs are illustrated as a function of recovery time, t (s), for two sets of FOWs.



3. The induced losses (L_I) for CGW FOW FN39 are illustrated as a function of recovery time, t (s).



4. The induced losses (L_1) of the data in Table I, Figures 2 and 3 are plotted as function of recovery time, t (s), for CGW and VC FOWs.



5. The observed hardening effect of three CGW FOWs (FN23, 27, and 28) is illustrated in the change of the ratio $R_3 = R_2/R_1$ as a function of number of Febetron shots (N_F).

THIS PAGE IS INTENTIONALLY LEFT BLANK

CHARACTERIZATION OF LOW-LOSS MULTIMODE OPTICAL FIBERS
FOR NUCLEAR DIAGNOSTICS*

J.W. Ogle, M.A. Nelson, T.J. Davies, S. Lutz,
C-H. Lin, K. Theobald, L.A. Franks, and N.J. Norris
EG&G, Santa Barbara Operations

P.B. Lyons
Los Alamos Scientific Laboratory

ABSTRACT

The application of low loss multimode optical fibers to nuclear diagnostics has been discussed in previous papers.¹⁻³ Fiber requirements for this application differ substantially from those for normal communications use. The emphasis for nuclear measurements has been on development of high frequency analog fiber optic transmission line systems, which range from 100 MHz to >500 MHz signals transmitted at 600 nm and 800 nm, respectively. Accordingly, specialized fiber characterization procedures over a wide spectral range have been developed. These techniques include measurement of material and modal dispersion, optical attenuation, and optical linearity. It is also important to know the prompt radiation response of optical fibers in nuclear diagnostics. Measurements of this type have been discussed in previous papers.^{4, 5}

*This work was performed under the auspices of the U.S. Department of Energy under Contract No. DE-AC08-76NV01183. NOTE: By acceptance of this article, the publisher and/or recipient acknowledges the U.S. Government's right to retain a nonexclusive royalty-free license in and to any copyright covering this paper.

Reference to a company or product name does not imply approval or recommendation of the product by the U.S. Department of Energy to the exclusion of others that may be suitable.

CHARACTERIZATION OF LOW-LOSS MULTIMODE OPTICAL FIBERS FOR NUCLEAR DIAGNOSTICS*

J.W. Ogle, M.A. Nelson, T.J. Davies, S. Lutz,
C-H. Lin, K. Theobald, L.A. Franks, and N.J. Norris
EG&G, Santa Barbara Operations

P.B. Lyons
Los Alamos Scientific Laboratory

INTRODUCTION

Optical fiber recording systems developed for nuclear diagnostics emphasize high frequency analog transmission. Systems typically include a radiation-to-light converter, optical fiber transmission link, detector such as photomultiplier tube (PMT) or microchannel plate (MCP), and oscilloscopes. Past and present sources of radiation-induced light include broadband fluors⁶ that have maximum fiber-PMT systems sensitivity at 600 nm, and Cerenkov emitters with a maximum fiber-MCP detector system sensitivity at 800 nm. Another system utilizes a dye laser carrier that is emitting at 640 nm and is modulated by a radiation-driven optical modulator. The variety of wavelengths used, their unconventional spectral locations, and the frequency response required of the fibers have forced development of specialized characterization procedures.

Measurement of dispersion in a fiber is necessary for several reasons. Modal dispersion, for example, is the ultimate bandwidth-limiting property of a fiber. Material dispersion measurement is also necessary. A high bandwidth system utilizing a broadband light source must use optical filtration to minimize pulse broadening. The necessary filter characteristics are dictated by the degree of material dispersion and the system bandwidth specification. Further, it is necessary to know optical fiber transit times accurately for trimming and timing purposes. Transit times conventionally measured by optical time domain reflectometers are at 800 nm to 860 nm wavelengths, for instance, while transit times are longer at the shorter wavelengths of interest. We will describe techniques we have developed for evaluating dispersion.

With the variety of fibers presently available from different manufacturers, it is necessary to measure optical attenuation in a fiber for system design and,

*This work was performed under the auspices of the U.S. Department of Energy under Contract No. DE-AC08-76NV01183. NOTE: By acceptance of this article, the publisher and/or recipient acknowledges the U.S. Government's right to retain a nonexclusive royalty-free license in and to any copyright covering this paper.

Reference to a company or product name does not imply approval or recommendation of the product by the U.S. Department of Energy to the exclusion of others that may be suitable.

during system development and installation, to determine the best working wavelength and system losses. We will discuss two techniques for making attenuation measurements.

Systems using a modest-power dye laser to supply a light pulse for modulation must consider fiber linearity. Measurements of optical linearity have previously been reported.⁷ We will briefly describe the measurement system and results.

MODAL AND MATERIAL DISPERSION

Measurement of material and modal dispersion is developed around analysis of a spectrally broad 50-psec Cerenkov light pulse launched near one end of a test fiber. The light pulses are generated by the DOE/EG&G electron linear accelerator (linac) which delivers a 50-psec burst of electrons at energies to 27 MeV, current densities to 100 A/cm², and repetition rates to 360 pps. A schematic diagram of this system is presented in Figure 1.

After traversing the fiber, the emerging Cerenkov pulse is passed through selectable narrow band optical filters and detected either by a statically focused crossed-field PMT with a cooled InGaAsP photocathode or, in cases where more limited spectral range is tolerable, an MCP detector. The output is then fed to the remote head of a sampling oscilloscope and displayed. Resolution of the system (~250 psec) is sufficient in most cases to measure to the modal dispersion limit for fiber lengths of interest. Fibers as long as 1.2 km have been measured. In fibers which demonstrate a permanent induced radiation absorption, the Cerenkov pulse is generated in a short auxiliary radiation-resistant fiber, such as plastic clad silica (PCS), attached to the test fiber.

Manufacturers design fibers to have highest frequency response around available sources and detectors, usually between 800 and 900 nm where fibers are generally used commercially. The optimum index profile for high frequency response in a fiber at 900 nm is a poor index profile for a system operating at 600 nm. This is illustrated by measurements of modal dispersion made on the linac with the previously described system. The results are given in Figure 2. Measurements were made through three graded-index (GI) fibers 1 km long using a 1-nm-wide spectral filter and detected with an MCP detector. Only the material dispersion due to the filter spectral width has been unfolded. Full width at half maximum (FWHM) of the system response was 358 psec.

The figure shows the pronounced increase in pulse broadening that occurs at the shorter wavelengths for fibers optimized in index gradient for near-IR transmission.

Modal dispersion at 600 nm is also measured with a mode-locked argon ion-pumped dye laser. The dye pulse width is 3 psec and its spectral width is 1 nm. A Pockels cell gates out single pulses from the modelocked cw pulse train. The pulse is launched into the optical fiber and detected by an ITT 100-psec-response photodiode. The output is then fed to the remote head of a sampling oscilloscope and displayed. Resolution of the system through 1 km of fiber is limited by material dispersion to about 270 psec and through a short length is detector-limited to about 100 psec.

Material dispersion as a function of wavelength is measured by noting the arrival time of various pulses with different central wavelengths.⁸ Figure 3 is an example of an unfiltered Cerenkov/fiber/detector spectrum measured with the previously described linac system. The OH radical absorption bands at 725, 825, 875, and 950 nm are clearly demonstrated along with the nonlinear scale relationship between wavelengths and time due to material dispersion.

The material dispersion ($\Delta t/l\Delta\lambda$) is:

$$\frac{\Delta t}{l\Delta\lambda} = \frac{t\Delta ch}{l\Delta\lambda}$$

where

t = time per channel

Δch = number of channels between known wavelengths

$\Delta\lambda$ = difference between known wavelengths

l = fiber length

Theoretical dispersion curves have also been calculated.⁹ A three-element Sellmeier expression was employed using coefficients published by Fleming¹⁰ of Bell Laboratories. All Corning fibers we have measured agree with the curve for 4.1% GeO₂ in SiO₂. ITT fibers have shown an approach to that curve as time progressed (and the bandwidth increased), but they still have higher dispersion and a slightly different curve shape. The good fit of the Corning data to the theoretical curve perhaps indicates that the gradient of doping across the fiber is not enough to make a significant change in dispersion.

Our data are an excellent fit to a power law throughout our commonly used wavelength range of 839 to 570 nm, which results from arrival time measurements of Cerenkov light pulses with filters at 60 to 70 nm intervals between 540 and 877 nm. The detector sensitivity limited us to this region in this measurement.

Table 1 sets forth our best data set; i.e., the points fall on a smooth curve with almost no scatter.

The error introduced by use of the 60- or 70-nm wavelength interval is negligible for the theoretical curves.

D_{cal} is from the best fit power law:

$$D_{cal} \text{ (psec-nm}^{-1}\text{-km}^{-1}\text{)} = 2.194 \times 10^{12} \lambda^{-3.543}$$

T_{cal} is obtained from the integral times the length in km:

$$T_{cal} \text{ (nsec)} = 8.63 \times 10^8 \left(\frac{1}{\lambda_1^{2.543}} - \frac{1}{\lambda_2^{2.543}} \right) 0.578$$

It is not practical to get the power law from the arrival times directly because there is an additive constant, namely the transit time at 877 nm, which is imperfectly known.

Figure 4 compares Corning fiber with a high-dispersion ITT fiber. Between 630 and 840 nm the points for the ITT fiber lie on a power law curve that is very similar to that of $\text{SiO}_2 + 13.5\% \text{GeO}_2$, but the two points at 919 and 1010 nm are significantly below the values calculated, which are in turn below the power law derived from the shorter wavelengths.

A more recent Cerenkov light dispersion measurement was made on the linac in conjunction with Corning personnel. The fiber was a special type, and a Ge avalanche photodiode detector was used to extend the spectral range to 1500 nm. The dispersion data are shown in Figure 5 to describe the smooth dispersion curve anticipated for this fiber.

ATTENUATION

Two techniques for determining fiber attenuation have been developed and used. A fiber analyzer instrument of the time domain reflectometer type has been developed which provides a single wavelength determination of average attenuation in the region of 850 nm.¹¹ The analyzer uses an injection laser as a probe pulse source and utilizes the back-scattered light signature from the fiber for the attenuation measurement.

Another attenuation measurement employs a continuum dc optical source and an optical multichannel analyzer (OMA) that operates in the 250- to 880-nm region. The spectral difference in the light transmitted through two fiber lengths is obtained directly with the OMA. An example of fiber attenuation in two graded-index fibers and a PCS fiber over the region 620 nm to 880 nm is shown in Figure 6.

OPTICAL LINEARITY

A flash-lamp-pumped dye laser, having wavelength of 595 nm, linewidth of 0.6 nm, pulse duration of 2 μsec , and peak power of 50 kW, was employed to investigate nonlinear optical transmission due to stimulated Raman scattering generated in a 510-m-long Corning multimode step-index fiber.¹² The first-order forward and backward stimulated Stokes emissions appeared as the peak injected powers reached 1.3 kW and 1.8 kW, indicating a linear power transmission limit for this fiber of about 1 kW each. At a peak pump power of 16 kW, up to six orders of forward Stokes emission and four orders of backward Stokes emission were observed, and the input wavelength component was severely depleted except the leading and trailing edges. In contrast, all four orders of backward Stokes emission were observed simultaneously. They were temporally separated, higher-order pulses following lower-order ones, and were all considerably steepened. These data are shown in Figure 7.

A 10-psec pulse switched out from the same dye laser, which was passively modelocked, was also used to study the stimulated Raman scattering and self-phase modulation in a 19-m-long multimode graded-index fiber. A continuum of over 200 nm wide was observed, as shown in Figure 8.

SUMMARY

Systems for characterizing optical fibers over the spectral region from 500 to 1500 nm have been developed. There are ongoing efforts to improve these techniques.

ACKNOWLEDGMENT

Certain phases of this work were developed under EG&G's internally directed R&D program sponsored by the U.S. Department of Energy through the Nevada Operations Office under Contract No. DE-AC08-76NV01183.

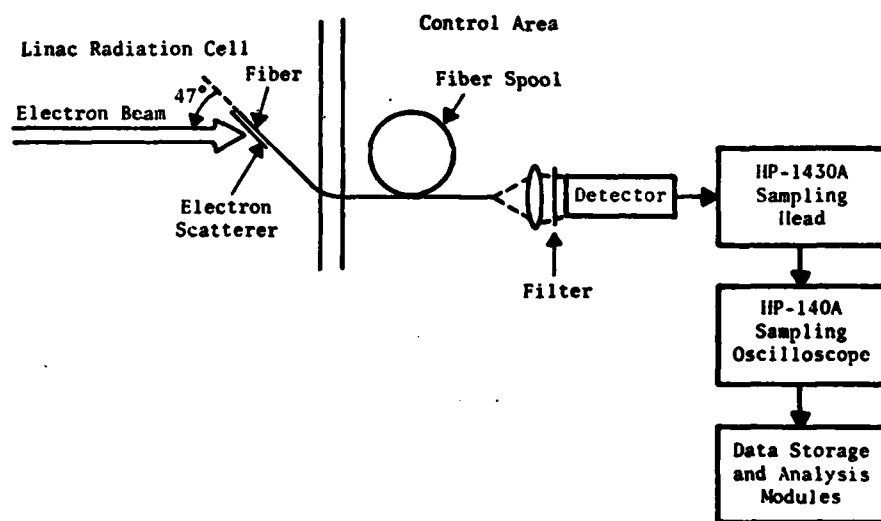
REFERENCES

1. Doyle, J.E., M.A. Nelson, T.J. Davies, and L.A. Franks, "Nuclear Radiation Measurements Using Cerenkov Light Generated in a Light Guide," *IEEE Trans. Nucl. Sci.*, NS-23, No. 1 (February 1976).
2. Golob, J.E., et al, "High Bandwidth Radiation Diagnostics With Scintillators and Fiber Optics," IEEE/OSA Conference on Laser and Electro-Optical Systems (CLEOS '78), San Diego, California (February 1978).
3. Lyons, P.B., et al, "Fiber Optics Utilization at the Nevada Test Site," Ninth Electro-Optical/Laser Conference (EOSD/LIA), Anaheim, California (October 1977).
4. Lyons, P.B., L.D. Looney, J.E. Golob, and R.E. Kelly, "Short Term Radiation Effects in Optical Fibers," in *Optical Fiber Communication Technical Digest* (IEEE, Washington, D.C.) (March 6-8, 1979).
5. Zagarino, P., et al, "Radiation Response Measurements of Fibers in the Picosecond Region," DNA Symposium on Fiber Optics in the Nuclear Environment (March 1980).
6. Lyons, P.B., L.D. Looney, S. Lutz, and M.A. Nelson, "Fiber Optic Application in Plasma Diagnostics," Conference on Optics, 1979.
7. Nelson, M.A., C-H. Lin, J.A. Ogle, and K. Theobald, "Fiber Optics Studies," Research and Development, FY78 Final Report, DOE Contract No. EY-76-C-08-1183 (December 1978).
8. Franks, L.A., M.A. Nelson, and T.J. Davies, "Cerenkov Pulse Dispersion in Two Low-Loss Fibers," *Appl. Phys. Lett.*, 27, No. 4 (August 1975).
9. Wemple, S.H., "Material Dispersion in Optical Fibers," *Applied Optics*, 18, No. 1 (January 1979).
10. Fleming, J.W., *J. Amer. Ceramic Society*, 59, No. 11, 12 (1976).

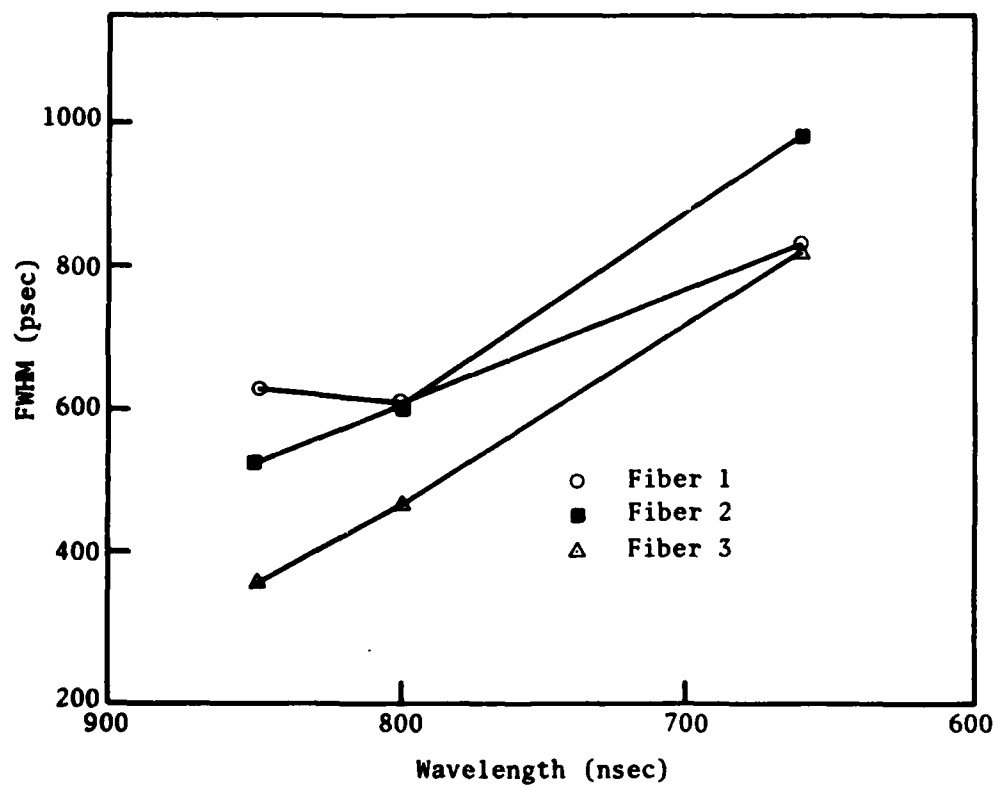
11. Nelson, M.A., et al, "A Fiber Optic Time Domain Reflectometer," Proceedings SPIE Vol. 139, *Guided Wave Optical Systems and Devices* (1978).
12. Lin, C-H., et al, "Forward and Backward Stimulated Raman Scattering in a Multimode Fiber," *Fiber Optics, Advances in Research and Development*, Plenum Publishing Company, New York, New York (1979).

Table 1. Bare Corning #30525103 578 m, 81.49 psec/channel

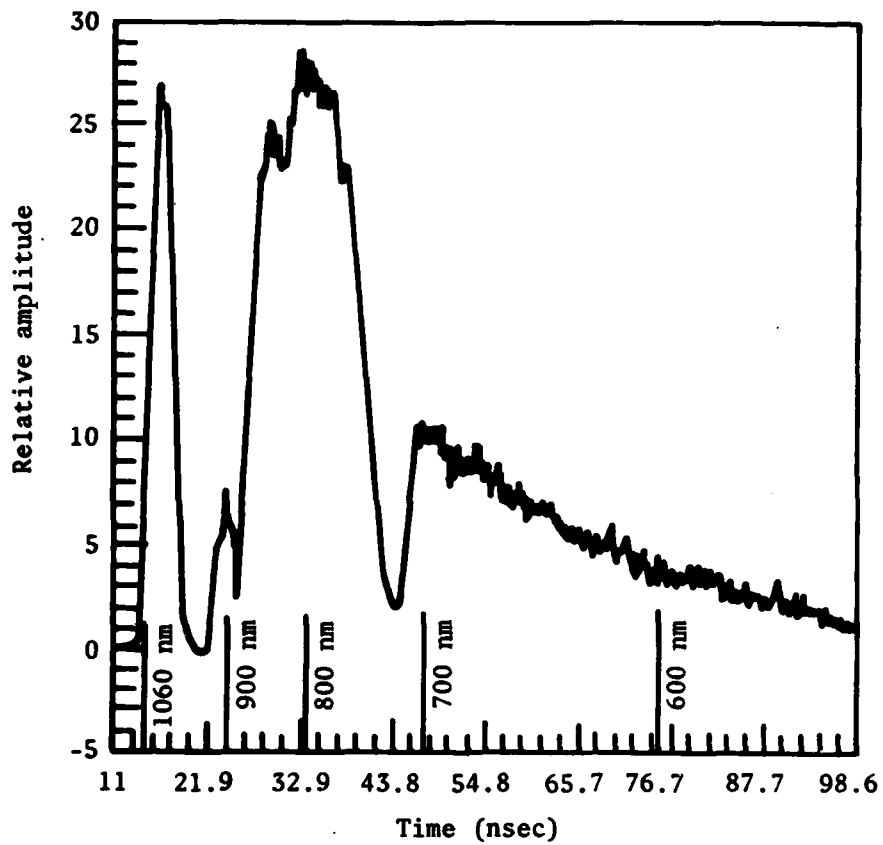
λ (nm)	Channel	D_m (psec-nm ⁻¹ -km ⁻¹)	D_{cal} (psec-nm ⁻¹ -km ⁻¹)	T_m (nsec)	T_{cal} (nsec)
877	220			--	--
839		96	96		
801	272			4.24	4.25
766		135	133		
730	340			9.78	9.76
695		185	188		
660	432			17.28	17.40
630		265	266		
600	545			26.48	26.67
570		381	379		
540	707			39.69	39.91



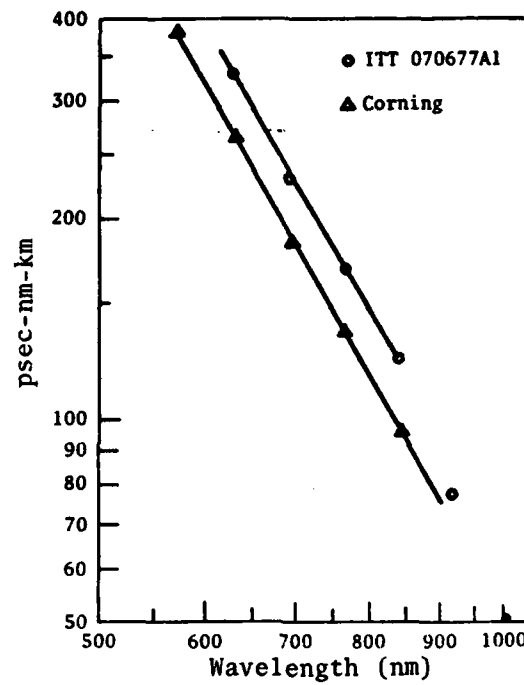
1. Experimental setup for measurement of modal and material dispersion in optical fibers.



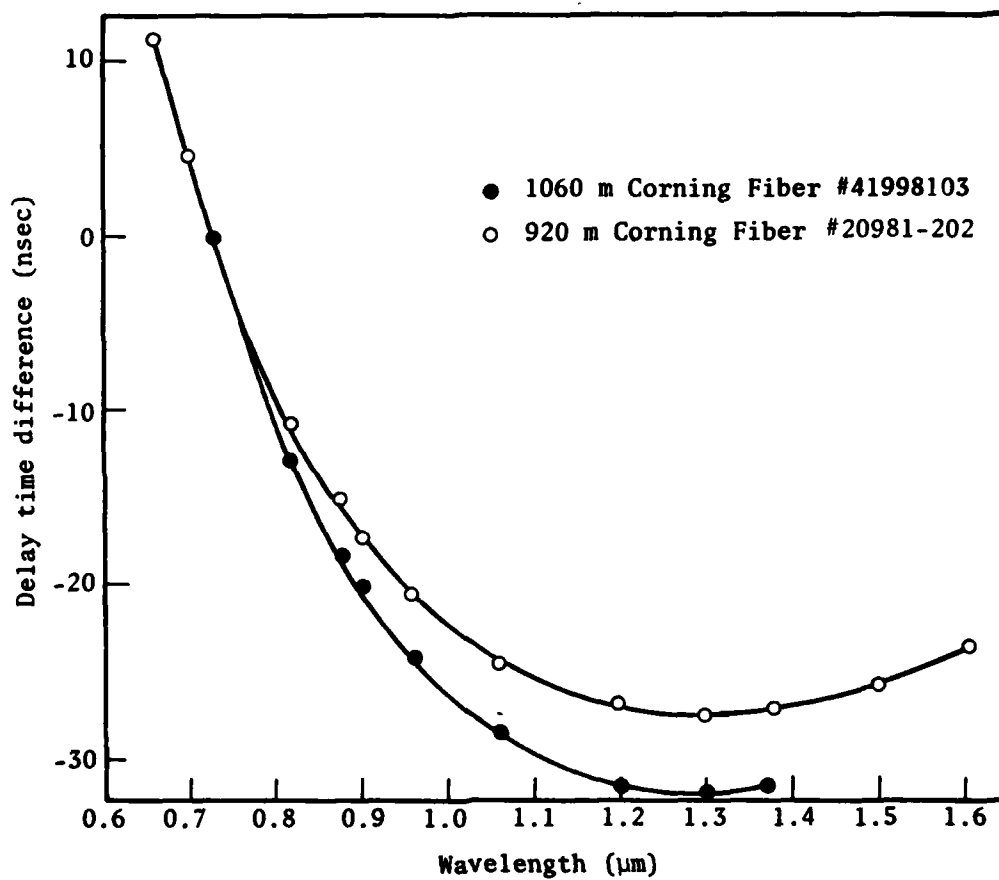
2. Modal dispersion measurements for three fibers.



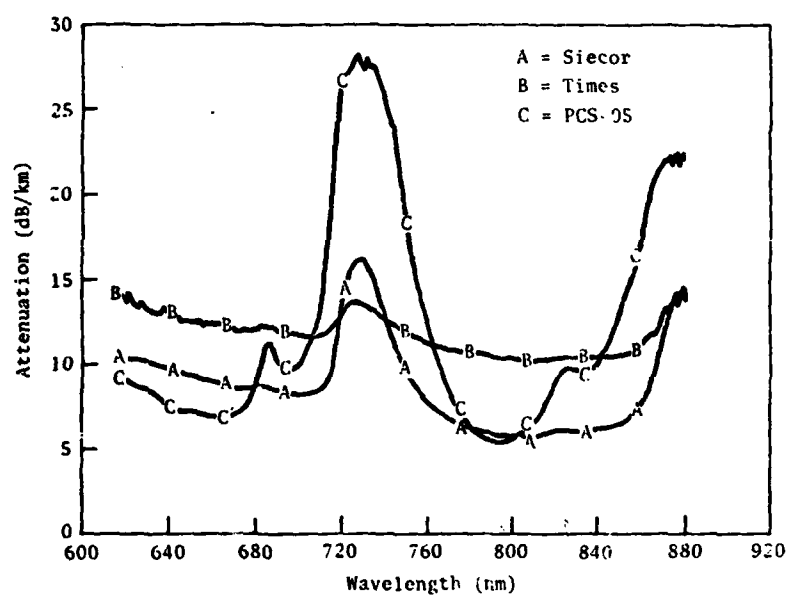
3. Broadband Cerenkov spectrum through 1 km of fiber recorded with a cross-field PMT.



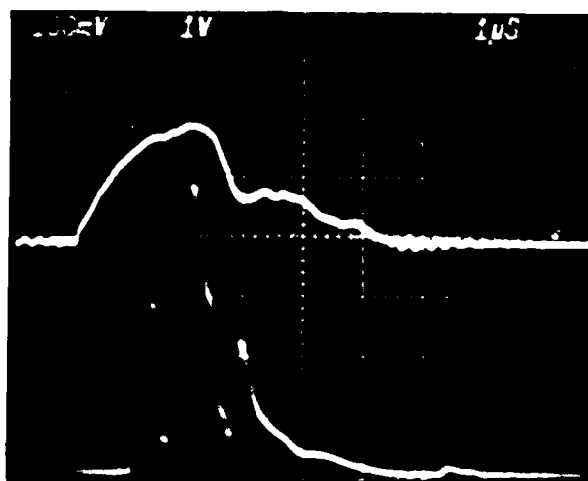
4. Comparison of material dispersion characteristic between Corning and ITT graded index fiber.



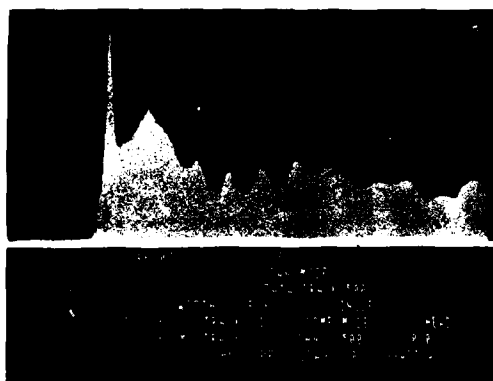
5. Transmission delay versus wavelength for two special Corning fibers.



6. Sample of attenuation in one PCS and two graded-index fibers.



7. Backward stimulated Raman scattering generated by a flashlamp pumped dye laser pulse in 510-m-long multimode step-index fiber at a peak injected power of 15 kW. Top trace: Fresnel reflection of the incident laser pulse from the entrance surface of the fiber; bottom trace: backward stimulated Raman scattering. Three pulses generated successively are first-, second-, and third-order Stokes emission, respectively.



8. OMA display of continuum generated by a picosecond modelocked dye laser pulse in a 19-m-long multimode graded-index fiber. Resolution of OMA is 0.55 nm/channel, and total coverage is 500 channels.

RADIATION DEGRADATION AND RECOVERY IN LONG FIBER OPTICS DATA LINKS

I. Arimura and R. S. Caldwell
Boeing Aerospace Company
Seattle, Washington 98124

INTRODUCTION

Ground-based, point-to-point communication links are susceptible to numerous radiation effects problems resulting from nuclear weapons bursts. Even if the receiving and transmitting terminals are located in a well shielded area, conventional cables can be destroyed by the large currents induced by the EMP from a nuclear burst unless extensive shielding techniques are utilized (which is not practical, in general, for long cables). All dielectric fiber-optic data links are immune to EMP effects and thus offer the possibility of being a low-cost substitute for conventional cables. However, long fiber-optic links suffer substantial performance degradation from gamma rays and neutrons resulting from nuclear bursts. Existing data on radiation-induced darkening of long optical fibers indicates that communication blackout might occur for seconds, minutes, and even hours (or longer) after nuclear exposure of most high-quality optical fibers. This large uncertainty in response can prevent the practical implementation of long fiber-optic data links for applications where radiation environments are of concern.

In order to determine the primary failure mechanisms, a prototype 2-km-long baseline fiber-optic data link was "designed" for analysis purposes. A link budget analysis was carried out for a point-to-point base-band analog fiber-optic link typical of ground-based communication requirements. Only off-the-shelf components were chosen for this analysis. The system was composed of a 0.82- μm LED emitter having an available output of -1 dBm, a 6-dB/km step index low-loss fiber, and a Si avalanche photodiode (APD) with a responsivity of 50 amps/watt and a noise equivalent power (NEP) of 10^{-12} W/(Hz)^{1/2}. The link length was assumed to be 2 km with one hard splice (0.5 dB loss) at 1 km. An input coupling loss at 19 dB, and an output loss of 1 dB were assumed. In addition, an allowance for temperature and temporal degradation was included at 3 dB each. For each case then a total link loss of 38.5 dB was used. By comparing the link loss with available receiver sensitivity data for each channel bandwidth (SNR 30 dB), a corresponding link margin was estimated.

The components selected for the baseline link consisted of a GaAs LED, a 2-km long Corning low-loss (B) step-index fiber, and a Si APD detector. A review of available transient absorption data on Corning low-loss fibers indicated that link transmission is degraded at doses on the order of several thousand rads to such a degree that "downtimes" on the order of hundreds and even thousands of seconds are likely for long link applications. These results are summarized in table 1.

TABLE 1
BASELINE FIBER OPTIC DATA LINK

<u>FREQ.</u>	<u>LINK MARGIN</u>	<u>DOWNTIME (5000 rads)</u>
6 MHz	7 dB	2.3 Hours
30 kHz	34	324 Seconds
10 kHz	37	290 Seconds

The results of the baseline link analysis indicated that different fiber materials and/or operating conditions were desirable for a hardened FO data link. A review of available literature indicated that the radiation-induced transient absorption is improved anywhere from a factor of two to more than ten by operating at a wavelength of 1.06 μm instead of 0.82 to 0.85 μm .

This analysis also indicated that fiber absorption losses on the order of 5 to 20 dB/km were of primary interest for long-link applications and that there were few available radiation test data in this region. A candidate hardened FO data link was proposed based on 1.06- μm operation, pure-fused silica core fibers, and silicon avalanche photodiode detector.

Two candidate pure-fused silica fibers were selected (a third became unavailable due to special holder requirements for radiation testing), the ITT PS-05-20 and Quartz Product QSF-A-200 low loss, polymer-clad, pure-silica fibers.

The only commercially available 1.06- μm LED with fiber pigtail attached is the Plessey GAL-103 InGaAs LED with Corning low-loss fiber pigtail attached. Four units were purchased to allow the construction of two fiber links and have two LED's available for radiation degradation tests.

An RCA silicon avalanche photodiode (C30817) with optimized response out to 1.06 μm was selected as the detector. Both temperature regulation and temperature compensation techniques were developed to compensate or eliminate the large Si APD response variations with temperature.

A complete single-fiber, one-direction link was then constructed using the Amphenol 905-906 series SMA fiber-optic connectors. The configuration is shown in figure 1 which also includes two jacketed fibers as intermediate coupling fibers to the 1-km-long unjacketed fibers which constitute the main long-link fiber.

TRANSIENT ABSORPTION TESTS

Low-dose transient absorption tests were performed on 1-km lengths of fibers of each type. Long fibers were selected to avoid the uncertainties inherent in the testing of short lengths at low absorption levels or at elevated doses and attempting to extrapolate the results to long-length/low-dose applications. Most data available in the literature are for optical fibers typically a few tens of meters in length. Even with a

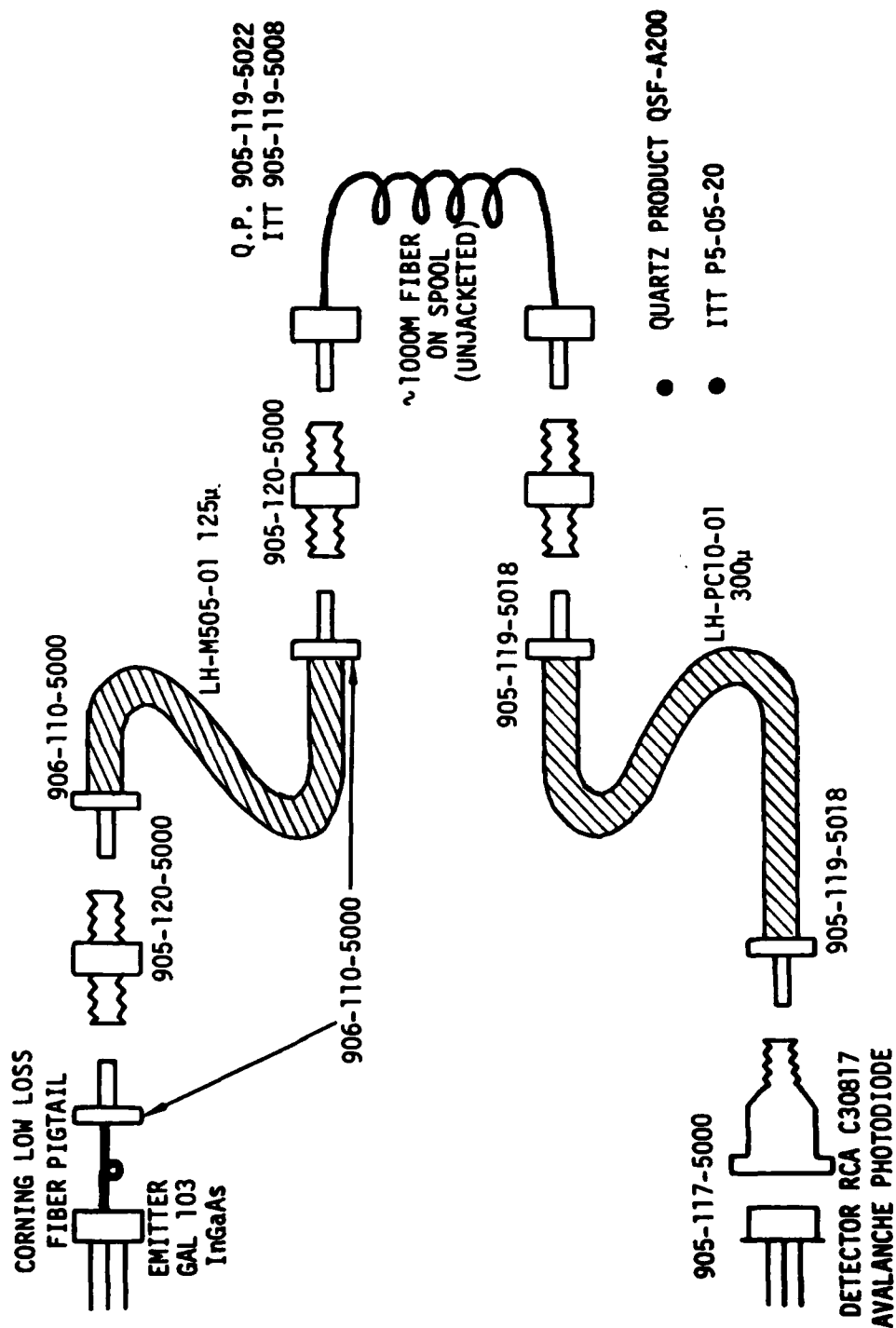


Figure 1. Fiber Optic Link for Testing Long PCS Fibers

reasonably well designed experiment (i.e., entrance and exit ends mode-stripped, input power monitored, etc.), the uncertainty can easily be on the order of 10 dB/km. Also, since many fiber materials (including some PCS fibers) display nonlinear dose dependence of absorption, extrapolation to lower doses (and probably higher, as well) can be very misleading.

Transient absorption tests were performed using the link configuration shown in figure 1 using the Boeing Radiation Effects Laboratory FX-75 flash x-ray. Exposures were performed using an x-ray energy spectrum peaked at about ~ 2 MeV. The 30-meter jacketed fibers were shielded with lead and used to connect to the 1-km unjacketed test fibers. A 10-kHz analog signal was used to monitor the transient absorption.

The results of these low dose tests are shown in figure 2 where the normalized transient induced absorption is shown as a function of time following the ~ 50 -ns x-ray burst. The transient absorption at early times was sufficiently large that no measurable signal could be observed for some time after the burst (one problem with using long fibers). The recovery for both these PCS fibers, even though complete, extends out to very long times—even out to hours for the ITT fiber. These data, when compared to previous test data on similar fibers using shorter lengths and higher doses, display significantly longer recovery times particularly in the 1- to 10-dB/km induced-absorption range.¹

STEADY-STATE IRRADIATION TESTS

A measurement of the transient absorption following a short radiation pulse basically characterizes the damage introduction rate and recovery behavior of the induced damage. Because of the complex recovery kinetics displayed by both fiber types, these results, even if completely done, would require a complex unfolding to predict the induced absorption in a long pulse, low dose rate environment. Thus, these transient absorption tests were accompanied by low dose rate, steady-state irradiations using a ^{60}Co gamma cell to aid in interpreting the long pulse fiber degradation.

A 300-m long portion of the previously tested ITT 1-km long fiber (which had completely recovered its preirradiation transmission after its 600 rad dose) was inserted into the BREL Gamma Cell 220 ^{60}Co source and the transmission monitored continuously. The dose rate of this ^{60}Co source is ~ 226 rad(Si)/sec. The transmission dropped immediately upon exposure. However, after approximately 15 seconds, the transmission reached a minimum loss of ~ 10 dB and started to improve with continued irradiation. After several minutes of exposure, the induced loss reached a steady-state value of ~ 2 dB and continued irradiation did not further darken the fiber. Upon removal from the radiation source, the induced loss completely recovered in times on the order of an hour or so. A subsequent second irradiation also displayed the "peaking" effect observed in the first irradiation—however, the magnitude of the peak was much lower. These results are shown in figure 3. Similar results were obtained for a 300-meter long, QSF-A-200 fiber. However the peak transient absorption was only about half as large as the ITT fibers. Similar results of this type of radiation degradation behavior have been reported previously by Maklad, et al.¹ and others.²

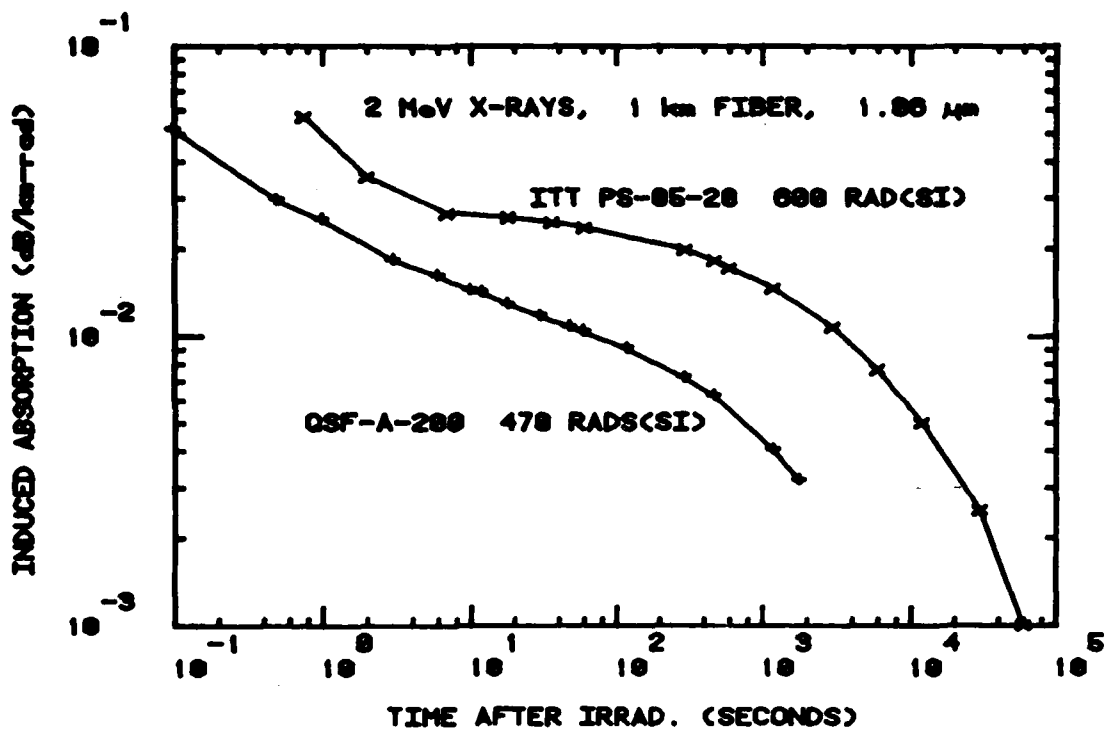


Figure 2. Recovery in Radiation-Induced Absorption for 1-km Long PCS Fibers

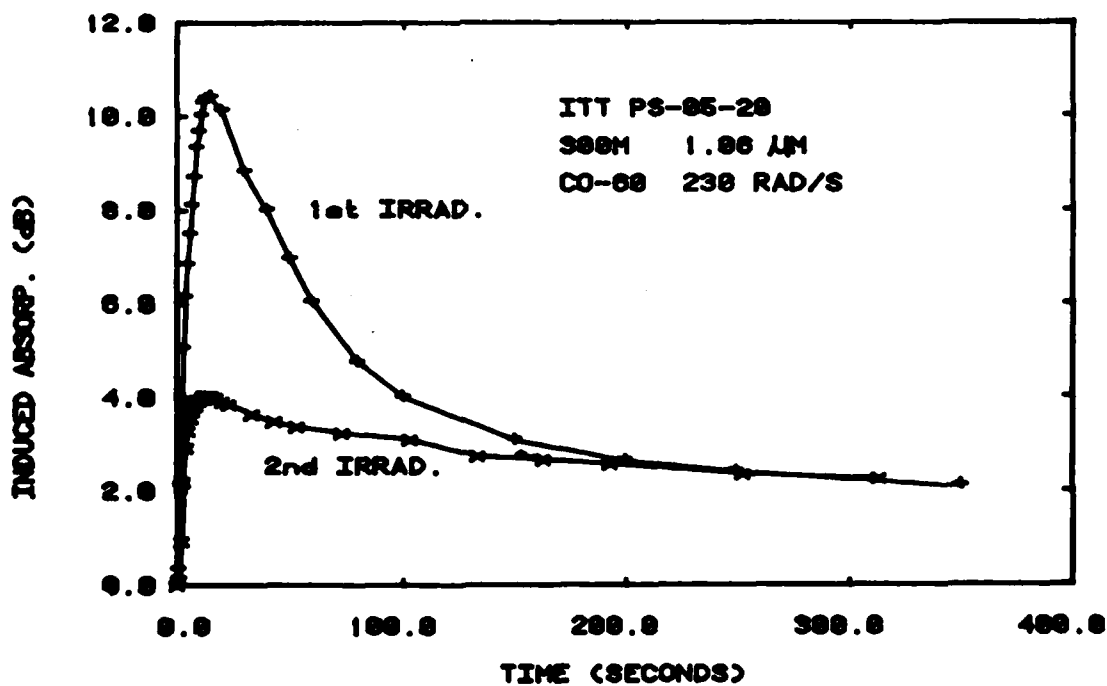


Figure 3. Radiation-Induced Absorption in PCS Fiber for Steady-State ^{60}Co Irradiations

NEUTRON IRRADIATION TESTS

In general, fast neutrons will cause darkening of fibers primarily by the accompanying total ionizing dose, either through direct neutron ionization (which is generally negligible) or through secondary buildup. This "additional" dose is generally quite small and/or is included in the normal dose environment specification. The principal degradation effects from fast neutrons will be on the transmitter and receiver, rather than the fibers. This is due to the degradation of the signal-to-noise performance of PIN and APD detectors and LED power emission (in addition to degradation of the conventional electronics).

Very few data are available on neutron effects for LED's operating at wavelengths $>1 \mu\text{m}$. One sample of the Plessey GAL-103 LED was irradiated at the Sandia Fast Burst Reactor (SPR-II) and measurements of the $1.06\text{-}\mu\text{m}$ power emission made a few days after each exposure. The relative power emission was not degraded significantly up to a fluence of nearly 10^{14} n/cm^2 (1-MeV eq.) as shown by the data points in figure 4. Also shown for comparison purposes is a summary of data taken on Si-doped GaAs LED's.³ Though these results are limited, it appears that the relative power emission for longer wavelength LED's is less sensitive to neutron damage. Note that this may be partly due to the lower initial power emission of the $1.06\text{-}\mu\text{m}$ LED—such results have been common even for shorter wavelength LED's.⁴

DISCUSSION OF LINK PERFORMANCE

It is clear from the radiation tests performed on the two PCS fibers selected that the original goal of a factor of two to ten greater radiation hardness was not achieved. Instead it turned out that the reduced link margin in operating at $1.06 \mu\text{m}$ and the longer recovery time of the two PCS fibers resulted in reduced hardness by anywhere from a factor of five to ten. This was primarily the result of a long slow recovery in the radiation-induced absorption observed for both PCS fibers—this "tail" in the recovery differs significantly from previous results on similar fibers.

Operation at $1.06 \mu\text{m}$ only decreased the link margin slightly more than 2 dB since the NEP is more like $5 \times 10^{-14} \text{ W/Hz}^{1/2}$ at the longer wavelength. This partially compensates for the lower power emission of the $1.06\text{-}\mu\text{m}$ LED selected. Table 2 below is an estimate of the system downtime for a 2-km, ground link operating at $1.06 \mu\text{m}$.

TABLE 2
PERFORMANCE OF $1.06\text{-}\mu\text{m}$ LINK

<u>FREQ.</u>	<u>LINK MARGIN</u>	<u>DOWNTIME*</u>
6 MHz	5 dB	$2.5 \times 10^4 \text{ s}$
30 kHz	32	10^3 s
10 kHz	35	$\sim 10^3 \text{ s}$

*At dose of 1000 rad(Si) for ITT fiber.

In applications where radiation exposure occurs over a longer time interval, the peak transient absorption of both PCS fibers tested for long link applications depended upon the dose rate, reaching a maximum value of ~ 5 to 30 dB/km at doses of 5000 to 10,000 rad(Si). Thus for applications where the dose rates are less than ~ 200 rad/sec, the Quartz Product fiber was adequate for low-bandwidth operation.

OPTICAL BLEACHING

The long recovery times present a significant problem in the use of PCS fibers for long-link applications even where relatively low radiation levels are involved. One possible technique for enhancing the recovery rate of fiber darkening is to substantially increase the power launched into the fiber during the period immediately following the radiation-induced darkening. This would potentially accomplish improvements in two ways: (1) to increase the received power above the noise level and (2) to optically bleach the fiber damage.

Optical bleaching has been shown to substantially reduce the absorption of neutron and gamma irradiated fused silica and quartz.⁵ Mitchell and Paige⁵ found optical bleaching of an absorption band at 5.7 eV (C-band) in quartz when illuminated with light of that energy. The entire absorption spectrum out to 1000 nm bleached uniformly for γ -irradiated quartz while early time bleaching occurred primarily for the C-band in neutron-irradiated quartz.

Experiments were carried out to determine if light could be used to bleach out the long-lived damage in irradiated fibers. A 0.5-meter section of a 5-meter long, Dupont PFX-S120 PCS fiber was irradiated to 120,000 rad(Si) and the transmission monitored with continuous and interrupted light injection. A clear dependence of recovery rate is obvious as shown by the results in figure 5.

This same fiber continued to display optical bleaching after a four-month storage as shown by the results in figure 6. The transmission started increasing immediately upon launching light into the fiber and continued to increase until the LED was turned off (except for the brief ~ 10 -second measurement time). During the period where the LED was off, recovery essentially halted and the power transmission even dropped slightly as shown by the portions labeled "off". The transmission immediately started to recover upon initiation of LED emission and continued to recover until reaching a saturated value after approximately 10^5 seconds of exposure. A dark period of approximately 10^5 seconds resulted in only a slight drop in transmission.

The question arises of whether the high doses used to darken the 0.5-meter portion of the 5-meter-long fiber results in only a small fraction of the damage being optically bleachable. An additional 5000 rad ^{60}Co irradiation was performed on the entire 5-meter fiber and the transmission again monitored with and without optical power applied. The recovery closely follows the behavior observed for the heavily irradiated fiber as shown in figure 7. Since no optical power was injected into the fiber during the irradiation, the "peak" absorption was not observed and the fiber

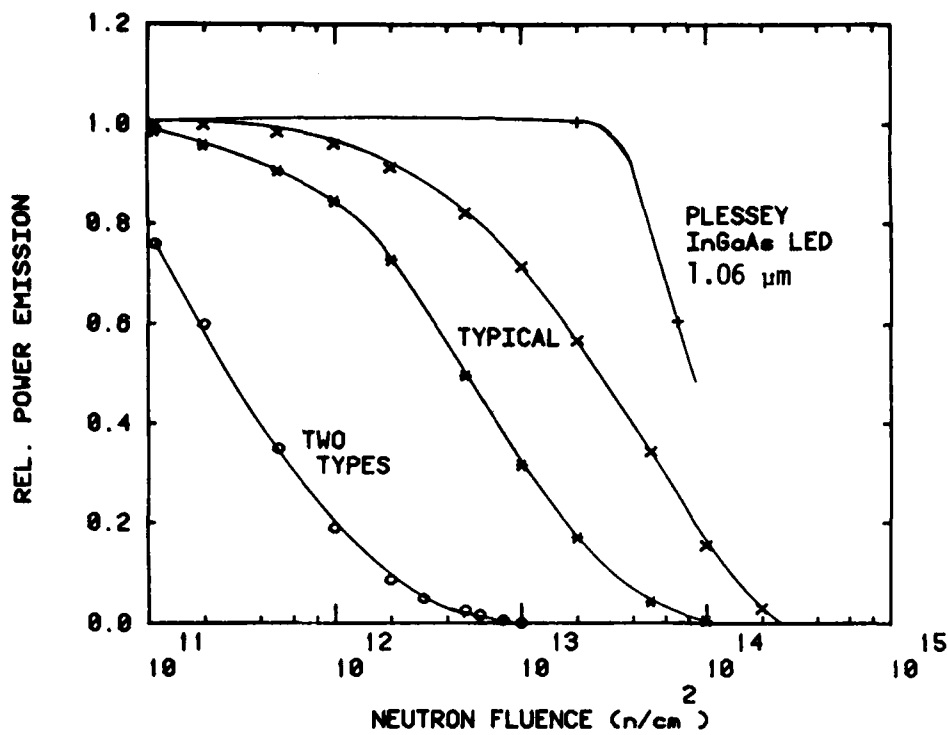


Figure 4. Comparison of 1.06- μm (InGaAs) and 0.93- μm (GaAs:Si) LED Neutron Degradations

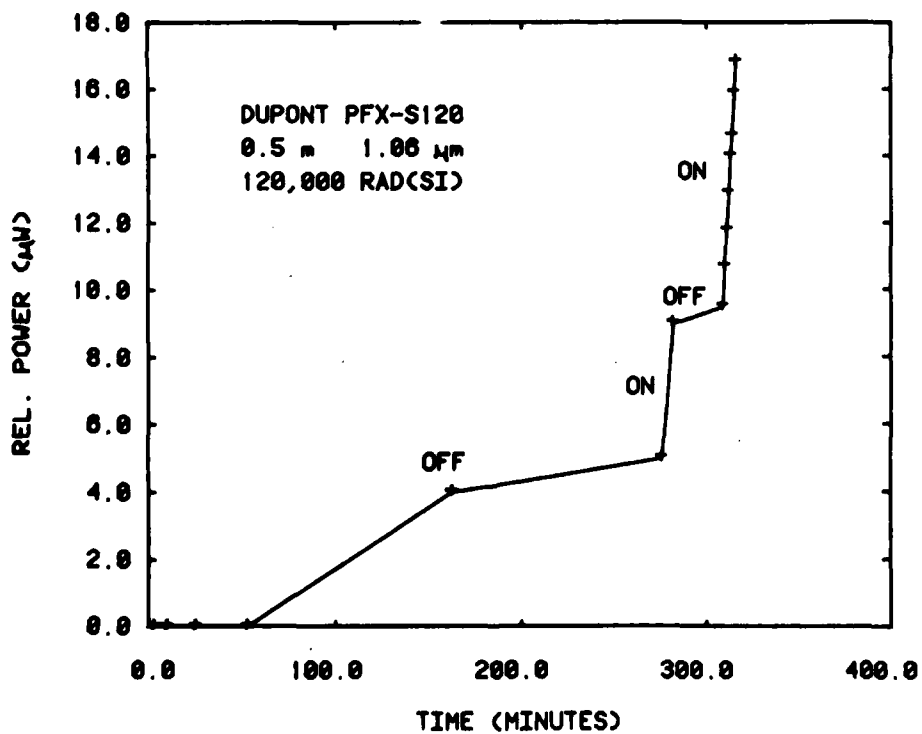


Figure 5. Effect of Optical Power Input on Irradiated Fiber Recovery

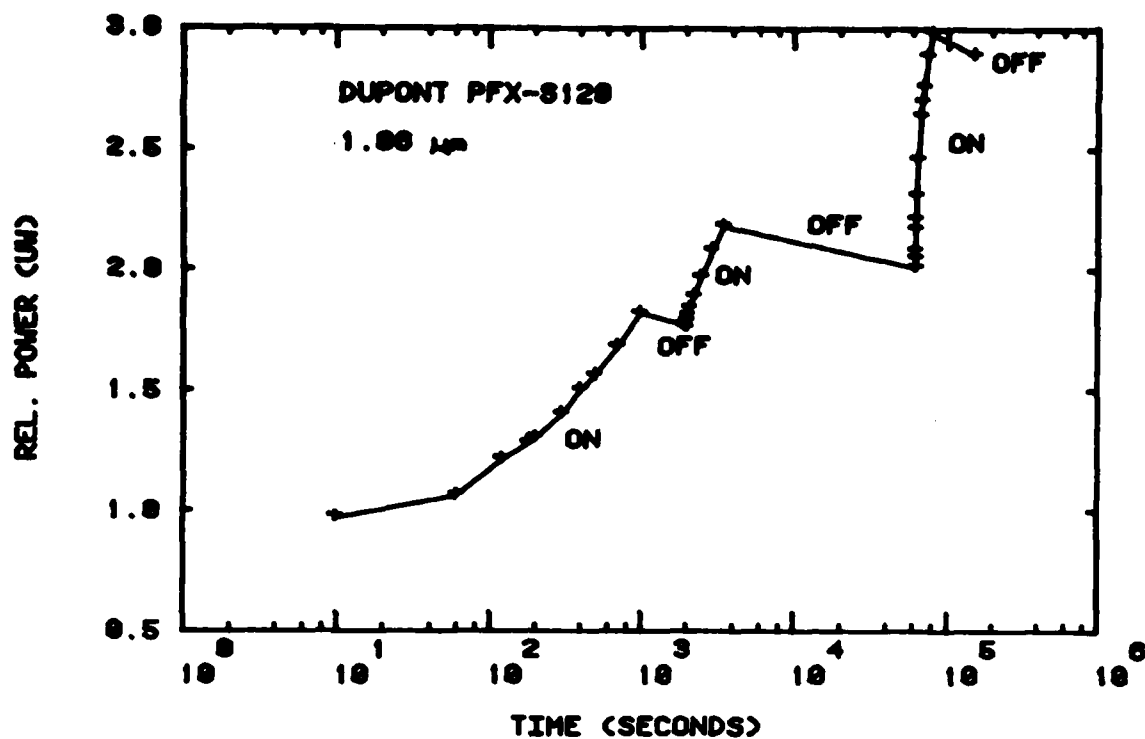


Figure 6. Effect of Optical Power Input on Fiber Recovery After Four-Month Storage

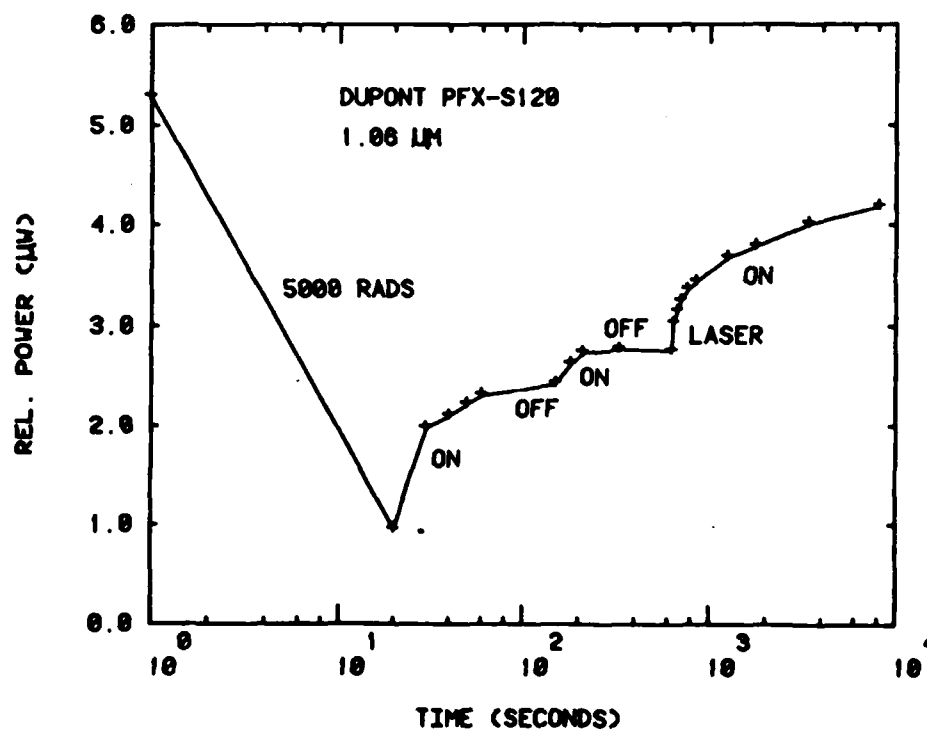


Figure 7. Degradation and Recovery of Irradiated PFX-S120 PCS Fiber for Various Optical Input

transmission increased quickly enough that the first post-irradiation data point has some scatter in its value. Clearly the application of optical power into the fiber greatly increases its recovery rate and, with sufficient light injection, the recovery is a substantial fraction of the irradiation darkening.

The observation that the recovery rate is dependent upon the optical power indicates that the rate of observed fiber darkening will be dependent upon the power as well (especially for low dose-rate buildup). This power dependence of the buildup and recovery was measured for a fresh 5-meter length of PFX-S120 fiber. Successive 5000-rad irradiations were performed at low and high optical power levels and the buildup and recovery monitored continuously with time. A comparison of two irradiations are shown in figure 8 where the induced absorption as a function of time is shown for the same fiber. This sequence was repeated for several additional cycles with nearly identical results, namely both the peak absorption loss and recovery rate are strong functions of the injected (and thus measurement) power levels.

A similar test performed using a 100-meter length of Corning step-index, glass-clad fiber (1505) did not display a power dependence as shown by the results in figure 9. While there is some uncertainty in the peak absorption loss, the high and low power absorption values are nearly the same upon cessation of the ^{60}Co irradiation. Additional irradiations using these same optical power levels produced similar results.

The observation that radiation-induced fiber absorption can be optically bleached raises the possibility whether high intensity optical pulses could be utilized to substantially shorten the downtime following irradiation. Since LED's have only limited power emission capabilities, a pulsed Nd-doped, glass rod laser was used to inject high intensity light into irradiated fibers to determine the effect of higher powers on optical bleaching. A previously irradiated PCS fiber (PFX-S120) which had recovered most (but not all) of its preirradiation transmission, was subjected to 4- μs long pulses of the 1.06 μm wavelength light output from the laser. Only about 3 watts could be coupled into the fiber without focusing—no recovery of the stable damage was observed after ~ 100 pulses.

However, if the laser pulse was applied during the recovery period of the transient absorption, a substantial increase in the recovery rate was observed. This is shown in figure 10 by the single laser pulse applied during the optical bleaching tests. A comparison of the relative bleaching rates using the $\sim 20 \mu\text{W}$ LED power and the $\sim 3 \text{ W}$ pulsed Nd-doped glass-rod laser shows that the annealing "efficiency" appears to be greater at the higher power levels. These results are very limited and many more tests are required to quantitatively establish the power and energy dependence of annealing rates. It does appear that the bleaching is not a simple function of injected optical power or energy—higher power appears to result in faster recovery rates compared to the same total energy injected over a much longer time.

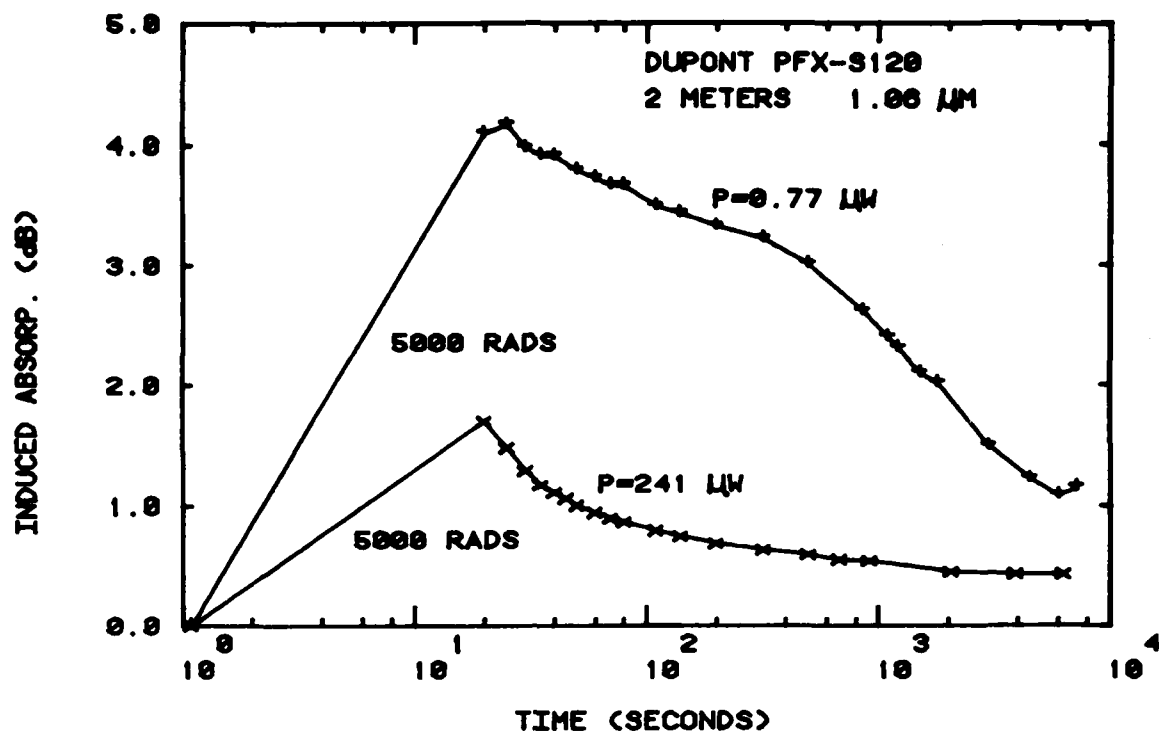


Figure 8. Comparison of Low and High Input Power on Fiber Absorption Buildup and Recovery for PFX-S120

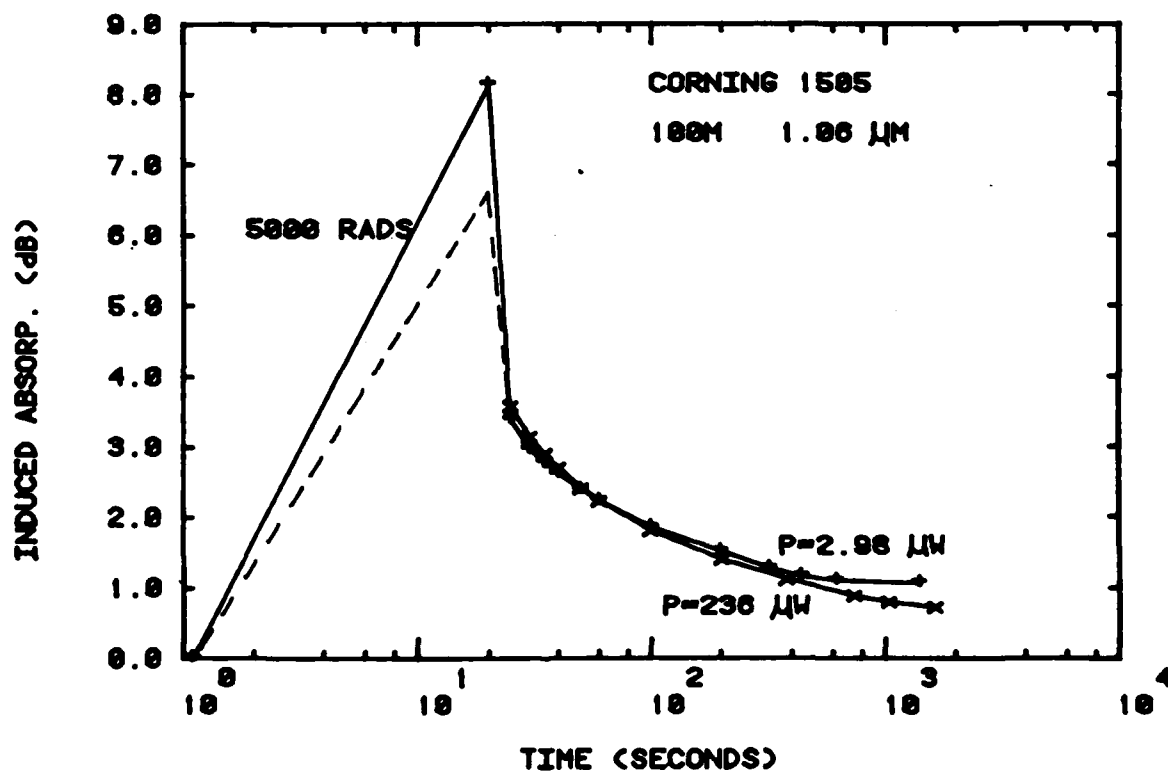


Figure 9. Comparison of Effects of Low and High Input Power for Corning SDF 1505 Fiber

DISCUSSION

Based on the results of the transient and steady-state absorption degradation for the two pure fused silica fibers tested, it is apparent that the radiation susceptibility is affected by processing variables of an, as of yet, unknown nature. One possible origin for the large variation in induced absorption is the water or OH^- content of fibers. Previous studies have shown that high OH^- fibers are more radiation resistant than low OH^- fibers.⁶ A good indication of the OH^- content of fibers is the magnitude of the OH^- overtone absorption band at 970 μm . Spectral measurements were performed on each of the 1 km long fibers using 10-m short fibers for references. These spectral measurements indicate that the OH^- content was ~ 800 ppm for the PS-05-20 fiber and ~ 16 ppm for the QSF-A200 fiber (using Keck's result that the magnitude of the 950 μm absorption is ~ 1.25 dB/km per ppm).⁷

It is apparent from these results that the much higher OH^- content of the ITT fiber compared to the QSF-A200 does not result in increased radiation hardness, and, in fact, it appears that the converse may be true.

Both the transient and steady-state irradiation-induced increase in absorption were significantly lower in the Quartz product fiber. Sigel, et al. have reported that "fat" PCS fibers have fewer drawing-induced defects and display greater radiation hardness.⁸ The Quartz product fiber tested had a 200- μm core diameter compared to the 125 μm core of the ITT fiber. Whether this was the critical difference is unknown.

One impact of the strong bleaching effect of optical power on fiber recovery rate is the nonuniformity of absorption along the fiber length. This is simply the result of the much lower power in the fiber core at the receiver end of the fiber compared to the power launched into the fiber at the transmitter end due to the initial and radiation-induced fiber absorption. With strong optical bleaching, a recovery "wave" will essentially propagate down the fiber.

In addition to the input power dependence, the effect of optical bleaching will be to introduce a dose and length dependence of measured absorption. This can be demonstrated by calculating the "average" radiation-induced fiber absorption assuming that the optical bleaching rate is proportional to the optical power and that the recovery is exponential with time. A comparison can then be made between the calculated recovery rates for long and short fibers. The result of such a calculation is shown in figure 10 where the average absorption, given by $\alpha = 10L^{-1} \log (P/P_0)$, is plotted as a function of time for 1-km and 100-m long fibers irradiated to the same dose. Note that the recovery for the longer fiber extends out to longer times as would be expected for the greatly reduced optical bleaching rates at the receiver end of the long fiber. In addition to a length dependence, optical bleaching will also affect the magnitude of the peak, radiation-induced absorption observed in low dose rate tests where the irradiation times are comparable to the bleaching rates. Again, this is simply due to the enhanced annealing rate with light and can be demonstrated by calculating the buildup and recovery of an optically bleachable fiber as shown in figure 11.

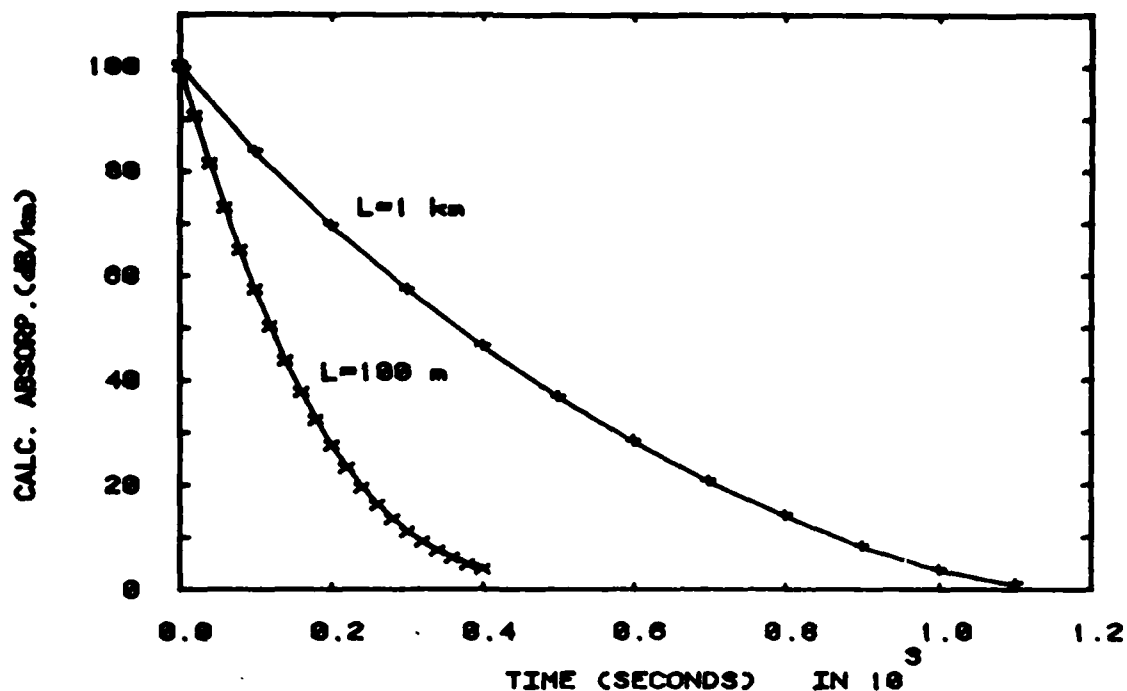


Figure 10. Calculated Recovery for Long and Short Fibers Assuming Optical Bleaching

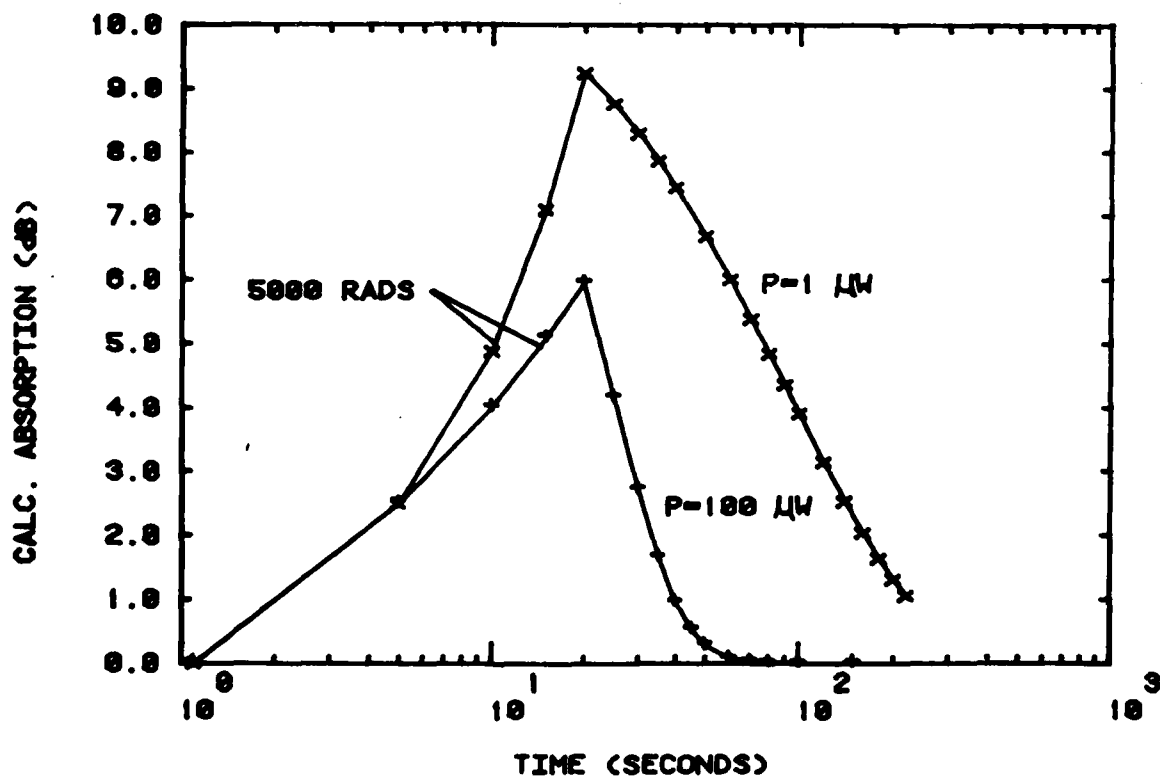


Figure 11. Calculated Effect of Optical Bleaching on the Buildup and Recovery of Fiber Absorption

GENERAL ELECTRIC CO SANTA BARBARA CA TEMPO F/G 20/6
PROCEEDINGS OF THE FIBER OPTICS IN THE NUCLEAR ENVIRONMENT SYMP--ETC(U)
APR 80 R C WEBB DNA001-79-C-0081

DNA-5308P-2

NL

23

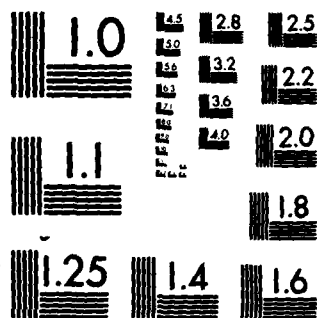
END

DATE _____

FBI WFOE ①

11

DTIC



MICROCOPY RESOLUTION TEST CHART
NATIONAL BUREAU OF STANDARDS-1963-A

SUMMARY AND CONCLUSION

Low dose, transient absorption measurements performed on long PCS fibers indicate that operation at 1.06 μm does not, by itself, provide the substantial improvement in hardness one might expect. Comparison with other test data taken at 0.82 μm on shorter fibers (100 m) does reveal that the degradation at shorter times is indeed greater at 0.82 μm than at 1.06 μm . However, at least for the two long fibers tested, the induced absorption at longer times is greater at 1.06 μm (see Ref. 1). This tail in the recovery can substantially increase the downtime of long fiber optic data links.

An investigation of low and high power optical bleaching indicates that this approach offers some promise in increasing the recovery rate and, thus, reducing the downtime. Optical bleaching was observed in one PCS fiber tested but was not a strong factor in the buildup or recovery in induced-absorption for a glass-clad, step index fiber (Corning 1505). The importance of optical bleaching can also be shown in its effect on fiber radiation-induced absorption measurements; test results can be affected by fiber length, input power, and radiation dose level where optical bleaching is an important phenomenon.

ACKNOWLEDGEMENTS

The authors would like to thank Dr. J. N. Polky for his assistance in the planning and carrying out of the long fiber link analysis and tests and D. F. Dann of his expert assistance in the instrumentation and testing.

REFERENCES

1. M. S. Maklad, G. W. Bickel, and G. H. Sigel, Jr., Paper TUD8-1 presented at Optical Society of America Meeting, Washington, D.C., 1977.
2. S. Kronenberg, H. L. Berkowitz, R. A. Lux, R. L. Pfeffer, H. V. Gordon, and V. Rosati, ERADCOM Report No. DELET-TR-78-13, June, 1978. See also, W. H. Hardwick and A. H. Kalma, IEEE Trans. on Nucl. Sci. NS-26, 4808 (1979) and E. J. Friebele, G. H. Sigel, Jr., and M. E. Gingerich, IEEE Trans. on Nucl. Sci. NS-25, No. 6, 1261 (1978).
3. C. E. Barnes, "Radiation Effects in Optoelectronic Devices", Sandia Laboratory Report SAND 76-0726, March, 1977.
4. S. Share, A. S. Epstein, and R. A. Polimadei, IEEE Tran. on Nucl. Sci. NS-20, No. 6, 256 (1973).
5. E. W. J. Mitchell and E. G. S. Paige, Phil. Mag. 1, 1085 (1956).
6. E. J. Friebele, D. L. Griscom, and G. H. Sigel, Jr., J. Appl. Phys. 45, 3424 (1974).
7. D. B. Keck and A. R. Tynes, Appl. Optics 11, No. 7, 1502 (1972).
8. G. H. Sigel, Jr., E. J. Friebele, M. E. Gingerich, and L. M. Hayden, IEEE Trans. on Nucl. Sci. NS-26, No. 6, 4796 (1979).

NEUTRON DAMAGE EFFECTS IN $\text{Ga}_{1-x}\text{Al}_x\text{As}$ LEDs*

C. E. Barnes

Sandia Laboratories[†]
Albuquerque, New Mexico 87185
(505) 264-6407

ABSTRACT

Several factors can influence the choice of an optimum wavelength for operation of a fiber optic data link, especially if the link is to be exposed to a radiation environment. For many applications the usable wavelength range will often be determined by the fiber rather than the LED. Consequently, there is greater flexibility and ease of fiber optic system design if LEDs, and also detectors, are available at a wide variety of wavelengths. For example, the use of $\text{Ga}_{1-x}\text{Al}_x\text{As}$ LEDs emitting below 900 nm rather than GaAs LEDs allows one to avoid the OH absorption band near 930 nm in water containing fibers and permits the use of $\text{Ga}_{1-y}\text{Al}_y\text{As}$ detectors in addition to Si photodiodes. Before such LEDs can be used in a military or space system, however, it is necessary to know how the devices will respond to irradiation. We have performed a neutron damage study of five sets of $\text{Ga}_{1-x}\text{Al}_x\text{As}$ LEDs with x values of 0, 0.02, 0.06, 0.12 and 0.20 in order to investigate the physical properties responsible for variations in radiation sensitivity as a function of x. All five sets consist of two epitaxial layers (n $\text{Ga}_{1-y}\text{Al}_y\text{As}$ ($3 \times 10^{18} \text{ Te}$) on p $\text{Ga}_{1-x}\text{Al}_x\text{As}$ ($2 \times 10^{18} \text{ Ge}$), $y = x + 0.1$) grown on p -type GaAs substrates at Texas Instruments. In these planar emitters a buried junction structure is achieved by diffusing Zn into the epilayers around the perimeter of the LEDs. Two additional sets were included in the study: a set with a GaAs active region and an n GaAs top layer, and a set with $x = 0.06$ and greater p type doping ($8 \times 10^{18} \text{ Ge}$). For purposes of comparison, results taken on Plessey high radiance $\text{Ga}_{1-x}\text{Al}_x\text{As}$ LEDs in a separate study will also be mentioned.

Prior to and following neutron irradiation at 300 K total light output, LED current, and electroluminescence (EL) spectra were measured as a function of applied voltage. These data were taken at both 76 K and 300 K.

Spectral measurements at 300 K reveal a single, broad EL band for $x = 0, 0.02$, and 0.06 which shifts to higher energy with irradiation. The magnitude of this shift is 13 nm (22 meV) for a fluence of $4.8 \times 10^{14} \text{ n/cm}^2$. For $x = 0.12$ and 0.20 the shift is weaker and a second low energy band is also observed. Pre-irradiation peak locations vary from 884 nm (1.40 eV) for GaAs to 756 nm (1.64 eV) for $\text{Ga}_{0.8}\text{Al}_{0.2}\text{As}$.

*This work supported in part by the Air Force Weapons Laboratory (AFWL), Kirtland AFB, Albuquerque, NM, under P.O. 77-027, and in part by the United States Department of Energy (DOE) under contract number DE-AC04-76-DP00789.
[†]United States Department of Energy Facility.

The current-voltage characteristic changes in approximately the same manner with fluence for all $\text{Ga}_{1-x}\text{Al}_x\text{As}$ LEDs independent of x . Neutron irradiation causes an increase in current at constant voltage the magnitude of which is greater at lower voltages. This neutron-induced excess space charge recombination current is partially responsible for the neutron induced decrease in total light output at constant current. It is interesting to compare these results with the high radiance Plessey devices which operate at much higher current densities than the Planer TI LEDs. In the Plessey LEDs, neutron-added currents are only seen at the lowest voltages. As one would expect, these LEDs have excellent radiation hardness for constant current operation.

The neutron-induced degradation of light output at both constant voltage and current proceeds at about the same rate in all the sets with two important exceptions. For $x = 0.20$ the degradation is much less, although at this x value the pre-irradiation output is substantially below that of the other LEDs. Secondly, the degradation rate for the set with greater p region doping is less than that for all x values at the lower doping level except for the $x = 0.20$ set. In contrast with $x = 0.20$, the high doping, $x = 0.06$ set had high pre-irradiation power output. These results, along with our previous work¹ on GaAs LEDs with varying p region doping, suggest that greater p-type doping enhances the radiation hardness more than adding a small ($x < 0.12$) amount of Al. Addition of more Al, say 20% or greater, also achieves radiation hardness, as shown by our results, but has two deleterious effects which outweigh the increased hardness. First, as indicated above the pre-irradiation power output is generally lower than for LEDs with $x < 0.15$. Second, the emission peak wavelength is short enough to put most of the light output in a spectral range where ionization induced transient fiber attenuation is severe. Consequently, achieving increased hardness through greater p region doping fits in much better with other desirable LED features.

We also wish to emphasize the greater hardness of high radiance LEDs due to the lack of neutron induced excess currents. This is a fortuitous result for the system designer since high radiance LEDs can be more efficiently coupled into typical optical fibers. Therefore, one achieves greater light output at the receiver simultaneously with increased radiation hardness.

¹C. E. Barnes, IEEE Trans. Nuc. Sci. NS-24, 2309(1977).

TEMPERATURE DEPENDENCE OF NEUTRON DAMAGE TO COMMERCIAL GaAsP LED DEVICES

J.M. Lambert and P.A. Treado
Georgetown University and Naval Research Laboratory
Washington, D.C. 20057 and 20375
R.G. Allas
Naval Research Laboratory
L. Leopold
Georgetown University

Abstract

The effects of broad spectrum, 15 MeV median energy, neutron irradiation on MV (Monsanto) GaAsP light emitting diodes (LEDs) have been studied by measuring the light emission degradation during neutron bombardment and before and after small doses of neutron irradiations. The electroluminescence spectra and the total light output were measured at 77K, 195 K and 273 K. The samples studied were Monsanto MV 5053, 5154, 5253, and 5353 GaAsP LEDs with phosphorus content in the range from 40% to 100%. The electroluminescence spectral peak varied from 595 nm to 690 nm and the FWHM was approximately (or less than) 50 nm at 300 K. The spectral output was a function of temperature and with small applied voltage variations at 77 K the spectral peak position varied by up to tens of nanometers for some of the samples. As expected each of the samples at each of the temperatures showed significant light emission degradations as a function of neutron fluence. The light emission degradation data can be fit to a quantitative description of the emitted light intensity, I , from radiative currents in LEDs by integrating the differential recombination rate over the neutral region in which recombination occurs with the assumption that a radiative center profile proportional to d^n , where d is the distance into the region, and by using an accepted expression for the excess minority carrier density due to diffusion. Then,

$$(I'/I)^{2/n+1} = 1 + C.F., \quad (1)$$

where F is the neutron fluence, and C is a constant depending on the cross section for irradiation induced recombination centers, the thermal velocity of the carriers and the rate of the fluence introducing recombination centers. The light emission degradation observed was significantly less at the lower temperatures for each of the four types of LEDs studied. In order to understand the damage mechanisms which predominate at each temperature, deep level transient spectroscopy was suggested but preliminary results were not encouraging. Measurements of the degradation of spectral components for the LEDs studied suggest that such measurements may be useful for the 100% phosphorus samples.

Introduction

Studies of radiation damage in LEDs can provide valuable information concerning the nature of the devices, damage mechanisms for the devices in specific radiation fields and methods of hardening these devices for applications in radiation environments. Properties which influence the radiation sensitivity of LEDs are: (a) type of radiative transition, (b) radiative and nonradiative center concentrations and distribution, (c) current flow mechanisms, both radiative and nonradiative, and (d) the constituent elements and actual production processes for the LED studied.

In high quality LEDs such as a liquid phase epitaxially grown GaAs devices with a low concentration of nonradiative centers and doped with typical concentrations of radiative recombination centers, e.g., 10^{16} to 10^{17} cm^{-3} , it is expected that the irradiation-induced degradation will proceed rapidly because the carrier diffusion length and lifetime are quite long; hence, a relatively small number of irradiation induced recombination centers significantly affect the lifetime. A quantitative description of the diffusion lifetime, τ , at any time during the irradiations (or after) is given by the following damage function^[1],

$$1/\tau = 1/\tau_0 + K.F \quad \text{or} \quad \tau_0/\tau = 1 + \tau_0 K F \quad (2)$$

In Eq. (2), τ_0 is the pre-irradiation diffusion lifetime, F is the fluence in neutrons/ cm^2 and K is a phenomenological damage constant which indicates the number of nonradiative centers introduced per unit fluence. In essence, $K = \sigma v R$, where σ is the cross section for irradiation-induced recombination centers, v is the thermal velocity of the carriers and R represents the rate of the fluence introducing recombination centers. The constant R depends on the type and intensity of the incident radiation, the sample temperature, the ionization level in the device during the irradiation and various metallurgical properties of the device being irradiated.

Prevailing carrier injection in LEDs depends on the applied voltage, the temperature and the material parameters. Different current flow mechanisms for the radiative and total current exist for our higher temperature, i.e., 300 K; but, at these temperatures and relatively high applied bias voltages thermal injection can dominate the tunneling processes which are more important at low temperatures and lower applied voltages.

The light intensity, I , described as in Eq. (1)^[2,3] gives a radiative-center profile-dependent (via n) interpretation of the radiation-induced degradation of the diffusion dependent light output for an irradiated LED maintained at constant voltage. Our data strongly suggest that $n = 1$.

Previous studies^[4] of irradiation-induced degradation of GaAs, GaP, and $\text{GaAs}_{1-x}\text{P}_x$ LEDs have suggested that light emission degradation can be diffusion based and due to the introduction of nonradiative recombination centers in the neutral region. We have observed that neutron-induced damage does indeed degrade the light output of the LEDs we have studied. The degradation is dependent on neutron fluence, the relative As-P concentration, on the in situ temperature of the irradiated LED, and, for the 100% phosphorus samples, on the wavelength of the spectral component studied.

Experimental Apparatus and Procedures

We have measured the light emission spectra and the light emission degradation due to bombardment with a 15 MeV median energy neutron beam at temperatures of 77K, 195K, and 273K for sets of commercial LED devices, Monsanto MV 5053, 5153, 5253, and 5353. The neutron spectrum, shown in Fig. 1, is generated by bombarding a thick Be target with a 35 MeV deuteron beam. The flux available at 10 cm from the Be target is 2×10^9 neutrons/ $\text{cm}^2/\mu\text{C}$ of beam and we usually used 1 μA to 10 μA of deuteron beam current. By means of neutron radiographs taken in the position of the sample and read with an optical densitometer, we are sure that the neutron flux is constant to within 2% (the radiograph/densitometer accuracy limit) over the volume of the LED samples studied.

Two systems have been used to measure the LED light output. During irradiations, at each of the three temperatures, the light output of an LED is recorded via a fiber optic link to an external area free of radiation where either a photodiode detector or an optical spectrometer viewed the fiber optic signal. The

photodiode detector and its amplifier had response functions which were flat in the spectral regions of the LED and fiber optic light outputs and constant over the dynamic range of the amplified signals. The optical spectrometer was calibrated at each of the photomultiplier voltages used with a standard source. All data were recorded on DVMs, on chart recorders and/or with an on-line computer for ease of off-line analysis.

The first measurements we obtained actually used a second LED as a detector and we measured the light-emission and light-detection degradation simultaneously in a crude manner. Crude though the measurements were, it was clear that the light-emission degradation was much greater, by something like a factor of 7, than the light-detection degradation. Thus, with the goal of trying to determine the degradation mechanism or mechanisms, we have devoted our time to studies of the light-emission degradation. This we began with room temperature measurements with the four LED types and with initial I-V values at various points on the I-V curves for the four sets of LEDs. Although there was some indication that the initial I-V value for a given type was somewhat important, one could not be sure that the variations were not due to irregularities in the LEDs. We used LEDs purchased over a 6-month period; therefore we assumed that we were sampling many production runs. In the process of measuring the light-emission degradation, we obtained spectra before and after irradiations for each of the LED types. Because we were not convinced that our goal would be accomplished, it was decided that measurements of both spectra and degradation must be carried out at two other temperatures. Liquid nitrogen and acetone and dry ice provide convenient working environments; thus, 77 K and 195 K were chosen.

The spectral outputs of all four types of LEDs were measured at 77 K, 195 K and 273 K by means of a Fastie-Ebert 0.5 m spectrometer with f/10 optics. Since much of our work depended on direct comparison of output intensities as functions of time, LED type, induced damage or the lack thereof, and temperature, great care had to be taken to reproduce the optical alignment in detail. The approach taken was as follows: the samples were mounted in a small aluminum rig such that the front end of the LED touched the end of an optical fiber which was similarly mounted in the aluminum rig. In this way the optical coupling between the LED and the optical fiber could be reproduced since both the attitude and the distance between the two components was determined and reproducible. To couple the fiber to the spectrometer, the spectrometer input slit was left in place and the fiber was butted up to the slit and epoxied in place. The slit was then removed which decreased the resolution of the instrument, but increased the radiative input as compared to the situation with the 25 micron slit in place. The dispersed radiation was detected with a 1P28 photomultiplier tube and recorded on strip chart recorder. Because of differing intensity output, it was necessary to change the photomultiplier high voltage over limited increments. The absolute gain of the system was calibrated both with standard light sources and with selected LEDs of each type. Thus, the data is normalizable to a known intensity and intensity comparisons are valid.

Experimental Results

The results of our work can be categorized for presentation in four areas: initial room temperature radiation damage data, spectral output measurements pre- and post-irradiation, temperature dependent radiation damage for the total spectral intensity, and spectral and temperature dependent radiation damage data. Because we are most interested in comparisons of the various data sets, it is best to consider the interrelationships of the data rather than as it is categorized.

In considering the spectral output data, we suggest that all samples exhibited apparent shifts in the wavelength position of the maximum radiative output power and some structure that depended in part on temperature and in part on the current or voltage applied. More importantly, it was only the green samples (GaP) that showed structure at all temperatures and all applied voltages. Clearly, if radiation damage affects different emission lines or bands to a greater or smaller degree, studies of the damage to specific components of the green LEDs would, in principle, contribute to the knowledge of the mechanisms of radiative transitions and the damage thereof. In addition, we found that output spectra tended to depend rather critically on the initial treatment of the samples. For instance, spectra taken at 273 K first and at 77 K second, for the same sample, differed sufficiently from data taken in the reverse sequence that one was forced to view the sample behavior as if it were in an unstable equilibrium and was going into one or two (or more) stable ones depending on sequence of sample treatment and/or data accumulation. In particular, it was observed that the LEDs had unstable I-V characteristics at 77 K, i.e., when attempts were made to measure the spectral output at a current of 20-30 mA the current would tend to change spontaneously to small currents (about 1 mA). With this information, to eliminate as many of the sequencing and current-mode side effects, we have been (curing) all samples by running each sample at 40 mA for one minute prior to data accumulation and have taken spectra for analysis with currents of 1 mA and 40 mA when the temperature is 77 K.

Table I provides both the color, model and phosphorus content information and the spectral peak position information for the LEDs studied. Figs. 2-5 show the pre-irradiation spectra for the three temperatures used for the four types of LEDs studied. Each of the spectra are tracings of the spectrometer's recorder data and are typical in that samples of the same color had peak positions within a few nanometers of those shown.

TABLE I. GaAs_{1-x}P_x LED Information

Color	Monsanto Number	X	Spectral Peaks (nm)		
			77K	195K	300K
Green	MV5253	1 $\begin{smallmatrix} +0.00 \\ -0.01 \end{smallmatrix}$	603,614,580	592,562	598,590
Yellow	MV5353	0.87 \pm 0.03	613 636	613 633 640	623
Gold(Orange)	MV5153	0.65 \pm 0.03	638	641	655
Red	MV5053	0.39 \pm 0.02	671	683	697

At each temperature, all of the light emission intensity, I, data show a strong monotonic decrease with the neutron fluence which is not exponential. Fig. 6 shows a chart recording trace of the output of the amplifier from the photo diode total-intensity detector and amplifier for a gold sample, one of about 50 such samples studied. To such data, we apply Eq. (1), with n = 1, and in the form

$$(I_0/I) - 1 = KF. \quad (3)$$

The variable I is function of time or previously incident neutron fluence and is measured during the irradiation of the sample for in situ measurements or before, during and after the irradiations for samples viewed by the spectrometer. The use of Eq. (3) is justified because the damage data produce essentially a straight line for the ranges of fluence and for the temperatures used with each of the LEDs studied. A computer program provides a least squares fit of the damage function to a straight line and parabolic functions. These fits show that the nonlinearity of the data (the damage function) is small and the computer program provides the slope and standard deviation for the bestfit straight line to the individual damage function.

Figs. 7 and 8 depict typical results for damage functions obtained; the room temperature damage data are shown in Fig. 7 and the 77 K data are shown in Fig. 8 with the two lines per color representing the small (1 mA) and large (40 mA) current conditions. It should be pointed out that the data shown in Figs. 7 and 8 are representative and that the data from the tens of samples of each color studied actually lie in bands of which the data shown are representative of the average data. Indeed, the data in Figs. 7 and 8 suggest that there is a significant difference in the slope of the damage function curve, dependent on the color or phosphorus content, x of the $\text{GaAs}_{1-x}\text{P}_x$ LEDs used. This dependence is observed at the three temperatures, 77 K, 196 K, and 300 K. Figs. 9 and 10 provide a description of this dependence at 77 K and 300 K. It is of importance to note that the curves labeled A, B, C and D are for samples having nominal phosphorus concentrations of 40%, 65%, 85% and 100%, respectively, and that the relative positions of the labeled curves are essentially the same for each of the Figs. 9 and 10. Of course, a glance at the fluence needed to produce a given amount of light degradation is significantly different; it is much less for the room temperature data and Figs. 9 and 10 immediately suggest that hardening is efficiently accomplished by operating the LEDs (any one of the colors) at 77K. Also, by referring to Figs. 7, 8, 9 and 10 it is relatively obvious that the best hardness is available for red and green LEDs operated at 77 K. Fig. 11 depicts such a conclusion.

In addition, we can consider the data obtained by spectral measurements prior to and after small irradiation doses have been administered. Figs. 12 and 13 show such data. For the green LEDs, which have shown the most spectral structure at all temperatures, both before and after any increment of irradiation, we have considered the relative damage for various spectral components. Because the resolution of the spectrometer is not sufficient to separate lines, or even strong bands, the intensity at a median wave length was compared. Table II gives representative samples of the data for such spectral-component damage. The indications are that some wavelength bands of the green LED spectrum are damaged less than others. Thus, even harder systems could be considered if a commensurate loss in intensity could be tolerated. One would have to be sure that the optical filters used would not be damaged significantly in comparison to the green LED spectral component region to be used.

TABLE II. Spectral Component Emission Degradation

Relative Fluence	High Current Components					Low Current Components		
	A	B	C	D	E	A	B	C
0	1.00	1.00	1.00	1.00	1.00	1.00	1.00	1.00
0.2	0.69	0.69	0.68	0.45	0.42	0.54	0.63	0.66
0.5	0.48	0.45	0.46	0.23	0.21	0.35	0.39	0.39
1.0	0.27	0.26	0.26	0.11	0.10	0.22	0.22	0.22

References

1. P.J. Dean, in Applied Solid State Science, ed. R. Wolfe, (Academic Press, NY, 1969), I, 1.
2. C.E. Barnes, IEEE Trans. Nuc. Sci. NS-18, 322 (1971).
3. S.M. Sze, in Physics of Semiconductors, (Wiley Interscience, NY, 1969), 99.
4. M.C Petree, Appl. Phys. Lett. 3, 67 (1963).

B.W. Noel, et al., IEEE Trans. Nuc. Sci. NS-18, 378 (1971).

A.S Epstein, et al., Appl. Phys. Lett. 23, 472 (1973).

R.A. Logan, et al., Appl. Phys. Lett. 5, 41 (1964).

C.J. Nuese, et al., Met. Trans. 1, 587 (1970).

A.S. Epstein, et al., Proceedings of the IEEE Conference on Nuclear and Space Radiation Effects, San Diego, 1976.

A.S. Epstein, et al., IEEE Trans. Nuc. Sci. NS-19, 386 (1972).

C.E. Barnes, J. Appl. Phys. 42, 1941 (1971).

C.E. Barnes, Sandia Report SAND 76-0726, (1977).

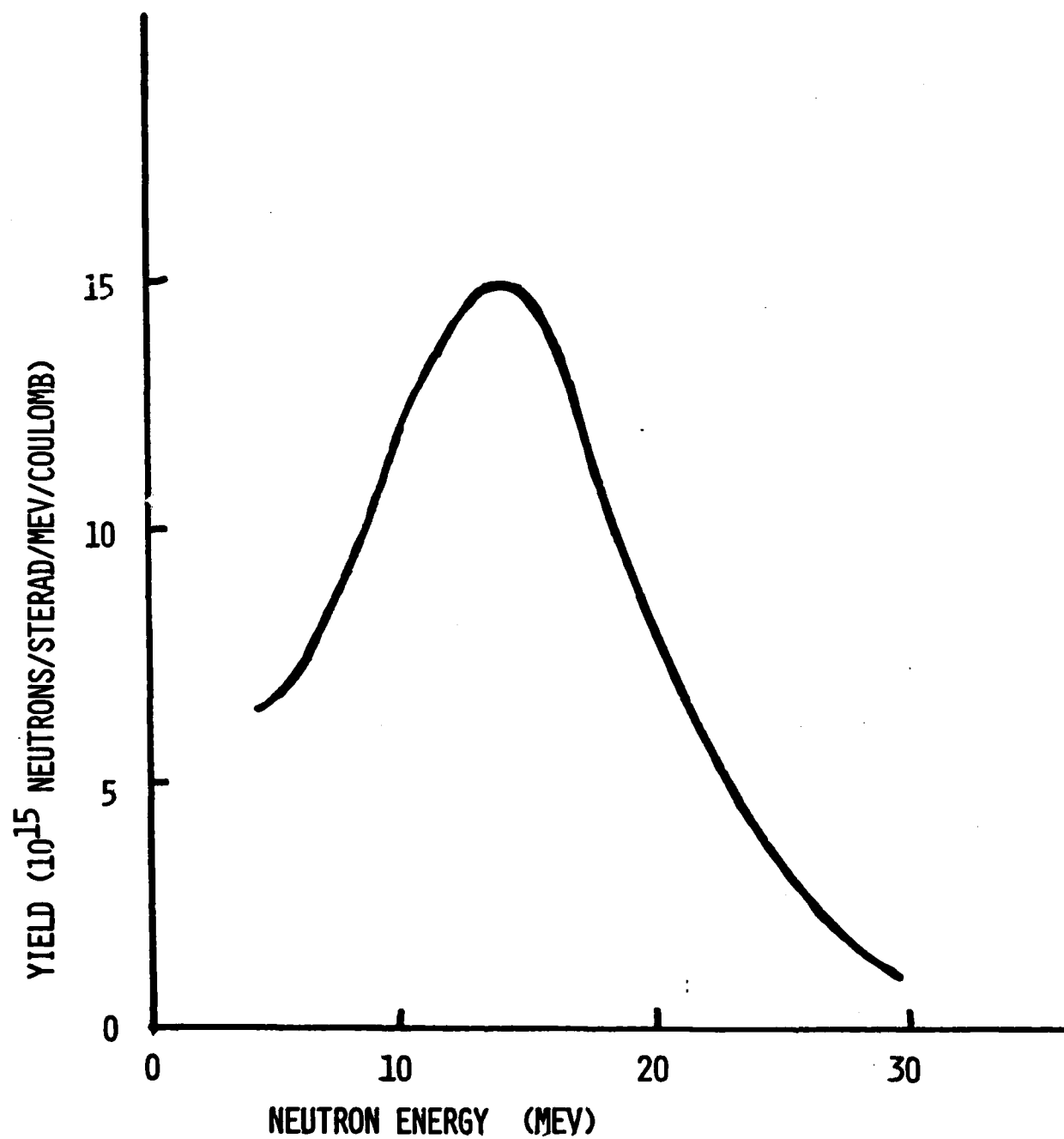


Fig. 1. Neutron energy spectrum from 35 MeV deuterons on thick Be.

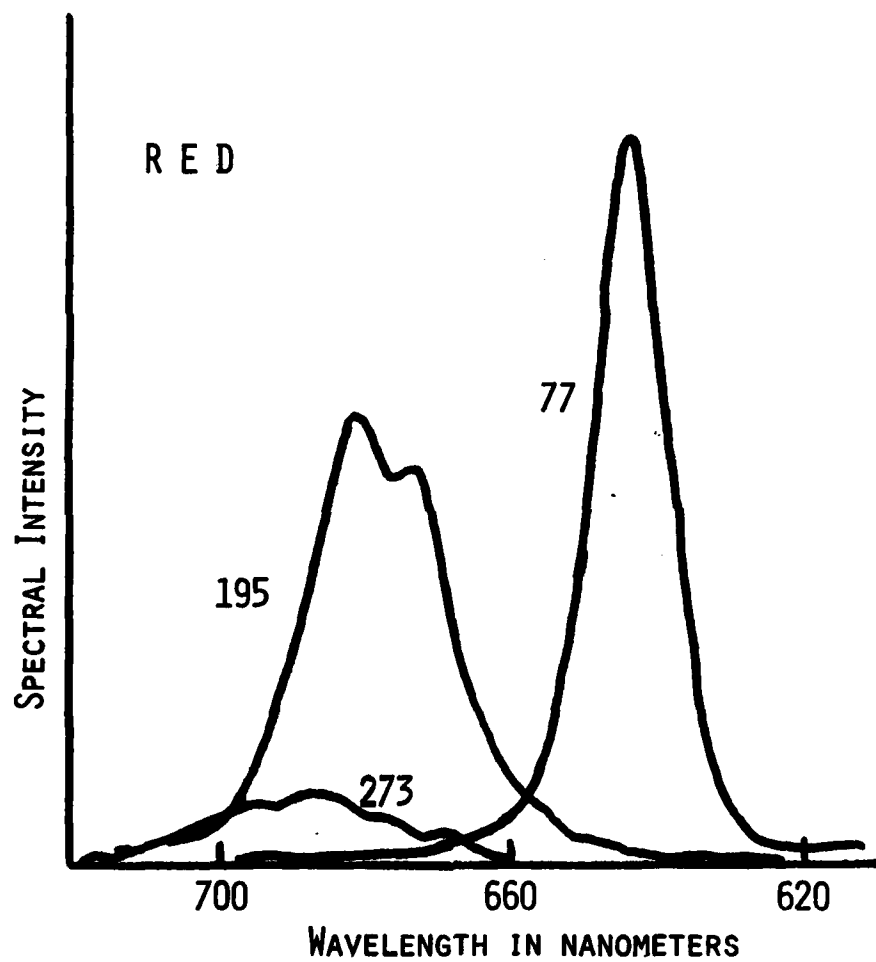


Fig. 2. Preirradiation spectra of red LED, 40 mA.

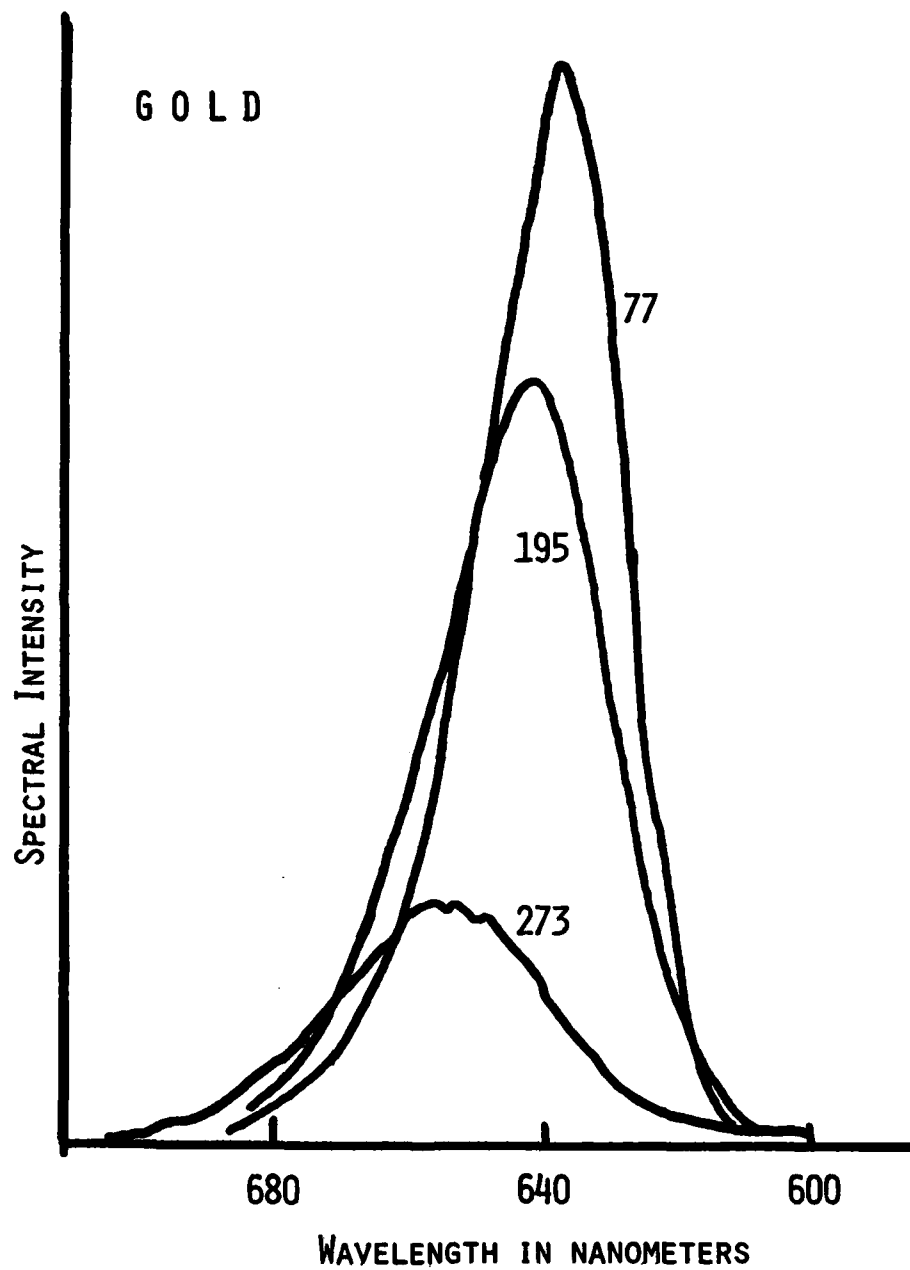


Fig. 3. Preirradiation spectra of gold LED, 40 mA.

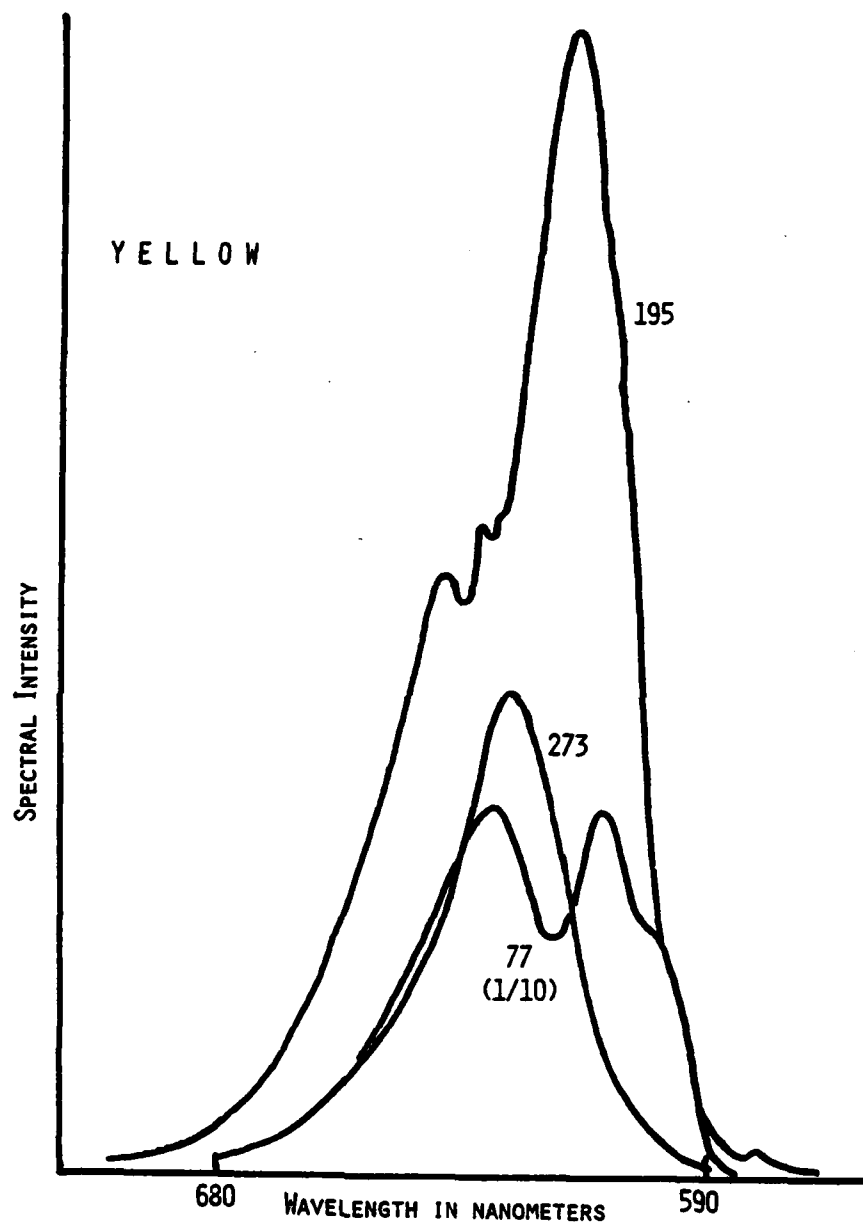


Fig. 4. Preirradiation spectra of yellow LED, 40 mA.

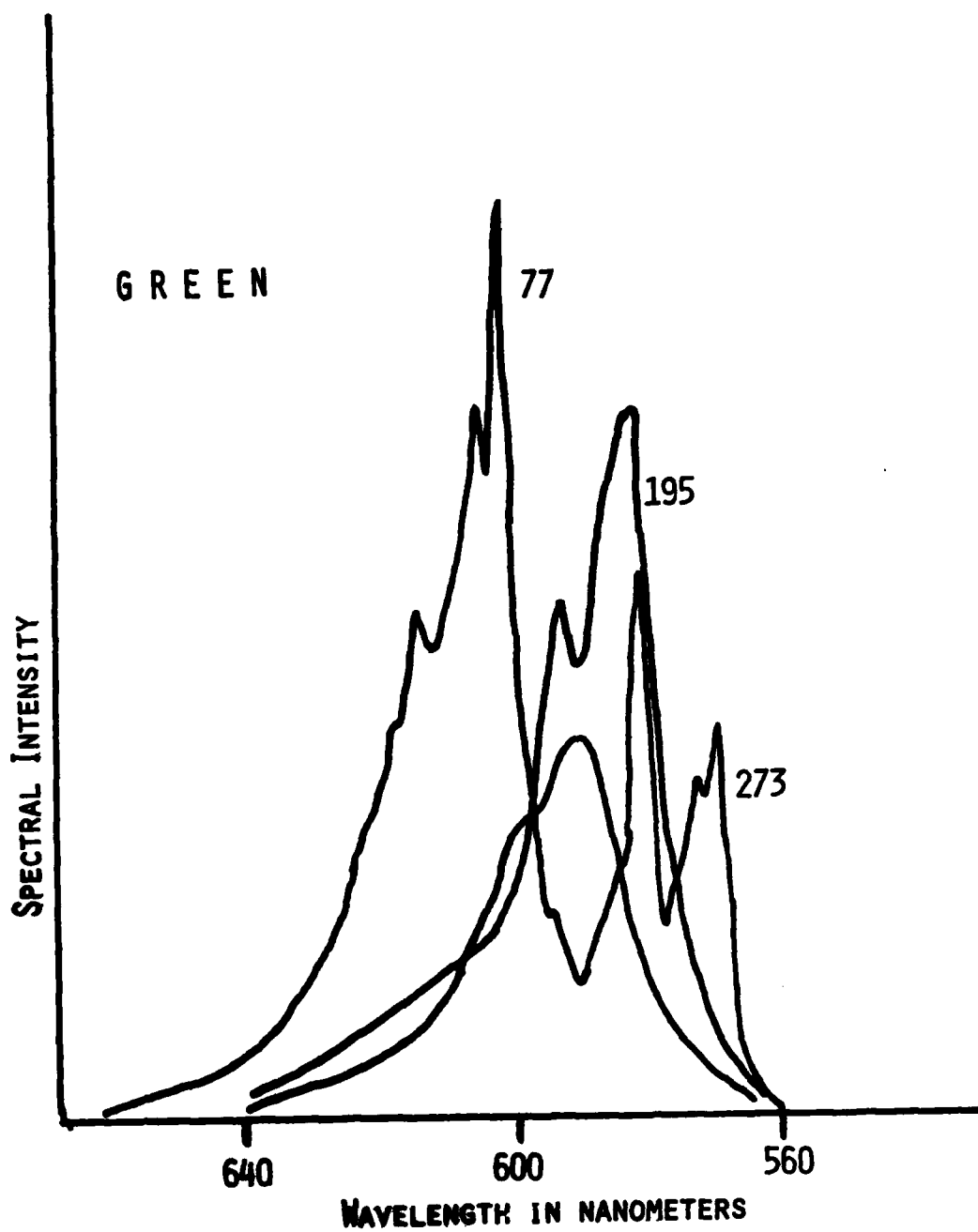
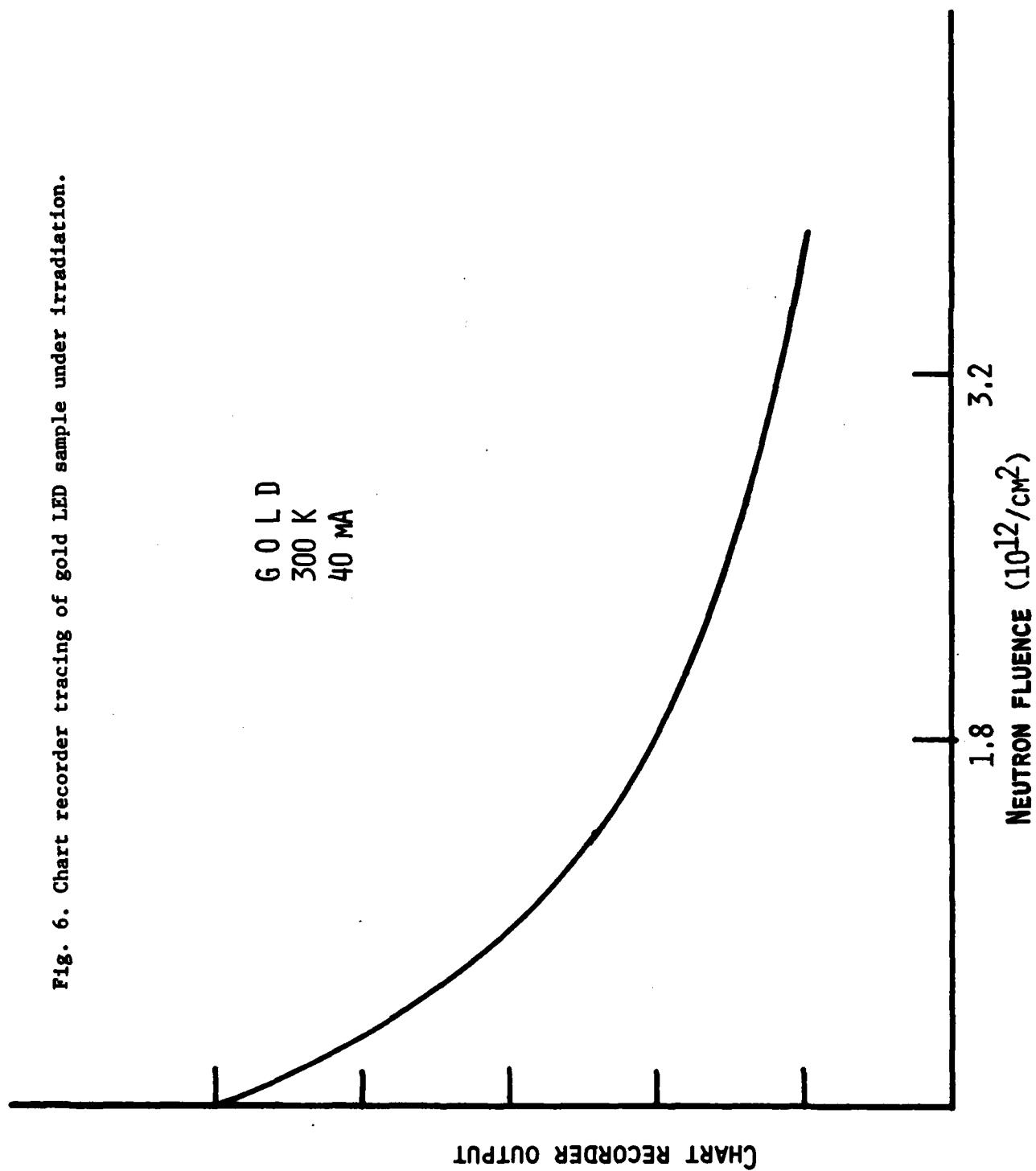


Fig. 5. Preirradiation spectra of green LED, 40 mA.

Fig. 6. Chart recorder tracing of gold LED sample under irradiation.



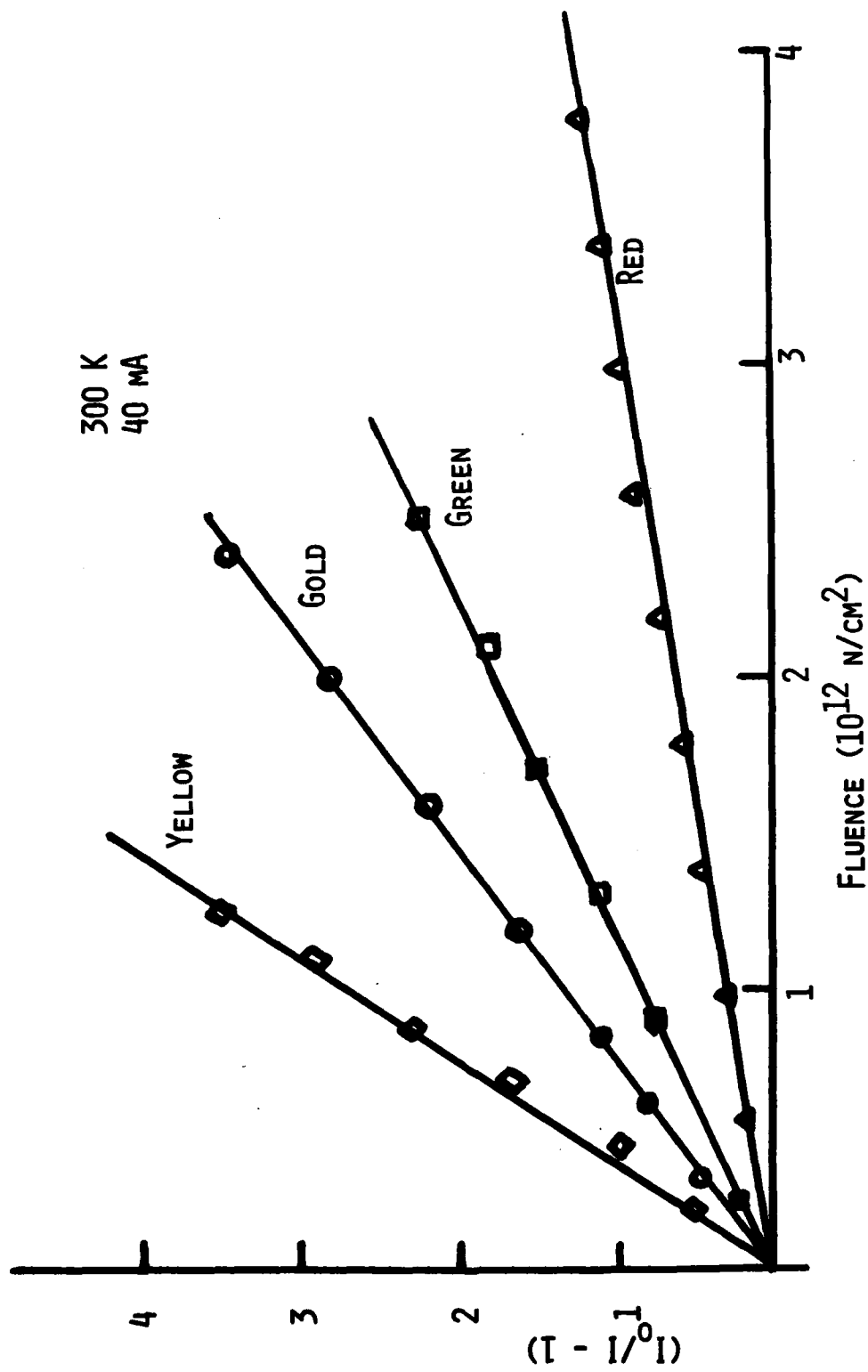


Fig. 7. Room temperature radiation damage data for the four types of LEDs.

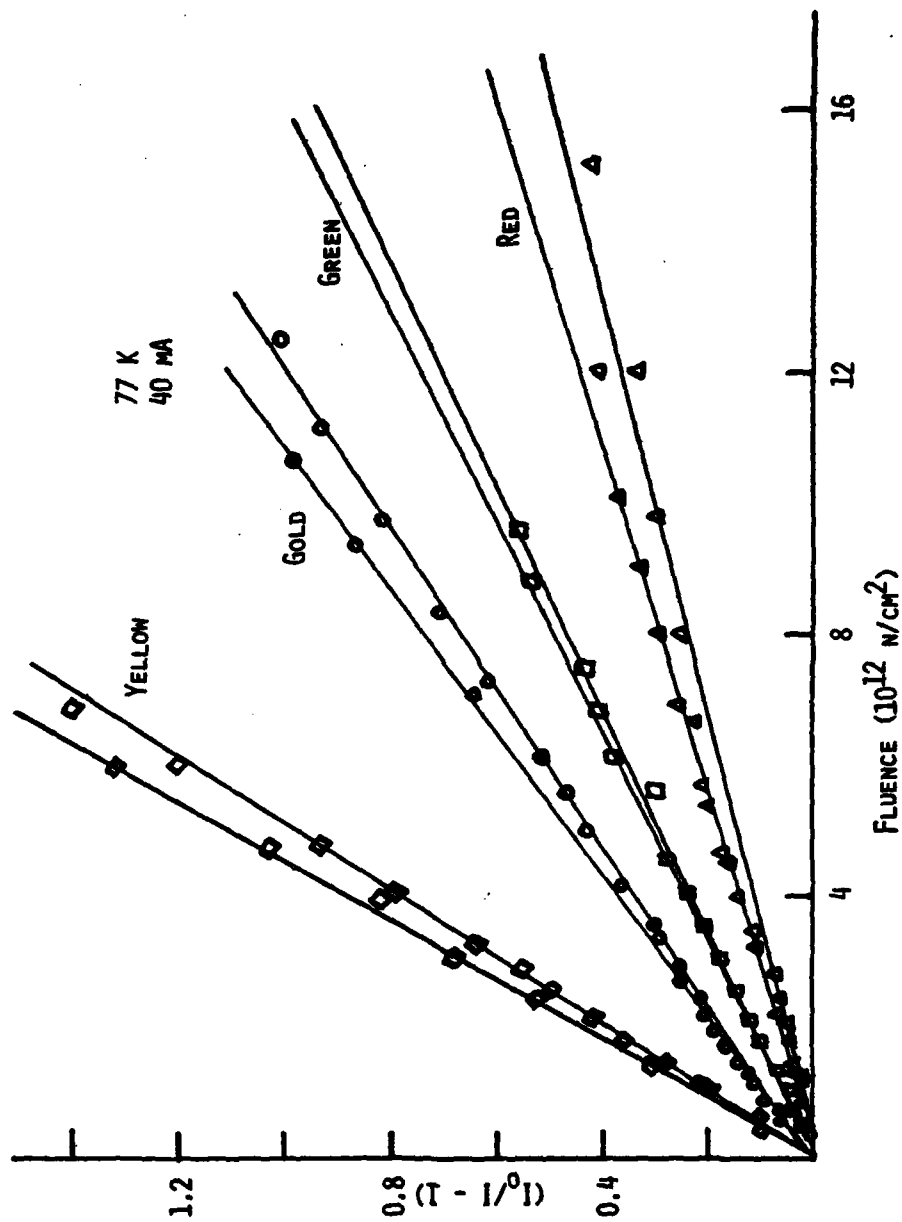


Fig. 8. Liquid nitrogen temperature radiation damage data for the four types of LEDs.

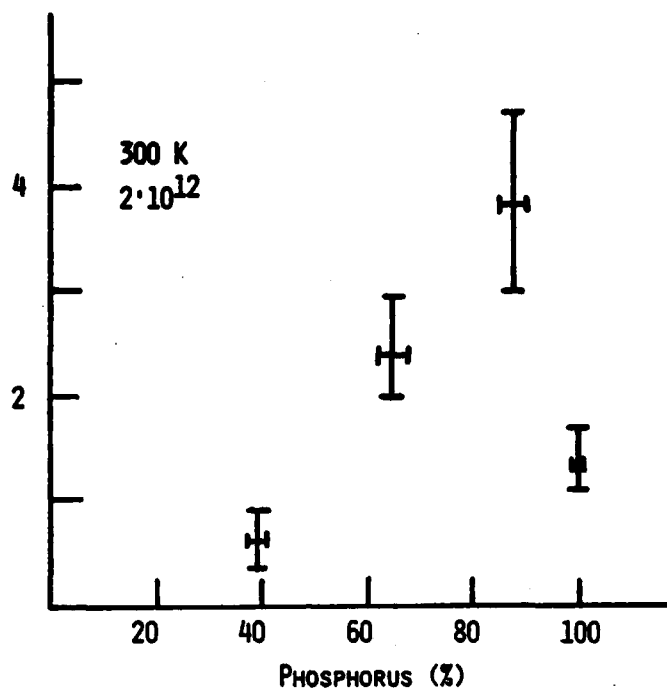


Fig. 9. Radiation damage as a function of phosphorus content.

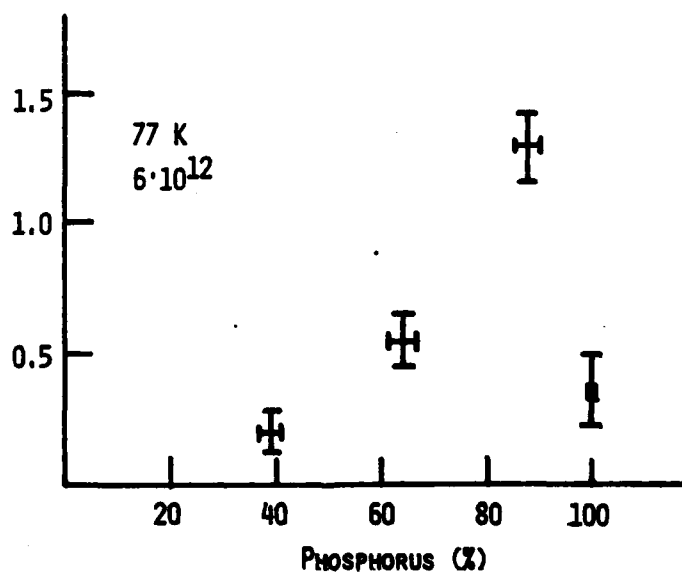


Fig. 10. Radiation damage as a function of phosphorus content.

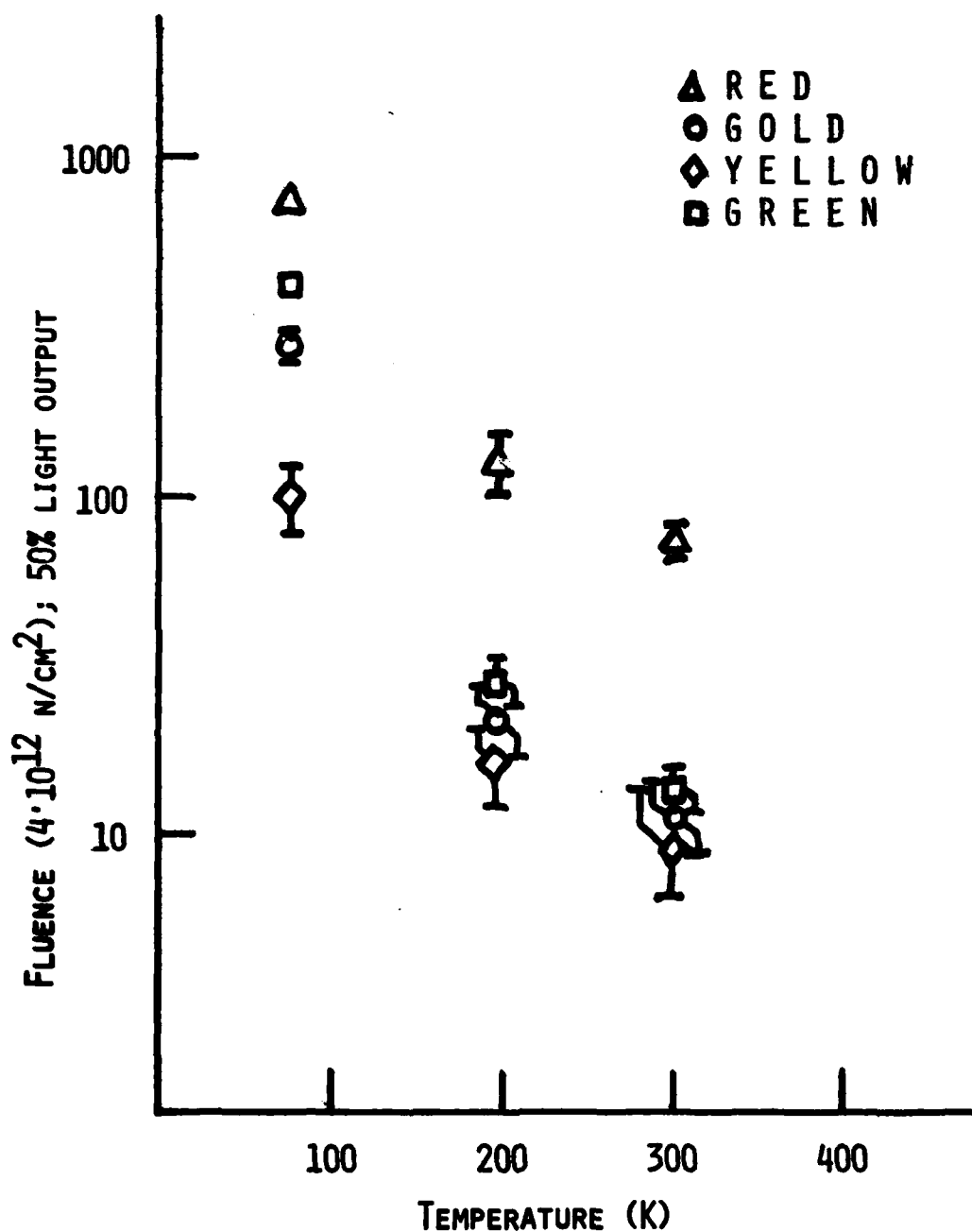


Fig. 11. Radiation damage with temperature and fluence for the four types of LEDs.

Fig. 12. Spectral data prior to and after small irradiation doses for one mode of the green LEDs.

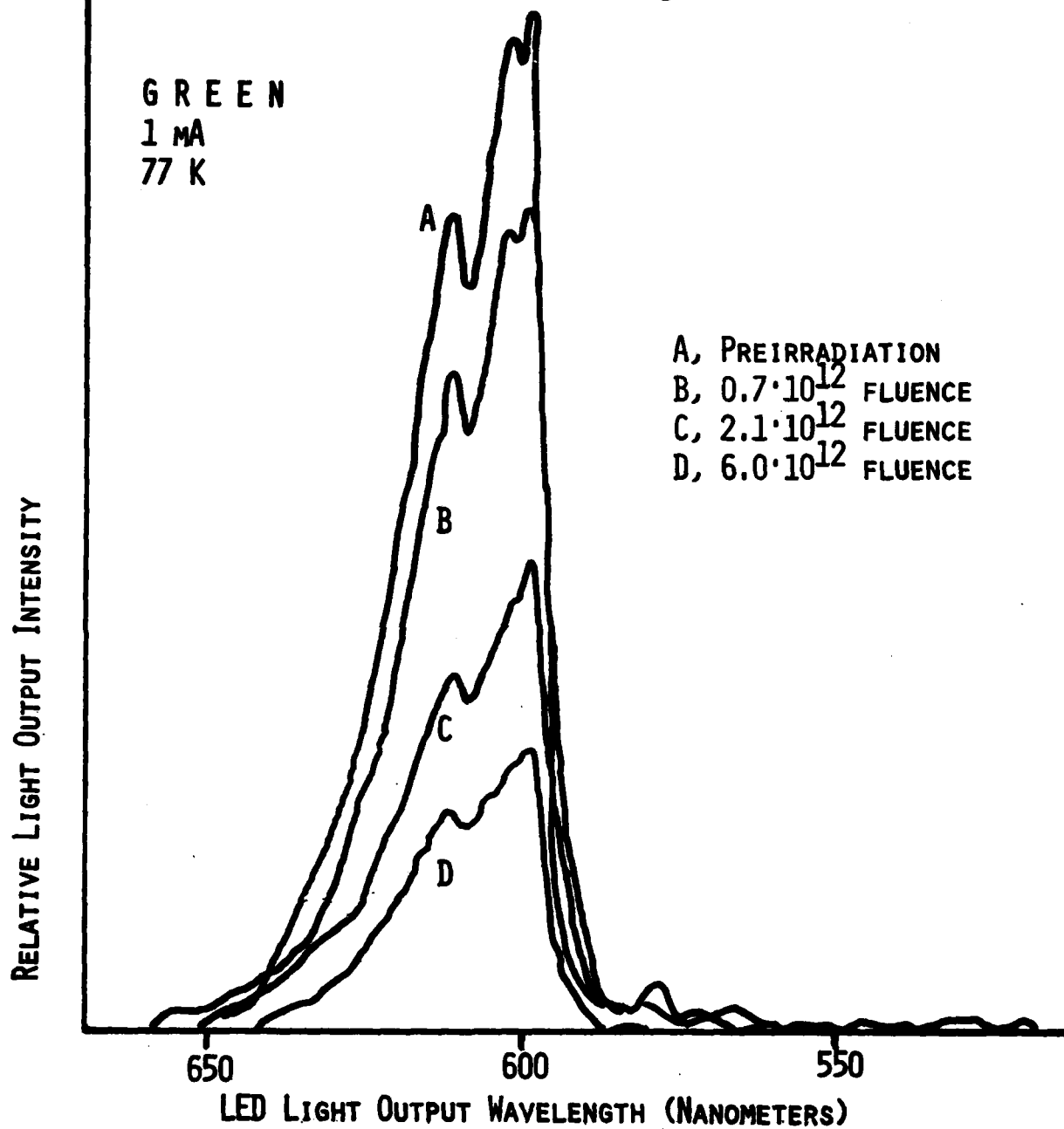
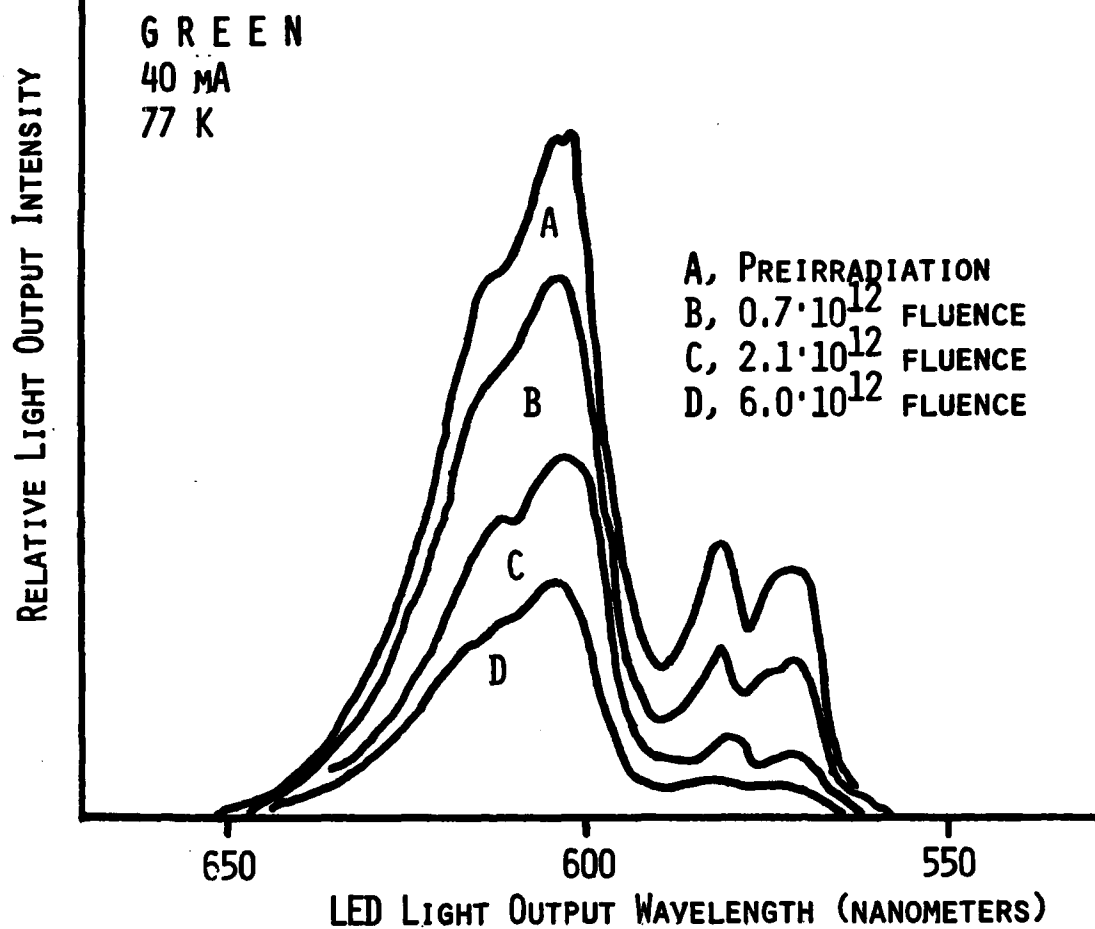


Fig. 13. Spectral data prior to and after small irradiation doses for another mode of the green LEDs.



TRANSIENT EFFECTS OF IONIZING RADIATION IN
Si, InGaAsP, GaAlSb, and Ge PHOTODIODES*

J. J. Wiczer, C. E. Barnes and L. R. Dawson

Sandia National Laboratories,† Albuquerque, New Mexico 87185

(505)844-9677

ABSTRACT

Certain military applications require the continuous operation of optoelectronic information transfer systems during exposure to ionizing radiation. In such an environment the optical detector can be the system element which limits data transmission. We report here the measured electrical and optical characteristics of an irradiation tolerant photodiode fabricated from a double heterojunction structure in the gallium aluminum antimonide (GaAlSb) ternary semiconductor system. A series of tests at Sandia Laboratories' Relativistic Electron Beam Accelerator (REBA) subjected this device and commercially available photodiodes (made from silicon, germanium, and indium gallium arsenide phosphide) to dose rate levels of 10^7 - 10^8 rads/sec. The results of these tests show that the thin GaAlSb double heterojunction photodiode structure generates less than one-tenth the unwanted radiation induced current density than that of the next best commercial device.

Introduction

Certain military applications require the continuous operation of optoelectronic information transfer systems during exposure to ionizing radiation. In this type of environment, the photodiode can be the element which limits system operation. In general, photodiodes respond to electromagnetic radiation of photon energy greater than the semiconductor bandgap; this includes x-ray photons, gamma ray photons, and optical photons. We report here on a photodiode structure specifically designed to reduce the effects of the undesirable ionizing radiation without reducing the effects of the desirable optical radiation. In addition, we report on the results of testing this device and other, commercially available photodiodes in an ionizing radiation environment. A figure of merit for ionizing radiation insensitivity is presented to allow the comparison of photodiodes fabricated from different semiconductor materials with varied device geometries.

Theory

To a first order approximation, the response of photodiodes to monochromatic optical radiation can be expressed as¹

$$I_0 = q \cdot A \cdot \phi \cdot Q \quad .$$

¹K. W. Mitchell, "Optimizing Photodetectors for Radiation Environments," IEEE Trans. on Nuclear Science, Vol. NS-24, pp. 2294 (1977).

*This work supported in part by the Air Force Weapons Laboratory (AFWL), Kirtland AFB, Albuquerque, NM, under P. O. 77-027, and in part by the U. S. Department of Energy (DOE) under Contract DE-AC04-76-DPO0789.

†A U. S. Department of Energy facility.

Here, I_0 is the optically induced photodiode current, q is the electronic charge (1.6×10^{-19} coulombs), A is the area of the device exposed to the optical energy, ϕ is the incident optical photon flux in units of photons/second, and Q is the quantum efficiency. The quantum efficiency factor is simply defined as the ratio of optical photons to the number of additional electrons flowing through the photodiode as a result of the incident photon flux. (Quantum efficiency is sometimes expressed as a percent.) The quantum efficiency factor simplifies the explanation of the photodiode by lumping the effects of semiconductor material properties, photodiode device geometry, bias condition, and surface reflectivity into one convenient parameter. Physically, the incident optical photons energetic enough to interact with the semiconductor lattice generate electron-hole pairs (e.h.p.). Those excess minority carriers generated within approximately one diffusion length of the electrical junction can be collected by the junction depletion region field and converted into majority carrier signal current. A diffusion length, L_D , will be defined here as the approximate distance an excess minority carrier can travel before recombining with its complement (electron-hole pair recombination). The effective collection length, L' , will be defined as the entire length in which excess minority carriers will be collected and converted to majority carrier current. The effective collection length is usually equal to the depletion region width, W_D , plus two minority carrier diffusion lengths. The spatial distribution of the optically created e.h.p. can be determined in part from the optical absorption properties of the semiconductor material. An optical absorption coefficient, α , can be defined by the following equation

$$\phi(x) = \phi_0 e^{-\alpha x}$$

where $\phi(x)$ is the photon flux density a distance x below the photodetector surface, and ϕ_0 is the incident photon flux density not reflected at the surface. Typical values of α for semiconductor materials of interest are shown in Table 1; α is usually a strong function of wavelength. It is clearly important that the effective collection lengths be larger than the inverse of the absorption coefficient to effect maximum excess minority carrier collection. The quantum efficiency can be significantly degraded if the optical absorption coefficient is relatively small, resulting in an e.h.p. distribution throughout the bulk of semiconductor device and the diffusion length is small only allowing collection of those carriers spatially close to the electrical junction. In addition, note that the quantum efficiency can also be degraded if the optical absorption is relatively large and the electrical junction is fabricated too far beneath the surface.

For the case of ionizing radiation in semiconductor materials, the situation of a single photon generating a single electron-hole pair is no longer valid. In fact, the ionizing radiation photons are so energetic, a single photon will generate many electron-hole pairs. In general, ionizing radiation uniformly generates electron-hole pairs throughout the semiconductor material. The conversion of these excess carriers to an ionizing radiation-induced current, I_R , can be represented as

$$I_R = q A \dot{\psi} g_0 L'$$

Here, $\dot{\psi}$ is the ionizing radiation dose rate and g_0 is the ionizing radiation-induced electron hole pair generation rate as shown in Table 1. Note that only those carriers generated within the effective collection length contribute to I_R .

To maximize the ratio of the signal current I_0 to the ionizing radiation-induced current I_R , we would like to select a material with a large optical absorption coefficient and a relatively small diffusion length. Ideally, the effective collection length should be large enough to collect most of the optically generated

TABLE I

Material	Wavelength (μm)	$\alpha(\text{cm}^{-1})$	$g_0(\text{rad}^{-1}\text{cm}^{-3})$
Si	.63	3500	4.0×10^{13}
	.90	400	4.0×10^{13}
	1.06	35	4.0×10^{13}
InP	.9	1.7×10^4	6.8×10^{13}
GaAsSb	1.1	$>10^4$	1.3×10^{14}
GaAs	.63	2.4×10^4	7.2×10^{13}
Ge	1.1	1.0×10^4	1.2×10^{14}
InGaAsP	1.1	$>10^4$	9.2×10^{13}

e.h.p. but not so large as to collect the ionizing radiation-induced e.h.p. found throughout the bulk of the material away from the region of optical absorption.

Finally, in addition to concerns for ionizing radiation insensitivity, the photodiode must respond to optical radiation at wavelengths compatible with the balance of the optoelectronic system components. Recent papers have suggested the need to operate optoelectronic data links in the 1.1 μm to 1.6 μm optical wavelength range for minimum optical fiber attenuation and maximum tolerance to ionizing radiation.²

Device Structure

From the criteria presented above, direct bandgap semiconductors were selected for further investigation. Direct bandgap semiconductors generally have large optical absorption coefficients and short diffusion lengths. Certain direct semiconductor alloys can be fabricated with bandgaps corresponding to the optical radiation range of interest.

The structure shown in Fig. 1 was fabricated to decrease the effects of ionizing radiation by decreasing the effective volume of e.h.p. collection and by utilizing the built-in electric fields associated with heterojunctions.

The alloy used in the top layer, $\text{Ga}_{.9}\text{Al}_{.1}\text{Sb}$, (an indirect bandgap semiconductor) passes optical photons corresponding to wavelengths greater than 1.1 μm (photon energies less than 1.1 eV) with only small absorption. The alloy used in second layer from the top, $\text{Ga}_{.9}\text{Al}_{.1}\text{As}$, is a direct bandgap alloy which absorbs optical photons corresponding to wavelengths greater than 1.6 μm . The large optical absorption coefficient for this material is responsible for the creation of optically-induced e.h.p. near the electrical junction, I_1 . At interface I_2 , a built-in electric field is formed by the energy bandgap mismatch between the $\text{Ga}_{.9}\text{Al}_{.1}\text{Sb}$ ($E_g = 0.8$ eV) and the $\text{Ga}_{.6}\text{Al}_{.4}\text{Sb}$ ($E_g = 1.2$ eV) layers. This field aids in the confinement of the optically generated e.h.p. The heterojunction formed at interface I_3 between the third layer $\text{Ga}_{.6}\text{Al}_{.4}\text{Sb}$ ($E_g = 1.2$ eV) and the substrate GaSb ($E_g = 0.7$ eV) establishes an electric field that tends to aid in the rejection of radiation generated e.h.p.

The quantum efficiency for this device has been measured as a function of wavelength and is shown in Fig. 2. Since approximately one-third of the incident light is reflected at the top surface due to index of refraction differences, a quantum efficiency in excess of 60% can be achieved with the same device structure by utilizing the proper anti-reflection coating. Figure 3 shows the current voltage characteristics for this device. Although dark current measurements indicate an undesirably high dark current density $J_D = 1.4 \times 10^{-4} \text{ Acm}^{-2}$, at .5 volts reverse bias, it is believed that much of this current is due to the defects at the sawed edges shunting the exposed junction surface with mechanical defects. It is further believed that an etched mesa or guard ring structure will significantly reduce the leakage current.

The effective collection length, L' , for the $\text{Ga}_{.9}\text{Al}_{.1}\text{Sb}$ structure has also been measured as a function of reverse bias voltage V_R . The device was examined from the edge in a scanning electron microscope as shown in Fig. 4. As the electron beam was slowly scanned across the junction region, the electron beam induced

²C. E. Barnes, "Radiation Effects in Optoelectronic Devices," Sandia Laboratories Report, SAND-76-0726, 1977.

GaAlSb Photodiode Structure (C-197)

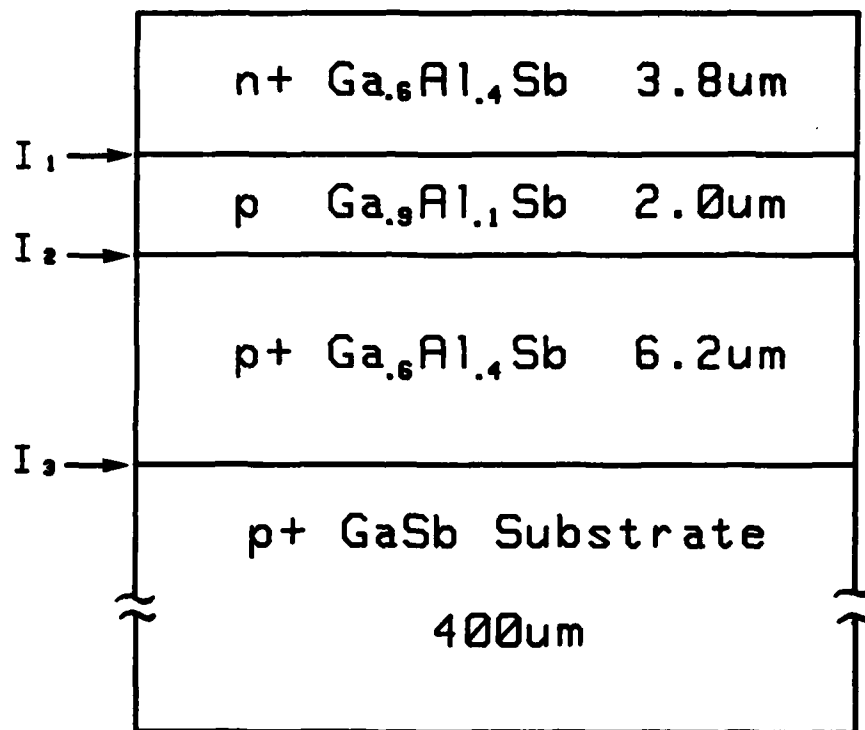


Figure 1. GaAlSb photodiode structure.

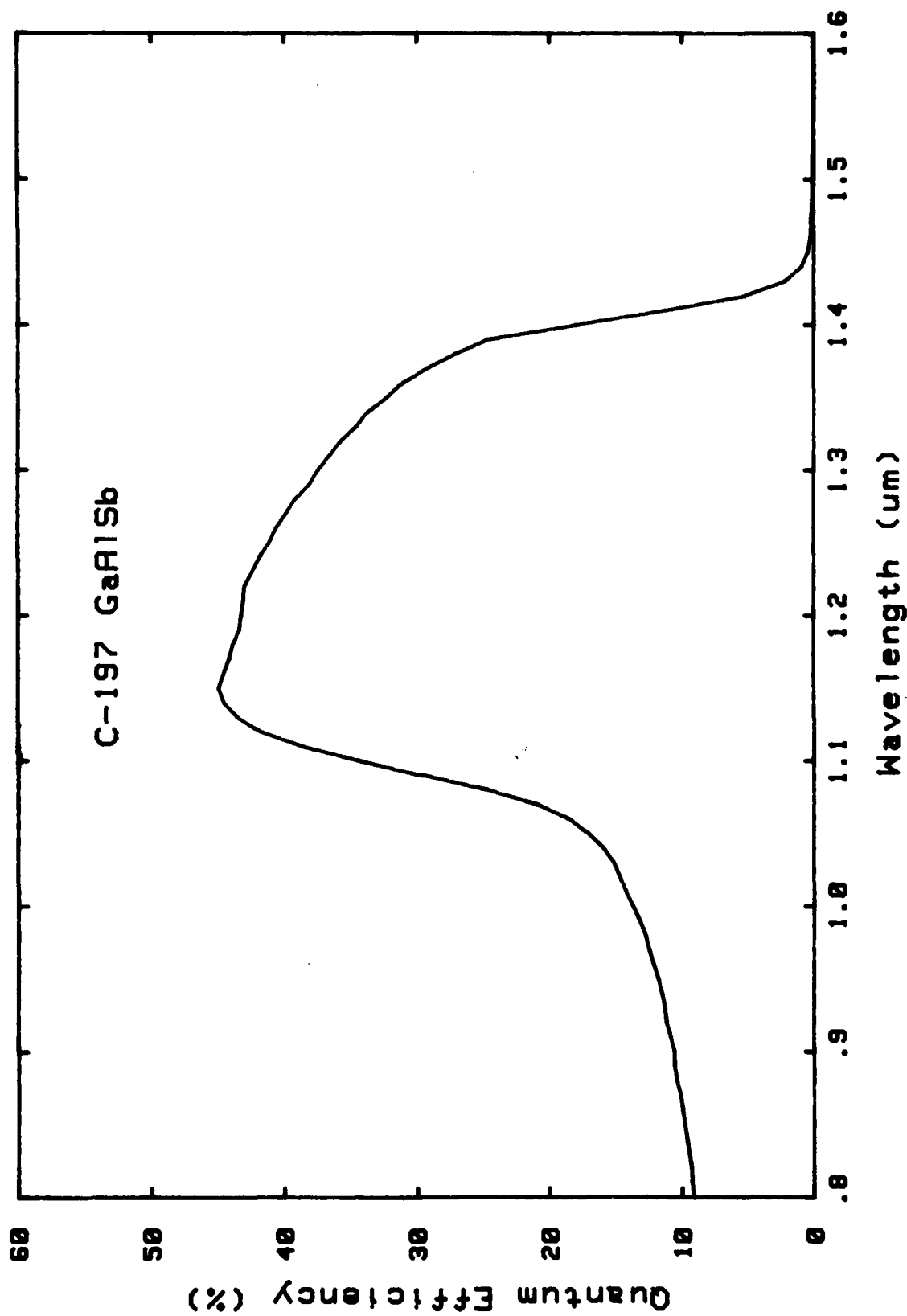


Figure 2. Measure quantum efficiency for GaAlSb photodiode structure

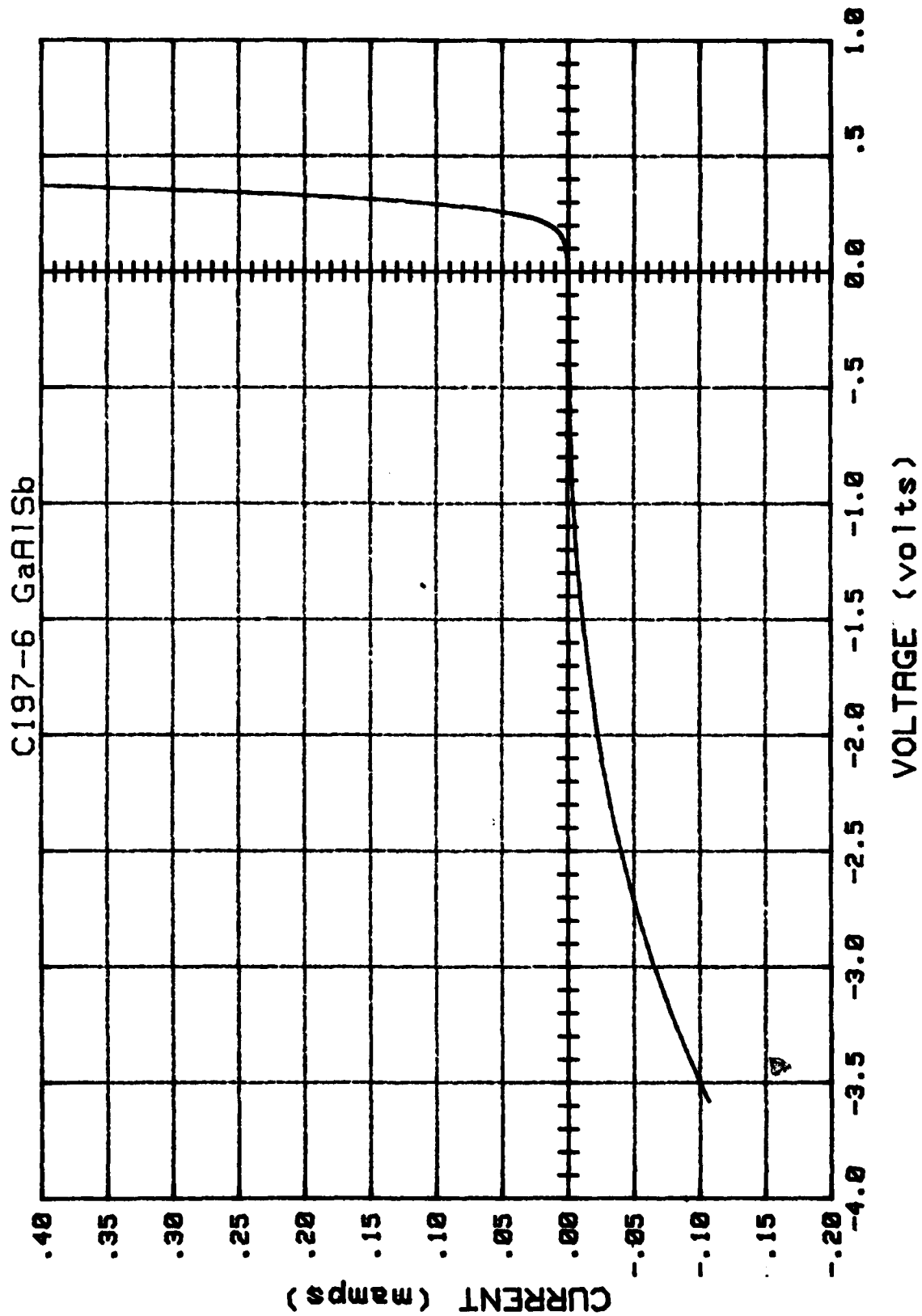


Figure 3. Measure current-voltage characteristics for the GaAlSb photodiode

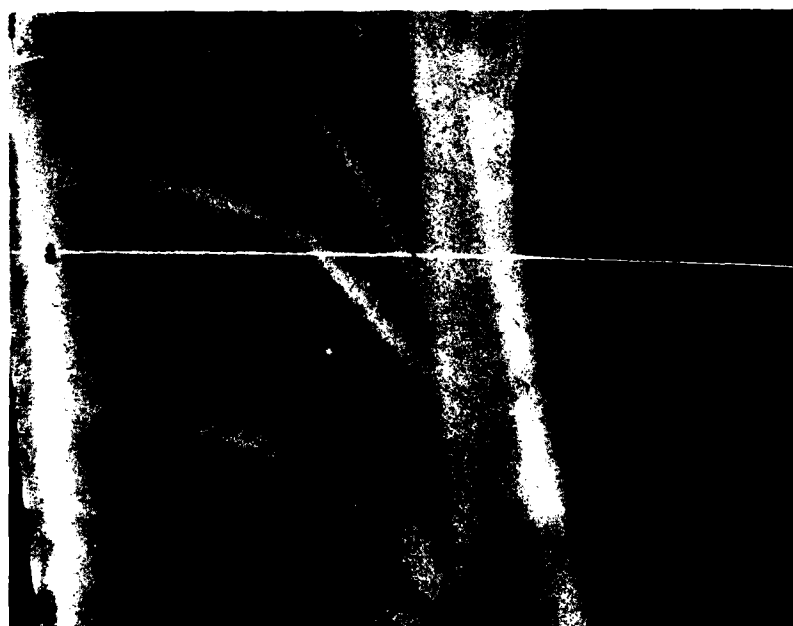
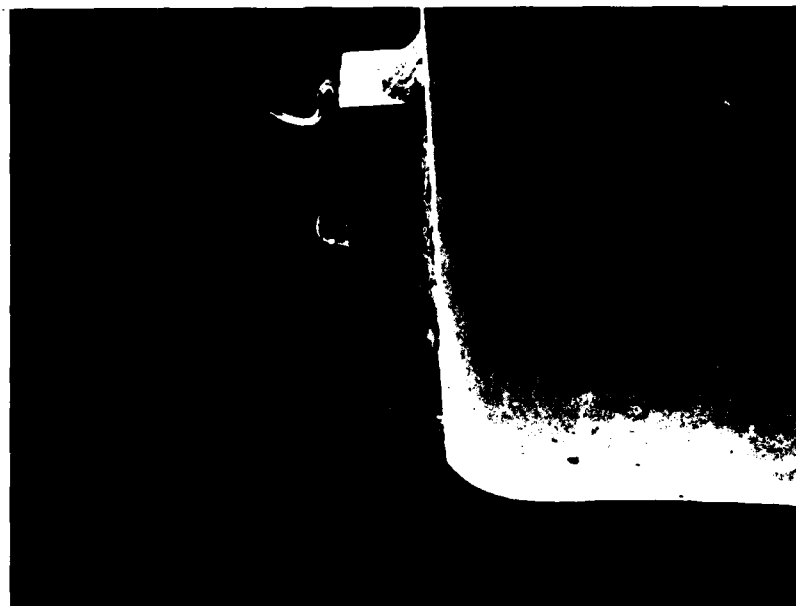


Figure 4. The upper photograph shows the GaAlSb photodiode as viewed from the scanning electron microscope. The lower photograph shows a close-up of the junction region and the electron beam scan for the EBIC study.

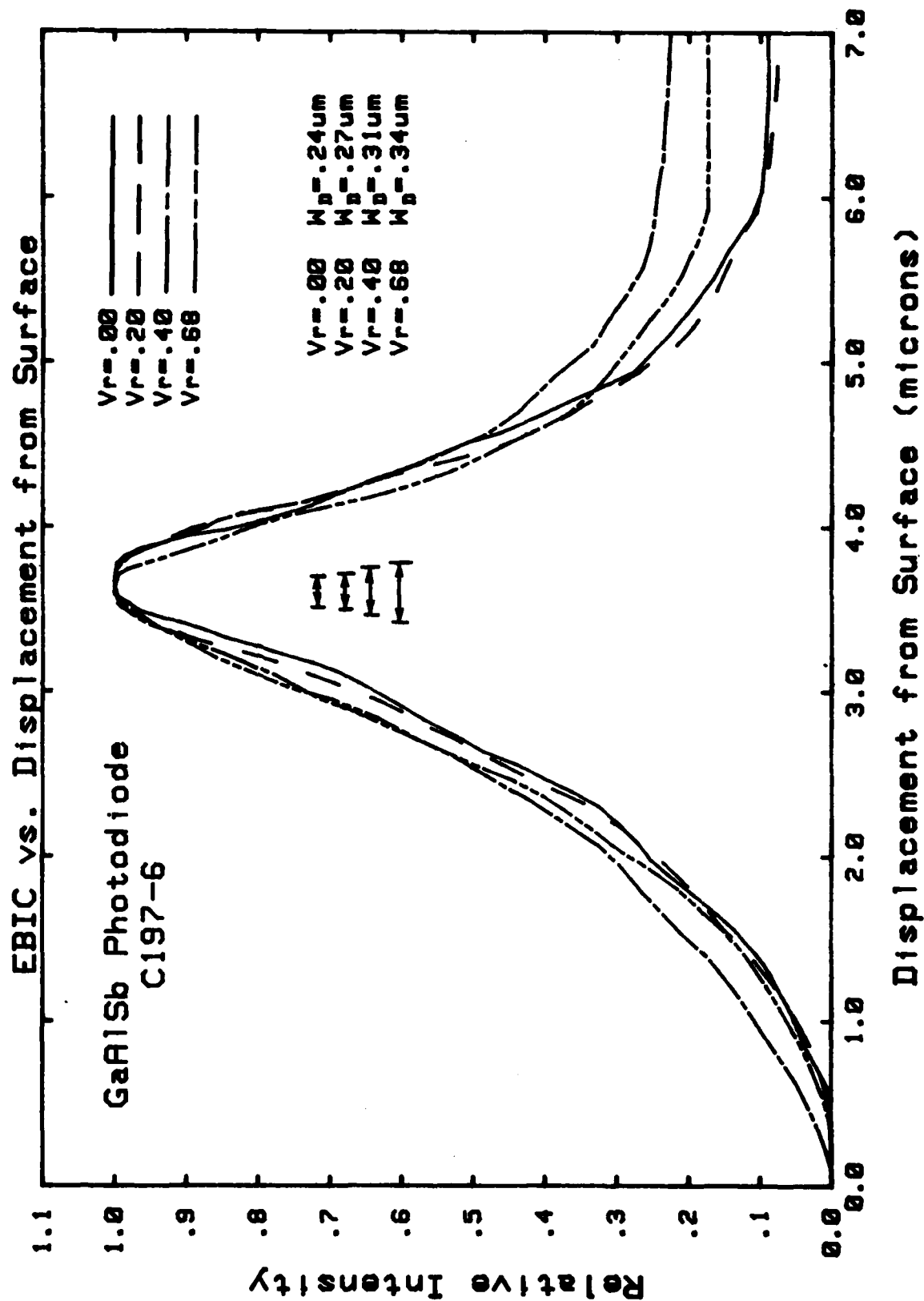


Figure 5. The electron beam induced currents as a function of displacement from the surface are shown.

currents (EBIC) were measured and recorded. At a V_R of .5 volts, the total effective collection length, L' , was determined to be $1.85 \mu\text{m}$. Note, as shown in Fig. 5, the value of L' was not changed significantly as a function of V_R over the range of interest. The diffusion length L_D was determined to be approximately $.9 \mu\text{m}$ from the exponential portion of this data.

Radiation Testing

The GaAlSb photodiodes described above and several commercially available photodiodes were exposed to ionizing radiation from Sandia Laboratories' Gamma Irradiation Facility (GIF) for low dose rate measurements ($\sim 10^2$ rads/sec) and to Sandia Laboratories' Relativistic Electron Beam Accelerator (REBA) for high dose rate measurements (10^7 - 10^8 rads/sec). The commercially available photodiodes tested include the following devices: InGaAsP photodiodes from Mitsubishi (PD-7001); two Si photodiodes from EG&G (FND-100 and YAG-100 optimized for $1.06 \mu\text{m}$ operation); and a Ge device from Rofin (E7460). Quantum efficiencies for these devices are shown in Fig. 6. The radiation induced currents measured at the GIF were small due to the low dose rate. The measured radiation-induced currents were comparable in magnitude to noise levels, and will not be reported further in light of the unambiguous signals measured at REBA.

Since REBA is a pulsed radiation source the circuit configuration shown in Fig. 7 was employed. Typical results are shown in Fig. 8. The peak voltage was used to determine the radiation-induced currents for all cases reported here. In order to make meaningful comparisons of the relative merits of each device in an ionizing radiation environment, we define a radiation response ratio A_{rr} . A_{rr} is the ratio of the signal current density per unit incident optical flux to the radiation current density per rad/sec of dose rate. The current density is simply the measured device current divided by the device cross-sectional area. Note that for systems considerations the signal to noise ratio is approximately proportional to A_{rr}^2 . For A_{rr} listed here, signal currents were measured prior to irradiation.

Results from these tests are compiled in Table II. Also found in Table II are the following parameters: the measured dark current density, the dose rate at which A_{rr} was measured, the peak quantum efficiency, the area of the device, the voltage bias used for the radiation measurements, and the semiconductor material type.

Conclusions

Results from our irradiation studies indicate that both the device structure and the type of semiconductor material are important factors in determining the photodiode response to ionizing radiation. Table II shows the radiation response ratio, A_{rr} for two devices fabricated from InGaAsP, a direct bandgap semiconductor material. This illustrates that the double heterostructure device has a better A_{rr} than the other InGaAsP device.

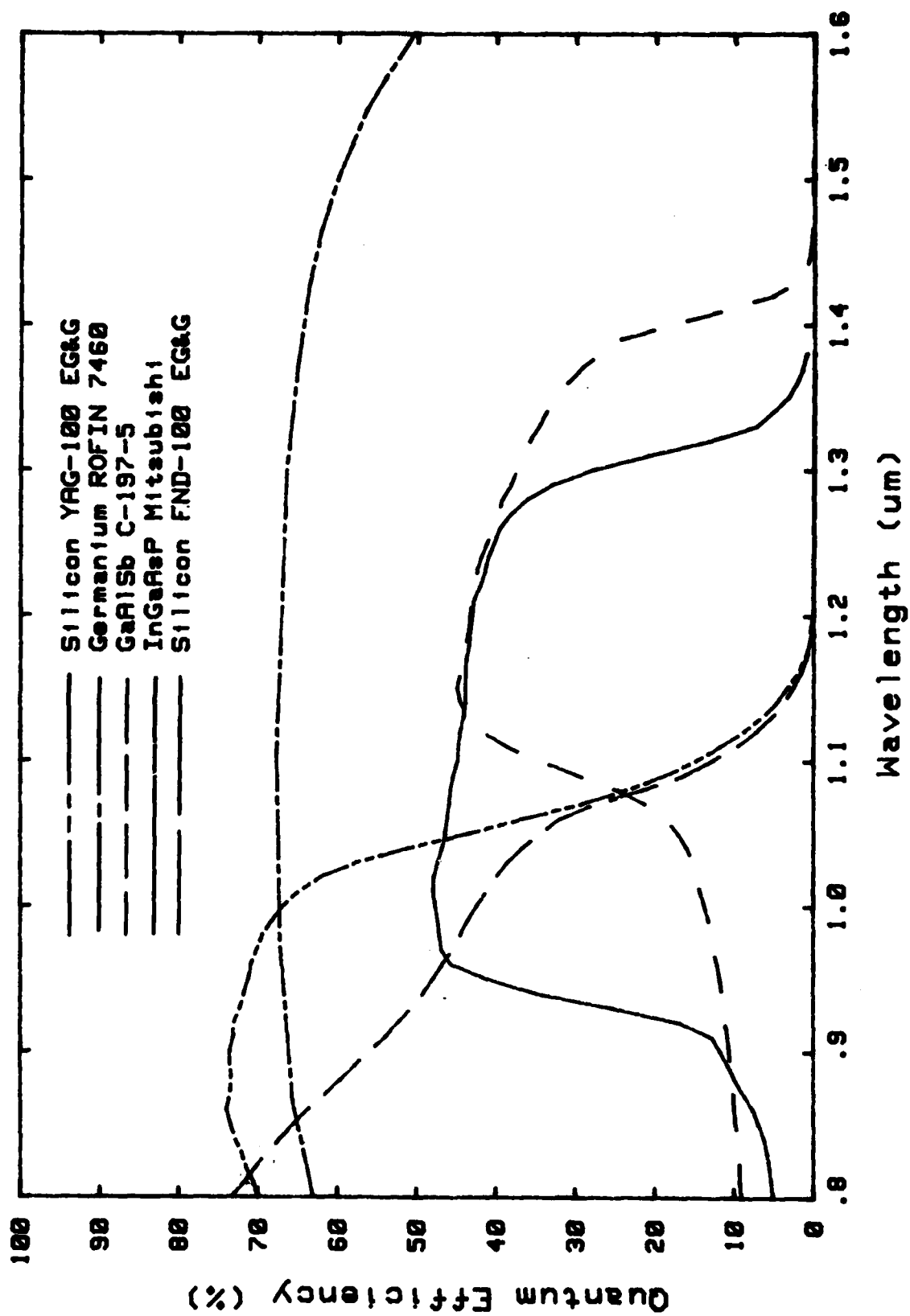


Figure 6. Measured quantum efficiencies for the tested devices.

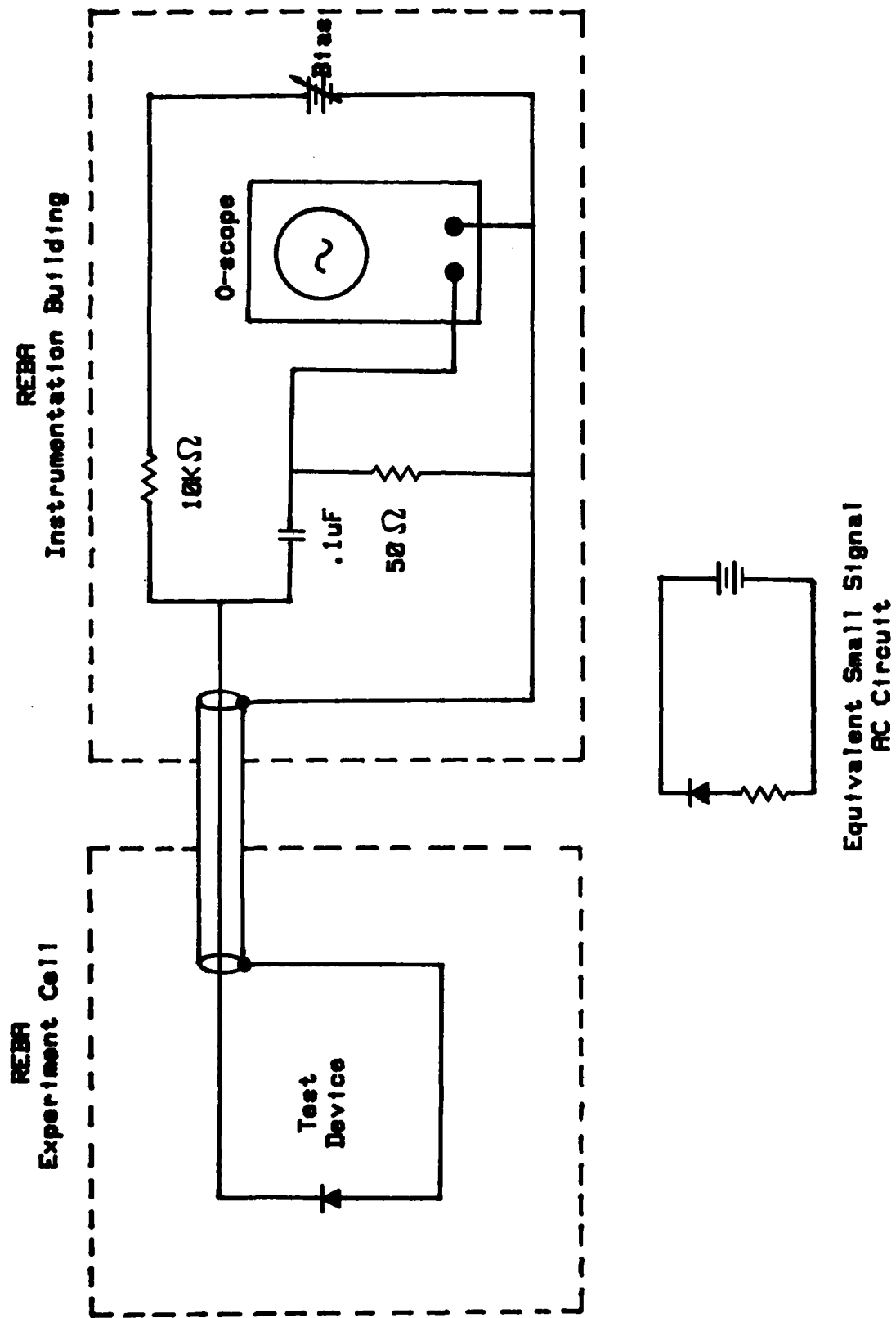


Figure 7. The test circuit configuration used at REBA.

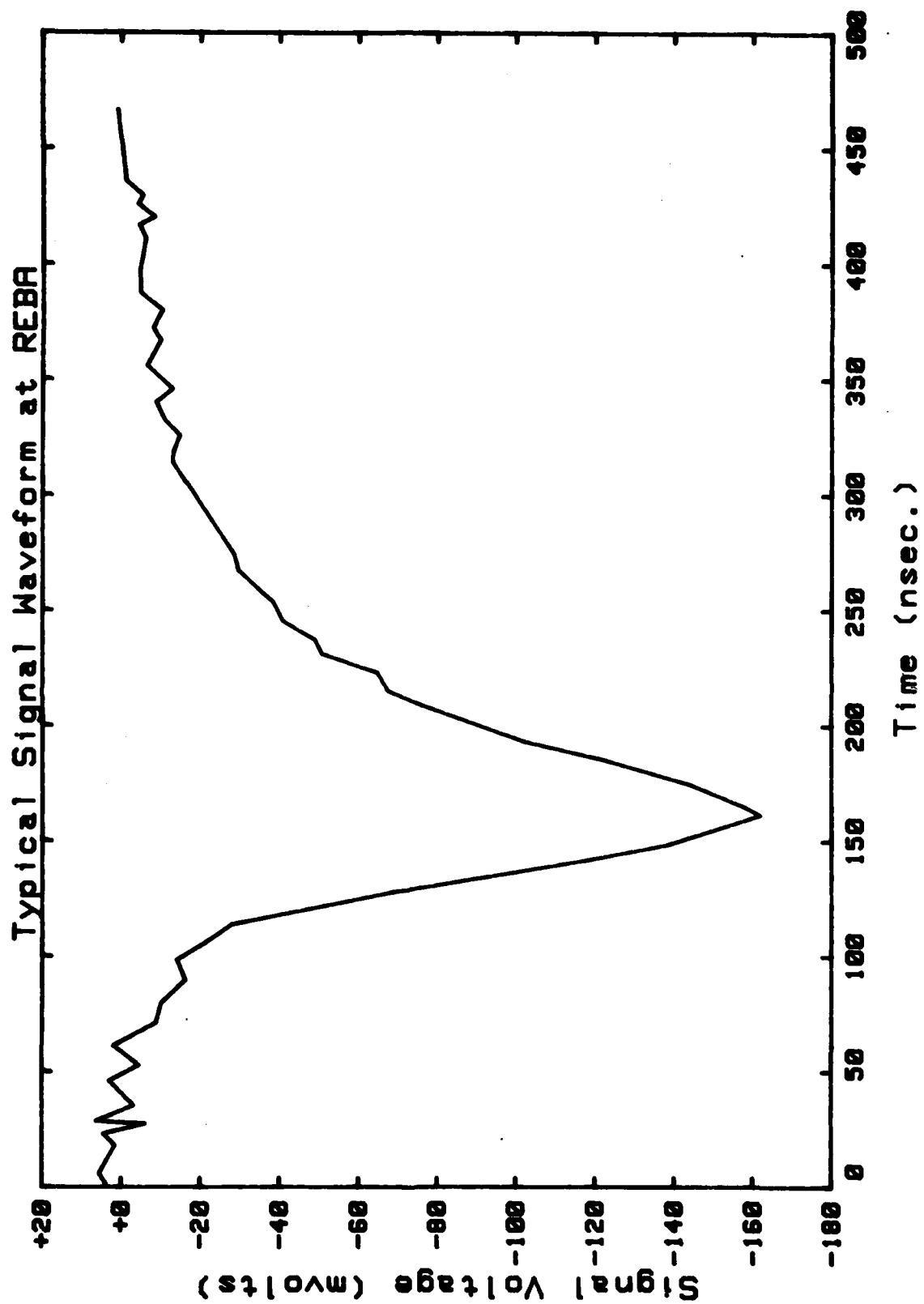


Figure 8. Typical signal waveform recorded during Reba tests.

TABLE II

Device Material and Device #	Peak Quantum Efficiency	Device Area (cm ²)	Device Dark Current Density (A/cm ²)	Diffusion Length μ m	* A_{rr}	Dose Rate (rad/s) @ A_{rr} Measurement	Reverse Bias Condition (volts)
Si							
YAG-100	83% @ 1.03 μ m	5.1×10^{-2}	7.54×10^{-8} $\phi_{vr} = 100$ V	115	4.4	2.1×10^7	80.
FND-100	90% @ .85 μ m	5.1×10^{-2}	1.78×10^{-7} $\phi_{vr} = 70$ V		7.0	2.1×10^7	80.
Ge							
#7460	65% @ 1.3 μ m	7.85×10^{-3}	7.6×10^{-4} $\phi_{vr} = 10$ V		6.6	2.5×10^7	5.0
GaAsSb							
#C-197	40% @ 1.18 μ m	1.45×10^{-2}	1.01×10^{-4} $\phi_{vr} = 0.5$ V	0.9	43.	4.1×10^7	1.0
C-195	35% @ 1.18 μ m	1.45×10^{-2}	1.99×10^{-4} $\phi_{vr} = 0.5$ V	0.9	16	2.0×10^7	1.0
InGaAsP							
Mitsubishi	46% @ 1.05 μ m	8.0×10^{-5}	2.50×10^{-5} $\phi_{vr} = 10$ V		1.8	2.1×10^7	10.
InGaAsP							
#E-008	37% @ 1.06 μ m	1.45×10^{-2}	1.14×10^{-4} $\phi_{vr} = 0.5$ V	1.1	46.	2.2×10^7	1.0

* A_{rr} units = 1.6×10^{-12} rad/optical photon, intended to be a relative measure of ionizing radiation insensitivity. For systems consideration A_{rr} is approximately proportional to the signal to radiation induced noise power ratio.

**A Radiation-Hardening Scheme
for an Analog Fiber-Optic Data Link**

Raine M. Gilbert

U.S. Army Electronics Research and Development Command

Harry Diamond Laboratories

Adelphi, MD 20783

Introduction

Analog fiber-optic systems are being relied on increasingly to transmit nuclear radiation-effects test data from the test point to remote data recording stations. A fiber-optic link designed for such purposes must operate reliably through the radiation pulse in spite of the irradiation of the fiber-optic transmitter and a portion of the optical fiber. The threats to the link from this exposure are a transient radiation effect in the transmitter electronics (TREE) and a transient optical darkening in the cable. Both tend to introduce a spurious signal component. When radiation fluences are sufficiently low in intensity or low in ability to penetrate dense materials, it may be possible to protect the link from these threats with a high-Z shield around the transmitter box and a high-Z loading of the exposed optical cable sheath. The more intense or energetic the radiation is, the more high-atomic-number material must be used to protect the link. One may expect to reach a practical limit on the extent of the fiber shield before reaching a similar limit on the transmitter shield. If this occurs, the threat of fiber darkening may necessitate an additional upset circumvention technique. Such a technique is described below; it calls for 1) optical storage of test data in the shielded transmitter box until the peak transient darkening in the exposed fiber has passed, and 2) a means of accomplishing a real time calibration of the link gain at the time the test signal leaves the transmitter storage and enters the external fiber.

The Link Configuration

Figure 1 shows how an analog fiber-optic data link is normally used in radiation-effects testing, whether the setting is an underground nuclear test or a laboratory simulator experiment. A field or current sensor located at a point of interest in or on the test object produces an electrical signal that is a measure of the test object's electromagnetic response to the radiation pulse. The typical response signal may be hundreds of nanoseconds long, even for radiation pulses much shorter, and may contain significant energy at frequencies as high as several hundreds of megahertz. This electrical signal is transduced to optical form by a laser in the wideband fiber-optic transmitter unit and injected into the optical fiber as an amplitude-modulated light wave. At the remote receiver, a PIN or avalanche photodiode detector converts the optical signal back into an electrical signal, which is then recorded using conventional means.

Figure 2 shows a block diagram of an analog fiber-optic data link modified to allow for both temporary storage of test data and real-time calibration of link gain. The test signal to be transmitted enters the radiation-shielded transmitter box, passes through a remote-controlled attenuator and a preamplifier, and then drives the injection laser diode.

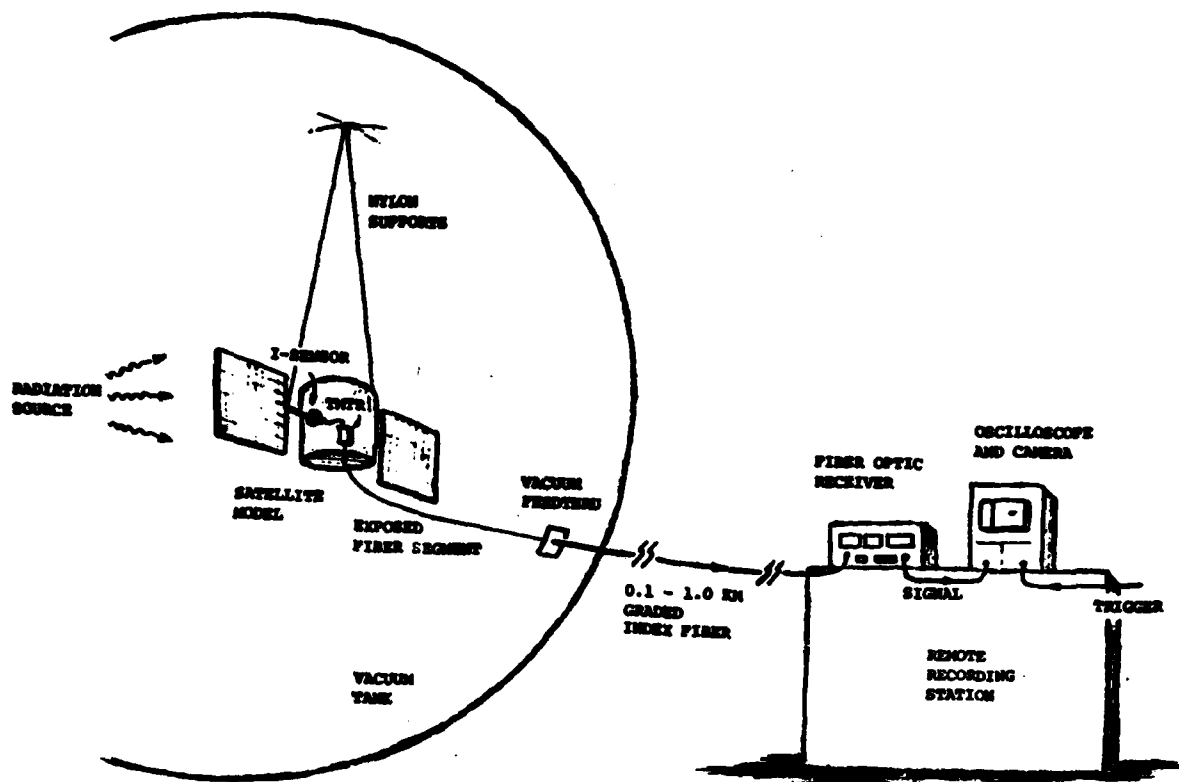


Figure 1. Typical deployment of a fiber-optic data link in a radiation-effects test

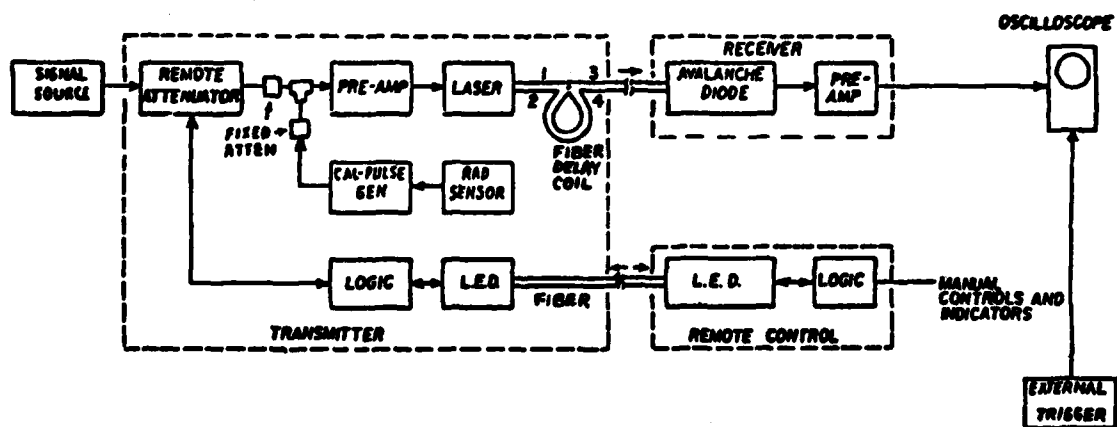


Figure 2. Radiation-hardened link with gamma-dot trigger

The resulting optical signal is launched into a short fiber-optic lead that forms a part of a four-port fiber-optic coupler. Two of the other three ports lead to opposite ends of a fiber delay coil contained in the transmitter box; the last is connected to the exterior optical cable that carries the test signals to the receiver and the remote recording equipment. When the optical test signal reaches the coupler, it divides into two parts; one part is delayed in the coil and the other passes out of the transmitter directly into the exposed fiber segment. In this discussion, it is assumed that this exposed fiber receives a large dose from the x-ray component of the environment and suffers extensive transient and permanent darkening. Depending on the fiber and its temperature, the e-fold times for recovery from the transient darkening vary upwards from at least several hundreds of nanoseconds. The undelayed portion of the signal is therefore assumed to be absorbed in the unrecovered fiber.

The length of the delay coil is chosen to insure that the delayed optical signal stays in the protected interior of the transmitter until the exterior fiber has recovered enough from darkening to allow passage of a detectable signal. Given that the delayed signal is detectable at the remote optical receiver, it nevertheless will be attenuated to some extent by the residual darkness of the fiber. Without a real-time measurement of this attenuation, no quantitative interpretation of test results is possible. The proposed solution to this problem explains why the entire signal is not simply stored in a series delay coil instead of being split in two, with half stored in a parallel delay coil. A calibration signal of known amplitude must precede the delayed test signal out into the exterior fiber by a time interval which is short compared to the fiber recovery time. The detected amplitude of this known calibration signal relative to the detected amplitude of the test signal then provides a complete calibration of the link gain, including the effects of attenuation in the exposed fiber. Accurate synchronization of calibration and test signals requires that the calibration signal be initiated by the same stimulus producing the test signal, namely, the radiation pulse. A gamma-dot sensor, such as a biased pin diode, can easily detect arrival of the radiation at the transmitter and, by its response, trigger a calibration pulse generator. Since such trigger operations consume at least tens of nanoseconds, it is clear that the calibration pulse cannot be injected into the exterior fiber cable ahead of the signal unless there is not only a delay of part of the test signal, but an opportunity for at least a measurable part of the calibration signal to bypass such delay and reach the transmitter exit port ahead of the reemerging test signal. The requirement that the calibration pulse reach the laser after the entire test signal has been transduced, the need to store data for hundreds of nanoseconds at the least, and the importance of insuring that the two parts of the transmitted composite signal are close enough together to preclude significant fiber recovery in the time interval separating them, all dictate the incorporation of a precise delay circuit in the calibration pulse generator. This delay circuit enables the generator to inject the calibration signal through a 10- or 20-nanosecond window which has been delayed the desired number of fiber-recovery time constants beyond the end of the radiation pulse.

Scaling the amplitude of the recorded test signal can be accomplished by using a straightforward scalar conversion factor, given a careful characterization of the coupler's division ratios, or as a differential unfold in frequency space. The latter is necessary only if the transmission

characteristics of the storage coil and signal cable are frequency dependent, such as occurs when fiber lengths are long enough to produce optical pulse dispersion.

Figure 3 shows a slightly different configuration that relies on the transmission of the calibrator trigger from the remote recording station. Since this signal must reach the transmitter through an optical fiber, two special requirements apply: 1) For the trigger signal reaching the transmitter to be strong enough to activate the calibrator, the amount of radiation-induced darkening in the trigger fiber must be suitably small at the time the trigger signal enters the radiation chamber. Thus the fiber used for this purpose must be either hard to radiation (as pure silica-core step-index fibers tend to be) or fast recovering from radiation-induced darkening. 2) The optical storage scheme requires synchronization of the calibration function with a precision of about 110 nanoseconds. This tight tolerance means that the remote station trigger has to be initiated by a radiation-keyed fiducial; the time required to obtain the fiducial and the additional time it takes to send the resulting trigger to the transmitter increase the time interval during which the test data must remain in storage. Pulse dispersion and intrinsic losses place natural limits on the allowable length of the delay coil, so that this configuration is practical only when the recording station is located within a hundred meters or so of the test point.

A final complication in these configurations should be addressed: If the radiation dose in the fiber is so large that permanent darkening is significant, then to that extent, the light intensities reaching the detector after the shot will be smaller than the preshot light level, even assuming complete dissipation of transient darkening by the end of the storage period. It follows that data signals detected then will also be small, since the detector sensitivity must be reduced to accommodate the higher light levels input to it immediately prior to the shot. The net effect is a loss in the effective dynamic range of the fiber-optic link. There is also the possibility that the rapid fluctuations in the transmitted light intensity caused by the onset and subsequent dissipation of fiber darkening may produce very large electrical transients in the receiver, transients large enough to saturate the receiver's electronics and cause loss of data. The solution to these problems appears to be a deliberate blockage of preshot light signals. If this is done, the receiver sensitivity can be maximized without fear of damage to the detector, and the fast transient associated with the onset of fiber darkening is avoided. Figure 4 shows how such a signal gate can be accomplished. A Pockels cell is inserted in the signal channel just in front of the receiver. Set to block preshot light, it is gated open only a safe time interval after the incoming light intensity drops to its postshot level, yet before the delayed test data and calibration signal arrive. The width of the time window in which this gate action must be completed is just the delay time constant of the storage coil. In most cases, this will be at least several hundred nanoseconds long; the timing precision required for a successful gate is therefore considerably less than that required for the calibrator in the fiber-optic transmitter.

An idealized version of what might be recorded on a data channel equipped with the fiber-optic link described above is shown in Figure 5. Appearing first is the undelayed half of the calibrator signal. Following it is the delayed portion of the test signal, and, at the end of the trace, the twice-

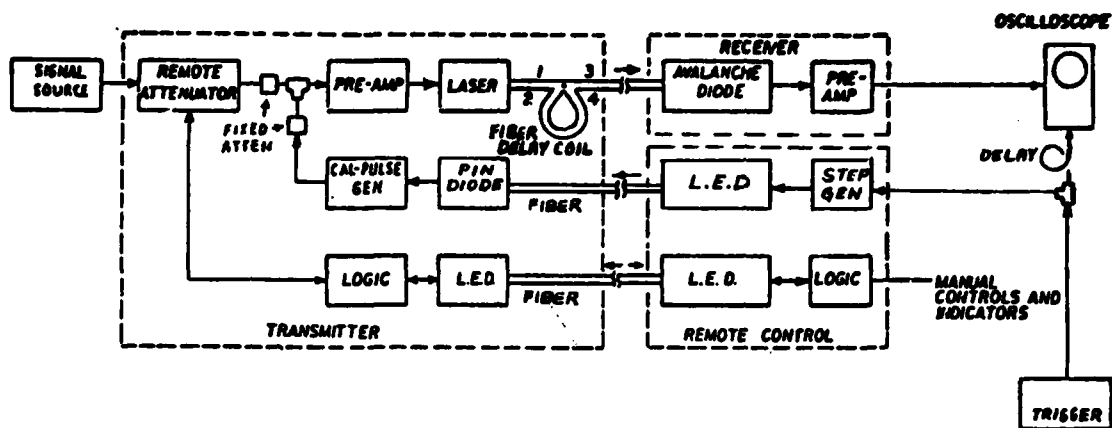


Figure 3. Radiation-hardened link with remote trigger

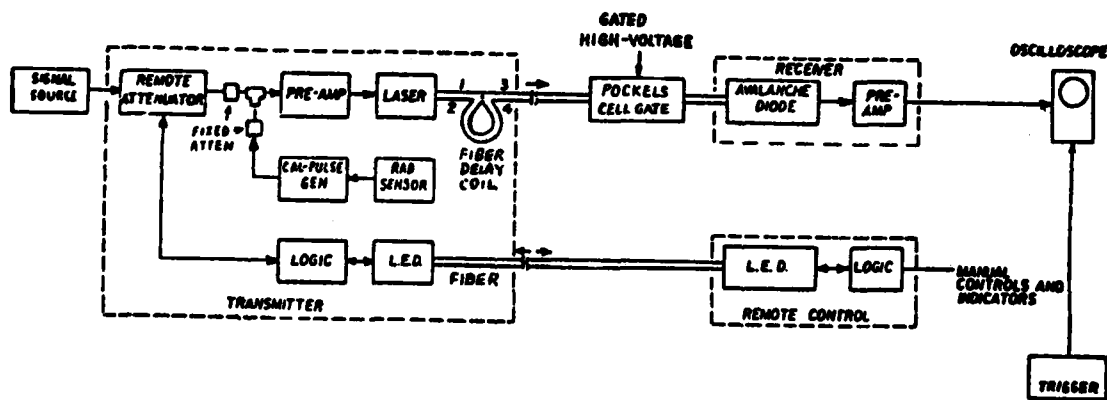


Figure 4. Radiation-hardened link with gamma-dot trigger and Pockels cell signal gate

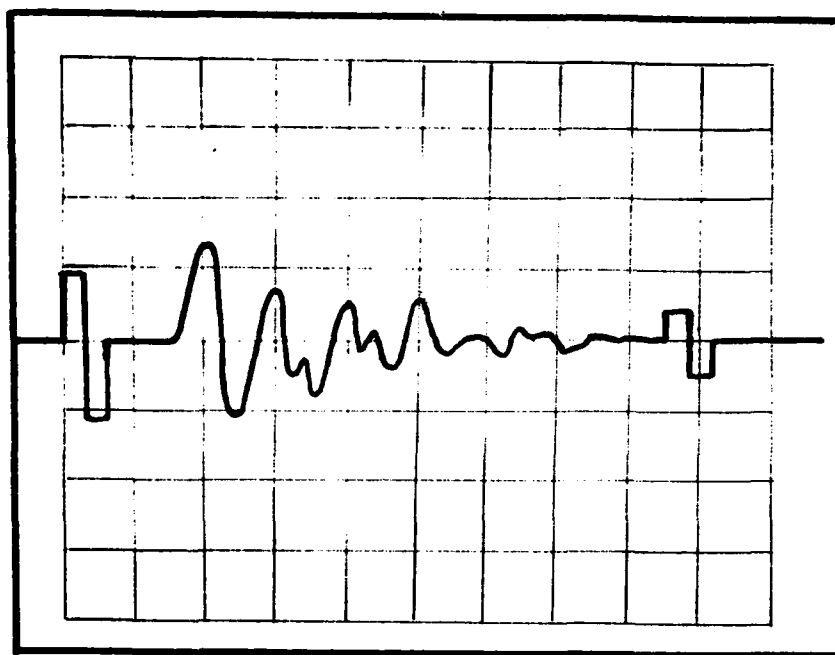


Figure 5. An idealized signal trace

divided calibration signal. The last appears only if a completely fortuitous balance of time constants is obtained; otherwise a delayed sweep would be necessary to record this signal. The ratio of the amplitude of the calibration signal measured preshot (without fiber darkening) to its amplitude on the shot trace provides the direct scaling factor needed to transform the test signal amplitude at the receiver to the desired amplitude at the transmitter.

Concluding Remarks

The radiation hardening scheme described in this paper depends on the exclusion of ionizing radiation from the interior of the transmitter box. In an underground nuclear test (UGT), there are usually three radiation components to consider: low energy photons, high energy photons, and neutrons. The low energy photons can be excluded from the transmitter interior with a reasonably thin high-Z layer sandwiched in the box walls. The high energy photons and the neutrons cannot be excluded without prohibitive shielding. There are two conditions that still make it practical to use this fiber-optic link design in a UGT experiment: 1) the dose associated with the penetrating portion of the photon fluence is relatively small and therefore may be regarded as a predictable perturbation to the fiber-optic signal; and 2) to an extent depending on the distance of the experiment from the radiation source point, the neutrons arrive at the transmitter box after the photons. Thus, there exists a time window through which stored test data may be safely transmitted, given that the signal fiber recovers quickly enough from its photon-induced darkening.

It is also appropriate to point out why the data storage must be accomplished optically rather than on hard-wire signal cable. As stated earlier, radiation-effects test data are usually high frequency response signals that demand wide-bandwidth analog transmission. If this information is stored on even the best wire cable for the time intervals required for fiber recovery, a strong selective absorption of the high frequencies occurs; i.e., a wire cable storage drastically reduces the link's bandwidth. In addition, the volume and mass of a wire cable are much greater than the volume and mass of an equal length of bare optical fiber. Thus, an enlarged transmitter with wire storage produces a greater perturbation to the electromagnetic response of the test object.

Finally, it is recognized that the fiber-optic coupler and its connections in the transmitter may increase the amount of modal noise present in the link. Since it is an artifact of the coherence of single-mode laser emissions and the interference (or speckle) effects associated with coherence, modal noise tends to be enhanced by discontinuities in the optical waveguide. To minimize this effect, the coupler and delay coil should be formed from a single length of fiber: the ends of the fiber are crossed, twisted, and fused, leaving two short leads for input and output and, coupled to them, the optical delay section. If modal noise content is still excessive, a "dither" (microwave modulation) of the laser's operating point may improve matters by reducing the effective coherence time of the laser.² An equivalent improvement might be obtained by using the new multimode injection lasers designed for fast pulse modulation.

References

1. R. M. Gilbert, R. C. Webb, and T. R. Oldham, "Fast Recovery in Optical Fibers Exposed to Pulsed Radiation," presented at DNA Symposium "Fiber Optics in the Nuclear Environment," 25-27 March 1980.
2. J. Blackburn and J. Vanderwall, "Some Artifacts of Modal Noise in Fiber-Optic Systems," Optics Letters, Vol. 4, No. 9, September 1979.

DISTRIBUTION LIST

DEPARTMENT OF DEFENSE

Assistant Secretary of Defense
Comm., Cmd., Cont. & Intell.
ATTN: Principal DASD (C31),
H. Van Trees

Assistant to the Secretary of Defense
Atomic Energy
ATTN: Executive Assistant

Defense Advanced Rsch. Proj. Agency
ATTN: STO C. Thomas
ATTN: R. Kahn
ATTN: H. Winsor

Defense Communications Agency
ATTN: Code C670 T. Trenkle

Defense Communications Engrg. Center
ATTN: Code R311
ATTN: R200

Defense Electronic Supply Center
ATTN: DEFC-ESA

Defense Nuclear Agency
ATTN: RAEV M. Kemp
ATTN: SPTD T. Kennedy
ATTN: RAEV G. Baker
ATTN: STSP
2 cy ATTN: SPSS T. Deevy
ATTN: STRA
10 cy ATTN: SPTD R. Webb
ATTN: DDST T. Knowles
4 cy ATTN: TITL
ATTN: RAAE

Defense Technical Information Center
12 cy ATTN: DD

Dep. Under Secy. of Def. Rsch. & Engrg.
ATTN: R. Moore

Field Command
Defense Nuclear Agency
ATTN: PCTC
ATTN: PCTMD W. Summa
ATTN: PCTMOF
ATTN: PCPR
ATTN: PCT
3 cy ATTN: PCTMEI
ATTN: PCTMD

DEPARTMENT OF DEFENSE (Continued)

Field Command
Defense Nuclear Agency
ATTN: FCPRL
ATTN: FCPRI

National Security Agency
ATTN: P. Szaeapanch
ATTN: H. Solomon
ATTN: N. Grove
ATTN: R-13 H. Hoehn
ATTN: S-65 P. Benson
ATTN: P. Lunney

U.S. Natl. Mil. Rep. SHAPE
ATTN: U.S. Documents Officer
for V. Mostovoj

Under Secy. of Def. for Rsch. & Engrg.
ATTN: R. Ruffine

DEPARTMENT OF THE ARMY

BMD Advanced Technology Center
ATTN: ATC-T M. Capps
ATTN: ATC-O F. Hoke

BMD Systems Command
2 cy ATTN: BMDSC-HW D. DeKalb
ATTN: BMDSC-AOL A. Dumas
ATTN: BMDSC-HLA T. Perdue
ATTN: BMDSC E. Williams

Construction Engineering Rsch. Lab.
ATTN: R. McCormick

Electronics Tech. & Devices Lab.
U.S. Army Electronics R & D Command
ATTN: DELET-R S. Kronenberg

Harry Diamond Laboratories
Department of the Army
ATTN: DELHD-N-P F. Wimenitz
ATTN: DELHD-N-EM C. Share
ATTN: DELHD-N-P
3 cy ATTN: DELHD-N-RBC R. Gilbert
ATTN: DELHD-N-RBC T. Conway
ATTN: DELHD-N-RBC J. Klebers

U.S. Army Ballistic Research Labs
ATTN: DRDAR-BLE J. Keefer
ATTN: DRDAR-BLV
ATTN: DRDAR-FLV

DEPARTMENT OF THE ARMY (Continued)

U.S. Army Cold Region Res. Engr. Lab.
ATTN: Technical Director

U.S. Army Comm-Elec Engr. Instal. Agency
ATTN: L. Stanley
ATTN: Tech. Library

U.S. Army Communications Command
ATTN: CC-OPS-WR R. Nelson

U.S. Army Comm. R&D Command
2 cy ATTN: DRDCO-COM-RM L. Dworkin
ATTN: DRDCO-COM-RM R. Christain
ATTN: DRDCO-COM-RM A. Mondrick
ATTN: DRDCO-COM-RM S. DiVita
ATTN: DRDCO-COM-RM I. Kulback

U.S. Army Corps of Engineers
ATTN: Tech. Library
ATTN: HNDED-P T. Bolt

U.S. Army Engr. Waterways Exper. Station
ATTN: Library
ATTN: Wesse L. Ingram
ATTN: F. Hanes
ATTN: B. Armstrong
ATTN: C. Welch

U.S. Army Foreign Sci. & Tech. Center
ATTN: DRCST-SD-1 C. Ward

U.S. Army Mat. & Mechanics Rsch. Ctr.
ATTN: DRDMR-H J. Hofmann

U.S. Army Missile R & D Command
ATTN: DRCPM-HEL-R T. Roberts
2 cy ATTN: Technical Library
ATTN: DRSMI-MSM D. Loney
ATTN: DRSMI-MSM M. Fecteau

U.S. Army Nuclear & Chemical Agency
ATTN: MONA-WE
ATTN: MONA J. Berberet

DEPARTMENT OF THE NAVY

Newport News Shipbuilding & Drydock Co.
ATTN: Dept. E11 H. Hubbnier
ATTN: Dept. E23 R. Swain

David Taylor Naval Ship R & D Center
ATTN: Code 1770
ATTN: Code 1740.1
ATTN: Code 177 E. Palmer

Naval Air Systems Command
ATTN: AIR-310B JP-1 R440 J. Willis
ATTN: AIR-360G JP-2 J. Schultz

DEPARTMENT OF THE NAVY (Continued)

Naval Coastal Systems Laboratory
ATTN: H. Larrimore

Naval Construction Battalion Center
ATTN: Code L51 R. Odello

Naval Electronic Systems Command
ATTN: Code 3101 F.C. Deckelman

Naval Ocean Systems Center
ATTN: C. Young
ATTN: 825 R. Kochanski
ATTN: Code 825 D. Williams
ATTN: Code 7309 R. Greenwell
ATTN: Code 9242 R. Lebuska
ATTN: Code 7309 J. Tinston

Naval Plant Representative Office
Lockheed Missile & Space Company
ATTN: C. Hashins

Naval Research Laboratory
ATTN: Code 6570 R. Ginther
5 cy ATTN: Code 5584 G. Sigel
ATTN: Code 7909 D. Griscom
ATTN: Code 5584 B. Evans
ATTN: Code 6500 T. Giallorenzi
ATTN: Comsat DR. Revese
ATTN: Code 5584 R. Allen
ATTN: Code 5503 J. MacCallum
ATTN: Code 7909 D. Garrett
ATTN: Code 7904 B. Evans
ATTN: Code 7904 B. Collins
ATTN: Code 7904 L. Abella
ATTN: Code 5584 E. Friebele

Naval Security Group Command
ATTN: W. Woodman

Naval Surface Weapons Center
ATTN: Code R15 G. Hammond
ATTN: C. Holton
ATTN: Code R14 I. Blatstein
ATTN: Code F31

Naval Surface Weapons Center
ATTN: R. Hudson
ATTN: DF-24 H. Lewis

Naval Weapons Center
ATTN: L. Hutcheson

Naval Weapons Evaluation Facility
ATTN: Code 721 R. Friedberg
ATTN: Code 72 R. Tillery

Office of Naval Research
ATTN: Code 474 N. Perrone

DEPARTMENT OF THE AIR FORCE

Air Force Aero-Propulsion Laboratory
ATTN: AAD F. Iozzi
ATTN: AAD E. Frier

Air Force Weapons Laboratory, AFSC
ATTN: ELP J. Mallis
ATTN: ELP R. Dunn
ATTN: SUL
ATTN: ELP M. McQuade
ATTN: ELP B. Rose
ATTN: DEX J. Renick
ATTN: DYC J. Emmes
2 cy ATTN: DYC E. Taylor

Air Force Wright Aeronautical Labs.
ATTN: AAD-3 K. Trumble
ATTN: AAD-3 D. Zann

Deputy Chief of Staff
Research, Development & Acq.
Department of the Air Force
ATTN: AFRDQSM

Headquarters Space Division/SK
Air Force Systems Command
ATTN: SKY C. Kennedy

Headquarters Space Division/YC
Air Force Systems Command
ATTN: YCPT D. Bartel
ATTN: YCD E. Brininstool
ATTN: YCD R. Spray
ATTN: YCP H. Staubs

Headquarters Space Division/YN
Air Force Systems Command
ATTN: YNV J. Turnispeed
ATTN: YN B. Brady
ATTN: YN J. Sweeney
ATTN: YN A. Varisco

Rome Air Development Center, AFSC
2 cy ATTN: ESR J. Wall
ATTN: ESR A. Yang

Strategic Air Command/XPPS
ATTN: E. Winger

DEPARTMENT OF ENERGY

Department of Energy
ATTN: CTID

OTHER GOVERNMENT AGENCIES

Institute for Telecommunications Sciences
ATTN: J. Hull

OTHER GOVERNMENT AGENCIES (Continued)

NASA
ATTN: R. Gallera

DEPARTMENT OF DEFENSE CONTRACTORS

Acurex Corp.
ATTN: K. Triebs

Advanced Research & Applications Corp.
ATTN: R. Armistead

Aerospace Corp.
ATTN: W. Blocker
ATTN: W. Otsuki
ATTN: S. Bower

Amphenol
ATTN: J. Makuch

University of Arizona
ATTN: J. Burke

Artec Associates, Inc.
ATTN: D. Baum

Automation Industries, Inc.
ATTN: D. Moltrup

BDM Corp.
ATTN: T. Neighbors

Bell Telephone Labs
ATTN: J. Fleming

Boeing Co.
ATTN: F. Davies
ATTN: O. Mulkey
ATTN: A. Johnston
ATTN: I. Arimura
ATTN: M/S 42-33 J. Kennedy
ATTN: R. Caldwell
ATTN: R. Dyrdahl

Brookhaven National Laboratory
ATTN: P. Levy

University of California at Los Angeles
Office of Contract & Grant Admin.
ATTN: J. MacKenzie

Catholic University of America
ATTN: J. Clark

Charles Stark Draper Lab., Inc.
ATTN: P. Kelly

DEPARTMENT OF DEFENSE CONTRACTORS (Cont.)

Computer Sciences Corp.
ATTN: D. Maxwell
ATTN: F. Eisenbarth

Consolidated Controls Corp
ATTN: R. Sherburne

Develco, Inc.
ATTN: D. Ray
ATTN: L. Rorden

Dupont Co.
ATTN: C. Furgatson

Effects Technology, Inc.
ATTN: D. Hogg
ATTN: W. Naumann
ATTN: E. Bick
ATTN: R. Wengler

EG&G, Idaho, Inc.
ATTN: M. Stanley/WCB-W2
ATTN: C. Lai/CF 689

EG&G/Kirtland
ATTN: S. Ornell

EG&G, Inc., Goleta
ATTN: M. Nelson
ATTN: T. Davies
ATTN: R. Lynn

EG&G, Inc., Las Vegas
ATTN: P. Zavaharo
ATTN: G. Hughes

EG&G, Inc., Los Alamos
ATTN: R. Robichaud

Eric H. Wang
Civil Engineering Research Fac.
ATTN: E. Wang
ATTN: N. Baum

Galileo Electro-Optics Corp.
2 cy ATTN: L. Owen
ATTN: J. Makuch

Gard, Inc.
ATTN: J. Ferro

General Dynamics Corp.
ATTN: K. Wilson

General Electric Company-TEMPO
ATTN: DASAC
ATTN: J. Schoutens

DEPARTMENT OF DEFENSE CONTRACTORS (Cont.)

General Electric Company
General Research & Development
ATTN: J. Whitten

Geocenters, Inc.
ATTN: L. Isaacson
ATTN: E. Marram
ATTN: McGuire

GTE Sylvania, Inc.
ATTN: J. Waldron

H-Tech Labs, Inc.
ATTN: B. Hartenbaum

Holmes & Narver, Inc.
2 cy ATTN: R. Briggs

Honeywell, Inc.
Radiation Center
ATTN: I. Abel

Honeywell, Inc.
Corporate Technology Center
ATTN: J. Ready

Hughes Aircraft Co.
ATTN: R. Blair

IIT Research Institute
ATTN: A. Tulus

Information Gatekeepers, Inc.
ATTN: P. Polishuk

International Communications & Energy (ICE)
ATTN: S. Elion

International Tel. & Telegraph Corp.
ATTN: A. Asam
ATTN: G. Wilhelm
ATTN: L. Huybrechts
ATTN: M. Maklad

IRT Corp.
ATTN: W. Hardwick
ATTN: A. Kalma

JAYCOR
ATTN: H. Hardwick
ATTN: L. Scott
ATTN: R. Poll

JAYCOR
ATTN: H. Linnerud

DEPARTMENT OF DEFENSE CONTRACTORS (Cont.)

Kaman Sciences Corp.
ATTN: F. Rich
ATTN: D. Sachs
ATTN: P. Tracy
ATTN: F. Shelton

Lawrence Livermore Laboratory
ATTN: L-200 J. Cortez
ATTN: H. Glenn
ATTN: L-14 W. Dickinson
ATTN: L-38 H. Reynolds

Litton Systems, Inc.
ATTN: J. Retzler

Lockheed Missile & Space Co., Inc.
ATTN: J. Heisey

Lockheed Missiles & Space Co., Inc.
ATTN: Dept. 52-51/202 K. Chow
ATTN: B. Kincaid
ATTN: D. Kohler
ATTN: D. Fisher
ATTN: K. Chan
ATTN: S. Salisbury
ATTN: R. Smith
ATTN: J. Bronko
ATTN: R. Bardin
ATTN: L. Chase

Lockheed Missiles & Space Co., Inc.
ATTN: H. Moving
ATTN: S. Taimuty
ATTN: J. Peterson
ATTN: J. Heisey
ATTN: M. Rovero
ATTN: C. Vlcek

Lockheed Missiles & Space Co., Inc.
ATTN: M. Polisky

Los Alamos Scientific Laboratory
ATTN: H. Agnew
ATTN: C. Keller
ATTN: P. Whalen
ATTN: R. Thorn
ATTN: E. Hodson
5 cy ATTN: MS/410 P. Lyons

Lovelace Biomed. & Environ. Rsc. Inst., Inc.
ATTN: R. Fletcher

Martin Marietta Corp.
ATTN: Tech. Library
ATTN: D. Easter
ATTN: R. Gaynor

DEPARTMENT OF DEFENSE CONTRACTORS (Cont.)

McDonnell Douglas Corp.
ATTN: R. Poppitz
ATTN: N. Campbell

McDonnell Douglas Corp.
ATTN: R. Halprin
ATTN: H. Campbell
ATTN: A. Suetzoff

University of Michigan
ATTN: V. Weston

Mission Research Corp.
ATTN: V. Van Lint
ATTN: B. Passenheim

Mitre Corp.
2 cy ATTN: J. Quarato
ATTN: B. Metcalf

Newport News Shipbuilding
ATTN: R. Harrington

Nichols Research Corp., Inc.
2 cy ATTN: N. Byrn

Northrop Corp.
ATTN: J. Srouer
ATTN: A. Kalma

Oak Ridge National Laboratory
ATTN: R. Weeks
ATTN: D. McCuf

Physics Applications, Inc.
ATTN: C. Vincent

Physics International Co.
ATTN: F. Sauer
ATTN: C. Godfrey
ATTN: Technical Library

Polytechnic Institute of New York
ATTN: A. Oliner

R & D Associates
ATTN: R. Poll
ATTN: C. Rogers
ATTN: C. MacDonald
ATTN: W. Graham, Jr.

Rockwell International Corp.
ATTN: R. Titus
ATTN: G. Messenger
ATTN: D. Still

DEPARTMENT OF DEFENSE CONTRACTORS (Cont.)

University of Rutgers
College of Engineering
ATTN: H. Smyth

Sandia National Laboratories
ATTN: K. Mitchel
2 cy ATTN: M. Landry
ATTN: L. Vortman
2 cy ATTN: C. Barnes
ATTN: E. Bernisse
ATTN: H. Miller
ATTN: ORG 2330 E. Barsis
ATTN: J. Plimpton
ATTN: R. Heckman

Science Applications, Inc.
ATTN: Technical Library

Science Applications, Inc.
ATTN: R. Miller

Science Applications, Inc.
ATTN: Technical Library
ATTN: W. Mendes

Science Applications, Inc.
ATTN: W. Chadsey

Science Applications, Inc.
ATTN: K. Sites

Southeastern Institute of Technology
2 cy ATTN: R. Watson

Spectronics, Inc.
ATTN: L. Stewart

Sperry Univac
ATTN: U2-T20 W. Davis

SRI International
ATTN: G. Abrahamson
ATTN: R. Lee
ATTN: D. Keough

Systems, Science & Software, Inc.
ATTN: D. Grine
ATTN: P. Coleman

Teledyne Brown Engineering
ATTN: B. Henderson
2 cy ATTN: G. Landwehr
ATTN: Technical Library
ATTN: M. Price

Tetra Tech., Inc.
ATTN: H. Hodara

DEPARTMENT OF DEFENSE CONTRACTORS (Cont.)

Times Wire and Cable Co.
ATTN: W. Primrose

TRW Defense & Space Systems Group
ATTN: S. Kimble
ATTN: J. Tambo
ATTN: P. Goldsmith
ATTN: R. Eastman
ATTN: G. Armstrong
ATTN: H. Rathien
ATTN: A. Thomas
ATTN: H. Gaar
ATTN: N. Lipner
ATTN: T. Walter - MI 1338

TRW Defense & Space Systems Group
ATTN: P. Dai

Valtec Corp.
ATTN: I Aggarwal